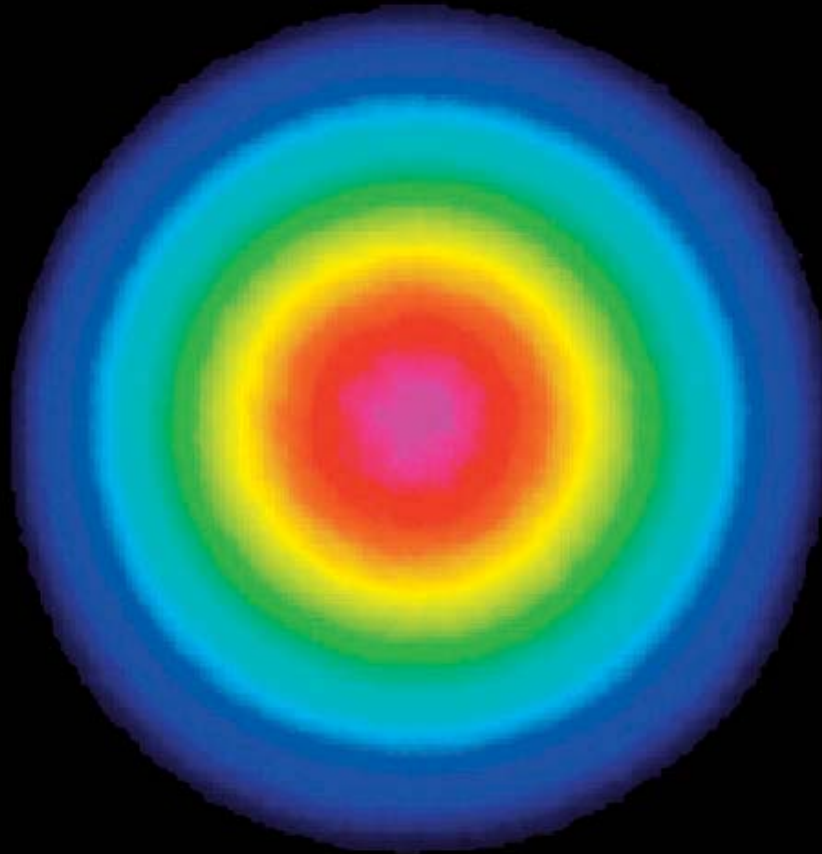


Louis McDonagh



**888 nm pumping of Nd:YVO₄
for high-power TEM₀₀ lasers**



Cuvillier Verlag Göttingen
Internationaler wissenschaftlicher Fachverlag

**888 nm pumping of Nd:YVO₄
for high-power TEM₀₀ lasers**

Dissertation

Louis McDonagh

Vom Fachbereich Physik der Technischen Universität Kaiserslautern zur Verleihung
des akademischen Grades „Doktor der Naturwissenschaften“ genehmigte Dissertation

Betreuer: Prof. Dr. Richard Wallenstein

Zweitgutachter: Prof. Dr. René Beigang

Datum der wissenschaftlichen Aussprache: 09.07.2008

D 386

Bibliografische Information der Deutschen Nationalbibliothek

Die deutsche Nationalbibliothek verzeichnet diese Publikation in der Deutschen Nationalbibliografie; detaillierte bibliografische Daten sind im Internet über <http://dnb.ddb.de> abrufbar.

1. Aufl. - Göttingen: Cuvillier, 2011

Zgl.: (TU) Kaiserslautern (Univ.), 2008

978-3-86955-028-2

© CUVILLIER VERLAG, Göttingen 2011

Nonnenstieg 8, 37075 Göttingen

Telefon: 0551-54724-0

Telefax: 0551-54724-21

www.cuvillier.de

Alle Rechte vorbehalten. Ohne ausdrückliche Genehmigung des Verlages ist es nicht gestattet, das Buch oder Teile daraus auf fotomechanischem Weg (Fotokopie, Mikrokopie) zu vervielfältigen.

1. Auflage, 2011

Gedruckt auf säurefreiem Papier

978-3-86955-028-2

Chaque année il y a un champion.

Arthémon Hatungimana

To Chris

Abstract

888 nm pumping of Nd:YVO₄ for high power TEM₀₀ lasers

For the last decade, neodymium-doped orthovanadate has established itself as the active material of choice for commercial solid-state lasers emitting in the 1 μm range, with output powers from several hundred milliwatts to a few tens of watts, in continuous-wave, short nanosecond Q-switched, or picosecond modelocked pulsed regimes. Its main advantages over other Nd-doped hosts such as YAG are a large stimulated-emission cross section leading to a high gain, a strong pump absorption allowing the efficient mode-matching of tightly-focused pump light, and a natural birefringence resulting in a continuously polarized output. The main drawbacks, however, are rather poor mechanical characteristics and strong thermal lensing, effectively limiting the maximum applicable pump power before excessively strong and aberrated thermal lensing prevents an efficient operation in a diffraction-limited beam, and ultimately the crystal's fracture. Put aside the power limitation, the association of vanadate with diode end pumping allows for the realization of highly efficient and reliable laser sources based on well-known technologies, which provides an advantage in terms of manufacturability and cost-effectiveness over other high-potential technologies such as disks and fibers.

This thesis introduces a novel pumping technique for Nd:YVO₄ that allows for the realization of significantly higher-power laser sources with a high optical-to-optical efficiency and diffraction-limited beam quality, while keeping the benefits of a well-established technology. It consists in pumping at a wavelength of 888 nm instead of the classic 808 nm, providing a low and isotropic absorption, which results in a smooth distribution of the absorbed pump light in long crystals, effectively limiting the deleterious effects of high inversion density such as crystal end-facet bulging, high crystal temperature, aberrated thermal lensing, and upconversion. After presenting vanadate's spectroscopic and physical characteristics, a complete analysis of the heat-generating effects is performed, allowing for side-by-side simulations of the thermal effects in practical 808 nm and 888 nm pumped systems, and for an evaluation of their respective thermal lensing behaviors.

Continuous-wave operation was thoroughly investigated, first in a multi-transversal mode oscillator to assess the maximum optical efficiency with optimum pump-mode matching and the thermal lensing characteristics. A TEM₀₀ resonator was then developed with a single crystal and one pump diode, providing 60 W of output power with an optical efficiency of 55% and a beam quality of $M^2 = 1.05$. This resonator was symmetrically replicated to form a periodic resonator, providing 120 W of output with the same optical efficiency and beam quality. This two-crystal configuration was then modified to an oscillator-amplifier configuration, providing a single-pass extraction efficiency of 53% and a total oscillator-amplifier output of 117 W without any beam-quality degradation. Intracavity doubling of the one and two-crystal configurations was achieved by inserting a non-critically phase-matched LiB₅O₃ (LBO) non-linear crystal in the resonator, providing up to 62 W of diffraction-limited green light at 532 nm with low-noise

characteristics thanks to a large number of oscillating modes, thus limiting the effects of the “green problem”.

A strong industrial interest resides in Q-switched lasers emitting nanosecond pulses, particularly with a high average power, high pulse repetition rate, and pulse durations of a few to several tens of nanoseconds. Achieving high-frequency and short-pulse operation both require a high gain, which explains the domination of Nd:YVO₄ over lower-gain materials such as Nd:YAG or Yb:YAG. Thus, an acousto-optically Q-switched oscillator was demonstrated with 50 W output power and 28 ns pulse duration at 50 kHz. Pulse duration, however, is inversely proportional to the pulse energy, so that an increase in repetition rate inevitably results in an almost linear increase in pulse width. A cavity-dumped Q-switched oscillator was built to circumvent this limitation, the pulse length being defined by the cavity roundtrip time and the electro-optic cell switching time. It provided a constant pulse duration of 6 ns up to a repetition rate of 100 kHz and a maximum output power of 47 W. Such short pulse durations are normally available with output powers of a few watts from Q-switched lasers, and conversely Q-switched lasers of similarly high output power deliver pulses of several tens to over 100 ns in duration.

There exists another strong interest in high average power quasi-cw picosecond sources, which allow for the efficient generation of green and UV radiation, or even red-green-blue for laser video projection. Passive mode locking with a semiconductor saturable absorber mirror (SESAM) is the preferred technique employed for the stable and self-starting generation of picosecond pulse trains, yet a high gain is necessary for achieving high repetition rates while avoiding the Q-switched mode-locking regime. Thus SESAM mode locking was applied to an 888 nm pumped oscillator, achieving 57 W of output power at a repetition-rate of 110 MHz and a pulse duration of 33 ps. Its output was efficiently amplified in a single pass up to 111 W without any beam quality, temporal, or spectral degradation. The high peak power of 30 kW allowed for the generation of 87 W of second harmonic at 532 nm with an efficiency of 80%, and 35 W of 355 nm third harmonic with a conversion efficiency of 33% in LBO crystals.

The wide range of high-power systems demonstrated in this work illustrate the benefits of the optimized pumping of Nd:YVO₄ at 888 nm, maintaining its highly-desirable characteristics such as a high gain and a polarized output while extending its power capabilities far beyond regular 808 nm pumped systems. This improvement should allow Nd:YVO₄ systems to compete with high-power technologies such as disks and fibers, which often struggle in the generation of short pulses because of their low gain and strong non-linear effects, respectively.

Kurzzusammenfassung

888 nm Pumpanregung für Hochleistung Nd:YVO₄ Laser

In den vergangenen zehn Jahren hat sich neodymdotiertes Orthovanadat als das Material der Wahl für den Einsatz in kommerziellen Festkörperlasern im Wellenlängenbereich um 1 μm bei mittleren Ausgangsleistungen von einigen hundert Milliwatt bis zu mehreren zehn Watt etabliert. Dieses Verstärkungsmedium eignet sich sowohl für die kontinuierliche Emission, als auch für die Güteschaltung im Nanosekundenbereich oder für den Betrieb im modengekoppelten Regime mit Impulsdauern im Bereich weniger Pikosekunden. Die wesentlichen Vorteile dieses Materials gegenüber anderen neodymdotierten Wirtskristallen wie beispielsweise YAG ergeben sich neben seinem großen Wirkungsquerschnitt für stimulierte Emission und der damit einhergehenden hohen Verstärkung auch aus der starken Pumplichtabsorption, die einen effizienten Überlapp zwischen der Lasermode und einem stark fokussierten Pumpstrahl ermöglicht. Darüber hinaus gewährleistet die natürliche Doppelbrechung des Kristalls eine stabile lineare Polarisierung der ausgekoppelten Strahlung. Als Nachteile sind neben den verhältnismäßig ungünstigen mechanischen Eigenschaften die Neigung zur Ausbildung thermischer Linsen anzuführen. Diese führen zu einer Begrenzung der maximalen Pumpleistung durch die damit verbundenen starken Aberrationen, welche die Emission in einem beugungsbegrenzten Strahl verhindern und letztlich auch zur Zerstörung des Kristalls führen können. Lässt man die Beschränkung der mittleren Ausgangsleistung außer Betracht, so bringt Nd:YVO₄ in Kombination mit der longitudinalen Anregung durch Diodenlaser hocheffiziente und zuverlässige Laserquellen auf der Basis wohlbeherrschter Technologien hervor und besitzt hinsichtlich Fertigbarkeit und Kosteneffizienz entscheidende Vorteile gegenüber scheiben- oder faserbasierten Lösungen.

Die vorliegende Arbeit stellt ein neues Verfahren zur Pumpanregung für Nd:YVO₄ vor, welches die Realisierung neuartiger Laserquellen mit signifikant höherer Leistung, hohem optisch zu optischem Wirkungsgrad und einer beugungsbegrenzten Strahlqualität ermöglicht, und gleichzeitig mit jenen Vorteilen verbindet, die durch die Nutzung einer etablierten Technologie entstehen. Die Besonderheit des Verfahrens liegt in der Anregungswellenlänge von 888 nm anstelle der klassischerweise verwendeten 808 nm. Dieses Vorgehen bietet den Vorteil einer niedrigen und isotropen Absorption, welche in einer gleichmäßigen Verteilung des absorbierten Pumplichts in langen Kristallen resultiert und somit eine Unterdrückung schädlicher Effekte bewirkt, wie sie durch eine hohe Inversionsdichte im Verstärkungsmedium auftreten. Dies sind vor allem Wölbung der Kristallendfacetten, hohe Kristalltemperatur, Aberrationen durch thermische Linsen so wie Upconversionprozesse. Nach einer einleitenden Darstellung der spektroskopischen und physikalischen Eigenschaften von Nd:YVO₄ folgt eine umfassende Analyse der wärmeerzeugenden Effekte im Rahmen einer vergleichenden Simulation in realitätsnahen Systemen mit Anregung bei 808 nm bzw. 888 nm, deren Ergebnisse im Hinblick auf die thermische Linsenwirkung bewertet werden.

Als Ausgangspunkt der umfassenden experimentellen Charakterisierung wurde zunächst der kontinuierliche Betrieb eines Oszillators mit mehreren Transversalmoden untersucht, um die

maximale optische Effizienz bei optimalem Pumpmodenüberlapp so wie die thermische Linsenbildung zu studieren. Im Anschluß daran wurde ein TEM₀₀ Resonator entwickelt, der einen einzigen Kristall beherbergte und mit einer einzigen Pumpdiode angeregt wurde. Diese Anordnung emittierte 60 W Ausgangsleistung mit einem optischen Wirkungsgrad von 55% und einer Strahlqualität von $M^2 = 1.05$. In einem nächsten Schritt wurde dieser Resonator repliziert, um in einer symmetrischen Anordnung einen periodische Resonator zu formen, welcher 120 W Leistung mit gleich hoher optischer Effizienz und Strahlqualität erzeugte. Dieser Aufbau wurde anschließend in eine Oszillator-Verstärker-Konfiguration überführt, die im Einfachdurchgang bei gleichzeitig unvermindert hoher Strahlqualität eine Extraktionseffizienz von 52% und eine Gesamtausgangsleistung von 115 W lieferte. Schließlich wurde sowohl für die Anordnung mit einem, als auch für jene mit zwei Kristallen durch resonatorinterne Frequenzverdopplung mittels nichtkritisch angepasstem LiB₅O₃ (LBO) grüne, beugungsbegrenzte Laserstrahlung bei 532 nm mit einer Leistung von 62 W erzeugt. Die frequenzverdoppelte Strahlung erwies sich aufgrund der hohen Zahl oszillierender Resonatormoden als äußerst rauscharm, was zur wirksamen Unterdrückung des störenden “grün Problems” beitrug.

Es besteht eine starke industrielle Nachfrage für gütegeschaltete Laser mit Emission im Nanosekundenbereich, insbesondere mit den Eigenschaften hoher mittlerer Ausgangsleistung, hoher Impulswiederholrate und Impulsdauern von einigen bis zu mehreren zehn Nanosekunden. Um sowohl eine hohe Wiederholrate als auch kurze Impulse zu erzielen bedarf es einer hohen Verstärkung, wie es Nd:YVO₄ bietet und daher gegenüber anderen geringverstärkenden Materialien wie Nd:YAG oder Yb:YAG dominiert. Daher wurde ein akustooptischer, gütegeschalteter Oszillator aufgebaut, mit dem eine Ausgangsleistung von 50 W bei 28 ns Impulsdauer und einer Wiederholrate von 50 kHz demonstriert wurde. Unglücklicherweise verhält sich die Impulsdauer umgekehrt proportional zur Impulsenergie, womit ein Anstieg der Wiederholrate unweigerlich in einer nahezu linearen Zunahme der Impulslänge resultiert. Um das vorangehend beschriebene Problem zu umgehen, wurde ein gütegeschalteter Oszillator mit cavity dumping realisiert. Die Impulsdauer ist in dieser Anordnung vorrangig durch die Resonatorumlaufzeit und die Schaltzeit des elektrooptischen Modulators bestimmt. Somit konnte eine konstante Impulsdauer von 6 ns bis zu einer Wiederholrate von 100 kHz hinauf und eine maximale Ausgangsleistung von 47 W generiert werden. Derart kurze Impulse sind üblicherweise nur mit gütegeschalteten Lasern mit wenigen Watt Ausgangsleistung möglich, umgekehrt liefern gütegeschaltete Laser mit ähnlich hohen Ausgangsleistungen Impulsdauern von mehreren zehn bis über 100 ns.

Besonderes Interesse an quasi-cw Hochleistungslaserquellen im Pikosekundenbereich besteht im Hinblick auf die effiziente Frequenzkonversion, mit der sich leistungsstarke grüne oder ultraviolette Strahlung erzeugen lässt. Mit besonders geeigneten Verfahren kann sogar das Tripel Rot, Grün und Blau (RGB) für den Einsatz in Laservideoprojektoren generiert werden. Die passive Modenkopplung mit einem halbleiterbasierten sättigbaren Absorber (SESAM) ist die bevorzugte Technik zur Erzeugung stabiler, selbststartender Pikosekundenimpulszüge. Hierzu wird eine hohe Verstärkung im Lasermaterial benötigt, damit bei hohen Wiederholraten keine gütegeschaltete Modenkopplung auftritt. Aus diesem Grund wurde ein SESAM in einen Oszillator eingebracht, der bei 888 nm angeregt war und 57 W modengekoppelte Ausgangsleistung

bei 110 kHz Wiederholrate und 33 ps Impulsdauer emittierte. Die Oszillatoremision wurde anschließend im Einfachdurchgang effizient auf eine Ausgangsleistung von 111 W verstärkt, ohne dabei eine Verringerung der Strahlqualität oder der zeitlich-spektralen Eigenschaften zu beobachten. Die dabei auftretende hohe Spitzenleistung von 30 kW ermöglichte unter Verwendung von LBO als nichtlineares Medium die Generierung von 87 W auf der zweiten Harmonischen bei 532 nm mit einer Konversionseffizienz von 80%. Die Frequenzverdreifung nach 355 nm lieferte 35 W Leistung mit einer Konversionseffizienz von 33%.

Die Vielfalt an Hochleistungslasersystemen, die im Rahmen dieser Arbeit demonstriert wurden, zeigen eindrucksvoll die Vorzüge der Anregung von Nd:YVO₄ bei einer Wellenlänge von 888 nm. Dabei bleiben wichtige Eigenschaften wie die hohe Verstärkung und der hohe Polarisationsgrad der Emission erhalten, während die erzielbaren Ausgangleistungen deutlich höher liegen als mit Systemen, die bei 808 nm gepumpt sind. Die Summe dieser günstigen Eigenschaften sollte Nd:YVO₄ das nötige Potential verleihen, mit hochleistungs Scheiben- und Faserlasern erfolgreich konkurrieren zu können, insbesondere auch deswegen, weil sich Letztere aufgrund der geringen Verstärkung und starker nichtlinearer Effekte häufig nicht zur Generierung kurzer Impulse eignen.

Publications

Journals

- L. McDonagh, A. Nebel, and R. Wallenstein, “111 W, 110 MHz repetition-rate, passively mode-locked TEM₀₀ Nd:YVO₄ master oscillator power amplifier pumped at 888 nm,” *Opt. Lett.* **32**, 1259–1261 (2007).
- L. McDonagh and R. Wallenstein, “Low-noise 62 W CW intracavity-doubled TEM₀₀ Nd:YVO₄ green laser pumped at 888nm,” *Opt. Lett.* **32**, 802–804 (2007).
- L. McDonagh, R. Wallenstein, and R. Knappe, “47 W, 6 ns constant pulse duration, high-repetition-rate cavity-dumped Q-switched TEM₀₀ Nd:YVO₄ oscillator,” *Opt. Lett.* **31**, 3303–3305 (2006).
- L. McDonagh, R. Wallenstein, R. Knappe, and A. Nebel, “High-efficiency 60 W TEM₀₀ Nd:YVO₄ oscillator pumped at 888 nm,” *Opt. Lett.* **31**, 3297–3299 (2006).

Conferences

- L. McDonagh, C. Theobald, M. Serr, R. Wallenstein, R. Knappe, and A. Nebel, “54 W, 150 MHz, Passively Mode-Locked TEM₀₀ Nd:YVO₄ Oscillator Pumped at 888 nm,” ASSP 2007, Vancouver, WA5.
- L. McDonagh and R. Wallenstein, “34 W CW Intracavity-Doubled TEM₀₀ Nd:YVO₄ Green Laser Pumped at 888 nm,” ASSP 2007, Vancouver, MD4.
- L. McDonagh, R. Knappe, A. Nebel, and R. Wallenstein, “888-nm pumping of Nd:YVO₄ for high-power high-efficiency TEM₀₀ lasers,” Photonics West 2007 (Invited), San Jose, 6451–13.
- L. McDonagh, R. Wallenstein, and A. Nebel, “35 W at 355 nm from a mode-locked Nd:YVO₄ MOPA,” Photonics West 2007, San Jose, 6451–77.
- L. Mc Donagh, R. Knappe and R. Wallenstein, “50 W, 5 ns, high repetition rate Cavity-Dumped Q-switched TEM₀₀ Nd:YVO₄ Oscillator,” Post-deadline paper PDP 4, ASSP 2006, Lake Tahoe.
- L. Mc Donagh, R. Knappe, A. Nebel, and R. Wallenstein, “High power and high efficiency TEM₀₀ Nd:YVO₄ oscillator pumped at 890 nm,” in CLEO/Europe 2005, CA6–5–THU.
- L. Mc Donagh, R. Knappe, A. Nebel, and R. Wallenstein, “Optimized pumping of Nd:YVO₄ with polarization-insensitive absorption for high power applications,” in Conference on Lasers and Electro-Optics (Optical Society of America, Washington, D.C., 2005), Baltimore, CMS5.

Patents

- L. McDonagh (principal inventor), R. Knappe, and A. Nebel, “Enhanced optical pumping of materials exhibiting polarization-dependent absorption,” EP 1482608, EP 1482607, US 2004/258117.
- L. McDonagh, “High-gain tapered laser gain module,” EP 1507321, US 2005/036532.
- L. McDonagh (principal inventor) and R. Wallenstein, “Apparatus and method for correcting a non-linear characteristic of a scanned light beam,” EP 1653266.

Magazines

- B. Hitz, “Generating High Green Power Without the Green Problem,” Photonics Spectra, May 2007, 92–93.
- B. Hitz, “Neodymium Vanadate Lasers Get Even Better,” Photonics Spectra, January 2007, 100–103.
- L. McDonagh and R. Wallenstein, “Optimized pumping of neodymium-doped vanadate for high-power lasers,” SPIE Newsroom, DOI: 10.1117/2.1200707.0708.

Contents

1	State of the art	1
1.1	Rods	2
1.1.1	End-pumped rods	2
1.1.2	Side-pumped rods	2
1.2	Slabs	3
1.2.1	End-pumped slabs	3
1.2.2	Side-pumped slabs	4
1.3	Disks	4
1.4	Fibers	5
1.5	Concept comparison	5
2	Optimized pumping of Nd:YVO₄	7
2.1	Nd:YVO ₄ . <i>A gifted laser material</i>	7
2.1.1	Physical structure	8
2.1.2	Spectroscopic properties	10
2.1.3	Heat generation	15
2.1.4	Thermo-optical and mechanical properties	22
2.2	End pumping. <i>High optical efficiency and high beam quality</i>	24
2.2.1	Pump-mode matching	24
2.2.2	Thermal lensing	26
2.2.3	Crystal stress and fracture	29
2.3	888 nm pumping of Nd:YVO ₄ . <i>The road to high power</i>	30
2.3.1	Limitations of 808 nm pumping	30
2.3.2	Absorption at 888 nm	31
2.3.3	Pump absorption, inversion, and gain	32
2.3.4	Energy-transfer upconversion	38
2.3.5	Finite element analysis	42
3	Continuous wave oscillation	49
3.1	Multimode resonator	49
3.1.1	Crystals	49
3.1.2	Diodes	52
3.1.3	Multi-transversal-mode oscillator	56

3.2	TEM ₀₀ resonators	62
3.2.1	Resonator design	62
3.2.2	TEM ₀₀ dynamically-stable resonator	66
3.2.3	Periodic resonator	69
3.3	Single-pass amplifier	71
3.3.1	Principle	72
3.3.2	Single-pass CW amplifier	74
3.4	Intracavity-doubled resonator	76
3.4.1	Second harmonic generation	77
3.4.2	Intracavity doubling	87
3.4.3	Intracavity-doubled TEM ₀₀ resonators	88
3.5	CW performance summary	91
4	Nanosecond pulse operation	95
4.1	Q-switching	96
4.1.1	Principle	96
4.1.2	Simulations	99
4.1.3	Q-switch technologies	102
4.1.4	Q-switched oscillator	106
4.2	Cavity-dumped Q-switching	109
4.2.1	Principle	109
4.2.2	CDQS oscillator	111
4.2.3	Stability	114
4.2.4	Second harmonic generation	117
4.3	Comparison	118
5	Picosecond pulse operation	121
5.1	Theory of passive mode locking	121
5.1.1	Principle of mode locking	121
5.1.2	Active mode locking	123
5.1.3	Passive mode locking	124
5.1.4	The semiconductor saturable-absorber mirror	126
5.2	Mode-locked oscillator with a saturable absorber mirror	129
5.2.1	Mode-locked oscillator design	129
5.2.2	Mode-locked oscillator performance	131
5.2.3	Mode-locked MOPA	134
5.3	Harmonic generation	134
5.3.1	Frequency doubling	135
5.3.2	Frequency tripling	136
5.4	Picosecond performance summary	139

6 Summary	141
------------------	------------

Bibliography	145
---------------------	------------

Chapter 1

State of the art

The initial goal of my thesis was to achieve a high-power red–green–blue (RGB) laser source in the 50 W white light power range for large-screen digital movie projection. High-power RGB is usually achieved by a high-power IR nanosecond [1], picosecond [2], or even femtosecond [3] mode-locked short-pulse laser source followed by a sequence of nonlinear stages including second-harmonic generation (SHG) and sum-frequency mixing (SFM), and an optical parametric oscillator (OPO) [2], or an optical parametric amplifier (OPA) and an optical parametric generator (OPG) [3]. Since such RGB generation stages have proven high conversion efficiencies up to 50% from IR to white light, the main limitation in scaling the power of these sources is the difficulties associated to the design of a high-power IR source. This is often achieved with a master-oscillator power-amplifier (MOPA) configuration, where a low-power pulsed source is amplified in multiple stages to reach ~ 50 W output power. More recently an 80 W thin-disk oscillator was chosen to directly achieve a high output power, yet at the cost of a complex system and limited optical efficiency [3].

Building on the RGB systems previously demonstrated in the group of Prof. Wallenstein, a picosecond mode-locked oscillator delivering from a few watts up to 20 W was assumed, yet the challenge resided in amplifying its output up to ~ 100 W in a minimum number of stages and with a high efficiency. This research led to the development of a specific pump–crystal combination that allowed the realization of high-power oscillators. Thus the initial goal of a high-power amplifier for an RGB source shifted to the design of a broad range of oscillators operated in cw, Q-switched, and mode-locked regimes. Finally a complete mode-locked MOPA delivering 111 W of average output power was constructed, which should allow for the production of ~ 55 W of white light.

Before going into the detail of the systems developed in this thesis, the following sections give an overview of the different technologies that would be candidates for a high-power high beam-quality IR source. Their strengths and weaknesses are outlined to explain the initial review process I conducted at the beginning of my work, and why a well-established technology that was believed to be inherently limited in terms of power scaling was chosen over more modern solutions. Thermal effects being the main limitation in power scaling, technologies fall into two groups: the ones that try to compensate thermal lensing (rods and slabs), and the ones that suppress thermal lensing by design (disks and fibers).

1.1 Rods

1.1.1 End-pumped rods

End-pumped lasers where the pump beam is absorbed in the gain medium colinearly to the laser mode provide a high efficiency and a high beam quality and symmetry thanks to the optimized mode matching. The most common combination in medium-power commercial systems consists in a Nd:YVO₄ crystal pumped by a fiber-coupled diode-laser source. Such system benefits from the high gain and polarized output of vanadate, and from the round homogenized pump profile providing an optimal overlap with a Gaussian mode. Average output powers of ~ 20 W are achievable by end-pumping the crystal from both sides [4]. When higher powers are sought, a periodic resonator comprising two or more crystals can be assembled [5], yet a single or multi-stage MOPA is often simpler and more reliable [6]. Other major advantages of such systems include the mature technologies and widespread know-how associated with the pump source, the crystal, and the resonator. Thus the cost and the availability of reliable components combined to the reduced product development times will facilitate market penetration and customer acceptance.

However the strong thermal lens and the absorption of the largest portion of the pump light close to the input facet of the crystal effectively limits power scalability, so other schemes are chosen when high output powers are sought. Yet recent developments have led to increased output powers with Nd:YAG and Nd:YVO₄ crystals, including direct upper laser-level pumping at 885 nm for YAG [7] and 880 nm for vanadate [8], multi-segmented rods with sections of increasing doping concentration along the length of the crystal for a more homogeneous heat load [9], and even rods with hyperbolic doping where this concentration gradient is directly created during the crystal growth for a continuous variation [10]. Undoped diffusion-bonded end-caps have also proven to improve heat-removal and minimize the bulging of end-facets, yet with a limited availability associated to manufacturing difficulties [11]. Cryogenically-cooled Yb:YAG lasers elegantly suppress thermal lensing thanks to the much higher thermal conductivity at cryogenic temperatures, yet such technique is totally unpractical for a commercial laser [12].

1.1.2 Side-pumped rods

Side-pumping of a rod consists in delivering the pump light to the crystal perpendicularly to the laser mode. Thus the crystal's end-faces are not subject to the pump light and power scaling is achieved simply by increasing the crystal length and the number of pump sources surrounding the rod. Some of this technology being inherited from the flash-lamp-pumped lasers, this technique is widely industry-proven.

High output powers > 200 W have been demonstrated along with diffraction-limited beam quality, yet with limited optical efficiencies of $\sim 20\%$ resulting from the necessary underfilling of the pump volume with the laser mode [13]. Most systems integrate Nd:YAG crystals since

they can be grown in large boules, so that > 100 mm rods are available. Its favorable thermo-mechanical properties allow for high overall pump power to be applied, yet the strong thermally-induced birefringence effects need to be compensated for achieving a polarized output. Thus it is necessary to insert a polarizing element such as a Brewster plate and compensate for the thermally-induced by integrating for instance two identical laser heads and a quarter-wave plate in the resonator to achieve a stable polarized output. Such oscillator further amplified in a two-head side-pumped stage provided 200 W of IR, which could be efficiently converted to 65 W of third harmonic at 355 nm [6].

1.2 Slabs

Slabs are crystals that exhibit a large aspect ratio between their width and their thickness. For a given crystal cross-section area along the optical axis, the larger the aspect ratio of the slab, the larger the top and bottom surfaces available for cooling. Thus a slab will allow a very efficient unidirectional heat extraction perpendicularly to these surfaces. However this leads to a unidirectional thermal lens that is more difficultly compensated than a symmetric lens. The gain volume is also strongly asymmetric so that achieving a good overlap with a near diffraction-limited mode is not straightforward. One solution consists in multipassing a small round mode to cover the whole width of the slab, yet this solution is better implemented in low thermal lens materials such as Nd:YLF [14]. Another technique is to design a stable/unstable resonator, the cavity being stable in the direction of cooling and unstable along the slab width [15, 16]. The output coupling is then achieved with a cut end-mirror, with the downside of diffraction on the mirror edge resulting in side-lobes on the beam. Cleaner beam profiles can be achieved by extracavity spatial filtering, yet at the cost of some power loss.

1.2.1 End-pumped slabs

Similarly to a rod, a slab can be end or side-pumped. End-pumping offers a homogeneous pump profile and its optimal matching to the laser mode without wasting pump power that is not accessible to the laser mode on the crystal edges as with side-pumping. The pump beam achieved by combining the output of several diodes in high-power systems should however be homogenized to minimize distortions on the laser mode. The main power limitation results from the input facet which is subject to the totality of the pump power, yet the spreading of the pump beam on a wide crystal makes this limitation much less restrictive than in regular end-pumped rods. End-pumped Nd:YVO₄ slab oscillators with output powers > 100 W have been demonstrated [15], combining the benefits of a high-gain material, the power-handling capability of a slab design, and the short length of a stable–unstable resonator. These favorable parameters allow for the production of short (< 10 ns) pulses with high average powers, which would be difficult to obtain with an end-pumped rod in a stable resonator.

1.2.2 Side-pumped slabs

Side pumping allows for the extension of the slab length and of the number of pump diodes for power scaling. However, the pump volume cross-section is inhomogeneous, with the crystal edges pumped to the highest level being left undepleted. A Nd:YAG thin-slab stable–unstable resonator provided 220 W in Q-switched operation with a near diffraction-limited beam quality ($M^2 = 1.5$) [16]. Very compact Nd:YLF and Nd:YVO₄ side-pumped slab modules in which the symmetric laser mode follows multiple passes to cover the whole crystal width have been operated as oscillators or in multi-stage power-amplifier systems [14].

Grazing-incidence slabs consist in bouncing the laser mode off the crystal’s side-pumped facet by total internal reflection at a very shallow angle. When pumping with one diode bar collimated on its fast axis for instance, the absorption can be made very high and the pump beam focused on a thin line since the pump light is spread on the whole width of the diode bar. The laser mode travels through a very small cross-section gain area, providing extremely high gain for the production of short Q-switched pulses at high repetition-rates > 500 kHz in a vanadate slab [17].

1.3 Disks

While thermal lensing is inevitable in rods and slabs for which the resonator design is critical for minimizing its effects, disks and fibers are inherently free from thermal lensing effects. A disk laser consists in a thin crystal in which the unidirectional heat flow resulting from pump absorption and cooling follows the same direction as the laser mode [18]. Thus the thermal gradient existing only on the laser mode axis, and not perpendicularly in the beam cross-section, no thermal lensing is created by the heat flow. Although a disk may be side or end-pumped, the most effective design for small-mode high beam-quality sources resides in end-pumping. This is achieved by coating a thin ($< 300\mu\text{m}$ thick) crystal with a HR coating on the back side and an AR coating on the front side, both for the pump and laser wavelengths. The disk is then cooled from a back side by soldering the crystal on a heat-sink, and pumped from the front side on a spot ranging from ~ 1 mm for medium-power systems to > 1 cm for high-power lasers. Since the double-pass pump absorption is very low because of the small crystal thickness, a large number of passes (up 16 or even 32) is necessary to achieve an efficient absorption. Thus a complex pump multi-passing cell integrating a parabolic mirror and roof prisms is required.

High average powers have been demonstrated with diffraction-limited beam quality, with 83 W in a mode-locked Yb:YAG oscillator producing 800 fs pulses, yet with a repetition-rate limited by the relatively low gain resulting from the large mode size, and an optical–to–optical efficiency under 25% [19, 3]. Scaling the power of thin-disk systems requires to enlarge the pump spot and mode size, achieving > 2 kW per disk, yet with a deteriorated beam quality of $M^2 > 5$ [20]. The degradation in beam quality arises from the thermally-induced mechanical deformation of the thin disk, which is all the more significant at high pump powers and when the laser mode is enlarged to cover a large area on the disk. Yet diffraction-limited output-beam quality is commercially available in cw, Q-switched [21], and mode-locked operation regimes [22] in the 50–100 W output power range.

More recently much progress has been made on optically-pumped semiconductor lasers (OPSL), where a semiconductor disk containing a thin active layer a Bragg reflector is optically end-pumped. Multiple-disk resonators have been demonstrated, achieving noise-free intracavity second-harmonic generation with > 50 W at 532 nm [23].

1.4 Fibers

Fiber lasers and amplifiers rely on a glass active fiber integrated a doped core as the gain medium. Since wave-guiding is achieved in a step-index or even a photonic-crystal structure, the temperature rise and thermal gradients have in principle no effect on the mode propagation. A double-clad architecture combining the benefits of a small single-mode core and large pump core allow for the efficient coupling of a low-quality diode pump beam, yet retaining the diffraction-limited mode quality inherent to a single-mode core. High cw output powers > 1 kW with diffraction-limited beam quality have been demonstrated in such configuration, yet high-power short-pulse lasers are limited by the nonlinear effects in a small core and long fiber, and ultimately by the damage threshold of the fiber's facets.

When high-power pulsed operation is sought, a large-mode-area (LMA) fiber where the core is enlarged to a diameter $> 50\mu\text{m}$ allows for the strong reduction of the mode power density, the increase of the laser-core to pump-core ratio and therefore the reduction of the fiber length while maintaining a high pump absorption. These combined improvements allow for much higher pulse energies and shorter pulses to be achieved before excessive nonlinear effects or fiber facet damage occur. Thus oscillator fiber-amplifier systems have demonstrated high-power operation with high beam quality in the nanosecond regime with 60 W of second harmonic [24], and in the picosecond regime with 80 W of green 530 nm radiation [25].

Even larger core diameters in the 50 – 100 μm range are achieved in rod-type fibers, where a photonic-crystal structure allows for the guiding of a single mode on a larger area than in a regular step-index fiber [26]. Such fiber being very sensitive to bending losses, its > 1 mm outer diameter provides the necessary stiffness and cooling area for removing the heat of fibers that are typically very short (< 1 m).

1.5 Concept comparison

None of the technologies briefly presented in this chapter is the ideal solution to all high-power requirements, yet their main strengths and weaknesses can be outlined to help selecting one or another for a given need in terms of cw or pulsed operation, pulse duration and repetition-rate, polarized emission, efficiency, and beam quality. Table 1.1 summarizes the potential of each technology for the main parameters characterizing the laser emission. Since this table is very synthetic, it gives a general trend for each technology group, although some specific arrangements, such as grazing-incidence slabs or rod-type fiber lasers may present different behaviors.

After a complete technology round-up, end-pumped vanadate appears to be the most versatile and all-round performing configuration, yet it is strongly limited in terms of average output power. Other technologies benefiting from much more promising power-scaling potential each suffers from its own weaknesses, wether in cw or pulsed operation, or simply in terms of simplicity, ease of manufacturing, or know-how establishment. This technology comparison and knowing the simplicity and versatility of end-pumped vanadate systems convinced me it was worth trying to push the average output power limits of this well-established technology, even if it didn't reach the same power levels as some more recent yet less versatile and more complex technologies. This is the subject of the work presented in this thesis.

Table 1.1: Comparison of the performance of high-power laser technologies for each determining laser output parameter. Systems refer to respectively end-pumped Nd:YVO₄ rods, side-pumped Nd:YAG rods, end-pumped Nd:YVO₄ slabs, side-pumped Nd:YAG slabs, Yb:YAG disks, and Yb-doped double-clad fiber lasers.

	Rod		Slab		Disk	Fiber
	End	Side	End	Side		
Average output power	–	+	+	+	+	+
Beam quality	+	–	–	–	+	+
Efficiency	+	–	+	+	–	+
Polarized output	+	–	+	–	+	–
Q-switching easiness	+	+	+	+	–	–
Short ns pulses	+	–	+	–	–	–
High repetition rate	+	–	+	+	–	–
Mode-locking easiness	+	–			+	–
Repetition rate	+	–			–	–
System simplicity	+	+	+	+	–	–

Chapter 2

Optimized pumping of Nd:YVO₄

Neodymium-doped vanadate has become the material of choice for medium-power commercial lasers delivering average output powers from under a watt to a few tens of watts, in cw, Q-switched, or mode-locked regime. Benefiting from many favorable optical and spectroscopic properties, its main drawback is a limited average output-power capability resulting from unfavorable thermo-optical and mechanical characteristics. Thus the physical structure, spectroscopic properties, heat-generation processes, and thermo-optical and mechanical properties of Nd:YVO₄ are first analyzed to get a good understanding of the physical effects responsible for its strengths and weaknesses. Then the end-pumping technique is presented, along with its pump-mode matching and the induced thermal lensing and crystal stress behaviors. With this deeper comprehension of the limitations of the end-pumped vanadate crystal combination, an optimized pumping scheme at 888 nm is proposed. The specific properties of 888 nm pump light absorption are outlined before a detailed comparison of the pump absorption, inversion, and gain is conducted between a state-of-the-art 808 nm-pumped system and the 888 nm configuration introduced in Chap. 3. The simulation of energy-transfer upconversion and its comparison with the other heat-generating processes is conducted to explain the differing thermal lensing properties between the two systems. Finally a finite-element analysis is applied to the two configurations to evaluate the crystals' temperature, stress, and strain maps, allowing for the simulation of the thermal lens and the end-facet bulging.

2.1 Nd:YVO₄. *A gifted laser material*

Neodymium-doped vanadate's potential for efficient laser action was noticed as early as 1966 [27], but it took almost three decades for it to become the most popular laser material in medium-power commercial systems. Crystal quality was gradually improved to the point where crystals of sufficiently large size and high quality could be end-pumped by laser diodes. Its strong absorption of the pump light at 808 nm is a perfect match to end-pumping for achieving high gain in a limited pump volume. Its main strengths are a large stimulated-emission cross section for a high gain, natural birefringence for a polarized output, strong pump-light absorption for tight focusing in short crystals, and relatively low cost in standard sizes. However its main

shortcomings arise from its relatively poor mechanical and thermal properties, as the material is much more brittle than YAG and exhibits a lower thermal conductivity. These properties limit the amount of pump light that can be absorbed before excessive thermal lensing and aberrations occur, ultimately leading to crystal fracture. In this section, the physical structure and parameters of Nd:YVO₄ will be discussed, followed by its optical parameters, and finally the thermal effects that hinder high-power operation.

2.1.1 Physical structure

Neodymium is a rare earth element belonging more specifically to the lanthanoid group. With an atomic number of 60, it presents the following electronic configuration:

$$\text{Nd: } 1s^2 2s^2 2p^6 3s^2 3p^6 3d^{10} 4s^2 4p^6 4d^{10} 4f^4 5s^2 5p^6 6s^2 \text{ or } (\text{Xe})4f^4 6s^2$$

Its first three electronic shells are completely filled, while the fourth has all s , p , and d orbitals filled and four f electrons, the fifth has complete s and p orbitals, and finally the sixth only two s electrons. Neodymium's valence electrons involved in ionization are the $4f^4$ and $6s^2$, so that when trivalent neodymium is ionized as Nd³⁺, it uses its two $6s$ and one $4f$ electrons for ionic binding. Therefore, the triply ionized ion has the following electronic configuration:

$$\text{Nd}^{3+}: 1s^2 2s^2 2p^6 3s^2 3p^6 3d^{10} 4s^2 4p^6 4d^{10} 4f^3 5s^2 5p^6 \text{ or } (\text{Xe})4f^3$$

As all other lanthanoids used for laser action (e.g. Ho, Er, Tm, Yb), absorption and emission lines used for laser action are due to transitions between these $4f$ states ($4f$ – $4f$ transitions). The three $4f$ electrons can rearrange themselves in different states that are split by three types of interactions, resulting in a large number of energy levels, as illustrated in Fig. 2.1. The first and strongest is the Coulomb electrostatic interaction between the three $4f$ electrons, effectively splitting the $4f$ states by $\sim 10,000 \text{ cm}^{-1}$, as between the 4I and 4F levels (see Fig. 2.1). Each level is then split by spin-orbit coupling in manifolds separated by $\sim 2000 \text{ cm}^{-1}$, giving birth to the ground states and the lower levels of the laser transitions (4I levels) and the pump and upper laser levels (4F levels). The final and weakest interaction is due to the effect of the crystal field on the $4f$ states. This Stark effect is limited here to an energy separation of $\sim 200 \text{ cm}^{-1}$, owing to the screening effect of the $5s^2$ and $5p^6$ on the $4f$ electrons, effectively restricting the influence of the surrounding local crystal field. Finally, each of the atomic lines corresponding to transitions between these energy levels is thermally broadened through electron-phonon interaction, where vibrational modes of the lattice are coupled to the $4f$ states. Again, the screening effect of the outermost electrons limits the magnitude of this thermal broadening so that the transition lines remain narrow even at room temperature.

The level nomenclature follows the $^{2S+1}L_J$ notation, where S is the total spin quantum number, L the orbital quantum number, and J the total angular momentum quantum number. Thus the ground level $^4I_{9/2}$ corresponds to a state in which $S = 3/2$, $L = 6$, and $J = 9/2$. Each level is then $(2J+1)$ -fold degenerate, as the quantum number m_J ranges from $-J$ to $+J$ in unit steps. However, the symmetry of the crystal field induces states of the same $|m_J|$ to have the

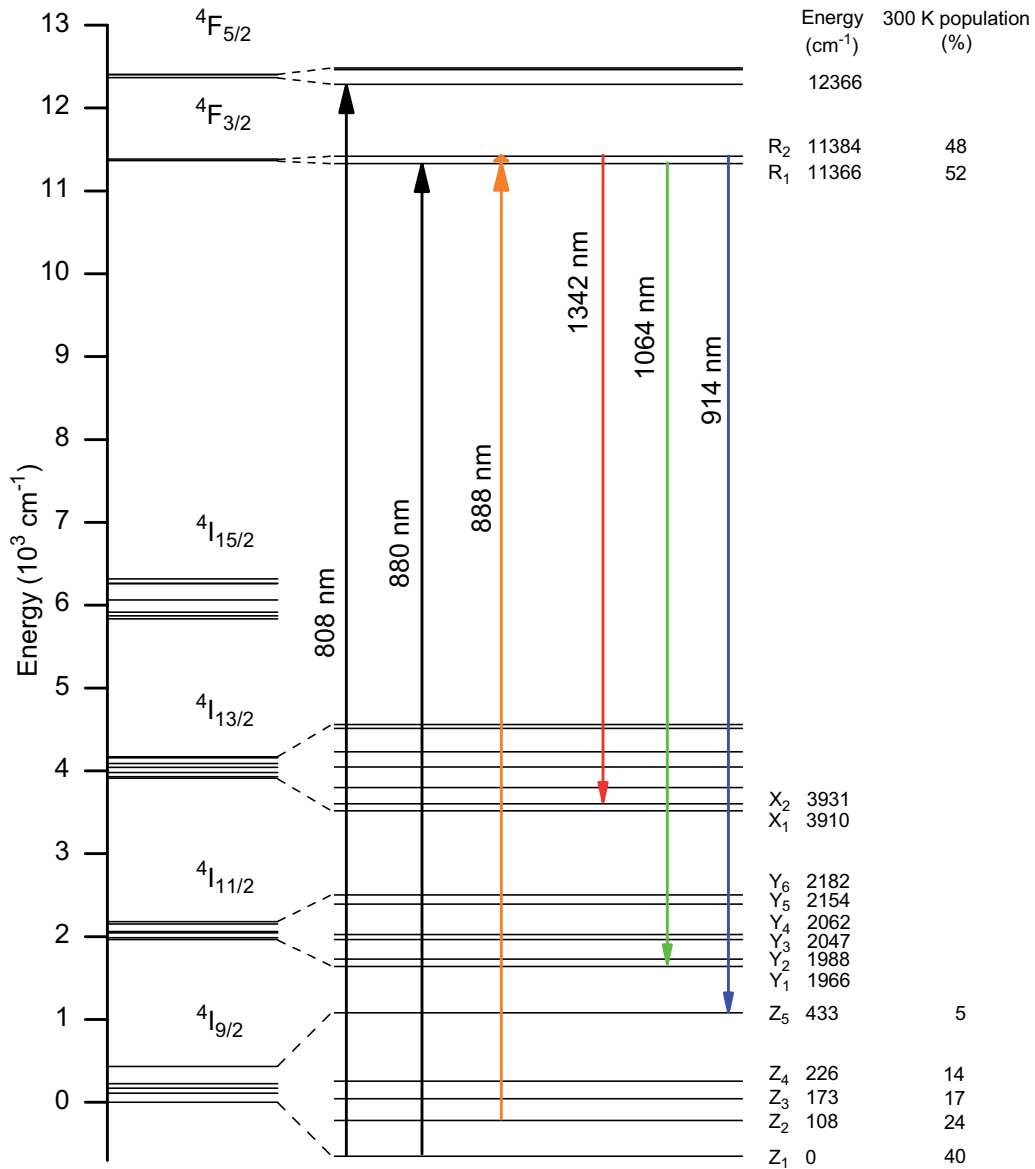


Figure 2.1: Energy level scheme of Nd³⁺ in an YVO₄ host crystal, its main pump and laser transitions, and the partial sublevel populations at room temperature. Level energies were measured at a temperature of 77 K [28], but tend to shift to lower values at higher temperatures [29].

same energy, so that each $^{2S+1}L_J$ level splits in $(2J + 1)/2$ doubly degenerate sublevels. As all sublevels are doubly degenerate, we can consider each of them as a single nondegenerate level. Therefore the ground level $^4I_{9/2}$, the lower laser level $^4I_{11/2}$, and the upper laser level $^4F_{3/2}$ respectively contain 5, 6, and 2 sublevels, as illustrated in Fig. 2.1.

The host in which an active ion is inserted should be selected for its physical properties and its influence on the ion's spectroscopic properties. The dopant ion size should closely match that of the atom it is replacing in the host to minimize the stress induced on the crystal lattice and allow doping with significant amounts of active ions. A hard material exhibiting a high fracture

stress, high thermal conductivity, low thermal dependence of the refractive index, and high optical transparency and low scattering losses is desired, while ease and cost of manufacturability should be taken into consideration. Then the effects of the host material structure on the active ion's energy levels, absorption and emission cross-sections, fluorescence lifetime, line widths, and spectral broadening are of prime importance.

YVO₄ or yttrium orthovanadate's structure is of zircon tetragonal type (space group D_{4h}) with $a = b$. Its structure is formed by chains aligned along the c axis containing alternatively VO₄ tetrahedron groups and YO₈ polyhedrons [30, 29]. These chains are linked together by oxygen atoms belonging to the YO₈ groups. The yttrium atoms can then be replaced by impurities or dopants of similar size. As the crystalline elementary cell contains four yttrium atoms, one can calculate from the given lattice constants a and c the Nd³⁺ atomic density when 1% of the yttrium atoms are replaced by neodymium, leading to $N_t = 1.26 \times 10^{20} \text{ cm}^{-3}$. Here the trivalent neodymium substitutes for trivalent yttrium, so no charge compensation is required. However the radius of Nd³⁺ is $\sim 5\%$ larger than that of Y³⁺, so that high doping levels will lead to strained crystals, yet the high pump absorption coefficients of Nd:YVO₄ limit the necessary doping level well below 1% for most applications. As the crystal lattice offers only one site for neodymium to be inserted in place of yttrium, each Nd³⁺ ion will see the same local field, thanks to the ordered nature of the crystalline structure. The line-broadening mechanism is therefore purely homogeneous, as opposed to glass hosts that exhibit a disordered structure and various sites for impurities, leading to inhomogeneous broadening of the transitions. Local field variations in a high-quality crystal such as Nd:YVO₄ available today can be as low as 0.5 cm^{-1} [31], much lower than the homogeneous room-temperature thermal broadening of the 1064 nm emission line of 6.9 cm^{-1} [29].

Nd:YVO₄ is usually grown using the Czochralski technique in an iridium crucible and under inert-gas atmosphere because of its high melting temperature of 1810 °C, where a single-crystal seed properly orientated is rotated and gradually pulled out of the melt as the crystallization occurs at the seed–melt interface. Optimized growing techniques now allow for the production of high-quality boules up to 50 mm in height. Although 50 mm long cut crystals have been produced, high quality-homogeneous crystals are now available commercially up to 30 mm in length [32].

2.1.2 Spectroscopic properties

Now that the physical structure and energy levels of Nd:YVO₄ have been described, the following section discusses its optical and spectroscopic properties, and how they are related to each other. The discussion will refer to Table 2.1 which summarizes the main optical parameters. As vanadate is now the most widely used laser material in medium-power commercial sources, one could expect that there exists a single set of values for optical parameters that are commonly agreed on. However, essential data such as the pump absorption coefficient or the stimulated-emission cross section are available within ranges greater than a factor two. As measurement uncertainties aren't sufficient to explain such variations, time will be taken here to precisely define each term and explain the source of the different values.

Table 2.1: Optical and spectroscopic properties of Nd:YVO₄ for 1 at.% doping. All values are given for the 1064 nm emission line at room temperature, unless stated otherwise.

Parameter	Symbol (unit)	a (o)	c (e)	Ref.
Crystal structure : Zircon tetragonal	(Å)	7.12	6.29	[30]
Nd ³⁺ atomic density	N_t (10 ²⁰ cm ⁻³)	1.26		
Refractive index	n	1.9573	2.1652	[32]
Laser wavelengths	λ_l (nm)	914, 1064, 1342		
Absorption coefficient (absolute peak)	α (cm ⁻¹)			
808 nm		10 (19)	40 (73)	[33, 34] ([35])
880 nm		5.5 (6)	11.5 (17)	[36] ([35])
888 nm		1.2 (1.7)	1.0 (1.6)	
Effective stimulated-emission cross section	σ_e (10 ⁻¹⁹ cm ²)			
1064 nm		4.4	12	[35, 37]
1342 nm			6	[37]
914 nm			0.48	[38]
Fluorescence Lifetime at 0.5 Nd at.%	τ (μ s)	100		[39, 33]
Linewidth (FWHM)	$\Delta\nu$ (nm)	0.8 (210 GHz)		[33, 29]
Saturation intensity	I_s (W/cm ²)	1560		

As orthovanadate presents a zircon tetragonal structure, its a and b axes are identical so that physical parameters should be given for two axes a and c only. In almost all practical cases, and in all systems described in this work, Nd:YVO₄ crystals are a -cut, that is with the optical axis along an a crystallographic axis. Therefore, the laser light (and pump light in case of end-pumping) will see a birefringent crystal with an ordinary axis a and an extraordinary axis c . Most mechanical, thermal, and optical parameters strongly differ between these two axes, so the pump and laser polarization states will have a major influence on the system's behavior.

Absorption

Although resonant pumping at 869 nm was used for the first demonstration of a diode-laser end-pumped Nd:YAG laser [40], it was soon replaced by 808 nm pumping for the strong absorption of the $^4F_{5/2}$ upper pump level and the availability of pump diodes at this wavelength. Conversely, vanadate is most commonly pumped around 808 nm at its peak absorption wavelength. Historically, this material was praised for its high absorption coefficients, especially along its c axis, which provided very short pump absorption depths while keeping the doping level within acceptable limits and avoiding the deleterious effects of a high doping concentration (see Sect. 2.1.3). This feature was most desirable as the diodes' brightness was very limited, so strong focusing of the pump light was necessary to achieve a high gain, which shortened the pump beam's Rayleigh range and conversely the depth over which a good overlap between the pump

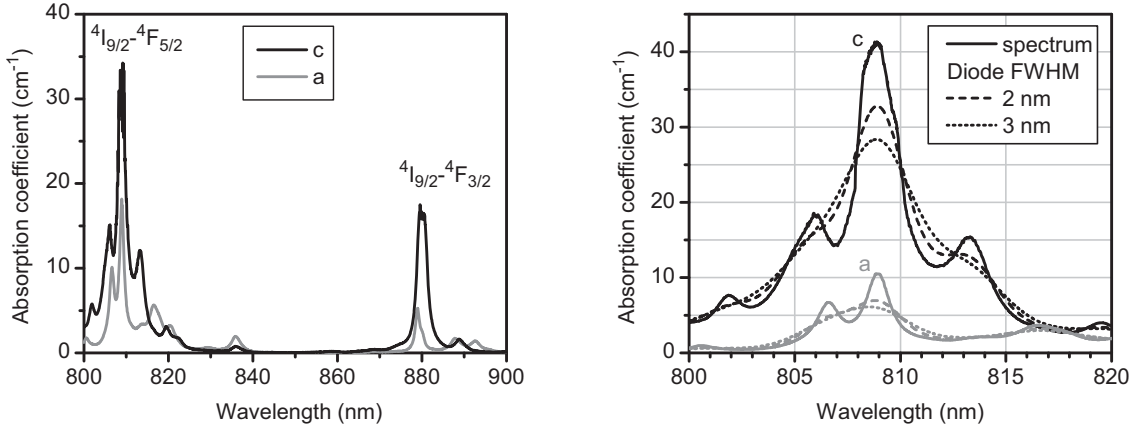


Figure 2.2: Absorption spectrum of Nd:YVO₄ and the transitions corresponding to the main absorption lines (left) [42], and effective absorption for 2 and 3 nm FWHM diodes at 808 nm (right).

and the laser mode was possible. Figure 2.2 (left) illustrates the absorption spectrum from 800 to 900 nm, where pump diodes are available. It should be noted that this measurement was optimized for a good resolution of the very low absorption peaks, therefore very little light was transmitted at the main absorption peaks, so the absorption coefficient values given in Table 2.1 are taken from the literature. Although absorption bands also exist at shorter wavelengths, they aren't used for diode pumping as they would lead to much higher quantum defect and heat generation. The multiple absorption peaks around 808 nm correspond to transitions from the ground level $^4I_{9/2}$ to the $^4F_{5/2}$ manifold, with a main absorption line at 808.7 nm corresponding to the $^4I_{9/2}(Z_1) \rightarrow ^4F_{5/2}(S_1)$ transition (see Fig. 2.1). Given the very short 9 ps lifetime of the $^4F_{5/2}$ level [41], the excited ions quickly relax nonradiatively to the upper laser level $^4F_{3/2}$, transferring the energy gap to the crystal as heat, so that the $^4F_{5/2}$ level is essentially empty at all times.

The very wide range of absorption coefficient values given in the literature can be explained by uncertainties in the crystal's doping concentration, but most importantly by the resolution of the spectroscopic measurement. Thus, a very fine resolution will resolve individual absorption lines and isolate a high peak absorption coefficient [35, 38], while a larger measurement bandwidth will smoothen the absorption peaks and produce lower peak absorption coefficient values [36, 33]. As presented in Table 2.1 the 808.7 nm absorption peak reaches coefficients of 19 and 73 cm⁻¹ on the *a* and *c* axes, respectively, but absorption coefficients of 10 and 40 cm⁻¹ reported in the literature are much closer to the effective absorption coefficients for diode light. Figure 2.2 (right) illustrates the reduction in effective absorption and the widening of the effective absorption bandwidth with increasing pump diode spectra from 2 to 3 nm FWHM. The effective absorption spectra have been obtained by convoluting the spectrometer data by an ideal Gaussian diode spectral profile, and closely match absorption coefficients measured in practical systems [43]. As most pump diodes will possess a spectral width in this range, we will use effective absorption coefficients of $\alpha_a = 7.5$ cm⁻¹ and $\alpha_c = 30$ cm⁻¹ for further simulations.

Thus the effective absorption for *c*-polarized light is ~ 4 times stronger than on the *a* axis, which leads to an inhomogeneous absorption of the pump light along the crystal length and polarization-dependent absorption and laser performance. The width of the main absorption peak of 1.8 and 1.3 nm on the *a* and *c* axes, respectively, associated to the lower neighboring absorption peaks, lead to an ~ 5 nm FWHM effective diode absorption bandwidth [33].

Demonstrated much more recently [36], direct upper laser level pumping of Nd:YVO₄ occurs from the $^4I_{9/2}$ to the $^4F_{3/2}$ level, with a peak absorption line at 878.6 nm, corresponding to the $Z_1 \rightarrow R_2$ transition [44]. Its peak absorption coefficients $\alpha_a = 6$ and $\alpha_c = 17 \text{ cm}^{-1}$ or effective values of $\alpha_a = 5.5$ and $\alpha_c = 11.5 \text{ cm}^{-1}$ lead to similar polarization-dependent behaviors as for 808 nm pumping. Yet the lower absorption was initially seen as a drawback when the brightness of diodes was limited, thus requiring higher-doped crystals [8]. However this technique has the advantage of reducing the quantum defect from 24% to 17% compared to 808 nm pumping for a laser wavelength of 1064 nm, effectively limiting the thermal load and thermal lensing for a given pump power, and leading to higher slope efficiencies. Therefore, a given resonator will accept more pump power and produce higher output power when pumped at 880 nm [8].

Emission

Now that the two main pumping processes have been described, the different possible laser transitions can be introduced. Excited Nd³⁺ in the $^4F_{3/2}$ level can relax to either of the $^4I_{13/2}$, $^4I_{11/2}$, or $^4I_{9/2}$ states, with emission wavelengths of 1342, 1064, and 914 nm, respectively, as illustrated in the unpolarized fluorescence spectrum represented in Fig. 2.3. Although these transitions are forbidden for an isolated ion (the selection rule for electric-dipole-allowed transitions is $\Delta J = 0$ or ± 1), they become weakly allowed due to interaction with the crystal field in neodymium's low symmetry site. Therefore the decay rate of the $^4F_{3/2}$ level is much slower than any other in the energy scheme, giving birth to a metastable level essential to the creation of population inversion and laser amplification. The upper-state lifetime τ of $\sim 100 \mu\text{s}$ being much shorter than in YAG (230 μs) or in YLF (480 μs) [33], it will not allow the large energy storage necessary to the production of high-energy pulses, but combined to the large emission cross-section it will be perfect for efficient cw or high-repetition-rate pulsed operation. The fluorescence lifetime τ , however, is subject to concentration-dependent fluorescence quenching, leading to a reduced lifetime at high doping concentrations. This effect caused by ion-ion interactions is still very moderate for doping below 1 at. %, as can be calculated from the following equation modeling this effect [39]:

$$\tau(C) = \frac{\tau_{sp}}{1 + \left(\frac{N_{t1\%}}{Q}\right)^2 C^2} \quad (2.1)$$

where $\tau_{sp} = 107 \mu\text{s}$ is the spontaneous emission lifetime, C is the Nd³⁺ concentration given in at.%, $N_{t1\%} = 1.26 \times 10^{20} \text{ cm}^{-3}$ is the Nd atomic density for 1 at.% doping, and $Q = 3.9 \times 10^{20} \text{ cm}^{-3}$ the concentration-quenching parameter [39]. Various values of τ_{sp} and Q are available in the literature, as these are obtained by fitting the fluorescence lifetime data measured for crystals of increasing concentration. These measurements are subject to uncertainties on the

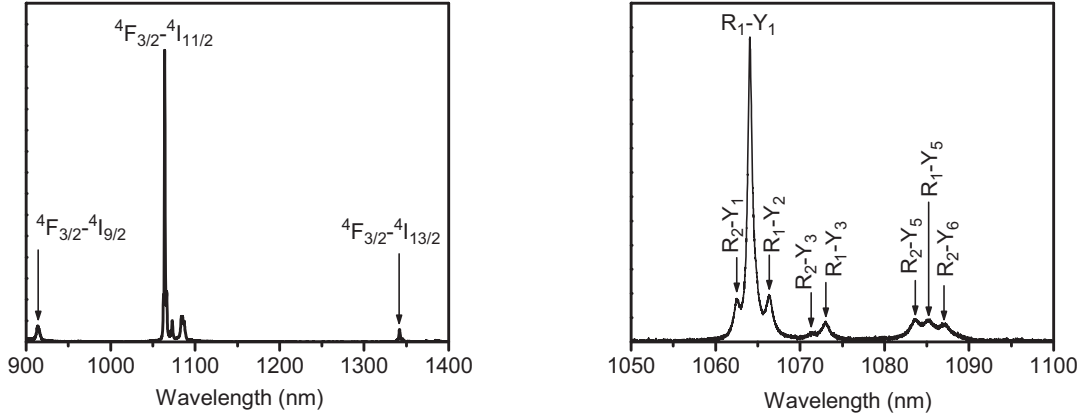


Figure 2.3: Unpolarized fluorescence spectrum of Nd:YVO₄ and the transitions corresponding to the main emission lines.

doping concentration, and the quenching effect will increase with the excitation trapping in lower-quality crystals (see Sect. 2.1.3). This model provides values of 104 and 97 μs at 0.5 and 1 at. % doping, respectively, so that we will use a value of 100 μs for all calculations, well within measurement uncertainties and $\sim 10\%$ variations among values available in the literature [39, 35, 45].

The 1 and 1.3 μm transitions correspond to purely four-level schemes while the 0.9 μm line results from a quasi three-level operation, the $^4I_{9/2}(Z_5)$ terminal laser level being only $\sim 2kT$ above the ground level at room temperature ($kT = 208 \text{ cm}^{-1}$ at 300°K). Figure 2.1 includes the fractional populations of the five sublevels of the $^4I_{9/2}$ manifold at room temperature calculated from Eq. 2.2, illustrating the 5% value reached for the Z_5 terminal level of the 914 nm transition. This high population will require high-intensity pumping and strong absorption to reach transparency and achieve a population inversion. However the most efficient laser action is obtained to the $^4I_{11/2}$ level, the strongest line corresponding to a wavelength of 1064.1 nm for c -polarized light, but determining the precise transition involved requires studying the high-resolution spectroscopy of the polarized fluorescence spectra at cryogenic temperatures ($\sim 85^\circ\text{K}$) where the line thermal broadening is minimal and consequently the line overlap is sufficiently small to allow the resolution of single lines [29]. Thus the $^4F_{3/2}(R_1) \rightarrow ^4I_{11/2}(Y_1)$ transition gives birth to the strongest line with a wavelength of 1063.8 nm at cryogenic temperatures, as calculated from the energies given in Fig. 2.1, but shifts to 1064.1 nm at 300°K, as calculated from the room-temperature energy level data [29]. The 1.06 μm fluorescence spectrum presented in Fig. 2.3 (right) illustrates the various possible transitions from the two $^4F_{3/2}$ to the six $^4I_{11/2}$ sublevels. Knowing that the laser amplification occurs on one single transition from one sublevel to another is of importance to the following discussion of the stimulated-emission cross section.

Again, fundamental values as the emission cross section vary greatly in the literature, from 11.4 to $30 \times 10^{-19} \text{ cm}^2$, but are split in two groups from 11.4 [35] to $15.6 \times 10^{-19} \text{ cm}^2$ [33] and from 25 [32] to $30 \times 10^{-19} \text{ cm}^2$ [29]. Each of these two groups corresponds to a different definition of the emission cross section. As the stimulated emission for c -polarized light occurs

solely from the R_1 sublevel, only its population will take part in the amplification process, and not the population of R_2 . However these two sublevels are strongly coupled due to their small energy gap of 18 cm^{-1} , so that the partial populations f_1 and f_2 of each sublevel are determined by the fast thermal equilibrium. Therefore their respective population can be calculated from the Boltzmann equation:

$$n_{R_2} = n_{R_1} \exp \left[-\frac{(E_{R_2} - E_{R_1})}{kT} \right] \quad (2.2)$$

where k is the Boltzmann constant and T the temperature. Thus 52% (f_1) of the total ${}^4F_{3/2}$ population lies in R_1 and participates to laser action, while 48% (f_2) remains in R_2 without contributing directly to stimulated emission. Knowing this, one can provide the peak stimulated-emission cross section σ value of the R_1 level, but only its own population n_{R_1} should be taken into account for calculating the gain, or one can define an effective cross section σ_e for the complete ${}^4F_{3/2}$ level and its total population n [31]. This definition has the advantage of not having to know the sublevel structure or the partial population of the level responsible for the transition to calculate the gain coefficient g :

$$g = \sigma n_{R_1} = \sigma f_{R_1} n = \sigma_e n \quad (2.3)$$

where the ${}^4F_{3/2}$ population n is assimilated to the population inversion density. This assumption is valid for the 1 and 1.3 μm transitions, the terminal laser level being empty, as the lifetime of the ${}^4I_{11/2}$ was measured at 700 ps [46]. We will therefore consider an effective emission cross-section of $12 \times 10^{-19} \text{ cm}^2$, in good agreement with many literature values [35, 37, 32] and within measurement uncertainties. Table 2.1 also gives a value of $6 \times 10^{-19} \text{ cm}^2$ for the 1342 nm line, leading to a higher laser threshold and lower efficiency at this wavelength, while the much lower emission cross-section of $4.8 \times 10^{-20} \text{ cm}^2$ at 914 nm coupled to the reabsorption losses results in a very high laser threshold and a low optical efficiency.

The homogeneous broadening of emission lines resulting from ion-phonon interactions, and as the number of phonons is highly dependent on lattice temperature, the laser transition linewidth should be measured at room temperature, or higher to account for the pump-induced crystal heating. Thus a linewidth of 0.8 nm (210 GHz or 7 cm^{-1}) full-width half-maximum (FWHM) is measured at room temperature for the 1064 nm transition [29]. Such linewidth allows the simultaneous oscillation of a large number of modes, and thus the generation of mode-locked pulses of only a few picoseconds in duration [47].

2.1.3 Heat generation

Thermal effects are the main limitation to power scaling in most solid-state laser materials, which is all the more the case in Nd:YVO₄. As it is naturally birefringent, thermally-induced stress birefringence has no effect on the laser mode polarization state and doesn't induce any further losses, as in isotropic materials such as Nd:YAG. Therefore the main thermal effect lies in thermal lensing which will be discussed later. But first the different heat-generating processes will be presented, and their relative importance in practical situations discussed.

When a laser crystal is pumped and operated in a laser resonator or as an amplifier, the fractional thermal loading η_h (the fraction of the absorbed pump power that generates heat) contains contributions from the nonradiative part of the deexcitation of ions, by laser and fluorescence emission, and from parasitic nonradiative processes. Thus it can be described by the following equation:

$$\eta_h = 1 - \eta_p \left((1 - \eta_o \eta_l) \eta_q \eta_{qd}^f + \eta_o \eta_l \eta_{qd}^l \right) \quad (2.4)$$

where η_p is the pump level efficiency (the fraction of ions excited to the pump level that deexcite non-radiatively to the upper laser level), η_o the pump-mode overlap efficiency, η_l the laser extraction efficiency (the fraction of excited ions that deexcite through stimulated emission, contributing to the laser radiation), η_q the fluorescence quantum efficiency (the fraction of excited ions that deexcite radiatively through spontaneous emission in absence of laser emission), and η_{qd}^l and η_{qd}^f the quantum defect ratios for laser and spontaneous emission, respectively. η_p is ~ 1 for 808 nm pumping, and obviously 1 for direct upper-laser-level pumping, so its influence can be neglected. η_l depends on the laser intracavity intensity, tending to 1 for a high laser photon flux in the pumped region and 0 under threshold, when the cavity is blocked, or in the pump spot regions with little overlap with the laser mode, but typical values are higher than 95% in cw lasing conditions. η_q contains contributions from the different non-radiative effects described below, and depends on doping concentration, population density, and laser photon flux. Figure 2.4 illustrates the different possible non-radiative mechanisms involving single excited ions with or without interaction with a photon flux, two excited ions, or one excited and one ground-level ion.

Quantum defect

The quantum defect encompasses the non-radiative decay from the pump level to the upper laser level and from the terminal laser level to the ground state. It is readily calculated from the pump and laser wavelengths for stimulated emission, yet in the case of spontaneous emission the excited ions relax to the lower levels ${}^4I_{9/2}$, ${}^4I_{11/2}$, and ${}^4I_{13/2}$ with their respective wavelengths λ_i and branching ratios β_i . Thus one can define an average fluorescence wavelength $\lambda_f = \sum_i \beta_i \lambda_i$, calculated for Nd:YVO₄ [44] or measured from the fluorescence spectrum [48] at ~ 1032 nm. The fluorescence and lasing quantum defects are therefore given by:

$$\eta_{qd}^f = \frac{\lambda_p}{\lambda_f} \quad (2.5a)$$

$$\eta_{qd}^l = \frac{\lambda_p}{\lambda_l} \quad (2.5b)$$

Table 2.2 gives the calculated quantum defect values for four lasing and fluorescence wavelengths, and for two pump wavelengths.

Several comments should be made regarding these values. Direct upper-laser-level pumping increases η_{qd} , with a more pronounced relative improvement at the shorter lasing wavelengths,

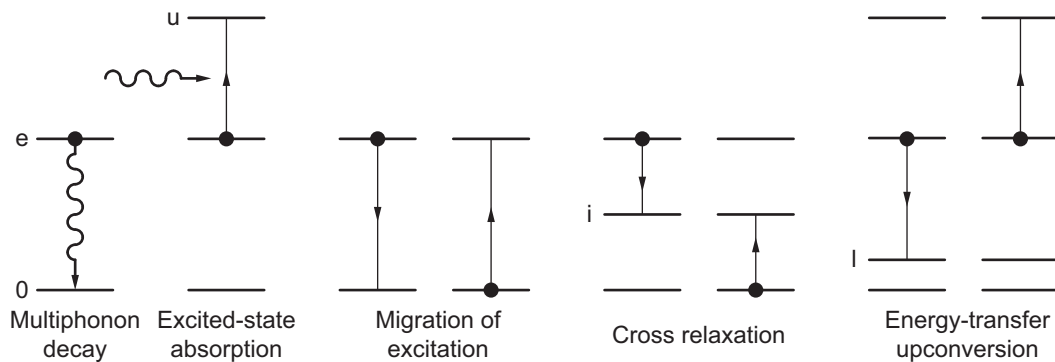
Table 2.2: Quantum defect ratios for laser and luminescence emissions at different pump wavelengths.

$\lambda_{l,f}$	λ_p	
	808	888
1342	0.60	0.66
1064	0.76	0.83
1032	0.78	0.86
914	0.88	0.97

effectively reducing the fractional thermal loading. The quantum-defect is a major source of heat generation for 1342 nm lasing, which will decrease if laser action stops and only fluorescence occurs. On the contrary, when lasing on the quasi three-level transition at 914 nm, the thermal load strongly increases when laser extraction stops. When lasing at 1064 nm, the quantum defect ratio increase without laser extraction has little effect on heat generation, whereas the non-radiative processes described below become dominant.

Multiphonon decay

An excited ion in the $^4F_{3/2}$ state could simply relax non-radiatively to lower levels by multiphonon decay, transferring its energy as lattice phonons and therefore generate heat. However the energy gaps involved are much larger than the highest phonon energy the YVO₄ lattice can sustain, thus requiring many phonons for the transition to occur and making it very unlikely. Such direct multiphonon decay can therefore be neglected for the ions lying in the metastable level, but will be the heat-generating mechanism subsequent to the following radiative processes which bring ions in intermediate or high-energy levels, before they relax to lower levels or to the ground state.

**Figure 2.4:** Possible energy-transfer schemes leading to heat generation.

Excited-state absorption (ESA)

When submitted to an electromagnetic field, an ion in the ${}^4F_{3/2}$ level can emit a photon through stimulated emission, but it can also absorb an incoming photon, being therefore further excited to higher levels. Figure 2.4 illustrates this process with an ion in the excited e state, absorbing an incoming photon at the pump or laser wavelength to an upper level u . Although ESA itself doesn't generate heat, the decay from the upper level u down to the metastable level e mainly through multiphonon decay will. Some mild fluorescence in the visible range can also be noticed [49, 45], but with an intensity far below other non-radiative processes. The depopulation of the upper laser level is given by:

$$\frac{dn}{dt} = - \left(\sigma_{ESA}^p F_p + \sigma_{ESA}^l F_l \right) n \quad (2.6)$$

where σ_{ESA}^p and σ_{ESA}^l are the absorption cross sections at the pump and the laser wavelengths, respectively, and F_p and F_l the photon fluxes in $\text{cm}^{-2} \cdot \text{s}^{-1}$. For ESA from the ${}^4F_{3/2}$ level to be possible, there should exist an upper-transition level of energy E_u , as calculated in Table 2.3. It appears that no manifold exists for a possible direct ESA at 808, 888 or 914 nm. Furthermore, when ESA is possible at a pump wavelength, it is usually much reduced due to the lower intensities of the pump light compared to that of the laser mode in an oscillator. However, at 1064 and 1342 nm, upper ESA levels exist and the effect has been observed and quantified [50]. At 1064 nm, the absorption cross section is ~ 100 times smaller than the stimulated-emission cross section, so that ESA has negligible effect on efficiency and heat generation. At 1342 nm however, σ_{ESA} is ~ 10 times smaller than σ_e , so that ESA has a much more pronounced effect on reducing the slope efficiency and increasing heat generation [45].

Ground-state absorption at the laser wavelengths is inexistent due to the absence of upper level in the $6300 - 11300 \text{ cm}^{-1}$ range, as can be seen in Fig. 2.1.

Table 2.3: Calculated upper ESA energy levels and corresponding manifolds and absorption cross sections for different pump and laser wavelengths. \emptyset indicates the absence of levels at the required energy for ESA to occur. Energy levels from Ref. [28].

$\lambda_{p,l}$ (nm)	$\sim E_u$ (cm^{-1})	Manifold	σ_{ESA} (cm^2)
1342	18827	${}^4G_{7/2}$	5×10^{-20}
1064	20773	${}^4G_{9/2} + {}^4G_{11/2} + {}^2K_{15/2}$	1.5×10^{-20}
914	22316	\emptyset	
888	22636	\emptyset	
808	23751	\emptyset	

Migration of excitation

The three following energy-transfer processes result from dipole–dipole interactions between two neighboring ions. In the migration of excitation process, an excited ion (donor D) relaxes to the ground state at a distance R from a ground-state ion (acceptor A), its dipole moment generates a nonradiating electric field, which then interacts with the dipole moment of the acceptor. The interaction energy $E \propto 1/R^3$ is significant only if the oscillating frequency of the dipole moment of D is nearly resonant with that of A , so there should be a good overlap between the emission spectrum of D and the absorption spectrum of A . The rate of energy transfer between D and A is shown to be $W_{DA} \propto 1/R^6$ [31]. As the average distance R between two neighboring ions decreases with higher doping concentrations C as $C \propto 1/R^3$, the energy transfer rate increases quadratically with doping concentration as $W_{DA} \propto C^2$. The migration of excitation itself doesn't generate heat, but increases the probability of an excited ion to transfer its energy to a color center, a dead site, or an impurity, which will subsequently relax nonradiatively and heat the lattice [51]. Although the migration of excitation alone could increase the effective radiative lifetime, the excitation trapping effect is predominant in Nd:YVO₄. The depopulation resulting from migration of excitation and the following excitation trapping can be expressed as:

$$\frac{dn}{dt} = -\frac{n}{\tau_{ME}} \quad (2.7)$$

with $1/\tau_{ME} \propto C^2$. This process will therefore become troublesome at high doping concentrations and contribute to concentration quenching.

Cross-relaxation or self-quenching

Similarly to the migration of excitation, cross-relaxation is a dipole–dipole donor–acceptor interaction. As illustrated in Fig. 2.4, an excited ion relaxes to an intermediate level i , transferring its energy to a neighboring acceptor. This effect becomes significant near resonance, when the relaxation energy from e is nearly equal to the excitation energy of the acceptor, that is without phonon assistance. The study of neodymium's energy levels reveals that the only non-phonon-assisted cross-relaxation transition is ${}^4F_{3/2} + {}^4I_{9/2} \rightarrow 2 \times {}^4I_{15/2}$, as no intermediate levels exist between ${}^4I_{15/2}$ and ${}^4F_{3/2}$. The two ions in the ${}^4I_{15/2}$ level subsequently relax to the ground state through multiphonon decay, passing by the ${}^4I_{13/2}$ and ${}^4I_{11/2}$ intermediate levels and generating heat. As for migration of excitation, the energy transfer rate is given by $W_{DA} \propto C^2$, so that we can define the depopulation resulting from cross-relaxation as:

$$\frac{dn}{dt} = -\frac{n}{\tau_{CR}} \quad (2.8)$$

with $1/\tau_{CR} \propto C^2$.

The combination of migration of excitation and excitation trapping with cross-relaxation is responsible for the concentration-quenching effect, resulting in shorter fluorescence lifetimes and higher heat generation at high doping concentrations [52]. As both effects increase quadratically with doping concentration, we can define a nonradiative decay time τ_{nr} as follows:

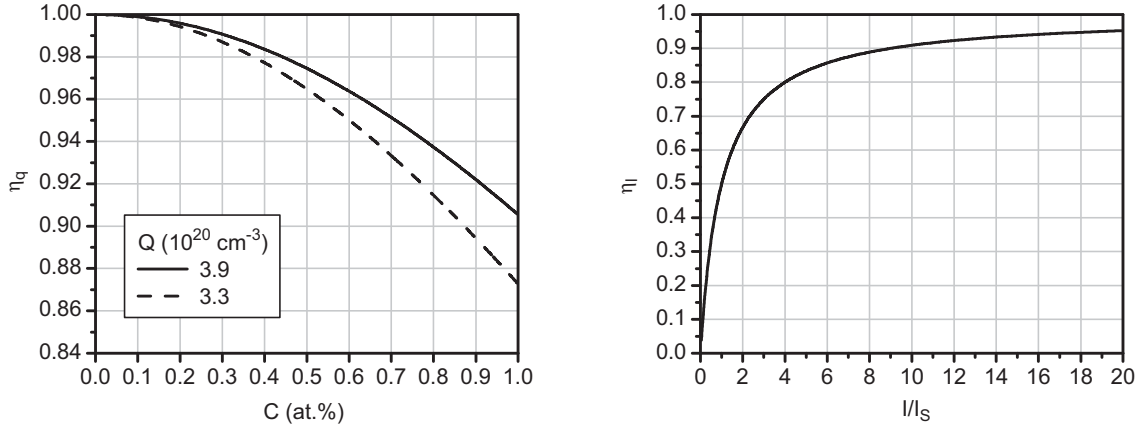


Figure 2.5: Concentration quenching of the fluorescence quantum efficiency (left). The quantum efficiency is plotted for two different concentration-quenching parameters available in the literature [39, 54]. Stimulated-emission efficiency function of I/I_s (right).

$$\frac{1}{\tau_{nr}} = \frac{1}{\tau_{ME}} + \frac{1}{\tau_{CR}} \propto C^2 \quad (2.9)$$

The fluorescence lifetime τ combining the effect of spontaneous emission and nonradiative decay is given by:

$$\frac{1}{\tau} = \frac{1}{\tau_{sp}} + \frac{1}{\tau_{nr}} \quad (2.10a)$$

$$\tau = \frac{\tau_{sp}}{1 + \frac{\tau_{sp}}{\tau_{nr}}} \propto \frac{\tau_{sp}}{1 + AC^2} \quad (2.10b)$$

with A a proportionality factor. This explains the model for the concentration quenching of fluorescence given in Eq. 2.1. The spontaneous-emission quantum efficiency η_q is therefore given by:

$$\eta_q = \frac{W_{sp}}{W_{sp} + W_{nr}} = \frac{1}{1 + \frac{\tau_{sp}}{\tau_{nr}}} = \frac{1}{1 + \left(\frac{N_{t1\%}}{Q}\right)^2 C^2} \quad (2.11)$$

where W_{sp} and W_{nr} are the spontaneous emission and nonradiative decay rates, respectively. This dependence is valid as τ_{sp} is constant regardless of the doping concentration or the level of excitation. Figure 2.5 illustrates the decrease in quantum efficiency with increasing doping concentrations. However, at 0.5 at.% doping $\eta_q = 0.97$, so this slight reduction in quantum efficiency isn't sufficient to explain the two-fold increase in thermal loading between lasing and non-lasing conditions in low-doped crystals [53]. We can therefore neglect concentration quenching as a significant cause of heating.

Energy-transfer upconversion (ETU)

Energy-transfer upconversion (ETU) or Auger upconversion occurs between two ions excited in their metastable state, one relaxing to a lower level and transferring its energy through dipole–dipole interaction to the neighboring ion, which is further excited or “upconverted” to a higher level (see Fig. 2.4). For this effect to be significant, it should occur resonantly without phonon assistance, so adequate higher levels corresponding to their lower-energy counterparts should exist. The possible upconversion processes consist of the transitions ${}^4F_{3/2} \rightarrow {}^4G_{7/2}$ and ${}^4F_{3/2} \rightarrow {}^4G_{9/2} + {}^4G_{11/2} + {}^2K_{15/2}$ which result from the down-conversion transitions ${}^4F_{3/2} \rightarrow {}^4I_{13/2}$ and ${}^4F_{3/2} \rightarrow {}^4I_{11/2}$, respectively. The down-conversion transition ${}^4F_{3/2} \rightarrow {}^4I_{9/2}$ doesn’t possess a corresponding direct upconversion transition for this process to happen effectively without the contribution of one or more phonons [55]. It is however difficult to estimate the relative contribution of each upconversion channel, so only the global effect will be quantified. In both cases, the energy lost as heat through multiphonon relaxation from the upper to the metastable level and from the lower level to the ground state is exactly the energy of an ion in the ${}^4F_{3/2}$ level.

Although upconversion processes are difficult to describe accurately, the following model is widely used to evaluate the influence of upconversion on the depopulation of the metastable level:

$$\frac{dn}{dt} = -\gamma n^2 \quad (2.12)$$

where γ is the upconversion rate or the upconversion macroparameter. It was shown that a more complex approach is necessary to accurately describe the upconversion effect [56, 48] and that the upconversion rate varies quadratically with neodymium concentration [52], yet this model offers the advantage of integrating a simple term in the rate equation to estimate the effective value of γ . It shows that, as the upconversion process involves two excited ions, the depopulation rate increases with inversion density. Therefore, high-gain end-pumped lasers in which the inversion density is very high, especially close to the input face of the crystal, will suffer mostly from upconversion-induced heat generation. Thus, for crystals below 0.5% doping, cross-relaxation becomes negligible compared to upconversion, often one order of magnitude smaller [52, 57], which will be all the more true when the inversion density is high, such as in a Q-switched oscillator or an amplifier. An upconversion rate of $\gamma \simeq 1.5 \times 10^{-15} \text{ cm}^3 \cdot \text{s}^{-1}$ was determined experimentally in a 0.5 at.% Nd:YVO₄ crystal [48]. A strong increase in thermal lensing from lasing to non-lasing conditions, reflecting a higher ETU-induced heating with higher inversion density has been observed, with factors from 2 at 0.3 at.% to 5 at 1 at.% [53]. These results indicate that the use of a long crystal with low and uniform absorption will be the key to reducing ETU effects. A comparison of the fluorescence rate $1/\tau$ with the upconversion-induced depopulation rate γn and the other sources of nonradiative decay will be conducted in practical cases to evaluate their relative importance (see Sect. 2.3.4).

Stimulated-emission efficiency

The stimulated-emission efficiency η_l represents the fraction of excited ions that deexcite through stimulated emission, generating heat only during the nonradiative decay from the terminal laser level to the ground state. It is expressed as the ratio of the stimulated emission rate over the total deexcitation rate:

$$\eta_l = \frac{W_{st}}{W_{st} + W_{sp} + W_{nr}} \quad (2.13)$$

where W_{st} , W_{sp} , and W_{nr} are the stimulated, spontaneous, and nonradiative depopulation rates, respectively. η_l is shown to be independent of the population inversion as all deexcitation rates are proportional to it if we neglect the influence of ETU during lasing operation:

$$\eta_l = \frac{\sigma_e F}{\sigma_e F + \frac{1}{\tau}} = \frac{1}{1 + \frac{1}{\sigma_e \tau F}} \quad (2.14)$$

The stimulated-emission efficiency is therefore solely dependent on the ratio between the laser mode intensity I over the saturation intensity I_s , or F and F_s in terms of photon fluxes:

$$\eta_l = \frac{1}{1 + \frac{F_s}{F}} = \frac{1}{1 + \frac{I_s}{I}} \quad (2.15a)$$

$$\text{with } I_s = h\nu_l F_s = \frac{h\nu_l}{\sigma_e \tau} \quad (2.15b)$$

Figure 2.5 (right) illustrates the growth of η_l with laser intensity in the pump spot. As $I_s = 1560 \text{ W/cm}^2$ for the 1064 nm line, most oscillators will exhibit an intracavity intensity far beyond I_s , so that η_l will be higher than 95%. However, this will not be the case of amplifiers with input intensities below or in the range of I_s .

This expression of stimulated-emission efficiency is valid locally in every point of the pumped volume with the space-dependent mode intensity and inversion. However the overall efficiency on the pump volume depends on the pump–mode overlap η_o [58]. For flat-top pump beams and laser modes overlapping perfectly, η_l will be constant over the whole cross section. However, for a single transversal mode laser, the Gaussian mode’s radius is usually taken to be 70–80% of the pump radius to avoid the thermal lens’ peripheral aberrations, so that the extraction through stimulated emission will be strongly reduced in the periphery of the pump spot. This effect is noticed as a brighter visible fluorescence in an outer ring around the laser mode, where undepleted inversion leads to stronger upconversion and deexcitation through fluorescence in the visible range. Although this overlap can be calculated with the help of overlap integrals [59], it is usually determined experimentally as the optimum pump–mode overlap depends on the effective pump profile along the crystal length and on gain and optical distortion considerations.

2.1.4 Thermo-optical and mechanical properties

Once the heat-generating processes have been described and their relative contributions to the total heating evaluated, the local heat load $Q(x, y, z)$ is determined in every point of the pumped

volume. The resulting temperature increase, thermal expansion and stress, and the subsequent thermo-optical effects affecting the laser mode are analyzed in Sect. 2.2.2. However, vanadate's mechanical and thermo-optical properties and key parameters are first presented. Table 2.4 gives the most important mechanical and thermo-optical parameters of Nd:YVO₄ necessary for the modeling of thermal lensing.

The thermal conductivity K indicates the material's ability to conduct heat, and although the crystal is birefringent, it is almost equal along the a and c axes. Therefore, with a radially symmetric pump volume and cooling surface, as is almost the case for a four-side cooled end-pumped crystal, the temperature distribution will also be radially symmetric around the crystal and pump optical axis. As vanadate exhibits a thermal conductivity approximately one half that of Nd:YAG, the same deposited heat will lead to a maximum temperature twice as high. The thermal conductivity has also been shown to decrease with higher temperatures in YAG, which leads to a larger temperature increase in the center of the pump volume and stronger aberrations on the resulting thermal lens [60].

Once the temperature map of the crystal is known, the thermo-optical coefficient dn/dT defines the change in refractive index with the temperature increase. As for most laser materials, dn/dT is positive, so that a pumped volume will always result in a positive thermal lens. Although dn/dT is almost three times larger for a -polarized light than for the c polarization, the c -polarized laser mode will only be sensitive to the lower value. Only the unpolarized pump beam will see a stronger thermal lens on one direction of polarization. This temperature dependence of the index of refraction is responsible for the gradient index or bulk thermal lens.

The thermal expansion coefficient α_T defines the relative expansion for a given temperature increase in one direction. As α_T is ~ 2.5 times larger along the c axis than on the a axis, the bulging of the crystal's end faces under pumping with a radially symmetric pump and cooling geometry will be asymmetric, with a stronger curvature along the a axis.

Young's modulus, or elastic modulus E defines the stiffness of the material, that is the ratio of stress σ over strain ε . A large Young's modulus indicates a stiff material in which a high stress is necessary to induce a small strain or deformation. Vanadate's elastic modulus of 133 GPa is > 2 times smaller than that of YAG (307 GPa), so that YVO₄ will deform more easily under a given stress.

Poisson's ratio ν is the ratio of the relative transverse strain (normal to the applied load), divided by the relative axial strain (in the direction of the applied load), and defines the compressibility of a material. A perfectly incompressible material will exhibit $\nu = 0.5$, tending to 0 for a very compressible material such as cork.

The maximum tensile stress σ_{max} is the maximum stress the material can tolerate in the direction of the load before fracture occurs. The calculated stress intensity will be compared to the maximum tensile stress to determine the crystal's ability to withstand a given pump load.

The thermal shock parameter R depends on the mechanical and thermal properties of the material, a high value indicating a higher permissible absorbed pump power before fracture occurs. It is defined as follows:

$$R = \frac{K\sigma_{max}}{\alpha_T E} \quad (2.16)$$

Table 2.4: Thermo-optical and mechanical properties of Nd:YVO₄

Parameter	Symbol	Unit	<i>a</i> (o)	<i>c</i> (e)	Ref.
Thermal conductivity	<i>K</i>	W/(m · K)	5.10	5.23	[61]
Thermo-optical coefficient	<i>dn/dT</i>	10 ⁻⁶ /K	8.5	3.0	[32]
Thermal expansion coefficient	<i>α_T</i>	10 ⁻⁶ /K	4.43	11.37	[61]
Young's modulus	<i>E</i>	GPa		133	[61]
Poisson ratio	<i>ν</i>			0.33	[61]
Fracture tensile stress	<i>σ_{max}</i>	MPa		51-53	[62, 61]
Thermal shock parameter	<i>R</i>	W/cm		4.8	[61, 58]

2.2 End pumping. *High optical efficiency and high beam quality*

End pumping has become the preferred pumping geometry for the realization of high-efficiency high-gain lasers, thanks to its ability to shape the pump beam and obtain a pump volume that closely matches the laser mode. However power scaling is limited by the absorbed power density on the crystal's input face, which is always subject to the total pump power. The following sections describe the pump-mode matching considerations and the thermal lensing resulting from the heat load and its removal from the crystal's sides.

2.2.1 Pump-mode matching

Although side-pumped lasers have produced high powers > 200 W in a TEM₀₀ mode [13], and that power scalability is achieved by linearly extending the length or the number of rods and the corresponding number of pump diodes surrounding them, their optical-optical efficiency is inherently limited by the pump coupling efficiency and the restricted pump-mode overlap. In order to avoid diffraction losses on the laser rod aperture while maximizing the beam overlap, the laser mode should not be larger than $\sim 1/\sqrt{2}$ of the rod radius, leaving the high-inversion outer regions of the rod undepleted. This leads to strong thermo-optical effects demanding that the mode size is reduced at high pump powers if a high mode quality is to be maintained. Therefore the optical-optical efficiency of such systems is often limited to $\sim 20\%$.

End-pumping consists in focusing a pump beam collinearly with the laser mode, both being kept significantly smaller than the crystal's aperture to minimize diffraction losses. The pump beam profile ranges from a Gaussian as for laser pumping of Ti:Sa to top-hat for fiber-coupled diode pump sources. Figure 2.6 (left) illustrates the Gaussian laser mode and top-hat pump beam in an idealized situation. As shown in Sect. 3.1.2, the pump beam profile can be approximated by a flat-top only in its focus where the fiber's output face is imaged. However

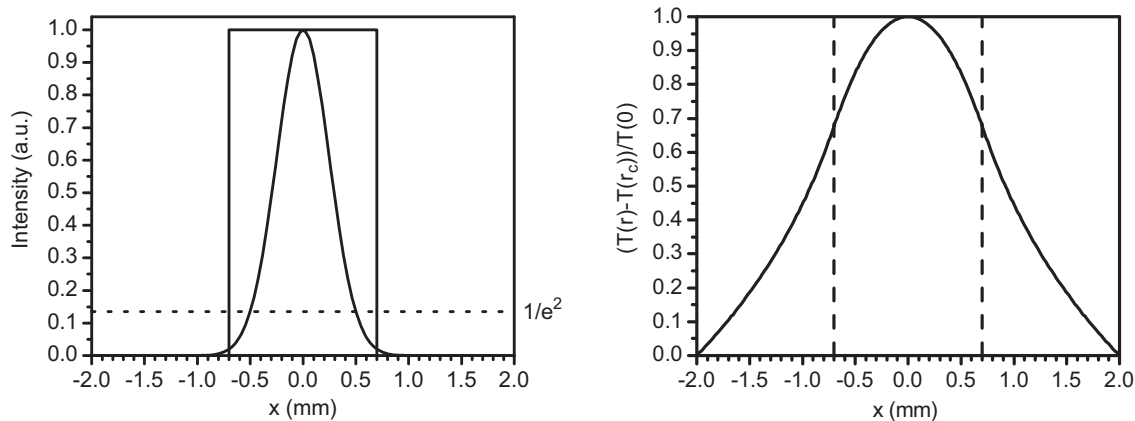


Figure 2.6: Pump–mode overlap (left) and temperature distribution for a top-hat pump profile represented by the dashed lines (right).

a constantly top-hat pump profile will be assumed in the simulations for the simplicity of the model and to isolate the key physical parameters without affecting the pump beam profile. Here the Gaussian mode of 1 mm in diameter at $1/e^2$ fills a pump spot of 1.4 mm in diameter with a fill factor of 70%. As the pump power is increased, the thermally-induced diffraction losses rise, so that the fill factor should be reduced to minimize their influence on mode quality and power loss.

Ideally, the optimum pump–mode overlap should remain constant over the whole pump absorption length to obtain the best compromise between extraction efficiency and beam quality. However the beam quality of the pump source being much worse than that of the laser mode, its beam will quickly diverge away from the focus, significantly reducing the pump–mode overlap. Figure 2.7 illustrates this effect for two pump configurations. The left scheme represents a classic state-of-the-art high-power pump–crystal configuration. A $4 \times 4 \times 12$ mm Nd:YVO₄ crystal is pumped by a 400 μm diameter, 0.22 NA fiber-coupled diode system with a corresponding beam quality of 44 mm·mrad or $M^2 = 170$ at 808 nm. The 700 μm diameter focus is placed close to the input facet to maximize power density where pump absorption is the strongest. However the pump beam quickly diverges out of the laser mode, making the overlap efficiency very poor towards the crystal’s exit facet. This limitation led vanadate to be praised for its strong absorption coefficients, making it possible to absorb most of the pump light before it diverges out of the mode. This strong heat load close to the input facet is of course limiting the maximum applicable power. As the brightness of commercially available diodes increased over the years, it became possible to lower the doping concentration and conversely extend the absorption length, while conserving an identical effective pump–mode overlap [4, 63]. Nowadays, the power available from fiber-coupled systems (> 400 W in 400 μm , > 100 W in 200 μm , or > 30 W in 100 μm , all with 0.22 NA [65, 66, 67, 68]) far exceeds the handling capability of such pump configuration.

Figure 2.7 (right) illustrates the same pump source focused in the center of a $4 \times 4 \times 30$ mm crystal on a 1400 μm diameter spot. The pump beam is now almost collimated within the

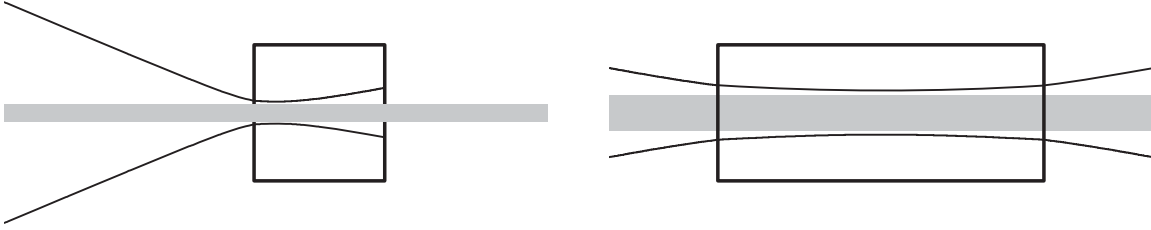


Figure 2.7: Pump beam focusing in a 12 mm long, 808 nm end-pumped crystal (left) and in a 30 mm long, low-absorption crystal with pump back reflection (right). The laser mode is illustrated in gray.

crystal, offering a good overlap with the laser mode along the whole length of the crystal. As the overlap efficiency is maintained on the crystal's output face, the nonabsorbed pump light can be retroreflected on the same beam path, benefitting from the same overlap efficiency as the first pass. Provided that a sufficiently low absorption is chosen, a total absorption length of twice the crystal length is now possible.

2.2.2 Thermal lensing

The following sections describe the temperature distribution resulting from the end-pumping process and the subsequent gradient-index lens and bulging of the crystal's end facets, both contributing to the thermal lensing effect.

Temperature distribution

In classical end-pumped systems, the pump light incident on one of both end faces is absorbed along the length of the crystal. A certain portion η_h of the created inversion doesn't participate in laser or spontaneous emission, thus transferring its energy locally as heat. The end facets being left uncooled in air, a heat transfer operates radially towards the crystal's sides, building a temperature gradient from the heat-generating center portion of the crystal to its cooled edges. In steady-state pumping, extraction, and cooling conditions, the local temperature $T(x, y, z)$ is related to the local heat load $Q(x, y, z)$ by the three-dimensional heat conduction equation:

$$\nabla^2 T(x, y, z) + \frac{Q(x, y, z)}{K} = 0 \quad (2.17)$$

where K is the thermal conductivity. Although an axial heat flow within the crystal along z is possible, it is neglected in the thin slice approximation if the pump beam diameter is significantly smaller than the crystal length. Thus only the radial heat flow is taken into account within one slice of the crystal of infinitesimal thickness dz , which is considered thermally independent from the next. Although the finite-element analysis (FEA) simulations performed in Sect. 2.3.5 do not require this simplification, we will adopt this assumption to describe the generation and behavior of the thermal lens. Conversely, the thermal conductivity will be considered isotropic

and the crystal and pump distribution radially symmetric. This would correspond to pumping a cylindrical rod with isotropic properties instead of a square-section crystal with different thermo-optical properties along the a and c axes, yet the resulting asymmetry in thermal gradient and stresses will be accounted for by the FEA simulations. The heat conduction equation simplifies to its cylindrical expression:

$$\frac{1}{r} \frac{\partial}{\partial r} \left(r \frac{\partial T}{\partial r} \right) + \frac{Q(r, z)}{K} = 0 \quad (2.18)$$

For a top-hat pump profile of radius ω_p , the constant heat deposition within the pump spot is given by:

$$Q(r, z) = \frac{\eta_h}{\pi \omega_p^2(z)} \frac{|dP_p|}{dz}(z) \Theta(\omega_p^2(z) - r^2) \quad (2.19)$$

where $\frac{|dP_p|}{dz}(z)$ is the absorbed pump power per slice thickness dz at a position z . Although $\frac{|dP_p|}{dz}(z) = \alpha P_p e^{-\alpha z}$ in the simplest case of single end-pumping with isotropic absorption, expressions for the absorbed pump power per length will be given in Sect. 2.3.3 for polarization-dependent absorption, single and double-pass absorption, and with saturation of absorption taken into account. Equation 2.18 is then solved to obtain the temperature gradient between a position at a radius r from the crystal center and the cooled crystal edges at the crystal radius r_c :

$$T(r, z) - T(r_c, z) = \frac{\eta_h}{4\pi K} \frac{|dP|}{dz}(z) \times \begin{cases} \ln \left(\frac{r_c^2}{\omega_p^2(z)} \right) + 1 - \frac{r^2}{\omega_p^2(z)} & r \leq \omega_p(z) \\ \ln \left(\frac{r_c^2}{r^2} \right) & r \geq \omega_p(z) \end{cases} \quad (2.20)$$

This solution reveals that the temperature distribution is parabolic within the pump spot and logarithmic outside the pump spot towards the crystal's outer surface. Thus for a given pump spot size, the maximum temperature located in the center of the crystal is directly proportional to the absorbed pump power per length. Such temperature distribution is illustrated in Fig. 2.6 (right) for $\omega_c = 2$ mm and $\omega_p = 700$ μm . When the crystal's side surfaces are kept at a constant temperature along its whole length, the temperature gradient between the center and a position at radius r follows a parabolic evolution within the pump spot:

$$\Delta T(r, z) = T(r, z) - T(0, z) = -\frac{\eta_h}{4\pi K} \frac{|dP|}{dz}(z) \frac{r^2}{\omega_p^2(z)} \quad (2.21)$$

Gradient index lens

Once the temperature map of the crystal has been determined from Equ. 2.21 for a given absorption pattern $\frac{|dP_p|}{dz}(z)$, the bulk part of the thermal lens can be directly calculated from the change in refractive index with temperature:

$$\Delta n(r, z) = n(r, z) - n(0, z) = \frac{dn}{dT} \Delta T(r, z) = -\frac{dn}{dT} \frac{\eta_h}{4\pi K} \frac{|dP|}{dz}(z) \frac{r^2}{\omega_p^2(z)} \quad (2.22)$$

The refractive index follows a parabolic decrease from the crystal center:

$$n(r, z) = n(0, z) \left(1 - \frac{2r^2}{b^2} \right) \quad (2.23a)$$

$$\text{with } \frac{1}{b^2} = \frac{dn}{dT} \frac{\eta_h}{8\pi n(0, z)K} \frac{|dP|}{dz}(z) \frac{1}{\omega_p^2(z)} \quad (2.23b)$$

which results in a gradient-index lens of power $D_{gr}(z)$ at a position z within a slice thickness dz , if we assume that the focal length is very long compared to the crystal length:

$$D_{gr}(z) = \frac{4n(0, z)dz}{b^2} = \frac{dn}{dT} \frac{\eta_h}{K} \frac{|dP|}{dz}(z) \frac{1}{2\pi\omega_p^2(z)} dz \quad (2.24)$$

When integrating Equ. 2.24 over the whole length of the crystal, the gradient-index thermal lens power appears to be proportional to the absorbed pump power P_{abs} divided by the beam cross section $\pi\omega_p^2$, if the pump beam is assumed to be collimated along the absorption length:

$$D_{gr} = \frac{dn}{dT} \frac{1}{2K} \frac{\eta_h P_{abs}}{\pi\omega_p^2} \quad (2.25)$$

Therefore in this simple model, the gradient-index thermal lens is independent of the crystal length and absorption coefficient. However, in practice a shorter crystal with higher absorption will induce higher inversion densities and temperatures, leading to stronger non-radiative effects (see Sect. 2.3.4) and stronger thermal lens aberrations caused by the reduction of thermal conductivity with increasing temperature. Thus a longer crystal with low and homogeneous inversion density will favor a lower and less aberrated gradient-index thermal lens.

Bulging of the end facets

In the case of Nd:YVO₄, the contribution of thermal stress-induced birefringence to the total differential optical path difference (OPD) can be neglected, so that the only other contribution to the thermal lens that needs to be accounted for is the bulging of the end facets. Although this bulging will be calculated in an FEA model, a simple expression for a radially symmetric and isotropic crystal is given. The axial strain distribution ε_{zz} in the direction of the optical axis is provided by [69]:

$$\varepsilon_{zz}(r, z) = (1 + \nu)\alpha_T \Delta T(r, z) \quad (2.26)$$

where ν is the Poisson ratio and α_T the expansion coefficient along the optical axis. Therefore the crystal lengthening and the resulting optical path difference $\Delta(r)$ will follow the temperature distribution as a function of r :

$$\Delta(r) = (n - 1)(1 + \nu)\alpha_T \int_0^l \Delta T(r, z) dz \quad (2.27)$$

With $\Delta T(r, z)$ given by Equ. 2.21, the OPD results in an equivalent lens of power D_{bul} :

$$D_{bul} = \frac{2\Delta(r)}{r^2} = (n-1)(1+\nu)\alpha_T \frac{1}{2K} \frac{\eta_h P_{abs}}{\pi\omega_p^2} \quad (2.28)$$

However in practice only the stresses within a region approximately of one pump radius away from the end surface contribute to the bulging of the end surface [33], so that the integration of $\Delta T(r, z)$ should be conducted only on this short portion of the crystal and therefore P_{abs} in Equ. 2.28 becomes the absorbed pump power within one pump radius depth from the input face. This results in a stronger bulging of the input face for a short highly absorbing crystal compared to a longer lower-doped crystal with equal total absorbed pump power. Thus the region close to the input face that contributes to the bulging reaches much higher temperatures than for a longer less absorbing crystal in which the heat load is spread in a larger volume away from the input face, without contributing to the bulging. As this effect is sensitive to many parameters, a more detailed investigation will be conducted with FEA models of two different pump-crystal configurations in Sect. 2.3.5.

2.2.3 Crystal stress and fracture

Although the onset of thermal lensing and aberrations will limit the pump power for efficient extraction in an undistorted diffraction-limited beam, higher pump powers will eventually induce stresses exceeding the crystal's mechanical capabilities, resulting in the crystal's fracture. Therefore the simulation of stresses is helpful in the design of a pump configuration in order to maintain a certain headroom between the normal operating conditions and the fracture point. Once the temperature distribution has been determined, the resulting stress and strain are investigated by FEA simulations. With the assumption of free crystal facets, which is true for the end facets and a good approximation for the sides held in a soft material such as indium, Hooke's law is used to link the strain and stress tensors [61, 70]. This technique will be used in Sect. 2.3.5 to determine the stress distribution for a given pump configuration, but a simpler approach relying on the plane stress approximation applied to a cylindrical isotropic crystal with single end-pumping helps in pointing out certain stress behaviors [58]. It is shown that the center portion of the crystal is under compression (negative stress magnitudes) while the periphery is under tension (positive stress magnitudes). Although the compressive stress amplitude is usually higher than the tension, most materials possess a higher resistance under compression than under tension. Thus crystal fracture will usually originate from the crystal edge on the input facet, where tensile stress is maximal. For a highly absorbing crystal ($\alpha l \gg 1$) and a pump spot significantly smaller than the crystal cross section ($\omega_p/r_c < 1/2$), the maximum tensile stress can be approximated by:

$$\sigma_{max} = \frac{\alpha_T E \eta_h}{4\pi K} \frac{|dP|}{dz} \quad (2.29)$$

Thus for a single absorption coefficient α , the maximum applicable pump power is given by:

$$P_{p,lim} = \frac{1}{\alpha} \frac{4\pi R}{\eta_h} \quad (2.30)$$

where R given by Equ. 2.16 is a thermal shock parameter which depends only on the thermal and mechanical properties of the material. A larger R will allow higher applicable pump powers before fracture occurs. As expected, a high thermal conductivity K , a high maximum tolerable tensile stress σ_{max} , a low coefficient of thermal expansion α_T , and a low Young's modulus E are desirable parameters for a material's potential for tolerating high pump powers. Equation 2.30 reveals that for a given material, the maximum permissible pump power scales with $1/\alpha$, as demonstrated experimentally [58]. Furthermore, minimizing all sources of nonradiative decay during lasing and nonlasing operation is crucial to keep the fractional thermal loading η_h as low as possible and close to the quantum-defect limit.

2.3 888 nm pumping of Nd:YVO₄. *The road to high power*

Now that the main optical and mechanical characteristics of Nd:YVO₄ and its end pumping have been presented, the limitations of 808 nm pumping for high-power systems are outlined, along with possible workarounds. An alternative pumping wavelength of 888 nm is then introduced, followed by a side-by-side comparison with 808 nm pumping and a detailed analysis of inversion, thermal load and lensing, and of the influence of ETU on heat generation.

2.3.1 Limitations of 808 nm pumping

The limitations of vanadate for high power systems mainly arise from the characteristics of absorption at 808 nm, namely its dependence on the polarization state of the pump light and the high absorption coefficients.

Polarization-dependent absorption

As illustrated in Fig. 2.2 (right), the effective absorption of Nd:YVO₄ is ~ 4 times stronger for c -polarized than for a -polarized light. This has two main consequences on the laser's performance:

- The pump distribution and the total absorbed pump power depends on the polarization state. If the pump light is partially polarized as is most often the case for fiber-coupled diodes, rotating the pump beam polarization or modifying the polarization state by rotating the fiber end or twisting the fiber will result in a varying distribution of the heat load along the crystal length and unstable absorbed pump and output powers. A possible workaround is to completely depolarize the pump light after exiting the fiber with a combination of retardation plates [71], but this doesn't suppress the inhomogeneous heat load. Another solution is to use polarized pump light with free-space propagation or short fibers [72], but this has the disadvantage of not allowing the physical separation of the pump diodes and the laser resonator, while a short fiber length doesn't provide an optimally homogenized beam profile at its output. However this technique is not applicable to high-power pump sources which often rely on the combination of orthogonally-polarized pump diodes.

- The input facet of the crystal is subject to a strong heat load. Since the total absorption is limited by the lower absorption on the a axis, the absorption on the c axis cannot be reduced without sacrificing absorbed pump power on the a axis. Thus the strong absorption close to the input facet induces high temperatures and stresses resulting in bulging, aberrated thermal lensing, and ultimately crystal fracture, and high inversion leading to strong ETU and saturation of absorption. The use of composite crystals comprising an undoped YVO₄ end-cap bonded to the crystal end by optical contact followed by a thermal treatment provides a heat-sink for additional heat removal along the optical axis, and further prevents the bulging of the input face [11]. Such technique extends the fracture-limited pump power by a factor of $\sim 1.4 - 1.5$, yet the availability and cost-effectiveness of high-quality composite crystals are limited by the difficulty in precise alignment of the c axes of the doped and undoped crystals [58].

High absorption coefficients

Although vanadate's high absorption coefficients were seen as an advantage when pump sources suffered from a low brightness, they now limit the maximum applicable pump power. As high-power high beam quality fiber-coupled pump diodes are now available, reducing the absorption coefficient while simultaneously extending the crystal length allows for extending the maximum permissible pump power, while maintaining a good pump-mode overlap [58]. This is usually achieved by reducing the crystal's doping concentration [63] from the typical 1 at.% used in low-power systems, to 0.2 – 0.3 at.% in most lasers over 10 W of output power. However, as the doping concentration is reduced, the non-uniformity and relative uncertainty of the crystal's doping increases, the latter reaching $\pm 50\%$ at 0.1 at.%. These variations exclude the use of such crystals in reliable systems or products so that most high-power commercial lasers are limited to doping concentrations $> 0.2\%$ and lengths < 15 mm.

2.3.2 Absorption at 888 nm

This section presents the characteristics of an alternative pump wavelength, suppressing the limitations of 808 nm pumping caused by the strong and polarization-dependent absorption. A detailed study of the absorption spectrum between 800 and 900 nm in Fig. 2.2 (left) reveals the existence of low absorption peaks around the main absorption lines at 808 and 880 nm, corresponding to transitions from sublevels of the ground state $^4I_{9/2}$ to sublevels of the pump level $^4F_{5/2}$ and of the metastable level $^4F_{3/2}$, respectively. Moreover, the absorption curves for the a and c axes cross at specific wavelengths, with neighboring absorption peaks of almost equal amplitude on both polarizations. Pumping at these wavelengths offers low and polarization-independent absorption, thus suppressing the limitations of 808 nm pumping previously described. Such wavelengths exist at ~ 819 and 888 nm, but we will concentrate on 888 nm for the rest of this work, since it provides a significantly smaller quantum defect than 819 nm. However it should be noted that at 819 nm, equal absorption coefficients of $\alpha_a = \alpha_c = 2.5 \text{ cm}^{-1}$ are measured, four times lower than the absorption on the a axis at 808 nm.

Figure 2.8 (left) provides a detailed view of the absorption spectrum from 884 to 894 nm, revealing neighboring absorption peaks of $\alpha_a = 1.7 \text{ cm}^{-1}$ at 887.9 nm and $\alpha_c = 1.6 \text{ cm}^{-1}$ at 888.8 nm. The analysis of the polarized absorption spectrum at cryogenic temperatures [29] reveals that these absorption peaks correspond to transitions from the second thermally-populated sublevel of the ground state $^4I_{9/2}(Z_2)$ to the $^4F_{3/2}(R_2)$ level on the a axis and to the $^4F_{3/2}(R_1)$ level on the c axis. Although these two absorption peaks are separated by ~ 0.9 nm, this shift is well within the diodes' emission spectra of 2–4 nm. Therefore an effective absorption spectrum was calculated by convoluting the data illustrated in Fig. 2.8 (left) by a 3.5 nm FWHM Gaussian diode spectrum, and also measured with a 3.5 nm FWHM diode system used for the initial experiments. Figure 2.8 (right) demonstrates the good accordance of the calculated spectrum for an ideal Gaussian spectral profile with the measured data for a real diode spectrum. Several key characteristics are observed:

- Absorption coefficients are almost equal at 888 nm with $\alpha_a = 1.2 \text{ cm}^{-1}$ and $\alpha_c = 1.1 \text{ cm}^{-1}$. Such isotropic absorption provides smooth exponential absorption of the pump light along the crystal length, restricting the thermal load of the input facet to a minimum. The absorbed pump power and laser performance becomes independent of the pump light polarization state, so that fiber-coupled diodes can be used without the need for depolarizing the pump beam at the fiber's exit.
- Absorption coefficients are much lower than at 808 nm, allowing the use of long crystals with homogeneous and controllable doping levels.
- Effective absorption curves are almost flat from 886 to 890 nm, so that the precise tuning of the pump wavelength is not necessary, the temperature regulation of the diodes is not critical, the precise wavelength matching of the different diode bars combined in a high-power source is not required, and the wavelength drift resulting from diode aging will have a limited effect on laser performance.

2.3.3 Pump absorption, inversion, and gain

In order to evaluate the potential benefits of pumping Nd:YVO₄ at 888 nm, a direct comparison between two practical high-power configurations, one at 808 nm and the other at 888 nm, is conducted, and the behavior of absorption, inversion, heat load, thermal lensing and stress, and the predominance of ETU are evaluated. The chosen 808 nm configuration illustrates a state-of-the-art high-power pump–crystal setup used in the industry, while the 888 nm configuration models the system used as a basis for most of the practical realizations presented in this work. All setup parameters and main simulation results are assembled in Table 2.5 for an overview of the key differences between the two systems. Furthermore, the fact that the small-signal gain is identical in both systems makes the comparison between most physical parameters very straightforward. A perfectly collimated pump volume is assumed to simplify the understanding of the simulations and isolate the influence of each differing parameter of the two systems, without adding the intricate perturbations of a divergent pump beam. Such simplification

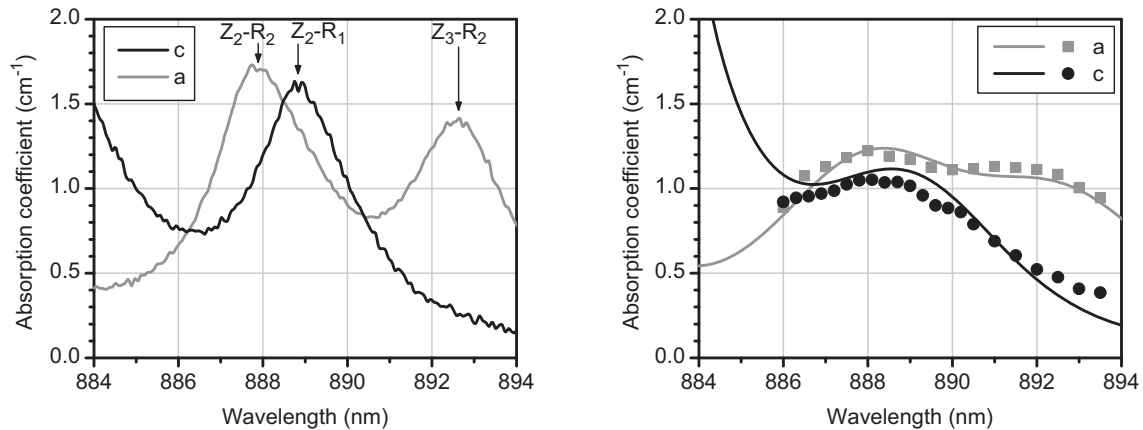


Figure 2.8: Nd:YVO₄ absorption spectrum (left) and effective absorption for a 3.5 nm FWHM diode spectrum (right).

however is perfectly valid as the high beam quality sources available today can be focused in an almost collimated beam within the crystal along the effective absorption length.

The crystal length and doping have been chosen to achieve an equally high absorption of the pump light in both cases. At 808 nm, a classic $4 \times 4 \times 12$ mm 0.27 at.% *a*-cut crystal is chosen, leading to absorption coefficients of $\alpha_a = 2 \text{ cm}^{-1}$ and $\alpha_c = 8 \text{ cm}^{-1}$. In the 888 nm configuration, a long $4 \times 4 \times 30$ mm 0.5 at.% *a*-cut crystal is selected, resulting in effective absorption coefficients of $\alpha_a = 0.60 \text{ cm}^{-1}$ and $\alpha_c = 0.50 \text{ cm}^{-1}$. Both crystals possess a doping concentration at which concentration quenching is not an issue, as illustrated in Fig. 2.5 (left). The pump beam is focused to a radius of $350 \mu\text{m}$ at 808 nm and to $700 \mu\text{m}$ at 888 nm, making the pump beam cross section exactly four times larger in the latter case. Up to 30 W of pump power at 808 nm is incident on the crystal, while 108 W are applied at 888 nm, thus illustrating the practical basic setup developed in this work. While the 808 nm pump light is absorbed in a single pass, the non-absorbed 888 nm pump light is collimated and refocused for a second pass absorption through the crystal, which is made possible by the high pump beam quality, maintaining an optimal pump-mode matching on both passes.

Local pump power

For totally unpolarized pump light, half of the total incident pump power P_p is polarized on each of the *a* and *c* axes, so that the power on each polarization $P_{a,c}(z)$ obeys to its own absorption rule along a crystal of length l :

$$P_{a,c}(z) = \frac{P_p}{2} e^{-\alpha_{a,c}z} \quad (\text{single pass}) \quad (2.31a)$$

$$P_{a,c}(z) = \frac{P_p}{2} \left(e^{-\alpha_{a,c}z} + e^{-\alpha_{a,c}(2l-z)} \right) \quad (\text{double pass}) \quad (2.31b)$$

and the total local pump power is given by:

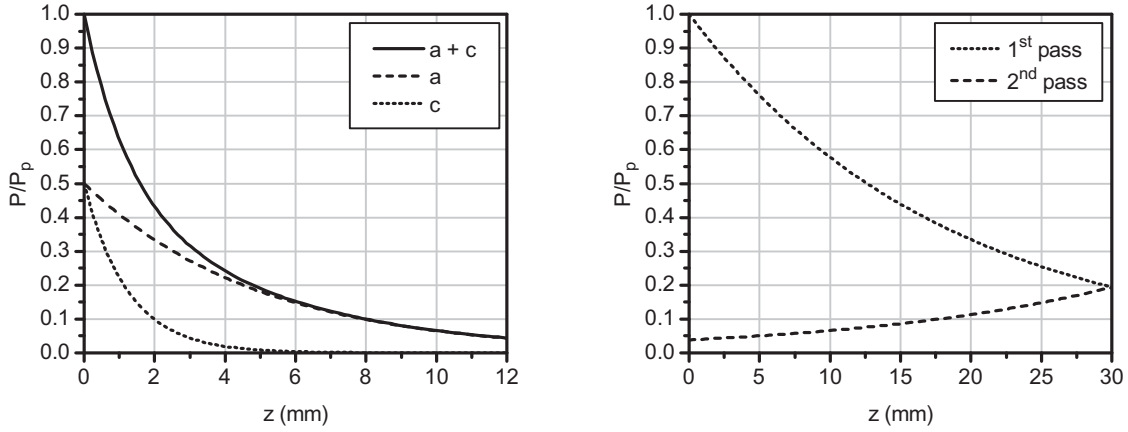


Figure 2.9: Local pump power within the crystal for single-pass absorption at 808 nm (left) and for double-pass absorption at 888 nm (right).

$$P(z) = P_a(z) + P_c(z) \quad (2.32)$$

Figure 2.9 illustrates the evolution of the local pump power along the length of the crystal. For 808 nm pumping the absorption on the a axis governs the absorption efficiency as the totality of the c -polarized light is already absorbed in the first half of the crystal, resulting in an absorption efficiency of 96%. Thus 80% of the c -polarized light is absorbed within 2 mm, while it takes four times longer for achieving a similar absorption on the a -axis. For 888 nm pumping, only the total local pump power is represented, since the two absorption coefficients are almost identical and the overall absorption decay very close to a pure exponential. An absorption efficiency of 80% is achieved in the first pass, while the remaining 20% are retroreflected and undergo the same absorption, resulting in a double-pass absorption efficiency of 96%, similar to that of the 808 nm system.

Absorbed pump power per length

The evolution of the absorbed pump power per length $\frac{|dP|}{dz}(z)$ in the crystal is a useful indicator of the level and homogeneity of the inversion density and the heat load for a collimated pump beam, the absolute value expressing the fact that the absorption in the second pass occurs in the opposite direction. Therefore the absorbed pump power per length $\frac{|dP_{a,c}|}{dz}(z)$ on each polarization is given by:

$$\frac{|dP_{a,c}|}{dz}(z) = \alpha_{a,c} \frac{P_p}{2} e^{-\alpha_{a,c}z} \quad (\text{single pass}) \quad (2.33a)$$

$$\frac{|dP_{a,c}|}{dz}(z) = \alpha_{a,c} \frac{P_p}{2} \left(e^{-\alpha_{a,c}z} + e^{-\alpha_{a,c}(2L-z)} \right) \quad (\text{double pass}) \quad (2.33b)$$

Thus the total absorbed pump power per length is expressed as:

$$\frac{|dP|}{dz}(z) = \frac{|dP_a|}{dz}(z) + \frac{|dP_c|}{dz}(z) \quad (2.34)$$

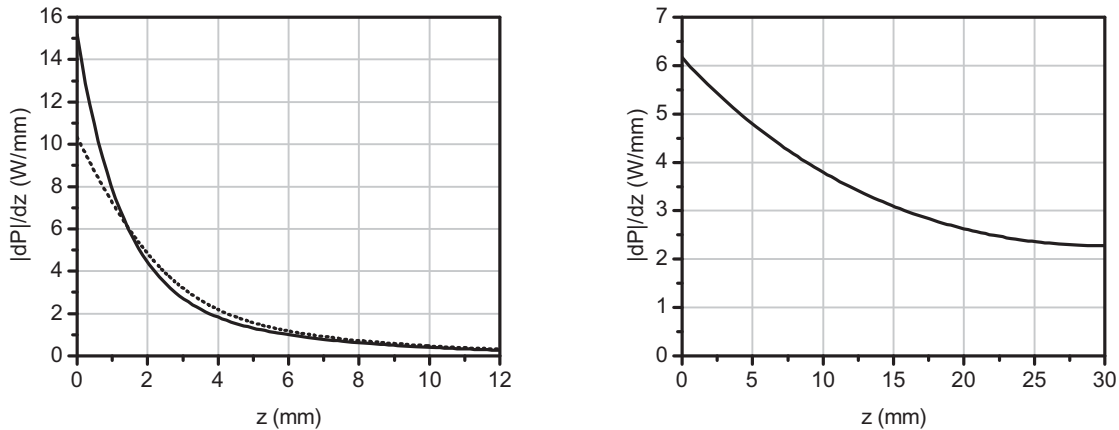


Figure 2.10: Absorbed pump power per length for single-pass absorption at 808 nm (left) and for double-pass absorption at 888 nm (right). Without any extraction, the high inversion density leads to a saturation of the absorption (dotted line), which can be neglected for 888 nm pumping as the inversion densities are much lower.

Figure 2.10 illustrates the strong differences in the level and homogeneity of the total absorbed pump power per length for the two systems. The 808 nm pumped crystal is subject to a very strong absorption load within the first millimeter with a peak of 15 W/mm, while the purely exponential absorption at 888 nm coupled to the pump back-reflexion leads to a much smoother absorption load, with only a factor of three between the input and output facets. As explained in the following paragraph, when no lasing effect occurs the inversion reaches a maximum, thus saturating the pump absorption where the inversion density is the highest. This effect leads to a reduction of the peak absorbed pump power per length from 15 to 10 W/mm for 808 nm pumping, while the much lower peak inversion density in the 888 nm configuration allows for neglecting this effect. In both cases, when lasing occurs, the inversion is clamped at its threshold value so that the saturation of absorption becomes insignificant.

Inversion density

In a four-level system, the pump and lower laser levels can be considered empty at all times, so that only the ground level and the upper laser level are populated. Thus the population of the metastable state is assimilated to the inversion density n , while the ground level population is given by $(n_t - n)$, where n_t is the total ionic density. Without laser extraction, the population inversion is determined by its rate equation:

$$\frac{dn}{dt} = R_p - \frac{n}{\tau} \quad (2.35)$$

where the volume pump rate can be expressed as:

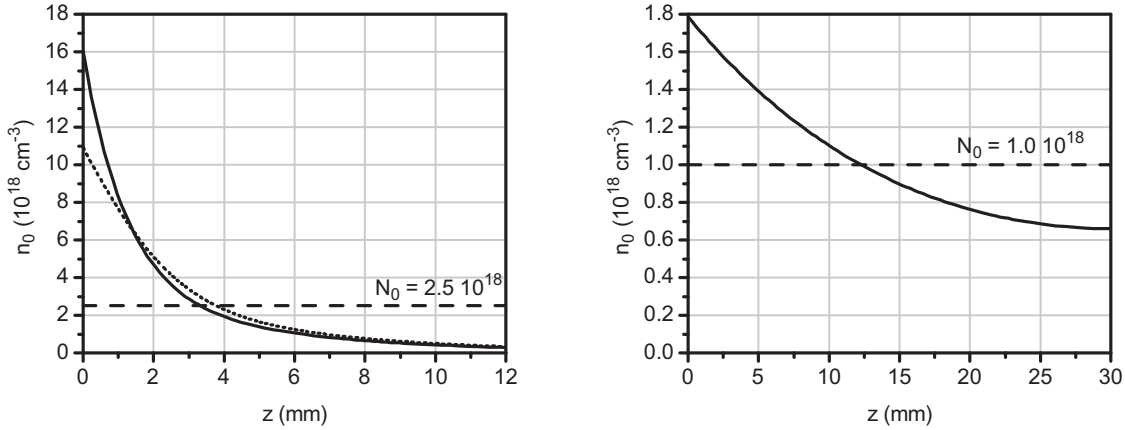


Figure 2.11: Inversion density for 888 nm (right) and 808 nm pumping (left) with (dotted line) and without (full line) taking into account the saturation of absorption. The average inversion density N_0 (dashed line) illustrates how the effective inversion departs from a perfectly homogeneous inversion density within the pump volume.

$$R_p = \alpha F_p \quad (2.36a)$$

$$= \sigma_p (n_t - n) F_p \quad (2.36b)$$

with σ_p the pump absorption cross section and F_p the pump photon flux per unit area:

$$F_p = \frac{P_p}{h\nu_p \pi \omega_p^2} \quad (2.37)$$

Thus for low intensity pumping and absorption and consequently low inversion, $n \ll n_t$ and the absorption coefficient $\alpha \approx \sigma_p n_t$ is constant. However for high inversion densities, the depopulation of the ground level cannot be neglected, and the absorption coefficient decreases linearly with the inversion density. Equation 2.35 is solved to obtain the steady-state inversion:

$$n = n_t \frac{\sigma_p F_p \tau}{1 + \sigma_p F_p \tau} \quad (2.38)$$

with $\sigma_p F_p = \sigma_a F_a + \sigma_c F_c$ for unpolarized pumping. Figure 2.11 illustrates the local inversion density without laser extraction, calculated with a numerical method to easily take into account the saturation of absorption. The much lower peak inversion at 888 nm allows for neglecting the saturation of absorption, even without laser extraction. As listed in Table 2.5, the maximum and average inversion expressed as a percentage of the total ionic density give a qualitative understanding of the absence of saturation of absorption in the 888 nm system, with $n_{max}/n_t = 2.9\%$ at 888 nm and 32% at 808 nm. Although the absorption is saturated at the input face of the 808 nm crystal, the total absorption efficiency remains at $\sim 96\%$ for both configurations.

Lasing and non-lasing conditions

The small-signal gain g_0l is obtained by integrating the inversion density over the crystal length:

$$g_0l = \sigma_e \int_0^l n(z) dz \quad (2.39a)$$

$$= \sigma_e Nl \quad (2.39b)$$

$$= \sigma_e \tau \frac{P_{abs}}{h\nu_p \pi \omega_p^2} \quad (2.39c)$$

where P_{abs} is the total absorbed pump power and N the average inversion density within the pump volume. For both configurations a small-signal gain of $g_0l = 3.6$ is calculated, as the lower N at 888 nm is compensated by the longer crystal length.

As the pump power is increased, the inversion builds up until the gain is sufficient to compensate for the roundtrip losses, including the output coupling transmission, the passive losses due to the residual transmission of mirrors and diffraction, and the active losses resulting from thermally induced diffraction and aberrations of the thermal lens. The threshold condition can be expressed as:

$$R_{oc} \exp(2g_0l - 2\alpha_0l) = 1 \quad (2.40)$$

where $\exp(-2\alpha_0l)$ encompasses all roundtrip losses cited above and R_{oc} is the output coupler reflectivity. Here R_{oc} is chosen for optimum output coupling R_{opt} or maximum output power at the nominal pump power, and can be approximated by [73]:

$$\ln R_{opt} = -2\alpha_0l \left(\sqrt{\frac{g_0l}{\alpha_0l}} - 1 \right) \quad (2.41)$$

Although one can calculate the optimum output coupling, the losses arising from thermal diffraction and aberrations are difficult to predict accurately, so that we will take here a value of $T_{opt} = 40\%$ obtained experimentally (see Sect. 3.2.2). For high gain systems such as is the case here, the losses remain much smaller than the transmission through the output coupler, so that Equ. 2.40 simplifies to:

$$g_0l_{th} = -\frac{1}{2} \ln(R_{oc}) \quad (2.42)$$

so that the small-signal gain at threshold is $g_0l_{th} = 0.25$. As the pump power is increased above threshold, the inversion density remains clamped at its threshold value n_{th} obtained for the threshold pump power P_{th} . When the systems are operated at their nominal pump powers, they lie over 14 times above threshold, corresponding to $P_{th} = 2.1$ W at 808 nm and 7.5 W at 888 nm. The pump power in excess of P_{th} then contributes solely to the laser output, so that the laser extraction efficiency η_l is given by:

$$\eta_l = \frac{P_p - P_{th}}{P_p} \quad (2.43)$$

so that when $P_p = 14 \times P_{th}$, the stimulated-emission extraction efficiency reaches $\eta_l = 0.93$.

2.3.4 Energy-transfer upconversion

During lasing operation, most non-radiative effects are likely to be neglected within the mode area where the stimulated-emission efficiency is $\sim 93\%$. Thus the inversion being clamped at its low threshold value, and the vast majority of excited ions participating in the stimulated-emission process, non-radiative processes such as ETU will not contribute significantly to the heat load, which is here mainly a result of the quantum defect η_{qd}^l (see Equ. 2.4).

However, when no lasing occurs as during the pumping period between pulses in a Q-switched laser, or when the extraction efficiency is low as in an amplifier, the inversion density will be much higher than at cw threshold, and the laser intensity lower than inside a cw resonator or even inexistent. The case of purely non-lasing operation is considered here to evaluate the variation in thermal load compared to that in cw lasing operation.

The inversion rate equation 2.35 is modified to include the ETU depopulation term (see Equ. 2.12):

$$\frac{dn}{dt} = R_p - \frac{n}{\tau} - \gamma n^2 \quad (2.44)$$

In a steady state without laser extraction, the inversion density n is obtained by solving Equ. 2.44 :

$$n = \frac{1}{2\tau\gamma} \left[\sqrt{1 + 4\tau^2\gamma R_p} - 1 \right] \quad (2.45a)$$

$$= \frac{1}{2\tau\gamma} \left[\sqrt{1 + 4\tau\gamma n_0} - 1 \right] \quad (2.45b)$$

with $n_0 = \tau R_p$ the initial inversion without ETU. Figure 2.12 illustrates the relative reduction of the population n/n_0 induced by ETU. From the maximum inversion densities on the input facet calculated in Fig. 2.11 ($n_{0max} = 11 \times 10^{18} \text{ cm}^{-3}$ at 808 nm and $1.8 \times 10^{18} \text{ cm}^{-3}$ at 888 nm), it is easily seen that ETU will strongly depopulate these highly inverted regions.

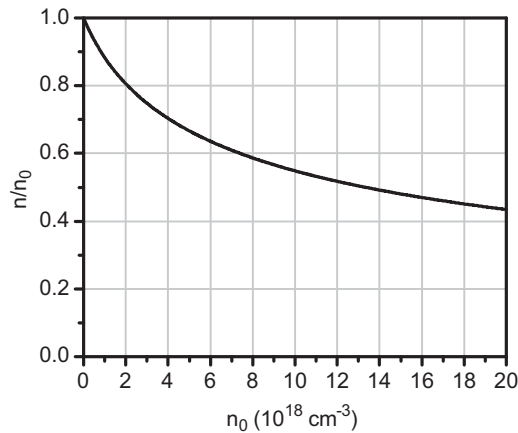


Figure 2.12: Relative inversion with ETU (n/n_0) function of the initial inversion without ETU (n_0).

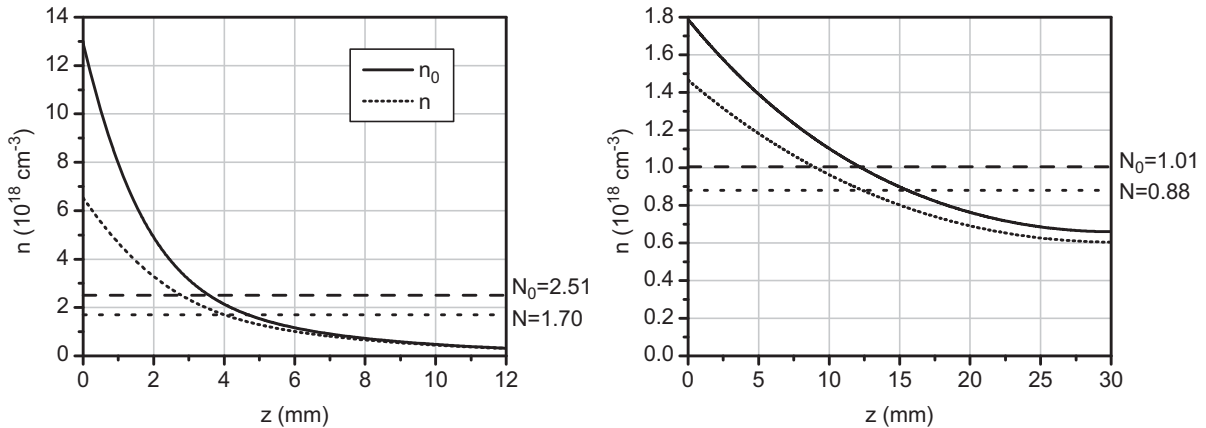


Figure 2.13: Inversion density for 808 nm (left) and 888 nm pumping (right) with (dotted line) and without (full line) taking into account ETU. The average inversion densities with N (dotted line) and without N_0 (dashed line) ETU illustrate the depletion of the total inversion caused by ETU.

The local inversion densities with and without ETU are compared in Fig. 2.13. For 808 nm pumping, the saturation of absorption is taken into account as ETU depopulates the metastable level and conversely repopulates the ground level, thus further increasing the absorption. The inversion n_0 is therefore calculated for the increased pump rate in presence of ETU, which explains why $n_{0max} = 13 \times 10^{18} \text{ cm}^{-3}$ is higher than the $11 \times 10^{18} \text{ cm}^{-3}$ in Fig. 2.11. Taking into account the saturation of absorption, the inversion densities are given by:

$$n = \frac{1}{2\tau\gamma} \left[\sqrt{(1 + \tau\sigma_p F_p)^2 + 4\tau^2\gamma\sigma_p F_p n_t} - (1 + \tau\sigma_p F_p) \right] \quad (2.46a)$$

$$n_0 = \tau\sigma_p F_p (n_t - n) \quad (2.46b)$$

The inversion densities are then integrated over the length of the crystal to obtain the average inversions with (N) and without (N_0) upconversion. The fractional reduction of the population inversion due to upconversion can be expressed as:

$$F_{uc} = \frac{N_0 - N}{N_0} \quad (2.47)$$

Figure 2.14 illustrates the evolution of F_{uc} with pump power for the two pump configurations, showing that the higher average and maximum inversions of the 808 nm configuration lead to a fast increase of the fraction of pumped ions contributing to upconversion, ultimately reaching 33% at the nominal pump power, while the lower inversion densities of the 888 nm system limit this effect to a maximum of 12%.

Once F_{uc} is known at the nominal and threshold pump powers, one can calculate the heat load under lasing and non-lasing conditions. For each pump photon contributing to ETU, its total energy is released as heat, while the others relax spontaneously, and a small portion

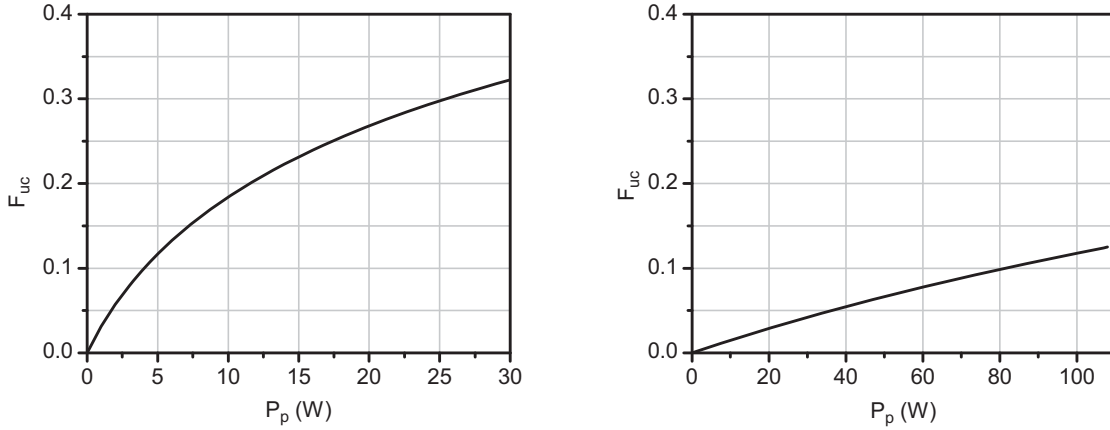


Figure 2.14: F_{uc} as a function of pump power for the 808 nm (left) and 888 nm (right) configurations.

undergo non-radiative decay, which is included in the fluorescence quantum efficiency term η_q . Thus the heat load under non-lasing conditions is expressed as:

$$P_{hNL} = \underbrace{\left(1 - \eta_q \frac{\lambda_p}{\lambda_f}\right) (1 - F_{uc}) P_{abs}}_{\text{Fluorescence}} + \underbrace{F_{uc} P_{abs}}_{\text{ETU}} \quad (2.48)$$

where P_{abs} is the total absorbed pump power. During lasing operation the inversion remains clamped at its threshold level, so that the fluorescence and upconversion depopulation rates remain constantly equal to their threshold levels, all additional pump power contributing exclusively to stimulated emission. The heat load under lasing conditions is therefore given by:

$$P_{hL} = \underbrace{P_{hNL}(P_{th})}_{\text{Fluorescence + ETU}} + \underbrace{\left(1 - \frac{\lambda_p}{\lambda_f}\right) (P_{abs} - P_{abs,th})}_{\text{Stimulated emission}} \quad (2.49)$$

where $P_{hNL}(P_{th})$ is the thermal load at threshold given by Equ. 2.48 and $P_{abs,th}$ is the absorbed pump power at threshold. Figure 2.15 represents the evolution of the thermal load with increasing pump power under lasing and non-lasing conditions. In lasing operation, the thermal load increases linearly with pump power from threshold, with a slope defined by the quantum defect. On the other hand, when no lasing occurs, the slope of the thermal load increases with pump power and the stronger upconversion effects.

The ratio R_h between the heat loads in non-lasing and lasing operation gives an indication on the increase in thermal lensing one can expect if extraction stops or is reduced, as in a Q-switched laser or an amplifier, and is expressed as:

$$R_h = \begin{cases} 1 & \text{below threshold} \\ \frac{P_{hNL}}{P_{hL}} & \text{above threshold} \end{cases} \quad (2.50)$$

Figure 2.16 shows that the heat load doubles without extraction in the 808 nm system, while it increases by 60% in the 888 nm configuration. Although the large ratio in F_{uc} between the

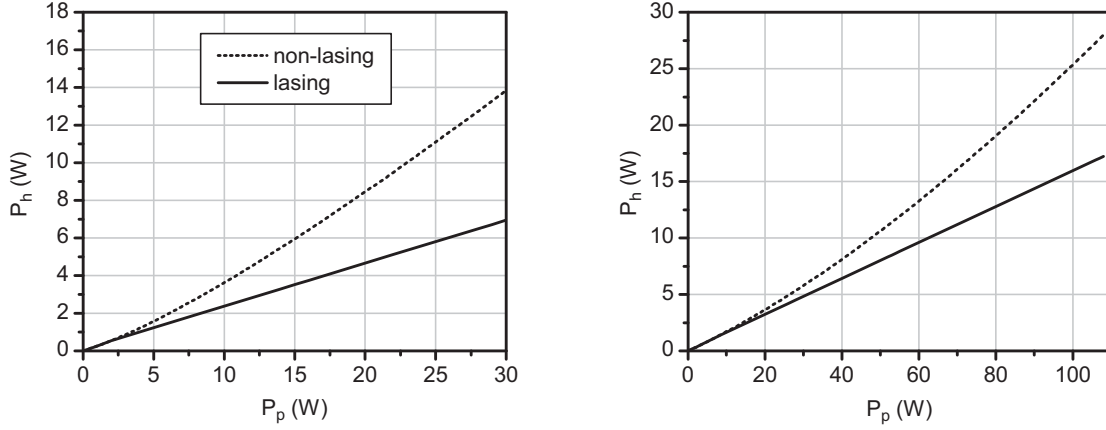


Figure 2.15: Heat load under lasing (solid line) and non-lasing (dotted line) conditions for the 808 nm (left) and 888 nm (right) systems.

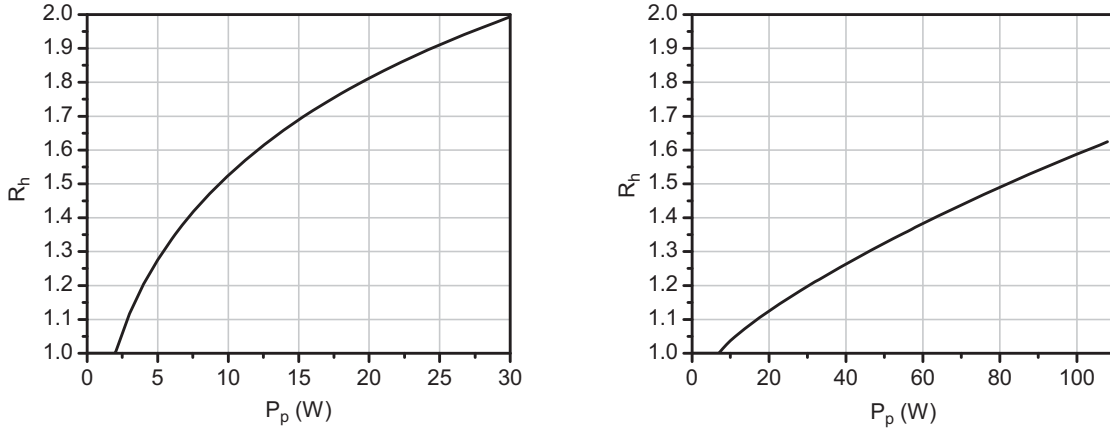


Figure 2.16: Ratio of the thermal loads under non-lasing and lasing operations, for 808 nm (left) and 888 nm pumping (right).

two configurations could let us expect a correspondingly large ratio in R_h , its effect is minimized by the fact that during lasing operation the heat load mainly determined by the quantum defect is much lower for 888 nm pumping, so that the heat generated through upconversion which corresponds to the full pump photon energy appears relatively larger.

Nevertheless the fractional thermal loading under lasing (η_{hL}) and non-lasing (η_{hNL}) operation is much lower for 888 than for 808 nm pumping, as illustrated in Fig. 2.17, and are deduced from Equ. 2.48 and 2.49:

$$\eta_{hNL} = \left(1 - \eta_q \frac{\lambda_p}{\lambda_f}\right) + \eta_q \frac{\lambda_p}{\lambda_f} F_{uc} \quad (2.51a)$$

$$\eta_{hL} = (1 - \eta_l) \eta_{hNL} (P_{th}) + \eta_l \left(1 - \frac{\lambda_p}{\lambda_l}\right) \quad (2.51b)$$

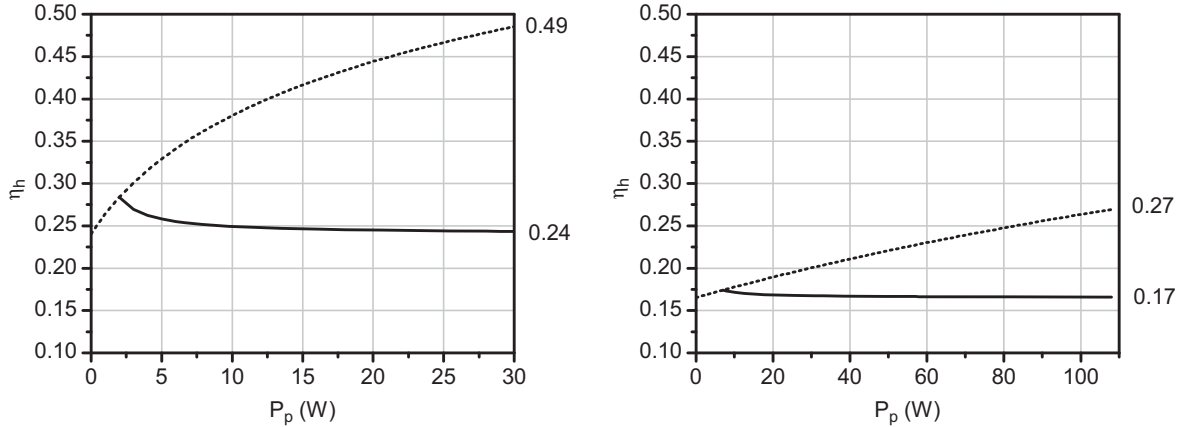


Figure 2.17: Fractional heat load under non-lasing (dotted line) and lasing (solid line) operations, for 808 nm (left) and 888 nm pumping (right).

where $\eta_{hNL}(P_{th})$ is the fractional thermal loading at threshold. As pump power is increased many times above threshold, η_l given by Equ. 2.43 tends to 1 and the contribution of the upconversion-induced heating at threshold becomes negligible. Thus during lasing operation, the fractional heat load within the laser mode is solely determined by the quantum defect of 24% at 808 nm and 17% at 888 nm, which results in a 30% lower heat load in the latter case. Furthermore the undepleted outskirts of the pump spot will benefit from a $\sim 50\%$ reduction in heat generation, further limiting the overall crystal temperature rise and the aberrations in the wings of the thermal lens.

This evaluation of the contribution of ETU to heat generation validates the assumption that other non-radiative processes such as cross-relaxation and excitation trapping are negligible in low-doped crystals (< 0.5 at.%) under intense pumping.

2.3.5 Finite element analysis

This section presents the results obtained by FEA simulations of the two pump–crystal configurations, providing the volume heat load, temperature, strain, and stress distributions. From this data, the gradient-index and end-facet thermal lensing is quantified, and the maximum stress intensity calculated. The finite-element analysis conducted with the laser-dedicated software Lascad [70] consists of three steps:

- Determining the heat load distribution from the pump configuration, the absorption coefficients, and the fractional heat load.
- Solving the three-dimensional heat conduction equation for the calculated heat load and given cooling geometry to obtain a temperature map of the crystal.
- Solving the differential equations of structural deformation and stress.

Table 2.5: Simulation parameters, inversion, gain, and heat load calculations, followed by FEA thermal lensing simulation results.

Pump wavelength	λ_p	nm	808	888
Crystal length	l	mm	12	30
Nd at. doping concentration	C	at.%	0.27	0.5
Nd ionic density	N_t	10^{19} cm^{-3}	3.4	6.3
Absorption coefficient	α_a	cm^{-1}	2	0.60
	α_c	cm^{-1}	8	0.50
Pump power	P_p	W	30	108
Pump passes			1	2
Pump absorption		%	96	96
Absorbed pump power	P_{abs}	W	28.8	103.7
Threshold pump power	P_{th}	W	2.1	7.5
Pump beam radius	ω_p	μm	350	700
Inversion, gain, and heat load				
Small signal gain	$g_0 l$		3.6	3.6
Maximum absorbed power per length	$ dP /dz$	W/mm	15	6
Lasing fractional thermal loading	$\eta_{h,l}$		0.24	0.17
Non-lasing fractional thermal loading	$\eta_{h,nl}$		0.49	0.27
Maximum inversion density	n_{max}	10^{18} cm^{-3}	11	1.8
	n_{max}/N_t	%	32.3	2.9
Average inversion density	N	10^{18} cm^{-3}	2.5	1.0
	N/N_t	%	7.3	1.6
Maximum inversion density at threshold	$n_{max,th}$	10^{17} cm^{-3}	7.6	1.2
	$n_{max,th}/N_t$	%	2.2	0.2
Average inversion density at threshold	N_{th}	10^{17} cm^{-3}	1.7	0.7
	N_{th}/N_t	%	0.51	0.11
FEA simulation				
Left face radius of curvature	R_1	m	0.37	2.60
Right face radius of curvature	R_2	m	15.08	6.14
Gradient-index thermal lens	D_{grad}	m^{-1}	5.18	3.22
Bulging thermal lens	D_{bulg}	m^{-1}	3.27	0.64
Total thermal lens	D_{th}	m^{-1}	8.46	3.86
Gradient-index thermal lens asymmetry	D_a/D_{cgrad}		1.01	1.01
Bulging thermal lens asymmetry	D_a/D_{cbulg}		1.15	1.02
Total thermal lens asymmetry	D_a/D_c		1.06	1.01
Bulging/gradient-index ratio	D_{bulg}/D_{grad}	%	63	20
Thermal lensing coefficient	α	$\mu\text{m}/\text{W}$	0.11	0.06

Thermal lensing

The thermal analysis is conducted for cw lasing operation where the heat is solely generated by the quantum defect between the pump and laser wavelengths. The inversion remaining clamped at its threshold value, additional non-radiative effects are negligible and saturation of the absorption can be omitted in the calculation of the absorbed power density. Table 2.5 summarizes the parameters used for the simulation, in addition to the thermo-optical and mechanical material properties listed in Table 2.4. A mesh cell size of 40 μm perpendicularly to the optical axis, and of 0.2 mm for the 12 mm crystal and 0.5 mm for the 30 mm length along the pump direction are selected to achieve sufficient resolution while using the maximum of the computer's memory capabilities. A much finer mesh is chosen in the beam cross-section as the heat load variations are much stronger in this plane than along the optical axis. Up to ten iteration are conducted to reach a satisfactory convergence of the temperature, strain, and stress distributions, while minimizing calculation time.

Figure 2.18 illustrates the heat load map in the ac plane cut in the middle of the crystal, given in W/mm^3 . The volume heat load is identical to that calculated with Eqs. 2.33 and 2.34 by dividing the absorbed pump power per length by the beam cross section. The much smoother heat load resulting from isotropic and double-pass absorption at 888 nm can be observed, and maximum heat load densities of 9.25 and 0.66 W/mm^3 for 808 and 888 nm, respectively, are obtained on the input facet.

The temperature rise distribution illustrated in Fig. 2.19 is then calculated for cooling along the full length and on the four sides of the crystal, while neglecting the temperature gradient at the mount–crystal interface. Maximum temperature rises of $\Delta T = 188$ K and 49 K are obtained for the 808 and 888 nm configurations, respectively.



Figure 2.18: Heat load distribution in the ac plane for the 808 nm (left) and 888 nm (right) systems.

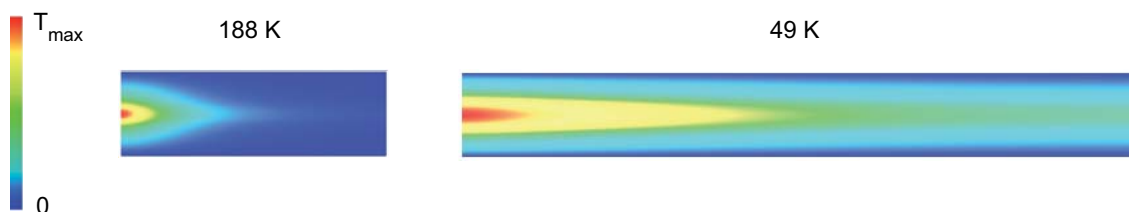


Figure 2.19: Temperature distribution in the ac plane for the 808 nm (left) and 888 nm (right) systems.

From the temperature distribution, a refractive index map is calculated for *c*-polarized light and fitted with a parabolic profile for each slice along the *z* axis, within a radius of 300 μm and 600 μm for 808 and 888 nm, respectively. The dioptric powers of the gradient-index lenses formed by each slice are calculated from the second derivative of the refractive index and Equ. 2.24, and summed to obtain the total gradient-index thermal lensing along the *a* and *c* axes. Table 2.5 gives values of D_{grad} of 5.18 and 3.22 m^{-1} for 808 and 888 nm pumping, respectively. As both configurations provide the same gain, the pump power density at 808 nm is 888/808 times higher than at 888 nm to produce the same inversion density integrated over the crystal length, or small signal gain. As the fractional thermal loading is higher at 808 nm, a correspondingly stronger heat will be generated. One can thus verify that the gradient-index thermal lenses given by FEA verify the following relationship:

$$\frac{D_{grad}(808)}{D_{grad}(888)} = \frac{[P_p/(\pi\omega_p^2) \times \eta_h](808)}{[P_p/(\pi\omega_p^2) \times \eta_h](888)} \quad (2.52)$$

Since the thermal conductivities are almost equal along the *a* and *c* axes, the index gradient is almost symmetrical, with only a slightly stronger value on the *a* axis, as $K_a = 5.10 \text{ W}/(\text{m K})$ and $K_c = 5.23 \text{ W}/(\text{m K})$. Thus the gradient-index lens asymmetry D_a/D_{cgrad} is limited to 1.01 for both configurations with four-side cooling.

The deformation of the crystal's end facets along the *z* axis is then derived from the strain tensor, followed by a parabolic fit to obtain the equivalent radius of curvature of the spherical center portion of the bulging within the pump spot. Table 2.5 provides the radii of curvature of the pump input facet R_1 and of the output facet R_2 , both bulging out, thus resulting in convex surfaces. The absorption being concentrated on the input face for 808 nm pumping, it presents a strong bulging of $R_1 = 0.37 \text{ m}$, while the right facet remains almost flat with $R_2 = 15 \text{ m}$ as almost no heat load is located in that portion of the crystal. For the 888 nm system, the combination of the isotropic absorption, the long absorption length, and the double passing of the pump light leads to a much weaker bulging which is also more balanced between the two facets, with $R_1 = 2.6 \text{ m}$ and $R_2 = 6.1 \text{ m}$. The total contribution of bulging to the thermal lensing is calculated with the thick-lens formula:

$$D_{bul} = \frac{1}{f} = (n - 1) \left[\frac{1}{R_1} - \frac{1}{R_2} + \frac{(n - 1)l}{nR_1R_2} \right] \quad (2.53)$$

where $R_1 > 0$ and $R_2 < 0$. In practice, the thin lens approximation is appropriate as $l \ll R_1$ and R_2 , so that the last term of the thick-lens formula can be neglected. Total dioptric powers of the bulging are then calculated to amount $D_{bulg} = 3.27$ and 0.64 m^{-1} at 808 and 888 nm, respectively. The bulging thermal lens asymmetry is calculated from the individual dioptric powers on the *a* and *c* axes, resulting in $D_a/D_{cbulg} = 1.15$ at 808 nm, and 1.02 at 888 nm. This strong asymmetry in the curvature of the end facets arises from the ~ 2.5 times larger thermal expansion coefficient α_T along the *c* axis than on the *a* axis (see Table 2.4). The stronger radial expansion along the *c* axis results in the flattening of the end facet along this axis. Such asymmetry has often been compensated by cooling the crystal on two opposite faces along the

c axis only, thus creating a larger gradient-index and bulging thermal lensing along the c axis [74].

The total thermal lens is obtained by summing the two contributions from index gradient and bulging, resulting in values of $D_{th} = 8.46$ and 3.86 m^{-1} for 808 and 888 nm pumping respectively, with overall thermal lens asymmetry D_a/D_c reaching 1.06 and 1.01. Thus thermal lens asymmetry is totally negligible in the 888 nm configuration, while it could lead to mode ellipticity and ultimately to a splitting of the resonator's stability ranges in a high-power dynamically-stable resonator pumped at 808 nm. Comparing the two systems with identical gain, the 888 nm pumped crystal will exhibit a thermal lens ~ 2 times lower than the 808 configuration, thus allowing a given resonator to be pumped stronger to achieve twice the gain and approximately twice the output power. Even though the quantum defect is only 30% lower at 888 nm, the added benefit of the lower bulging is responsible for the $> 50\%$ reduction of the total thermal lens. It is therefore practical to define the thermal lensing coefficient as the thermal lens dioptric power per absorbed pump power density:

$$\alpha = D_{th} \frac{\pi \omega_p^2}{P_{abs}} \quad (2.54)$$

Although an ideal material with temperature-independent heat conductivity would exhibit a constant thermal lensing coefficient independently from the pump power and pump spot size if bulging is neglected, in practice the thermal lensing coefficient will rise at high pump power densities and short absorption lengths as the bulging represents a stronger and stronger portion of the total thermal lens. Values of $\alpha = 0.12$ and $0.06 \text{ } \mu\text{m}/\text{W}$ are obtained for the 808 and 888 nm systems, which is comparable to the values available in the literature of $0.09 - 0.14 \text{ } \mu\text{m}/\text{W}$ for 808 nm, and $0.06 - 0.10 \text{ } \mu\text{m}/\text{W}$ for 880 nm, the wide ranges accounting for the various pump power and spot size configurations [73].

Stress

Although thermal lensing is the main limitation to a resonator's stability, pumping with even higher powers eventually induce internal stresses sufficiently strong to exceed the material's stress fracture limit, leading to the cracking of the crystal. Thus the internal stress tensor is calculated by FEA for the two configurations, providing a volume map of tensile and shear stresses. It has been shown that calculating the stress intensity σ_I gives a better indication on the fracture limit than individual stress components [70], and is expressed as:

$$\sigma_I = \max(|\sigma_1 - \sigma_2|, |\sigma_2 - \sigma_3|, |\sigma_3 - \sigma_1|) \quad (2.55)$$

Figure 2.20 provides a view of the stress intensity distribution from the input face where the stresses are maximum. For the 808 nm configuration a maximum stress intensity of 73 MPa is reached while this is limited to 35 MPa at 888 nm. The strongest stress intensities located on the corner of the input face and the cooled surfaces along the c axis correspond mainly to tensile stress in the radial a axis direction. This explains why Nd:YVO₄ normally breaks on the input face with a crack originating from the edge and extending towards the pump spot

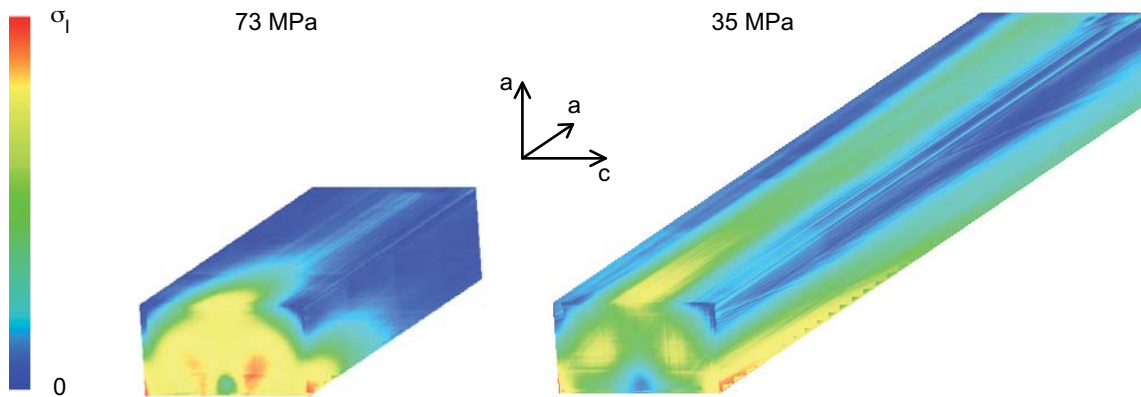


Figure 2.20: Stress intensity distribution with the crystal volume cut in the ac plane for the 808 nm (left) and 888 nm (right) systems.

along the c -axis. It is difficult to correlate the absolute value of the calculated stress intensity to the maximum tensile stress of 53 MPa given in the literature, but one should compare the calculated stress values for known experimental fracture limit conditions. Furthermore, the stress was calculated here for full laser extraction, whereas an underfilled pump spot will result in additional heating and stresses. Crystal fracture can also occur for a configuration designed close to its fracture limit, if lasing is interrupted or if an amplifier is unseeded.

Chapter 3

Continuous wave oscillation

This chapter focuses on the implementation of 888 nm pumping of Nd:YVO₄ in systems operated in continuous wave. A multi-transversal-mode oscillator is first built for a basic characterization of the maximum extractable output power and of the thermal lensing, without having to care about mode-matching considerations. Different crystal and cooling geometries are tested and the specific benefits of 888 nm pumping verified. A TEM₀₀ oscillator is then optimized for high-power high beam-quality operation, and its power is scaled in a periodic resonator arrangement. The high-gain module is then used for efficient single-pass amplification of the oscillator's output. Finally, intracavity doubling of these resonators allows for the generation of high-power, low-noise cw green light.

3.1 Multimode resonator

The systems built to demonstrate 888 nm pumping of vanadate relying on custom crystals and diodes, these two key components are detailed through the two following sections preceding the description of their implementation in a multimode oscillator.

3.1.1 Crystals

Nd:YVO₄ crystals commonly used in commercial systems range from 3 mm in length and 1 at.% for low-power lasers to 15 mm and 0.2 at.% for higher-power configurations. Crystal cross section can be round or square, from 2 to 4 mm in width depending on the pump spot size. Although a round cross section allows for a radially symmetric cooling, no mechanical axis is available for the orientation of the crystallographic *c* axis and therefore of the laser polarization. Thus many crystals are cut with a square cross section and the *c* axis aligned to the mechanical vertical axis. Cooling can be achieved on the periphery of the cylindrical crystal or on all sides of the square cross-section crystal, yet two-side cooling is often preferred for its simplicity as the crystal mount requires only two pieces pressing the crystal on opposite sides, while the two other sides are left free for a laser beam to be folded by near-normal incidence pump mirrors. If the pump spot is significantly smaller than the crystal cross section, no astigmatism of the gradient-index thermal lens is noticeable. The crystal is then held in a copper block acting as a heatsink,

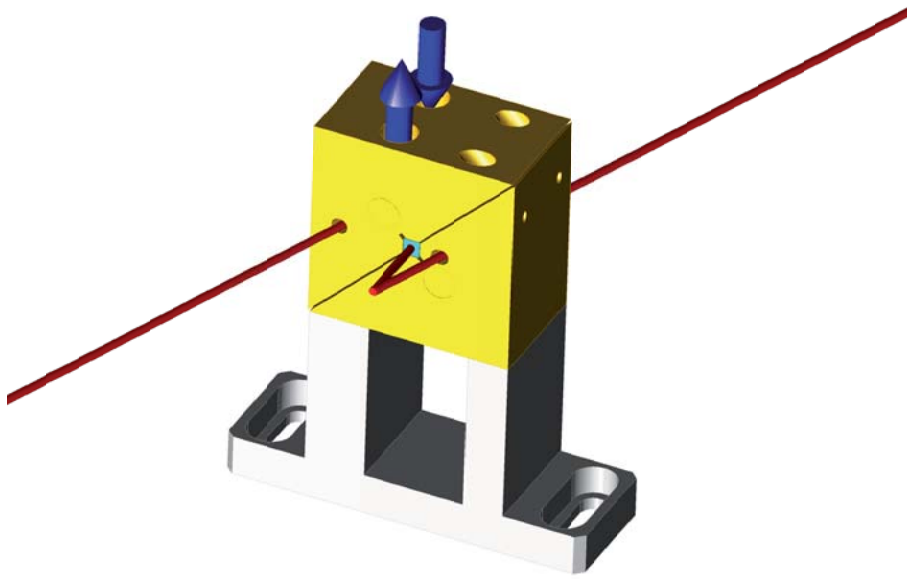


Figure 3.1: Four-side water-cooled crystal mount. The lower water circuit and the 10° incidence-angle pump mirrors are not represented.

which is then conduction cooled for low-power systems, or water cooled in high-power lasers. The excellent $400 \text{ W}/(\text{m}\cdot\text{K})$ thermal conductivity of copper allows for an efficient heat transfer from the crystal to the outside or to the cooling water, thus minimizing the temperature gradient between the two and effectively limiting the maximum temperature attained in the center of the pump spot. A layer of indium is added between the crystal and the mount to act as a mechanical buffer layer. Indium is chosen for its softness at room temperature, allowing it to fill all crystal and heatsink surface imperfections for an optimal thermal coupling, and to eliminate the local stress at contact points and the overall stress caused by thermal expansion of the crystal or the heatsink. Its relatively high thermal conductivity of $82 \text{ W}/(\text{m}\cdot\text{K})$ associated to a foil thickness of $100\text{--}200 \mu\text{m}$ minimize its additional thermal gradient. The crystal's sides are fine-ground to avoid parasitic lasing within the crystal, while one of the end facets is wedged with an angle of 0.5° for the same reason. Thanks to the crystal's birefringence, laser oscillation on the a and c axes require a slight tilting of one of the end-mirrors to compensate for the stronger prism effect on the c axis, as $n_c > n_a$. Thus when the resonator is aligned for the c polarization, it is out of alignment for the a axis, thus insuring high output polarization purity.

The low absorption coefficients at 888 nm require long crystals, so that lengths of 20 mm and 30 mm were selected with respective doping concentrations of $0.7 \text{ at.}\%$ and $0.5 \text{ at.}\%$. Such concentrations allow a high crystal-to-crystal repeatability, which was verified by comparing the absorption and laser performance of different crystals inserted in the same resonator. The long crystal length is achieved by cutting a large portion of the total boule, so that doping homogeneity and crystal quality can be problematic. Although no means to quantify these effects were employed, consistent performance was achieved with crystals provided by Casix, Fuzhou, China, while the 30 mm sample from Castech, also in Fuzhou, China, provided significantly lower

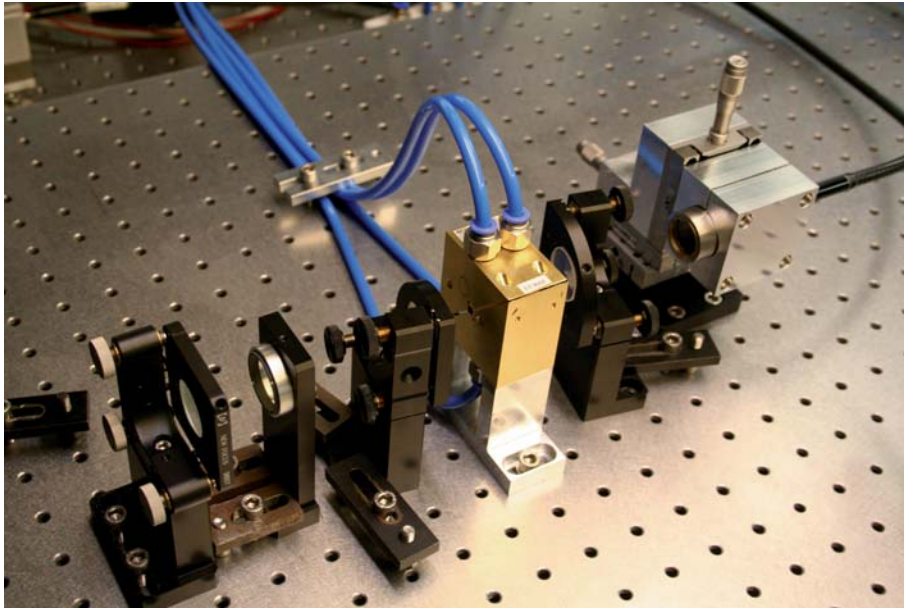


Figure 3.2: Pump–crystal setup including a $4 \times 4 \times 30$ mm 4-side cooled crystal, pump delivery optics for the fiber-coupled source (right), and pump back-reflection with a lens–mirror combination (left).

performance and stronger thermal lensing. Thus, unless stated otherwise, all systems were based on Casix crystals. Square cross sections of 4×4 mm were selected for easy mounting with a sufficiently large side surface and to avoid pump clipping and diffraction of the laser mode. Although two-side cooling was tested, four-side cooling provided more efficient heat extraction with no measurable thermal lens ellipticity (see Sect. 3.1.3). The 30 mm long crystal configuration used as the building block for most of the systems described in this work is illustrated in Fig. 3.1. The crystal is held between two half-square blocks with a central portion cut in the crystal’s location. Each corner possesses a slit to avoid exerting any pressure on the crystal’s corner which would result in its fracture. Adding a $200 \mu\text{m}$ layer of indium on each side of the crystal, a uniform pressure is exerted on each face of the crystal perpendicularly to its surfaces, thanks to the softness of indium which suppresses any shear stress. Each half block possesses its own water circuit (not represented in the lower part) placed along a diagonal to insure identical cooling of the two faces. The copper blocks are further gold plated to limit corrosion. The crystal being inserted in a z-folded resonator, holes are drilled with an angle of 20° with respect to the optical axis to allow for the folding of the laser mode on the two 10° incidence-angle pump mirrors.

Figure 3.2 illustrates the crystal assembly between the two pump mirrors tilted at 10° with respect to the optical axis. On the right, the fiber-coupled pump light is focused in the crystal with a collimating and focusing lens assembly mounted on a 3-axis translation stage. The non-absorbed pump light is then collimated by a plano-convex lens and retroreflected on a flat mirror on the left side of the crystal mount.

3.1.2 Diodes

Since the first diode laser was demonstrated in 1962 [64], the power, brightness, efficiency, and lifetime of commercially-available diodes has made tremendous progress. The multi-emitter 1 cm wide bar design has emerged as the standard for high-power sources. Output powers up to 500 W and electrical-to-optical efficiencies of 70% at room temperature have been recently reported from a single 1 cm bar [68]. Conversely, standard commercial bars are now available with an output power of 75 W with conduction cooling [68] and 120 W with micro-channel cooling [75]. Conduction cooling presents the advantage of simplicity, reliability, and cost, as the diode bar is soldered on a copper block which will then be in contact to an air or water-cooled heatsink. Thus industrial-grade water can be used to cool the heatsink through large cross-section conducts, the diode being electrically isolated from the water which remains out of the optical cavity, preventing any risk of leaks or contamination.

Micro-channel cooling consists in mounting the diode bar on a thin mount composed of sandwiched layers of copper in which very fine channels of $\sim 300 \mu\text{m}$ in diameter are drilled for the water to pass very close to the diode junction. The small dimensions of these conducts opposing a strong resistance to the water flow, high-pressure pumps are necessary to achieve a sufficiently high coolant flow. The water attaining a high speed of $> 3 \text{ m/s}$ within these micro-channels, very clean water is necessary to minimize erosion and maintain high cooling efficiency over time. Furthermore, the diode being in electrical contact with the coolant, de-ionized water is necessary to avoid current leaks. Thus micro-channel cooling requires an excellent control of water quality and resistivity to reach a good lifetime. Yet the $\sim 2 \text{ mm}$ thickness of these submounts allows for their stacking to form high-brightness diode stacks, which couldn't be achieved with the much bulkier passive submounts.

Independently of the mounting technique, the beam emerging from a 1 cm bar is highly elliptic and with asymmetric beam quality. As waveguiding occurs only in the direction of the junction or fast axis, the beam is near diffraction-limited along this axis with $M^2 \approx 1.5$, and a large divergence of $\sim 30^\circ$ FWHM resulting from the $\sim 2 \mu\text{m}$ thick junction. In the perpendicular direction or slow axis, the quality of the beam emerging from the 1 cm wide emitting area with a $\sim 10^\circ$ FWHM divergence is much worse with $M^2 \approx 2000$. Thus such a beam of very asymmetric quality cannot be coupled directly into an optical fiber of small diameter. Beam shaping needs to be applied to convert this beam in one with a more symmetric quality. This can be achieved with two mirrors [76], micro-lenses [77], stair mirrors [78], or tilted glass plates [79], but in all cases it consists in collimating the beam along the fast axis before cutting it in several pieces along its wide, low beam-quality direction. Each beam section is then rearranged above each other, effectively reducing M^2 by the number of beamlets in the slow axis, and increasing it by the same number along the fast axis. This square cross-section beam can then be effectively coupled in an optical fiber of sufficient diameter and numerical aperture.

The development of diodes at specific wavelengths has mostly been application-driven. Thus AlGaAs/GaAs material is used in 808 nm diodes for Nd:YAG and Nd:YVO₄ pumping, while InGaAs/GaAs allows for the production of diodes emitting in the 9XX range, thus 915, 940, and 976 nm for pumping Yd-doped crystals, glass, or fibers. The most reliable diodes available today

Table 3.1: Fiber-coupled diode systems characteristics.

Manufacturer		Laserline	Limo
Model		LDF 400-300	100-F400
Number of bars		2×7	4
Cooling		micro-channel	conduction
Bar characteristics		Unit	
Nominal power	W	50	40
Bar width	mm	8	10
Number of emitters		40	19
Pitch	μm	200	500
Emitter width	μm	100	130
Threshold current	A	10	6
Slope efficiency	W/A	1.1	1.1
Nominal current	A	55	43
Efficiency	%	49	56
System characteristics			
Output power	W	300	115
Operating current	A	55	40
Fiber-coupling efficiency	%	43	76
Electrical-to-optical efficiency	%	21	43

are in the 980 nm range, thanks to the intensive research and development conducted for telecom applications where the sources cannot be serviced during their lifetime. The more recent drive for the development of diodes emitting at 880 and 885 nm for Nd:YVO₄ and Nd:YAG direct upper-laser level pumping hasn't been sufficient for making such sources widely available yet.

Thus the experimental demonstration of high-power 888 nm pumping of vanadate required the development of custom semiconductor wafers, the mounting of the bars on submounts, and finally their integration in a fiber-coupled system. All wafers were produced at the Ferdinand-Braun-Institut für Höchstfrequenztechnik (FBH) in Berlin and the bars mounted at Jenoptik Laser Diode GmbH in Jena. The first batch of bars were designed for micro-channel cooling and integration in a fiber-coupled system at Laserline GmbH to have a large excess of power available for the first experiments. The second batch was designed for passively-cooled submounts to be integrated in fiber-coupled systems at Limo GmbH, producing sufficient power for the basic setup devised in the initial experiments, while benefiting from a much simpler and more compact solution. Table 3.1 summarizes the main characteristics, design parameters, and performance of the two systems.

The Laserline system comprises two stacks of 7 micro-channel-cooled bars, followed by cylindrical lenses for fast-axis collimation, polarization coupling of the two stacks, and titled glass plates for beam shaping [79]. All bars are electrically connected in series so that the

power supply needs to provide a current equal to each bar's nominal current, but under ~ 26 V corresponding to 14 times the nominal bar voltage of 1.8 V. The rearranged compound beam is then injected in a 400 μm diameter, 0.22 NA, 5 m long fiber cable with free-standing fiber ends to minimize heating on the input and exit ferrule facets. Each 8 mm wide bar comprising 40 emitters with a fill-factor of 50% provides 50 W of power for a nominal current of 55 A. With a classic 1.1 W/A slope efficiency and a relatively high threshold current of 10 A, the electrical-to-optical efficiency approached 50%. The system provides 300 W of power out of the fiber as the efficiency of the beam shaping and of the coupling is limited to $\sim 43\%$. This relatively low number is attributed to the use of standard polarization-coupling components designed for 808 nm instead of 888 nm, and to the possibly non-optimal bar width and divergence characteristics for the given beam-shaping system.

The Limo system contains only four bars followed by cylindrical lenses for fast-axis collimation and micro-lenses for beam shaping [77], before in-coupling in a similar fiber as above. The conduction-cooled submounts and the resulting larger temperature gradient between the cooling water flowing through the heatsink and the diode bar limit the output power to 40 W for a nominal current of 43 A. However the lower threshold of 6 A leads to a higher efficiency of 56%. The output power reaches 115 W at a nominal current of 40 A, thanks to the high coupling efficiency of $\sim 76\%$, benefiting from a bar design optimized for the available beam-shaping optics.

The Laserline system was used for the initial experiments while the Limo diodes were integrated in the following cw, ns, and ps experiments. The key characteristics of one of the two systems are illustrated in the following figures. Figure 3.3 illustrates the dependence of power and wavelength on current and water temperature for the Limo diode. Once the current has reached the ~ 6 A threshold for the four diodes, the output power increases linearly with a slope of 3.4 W/A, corresponding to the ~ 1.1 W/A slope efficiency of each bar and the high coupling efficiency of $\sim 76\%$, reaching 114 W at a nominal current of 40 A. Although the water temperature is held constantly at 18°C, the heat generated at the diode junction increases linearly with current above threshold, thus the temperature gradient between the water and the junction follows the same evolution. As the current and junction temperature increase, the emission center wavelength shifts to longer values, with a constant slope of ~ 0.18 nm/A above 20 A. As is illustrated in Fig. 3.3 (left), the wavelength reaches 886.7 nm at nominal current, so that the water temperature needs to be increased to reach 888 nm. Figure 3.3 (right) illustrates the linear shift of the emission wavelength with water temperature at a constant current of 40 A, leading to a typical slope of 0.3 nm/°C. Thus a center wavelength of 888 nm is reached for a water temperature of 22.5°C. Although such water temperature allows the diode's operation in a wide range of environmental conditions without the risk of water condensation, the relatively large temperature gradient of 13°C between the water and the diode submount inherent to the system's design, leads to diode temperatures $> 35^\circ\text{C}$ which could reduce its lifetime. Thus future bar designs should target a center wavelength 1–2 nm longer to keep water temperature in the 15–20°C range, thus reducing the junction's own temperature. As the temperature is increased by 5°C, the output power drops by only $\sim 1\%$, so that this effect can be neglected

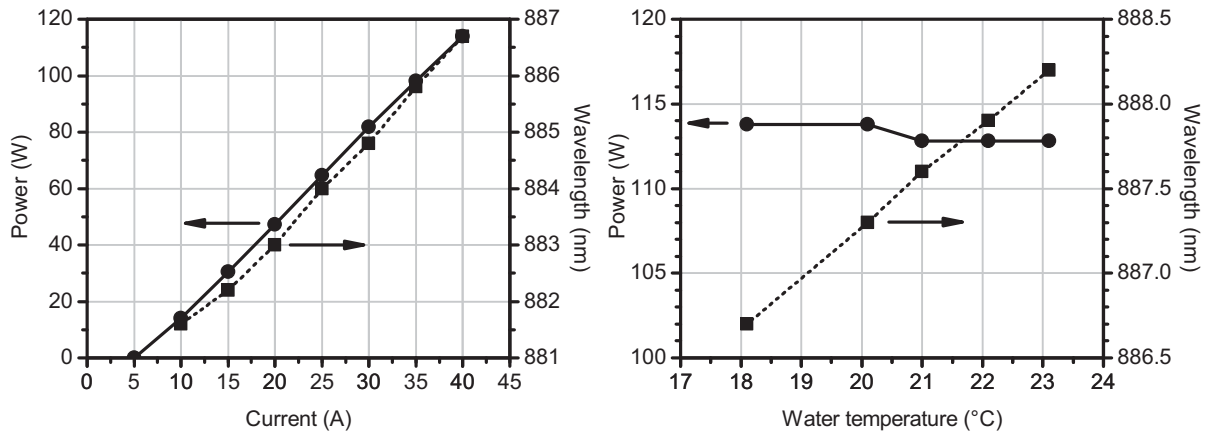


Figure 3.3: 100 W Limo diode output power (solid line) and wavelength (dotted line) function of current for 18°C water temperature (left) and function of water temperature for 40 A current (right).

during the adjustment of temperature for wavelength tuning. The bars of the Laserline system however, were designed with a too long wavelength, so that the output power was limited to 125 W at 25 A for 15°C water if a wavelength of 888 nm was to be maintained. This imprecision in the design wavelength is easily explained as these bars weren't part of a standard production and the mounting and cooling technique has a strong influence on the junction temperature for a given coolant temperature.

The emission spectrum remains within a 2–3 nm FWHM range when the current and temperature are varied and as the ~ 2 nm spectrum of each diode bar shifts and changes in shape. The Laserline diode's spectrum was slightly wider in a range of 2.9–3.8 nm, as the system integrates 14 bars that have not been individually selected for optimal wavelength matching, as opposed to what was done for the Limo systems. Thus the emission spectrum does not retain an identical shape when temperature or current are varied, and depends on the inherent shift between the different bars integrated in the system, as illustrated in Fig. 3.4 (left) for the Laserline diode operated at 22 A and 15°C water temperature.

Figure 3.4 (right) illustrates the beam shape of the Laserline's 5 m fiber output facet imaged to a 1.2 mm diameter spot with a 50 mm focal length collimating achromat, and a 150 mm focusing plano-convex single lens. The beam is almost flat-top, with a slightly increasing intensity towards its center, yet the precise shape depends on the in-coupling parameters and fiber length. Thus for similar 5 m long, 400 μm , 0.22 NA fibers used in the Laserline and the various Limo systems, a good homogenization is achieved over the fiber length, but a stronger intensity is noticed in the beam center as not all fiber modes are excited when in-coupling below the fiber's acceptance NA or diameter. The long fiber is however desirable to minimize the influence of bending and twisting of the fiber on the output beam profile.

Figure 3.5 illustrates how the near flat-top profile in the image plane of the output facet gradually shifts towards a Gaussian-like profile when moving away from the focus position. This evolution is generally of no importance when the pump light is absorbed in a very short distance,

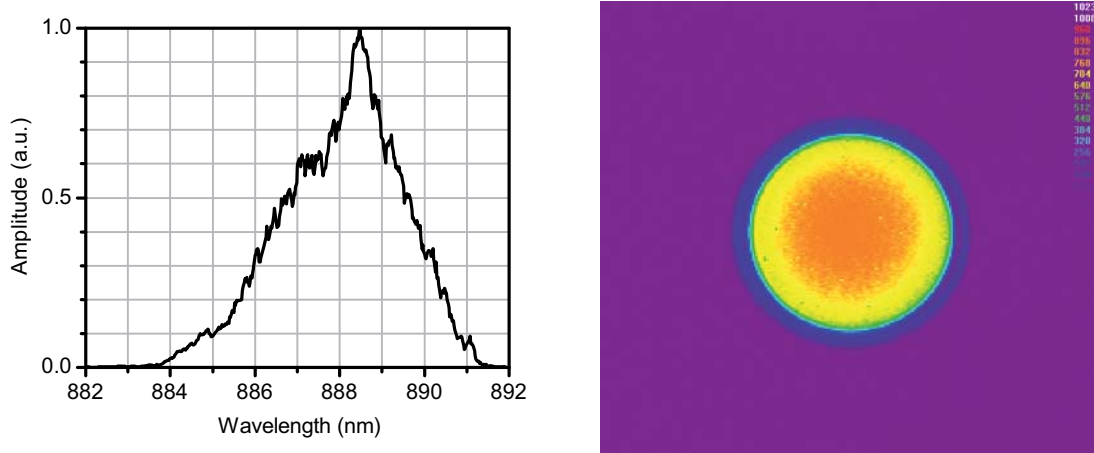


Figure 3.4: Laserline diode spectrum centered on 888 nm for a 22 A current and 15°C water temperature (left) and beam image in the focus (right)

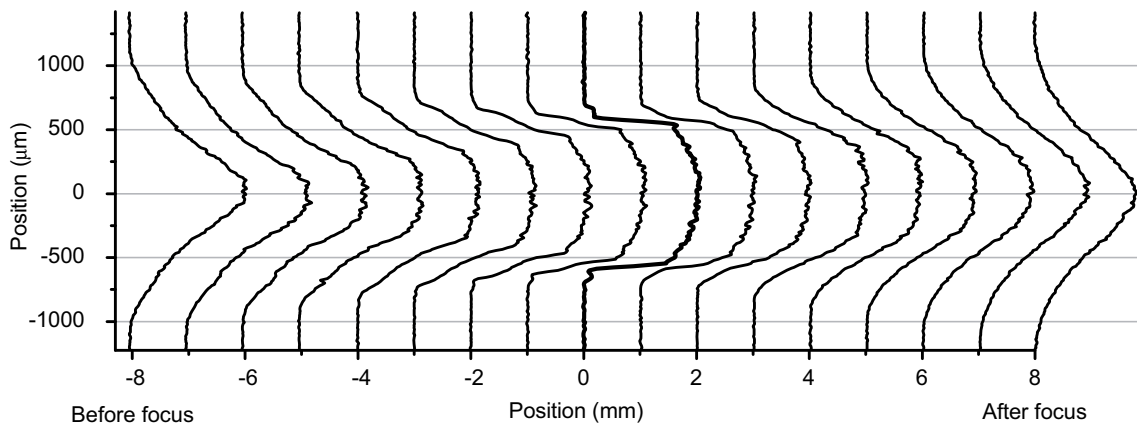


Figure 3.5: Evolution of the pump beam profile before and after the image of the 400 μm , 0.22 NA, 5 m-long fiber end facet for a 1.2 mm pump spot diameter.

but it should be considered here as the pump light will be effectively absorbed along the full length of the 30 mm crystal. Thus the evolution of the profile is measured in a range of ± 8 mm in air around the focus, corresponding to ~ 32 mm in the crystal. It can be noticed that the beam profile is slightly more triangular before the focus and more Gaussian-like after the focus, which could result from spherical aberration. However, the large pump spots > 1.2 mm in diameter allow for neglecting such effects, so that single plano-convex lenses are used without any significant beam degradation.

3.1.3 Multi-transversal-mode oscillator

Although end pumping with fiber-coupled diodes brings the most benefits to diffraction-limited sources, the initial evaluation of 888 nm pumping was conducted on multi-transversal-mode oscillators to eliminate pump-mode matching considerations of the basic characterization. Thus

when the resonator is kept very short, the fundamental mode diameter of a few hundred μm is much smaller than the pump spot, so that the latter naturally fills with many higher order transversal modes. The output beam quality is of course very poor, but the large number of modes allows an excellent total overlap with the pumped region in the crystal, resulting in an optimal power extraction. The optical efficiency reached in such system is then taken as an upper limit that a single transversal mode oscillator can only approach due to the reduced overlap integral between the pump and the Gaussian mode.

Experimental setup

Figure 3.6 (left) illustrates the basic setup used for these initial characterizations. The output of the 400 μm , 0.22 NA Laserline system is collimated by a 50 mm focal length achromat L_1 to minimize spherical aberrations. The light out of the fiber is almost completely unpolarized thanks to the 5 m long fiber and the two polarization-combined diode stacks, so that the first thin-film polarizer (TFP) tilted at a Brewster angle of 56° dumps half of the power on the vertical s polarization. The transmitted p horizontally-polarized light is then rotated with a half-wave plate and followed by a second TFP to form a variable attenuator. This setup offers the advantage of a continuous variation of the pump power without any shift in wavelength or change in the spectrum shape that would occur when varying the diode current. Furthermore, the 300 W of output power provide almost 150 W of polarized light on the crystal. As a wavelength of 888 nm could not be achieved at high current with water temperatures above 15°C , the diode was operated at a current of 40 A and a water temperature of 20°C , leading to a wavelength of 891.5 nm. As illustrated in Fig. 2.8 (right), $\alpha_a = 1.1 \text{ cm}^{-1}$, so that pumping with a -polarized light at this wavelength is equivalent to unpolarized pumping at 888 nm. The collimated pump beam is then focused with a 150 mm focal-length single lens L_2 in the center of the $4 \times 4 \times 30 \text{ mm}$, 0.5 at.% Nd:YVO₄ crystal placed between two flat dichroic pump mirrors M_1 and M_2 .

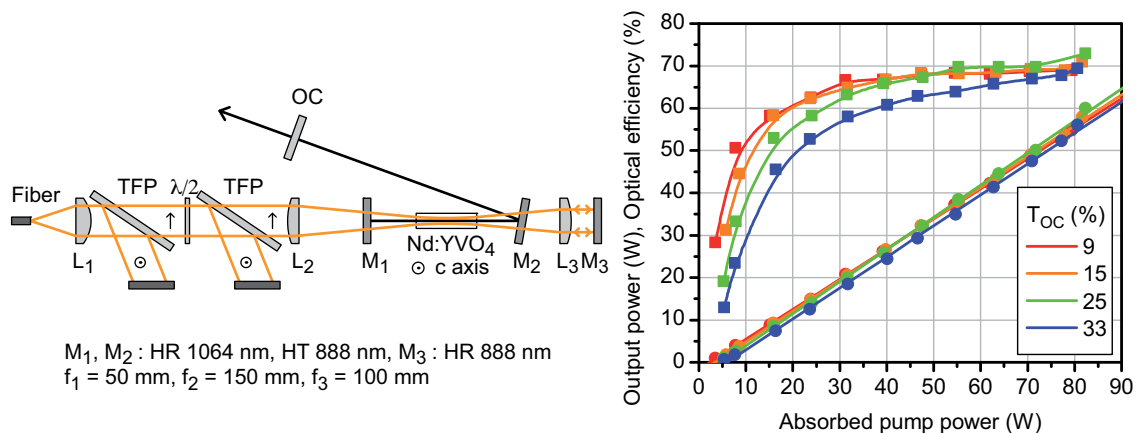


Figure 3.6: Multimode oscillator setup with continuously adjustable polarized pump power (left), its output power (dots), and optical efficiency (squares) with single-pass pump absorption for varying output coupler transmission (right).

M_1 and M_2 , HR at 1064 nm and HT at 888 nm for 0–20° incidence. The 20% transmitted pump light are then collimated by L_3 and retro-reflected by a flat mirror M_3 . The resonator is then formed between M_1 and a flat output coupler OC by tilting M_2 at 10°. Mechanical constraints limit the resonator length to a minimum of 130 mm.

Performance

Figure 3.6 (right) illustrates the output power and optical efficiency as a function of absorbed pump power for single-pass absorption, when M_3 is removed and the non-absorbed pump power measured. A maximum optical efficiency of 70% is achieved at 80 W absorbed pump power for an output coupling of 25%, corresponding to a threshold of 5 W and a slope efficiency of 76%. The limited variation in threshold and optical efficiency for output coupling ranging from 9% to 33% indicates the system’s high gain. An optimization of the output coupling will be performed for the TEM₀₀ oscillator in Sect. 3.2.2, as the laser mode is then subject to a slightly higher gain in the center portion of the pump profile. The perfectly linear evolution of the output power without any rollover indicates an optimum pump–mode overlap left unaffected by the increasing thermal lens.

The oscillator is then operated with pump back reflection and its performance function of total pump power is illustrated in Fig. 3.7 (left). For an identical output coupling of 25%, the optical efficiency is limited to 66% and the slope efficiency to 69% with respect to total pump power. However, if the system’s performance is evaluated as a function of the absorbed pump power which represents $\sim 96\%$ of the incident pump light, the single and double-pass absorption systems are very similar, as illustrated in Fig. 3.7 (right). It indicates that the retro-reflected 20% of the incident pump light contribute almost as efficiently to the output power as the first pass, so that the pump–mode overlap is equivalent on the first and second passes. This behavior is later verified in the TEM₀₀ resonator, where the second pump pass does not degrade beam quality nor does it reduce the optical efficiency with respect to absorbed pump power.

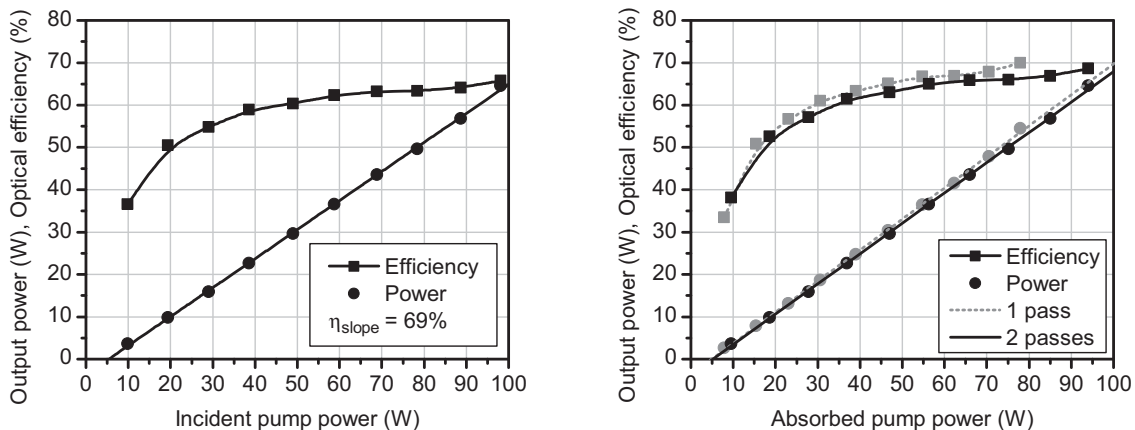


Figure 3.7: Output power and optical efficiency function of incident pump power for double-pass absorption (left), and function of absorbed pump power for single and double-pass absorption (right).

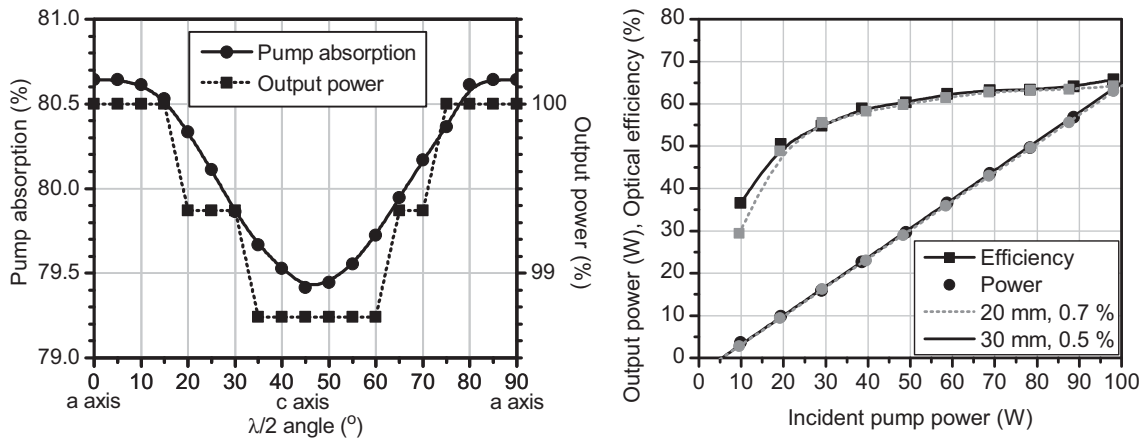


Figure 3.8: Single-pass pump absorption and relative output power for 888 nm polarized pump light rotated from the a to the c axis (left). Oscillator performance for a 20 mm, 0.7 at.% and a 30 mm, 0.5 at.% crystal function of incident pump power in double-pass absorption (right).

As 888 nm is to benefit the stability of lasers under unpolarized or partially polarized pumping, the worst-case scenario of fiber-coupled diode pumping is simulated by rotating the a -polarized pump light up to 90° on the c axis. This is achieved by adding a half-wave plate after the second TFP (see Fig. 3.6 (left)) and monitoring the transmitted pump power after M_2 . In practical systems the light emerging from the fiber is always partially polarized, so that pump absorption and output power variations will be smaller than that measured here. Figure 3.8 (left) illustrates the single-pass pump absorption and the relative output power variations when the polarization of the 888 nm pump light is rotated from the a to the c axis. The stronger absorption of 80.6% on the a axis is reduced to 79.4% only on the c axis. This results in a $\sim 1\%$ variation in output power, the precision of the measurement being limited here by the resolution of the power measurement. Thus regular fiber-coupled sources will provide very stable absorption and output power without the need for depolarization of the pump light.

Finally, the system is pumped in double-pass with unpolarized light by removing the two TFPs and the half-wave plate, and by reducing the diode current and tuning the cooling water temperature to reach 888 nm. It then provides identical performance as for polarized pumping, thus proving the validity of the characterization conducted with polarized light.

Figure 3.8 (right) illustrates the unchanged performance in terms of output power and optical efficiency when the 30 mm, 0.5 at.% doped crystal is replaced by a 20 mm, 0.7 at.% crystal, both offering almost equal absorptions well within the uncertainty on the doping concentration of each crystal. This proves that the concentration quenching effect can effectively be neglected at these doping levels under lasing operation. However, the influence of the stronger absorption and shorter crystal length on thermal lensing will be studied in the next section, as the performance of a longer TEM₀₀ resonator will depend on the strength and aberrations of the thermal lens.

Thermal lensing

Although the multimode resonator presented in the previous section is totally insensitive to thermal lens variations, the performance of a TEM₀₀ oscillator will be highly dependent on the thermal lens and the resulting diameter of the fundamental mode within the crystal. Thus it is important to get an idea of the characteristics of the thermal lens before designing the single transversal mode oscillator.

A complete characterization of the thermally-induced phase distortion can be achieved through interferometric means, by measuring the total single-pass phase distortion in a Mach–Zehnder interferometer [80], or even by isolating the bulging-induced distortion in an interferometric measurement with the reflection on an end facet [61]. Such measurements provide the thermal lens dioptric power, asymmetry, and aberrations, but require a high level of stability for the measurement system and data processing to convert the fringe patterns in useful data. The distortions of a probe laser beam can also be measured after a single pass through the pumped crystal under lasing or non-lasing conditions [80, 53], providing the strength of the thermal lens and the degradation in beam quality or increase of M^2 at higher pump powers. A similar technique is employed here, but without measuring the beam quality degradation, as the power available from the probe beam was too low for the ModeMaster M^2 measurement system. The effect of optical distortions will be verified in the single-pass amplifier experiments described in Sect. 3.3.2.

Figure 3.9 (left) presents the thermal lensing measurement setup based on the short multimode resonator illustrated in Fig. 3.6 (left). As the pumped volume is very long compared to its diameter, the probe beam should be perfectly collinear to the pump beam to avoid adding astigmatism and peripheral aberrations to the measurement. Thus two dichroic mirrors M_1 and M_4 , HR at 633 nm and HT at 888 nm, are inserted on the pump beam path to inject and extract the probe beam. In order to avoid any amplification or absorption effects that would disrupt the thermal lensing measurement, a He–Ne laser emitting a polarized diffraction-limited beam at 633 nm is chosen, so that it will not be significantly absorbed nor amplified in the crystal. Its polarization is orientated vertically to match the crystal’s c axis for measuring only the thermal lens affecting the c -polarized laser mode. The probe beam radius is then adjusted to $\sim 400 \mu\text{m}$ in the crystal to measure the thermal lens dioptric power in the center of the crystal on a radius just below the fundamental mode size of $\sim 500 \mu\text{m}$ when a TEM₀₀ resonator is designed (see Sect. 3.2.2). The transmitted probe beam is then characterized with a Photon Inc. BeamScope scanning slit system and the corresponding thermal lens power calculated on both axes for each pump power. The variation in thermal lensing with and without laser action is simply obtained by blocking the cavity to prevent laser extraction.

The first measurement consisted in comparing the thermal lens on both axes for 2 and 4-side cooled 30 mm long crystals in lasing operation. Figure 3.9 (right) illustrates the purely linear evolution of the thermal lens dioptric power function of the absorbed pump power in single-pass. With 4-side cooling, the thermal lens is perfectly symmetric, showing no astigmatism as was predicted by the FEA simulations in Sect. 2.3.5. The thermal lens increases with a slope of $\sim 0.09 \text{ m}^{-1}/\text{W}$, corresponding to a thermal lensing coefficient of $0.06 \mu\text{m}/\text{W}$ for an effective

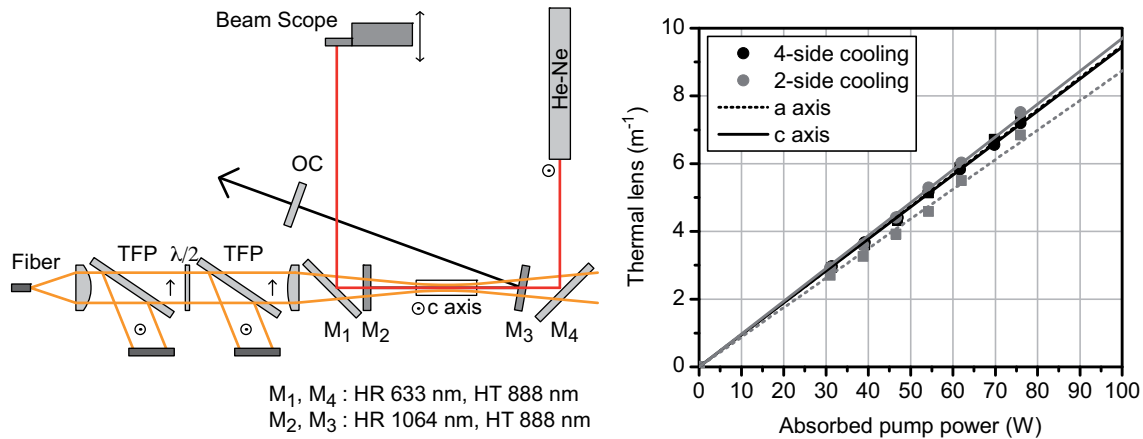


Figure 3.9: Thermal lens measurement setup (left) and thermal lensing along the a and c axes for a 2 and 4-side cooled 30 mm, 0.5 at.% crystal under lasing operation (right).

pump radius of $700 \mu\text{m}$, as predicted by FEA. When the crystal is cooled only on two sides along the vertical c axis, the temperature gradient is greater in this direction than along the a axis, resulting in a $\sim 10\%$ thermal lens asymmetry. As this will degrade the beam quality and efficiency of a dynamically-stable resonator optimized for high pump powers, which would then suffer from a splitting of its stability ranges on the vertical and horizontal axes, a 4-side cooling geometry is adopted for all systems.

Figure 3.10 (left) illustrates the evolution of thermal lens as a function of absorbed pump power for a $4 \times 4 \times 30$ mm, 0.5 at.% doped crystal and single-pass pump absorption. As previously observed, the evolution of dioptric power is perfectly linear in lasing operation, reaching 9 m^{-1} at 100 W of absorbed power. When the cavity is blocked and no extraction occurs, the thermal lens increases non-linearly, as emphasized by the quadratic fit. This evolution results from the higher inversion without laser action and the stronger non-radiative effects it induces, such as ETU. The increase in thermal lensing is limited however to $\sim 20\%$ at 100 W absorbed pump power, compared to a 50% rise of the heat load predicted when simulating the effects of ETU (see Fig. 2.15 (right)). Such difference may result from the simplicity of the ETU model and the uncertainty on the upconversion parameter value. However such measured 20% rise is much lower than the $\sim 100\%$ increase measured in crystals of similar doping level pumped at 808 nm [61, 53]. A low increase in thermal lensing when laser action is completely suppressed will be highly desirable in Q-switched lasers or amplifiers in which the inversion rises above the threshold level. This effect should specifically help reducing the beam quality and divergence variations with repetition rate of Q-switched systems.

Figure 3.10 (right) illustrates the same measurement for a $4 \times 4 \times 20$ mm, 0.7 at.% doped crystal. The shorter absorption and higher doping induce higher inversion densities and stronger end-facet bulging, resulting in a stronger thermal lens of 11 m^{-1} at 100 W absorbed pump power. This stronger value is also a consequence of the smaller effective pump radius, as the pump light is absorbed on 20 mm instead of 30 mm, resulting in smaller pump spots on the crystal's facets.

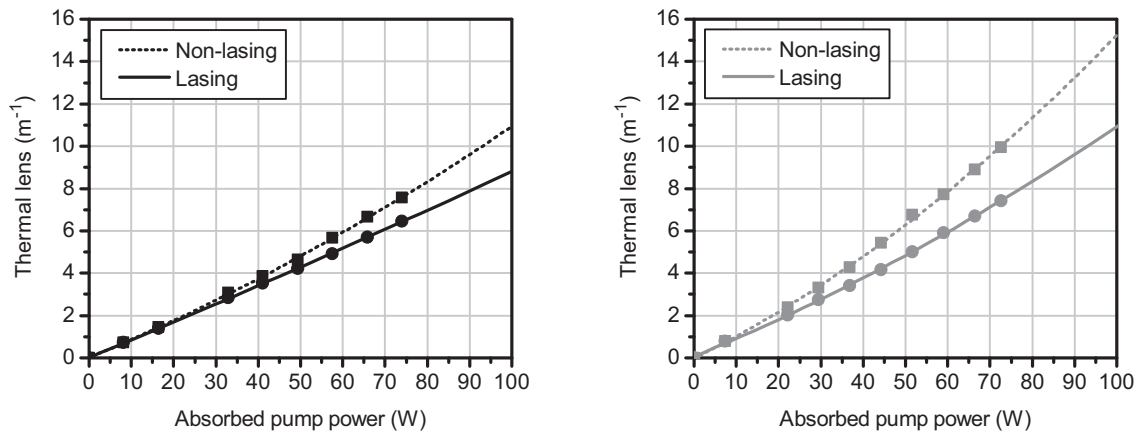


Figure 3.10: Thermal lensing under lasing and non-lasing operation for a 30 mm, 0.5 at.% crystal (left), and a 20 mm, 0.7 at.% crystal (right).

The evolution is also slightly non-linear, as illustrated by the quadratic fit. When no lasing occurs, the evolution of thermal lens is much more non-linear, with a $\sim 40\%$ increase compared to lasing operation at 100 W absorbed pump power, resulting from the stronger inversion and ETU effects. Thus the 30 mm long crystal is chosen for building the following cw, ns, and ps oscillators and amplifiers, which all exhibit variable degrees of laser extraction. The 20 mm crystal would be preferred for lower-power systems designed for smaller pump-mode sizes in which the pump beam divergence would be too large for keeping a good pump-mode matching along the whole length of a 30 mm crystal.

3.2 TEM₀₀ resonators

This section retraces the path followed for the design of a high-power TEM₀₀ oscillator, before presenting the final configuration and its performance. Finally, its output power is scaled by building a periodic resonator containing two crystal-pump modules.

3.2.1 Resonator design

When designing a resonator for fundamental transversal mode operation, several conditions should be met to achieve an efficient and stable operation with a high-quality beam. The mode size in the crystal should optimally match the pump volume to achieve a high extraction efficiency while limiting thermally-induced diffraction and aberrations in the outer portion of the pump spot. Thus mode-to-pump diameter ratios of 70–80% are often found to offer the best compromise and therefore the optimal performance. The resonator should also be designed so that the nominal operation point lies in a region where the mode size in the crystal varies little with small thermal lens changes. This will ensure that the high extraction efficiency and beam quality are maintained if the diode's output power varies, or if the thermal lens is not constant as in a pulsed system of varying repetition rate.

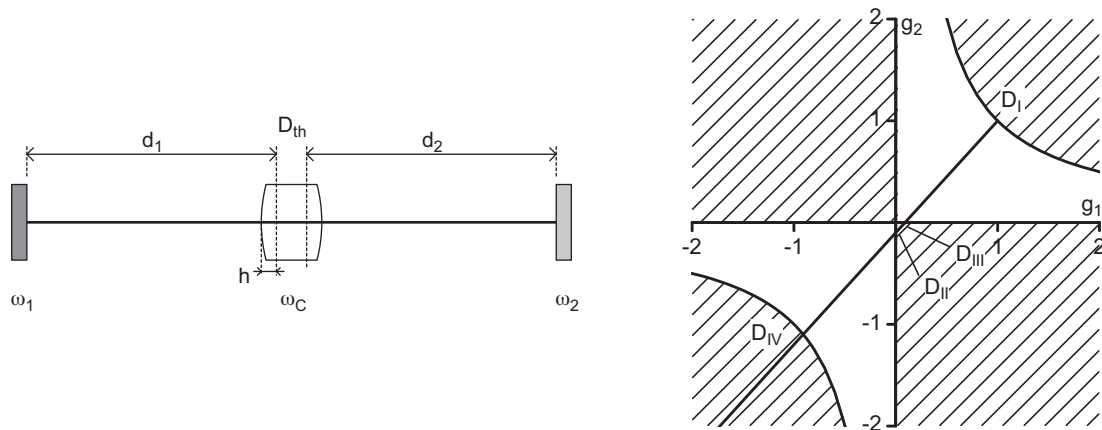


Figure 3.11: Near-symmetric resonator with flat HR and OC mirrors containing a pumped crystal modeled as a thick lens (left). Corresponding g-diagram illustrating the resonator's stability for thermal lens dioptric powers from D_I and D_{III} and from D_{II} and D_{IV} (right).

Figure 3.11 (left) illustrates a 2-mirror linear resonator with flat HR and OC mirrors, containing a crystal which is assimilated to a thick lens of power D , with principal planes at a distance $h = l/(2n_0)$ of its end facets, where l is the crystal length and n_0 its refractive index. The resonator is then equivalent to one containing a thin lens of power D at distances d_1 and d_2 from the end mirrors, as illustrated in the scheme. In order to study the resonator's stability and the evolution of mode sizes with thermal lensing, the concept of equivalent g-parameters is applied [73]. Thus the resonator containing a thermal lens is equivalent to an empty resonator with the following parameters, in the case of flat end-mirrors:

$$g_i^* = 1 - Dd_j \quad i, j = 1, 2; i \neq j \quad (3.1a)$$

$$L^* = d_1 + d_2 - Dd_1d_2 \quad (3.1b)$$

where g_1^* and g_2^* are the equivalent g-parameters and L^* the length of the equivalent empty resonator. The resonator is then stable if $0 < g_1^*g_2^* < 1$, as illustrated in Fig. 3.11 (right) for a resonator which is almost symmetric with $d_2 < d_1$. When no thermal lens exists, the resonator consists of two plane mirrors and lies on the edge of the stability limit in D_I where $g_1^* = g_2^* = 1$. Then as the pump power is increased and the thermal lens builds up, the resonator becomes unstable between D_{III} and D_{II} , as the near-symmetric equivalent resonator misses the confocal configuration. The resonator then enters the second stability zone until it comes close to a concentric configuration and becomes unstable for $D > D_{IV}$. The stability limits are given by:

$$g_1^* g_2^* = 1 \text{ and } g_1^* > 0 \quad D_I = 0 \quad (3.2a)$$

$$g_1^* = 0 \quad D_{II} = \frac{1}{d_2} \quad (3.2b)$$

$$g_2^* = 0 \quad D_{III} = \frac{1}{d_1} \quad (3.2c)$$

$$g_1^* g_2^* = 1 \text{ and } g_1^* < 0 \quad D_{IV} = \frac{1}{d_1} + \frac{1}{d_2} \quad (3.2d)$$

$$(3.2e)$$

Even when a symmetric resonator is designed with $d_1 = d_2$, the slightly stronger thermal lens on the crystal's pump input face will not allow the resonator to be stable near the confocal point, thus $D_{II} \neq D_{III}$. Figure 3.12 (left) illustrates the mode size on the thermal lens principal planes ω_L and on the end-mirrors ω_1 and ω_2 . The resonator is almost symmetric with $d_1 = 300$ mm and $d_2 = 290$ mm, so that the mode sizes away from the stability edges are close to that of a perfectly symmetric resonator, as illustrated in Fig. 3.12 (right) for $d = d_1 = d_2 = 300$ mm. As the resonators will always be operated away from the stability edges where the mode sizes quickly diverge with small thermal lens variations, only the simplified expression for the mode radii in the crystal and on the end-mirrors ω_M of a perfectly symmetric resonator need to be considered:

$$\omega_M^2 = \frac{\lambda}{\pi} \sqrt{\frac{L^*}{D}} \quad (3.3a)$$

$$\omega_L^2 = \omega_M^2 \left(1 + \frac{d^2 D}{L^*} \right) \quad (3.3b)$$

The minimum mode size in the crystal is reached for $D = 1/d$ where $\omega_L = \sqrt{2} \omega_M$. Thus $\omega_{L,min}$ is given by:

$$\omega_{L,min} = \sqrt{\frac{\lambda L}{\pi}} \quad (3.4)$$

with $L = 2d$ the cavity length. As the pump spot and laser mode radii are increased, the thermal lens D given by Equ. 2.54 decreases, but conversely the stability range $\Delta D = 4/L$ narrows. It is thus shown that the stability range in terms of pump power ΔP_p is constant for a given thermal lensing coefficient α when the resonator length and pump spot sizes are varied:

$$\Delta P_p = \frac{4\lambda}{\alpha} \left(\frac{\omega_p}{\omega_L} \right)^2 \quad (3.5)$$

Thus increasing the pump spot size only provides lower inversion densities leading to slightly lower thermal lensing and aberrations, but does not allow power scaling. As illustrated in Fig. 3.12 (left), it is possible to achieve the same mode radius in the crystal in the two stability zones, so it seems desirable to operate the resonator in the highest pump power zone to reach high output powers. Furthermore it has been shown that the misalignment sensitivity in zone II is

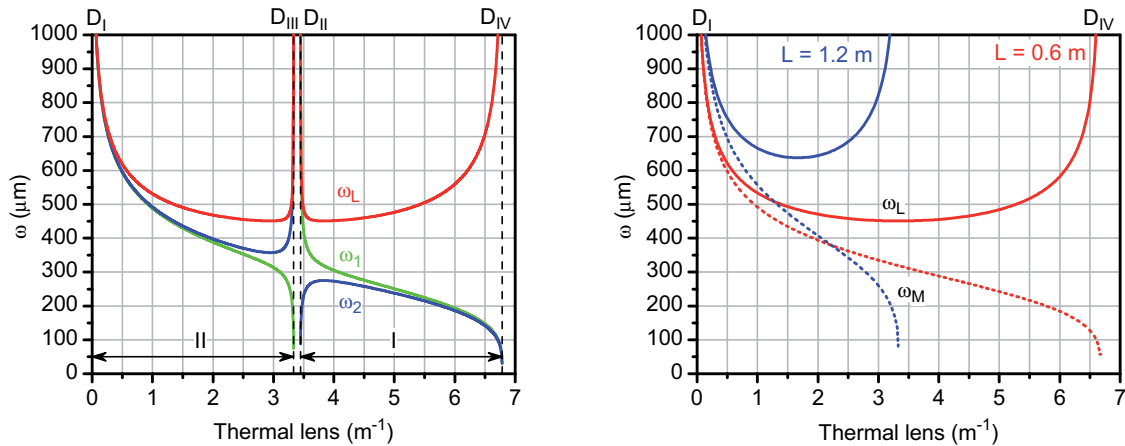


Figure 3.12: TEM₀₀ mode radius in the laser crystal ω_L and on the end mirrors ω_1 and ω_2 for the resonator illustrated in Fig. 3.11. A near-symmetric configuration is unstable near the confocal point (left). The dependence of mode size and stability range on cavity length is illustrated for two 0.6 and 1.2 m long symmetric resonators (right).

greater than in zone I [81], yet the stronger thermal lens aberrations and higher temperatures in zone I also require a reduction of the pump–mode overlap, thus limiting the system’s efficiency. Therefore a TEM₀₀ resonator will be designed to operate in zone II for stable and efficient operation.

One technique for scaling the power of such resonator is to compensate for some of the thermal lens, thus shifting the stability zones to higher pump powers. This can be achieved by the addition of divergent lenses or concave mirrors close to the crystal to provide a static compensation, with an adjustable telescope [82], or a variable-radius mirror [83] which allow for a dynamic compensation on a large range of pump power. Here a static compensation method will be applied as the system is to be operated at a fixed operation point. The near-symmetric resonator described above would most likely be best operated in a thermal lens range of 2–3 m⁻¹ in zone II where the variations of mode radii in the crystal and on the end-mirrors, and also of output beam divergence are minimal. By adding two divergent lenses of –500 mm focal length or two concave mirrors of +1000 mm radius of curvature close and symmetrically to the laser crystal, the resonator’s configuration and mode radii remain also unchanged if Fig. 3.12 (left) is shifted by the static thermal lens compensation of 4 m⁻¹. Thus D_I and D_{III} will shift to 4 m⁻¹ and 7.3 m⁻¹, respectively. The resonator will then be operated in the 6–7 m⁻¹ range for optimum performance, the resonator reaching geometrical stability at a much higher power than the laser threshold defined as gain larger than losses. Such technique can only be applied with a reasonably low amount of thermal lens compensation, as the resonator becomes more and more sensitive to misalignment with strongly divergent optics, and as the aberrations are not compensated by simple spherical optics.

3.2.2 TEM₀₀ dynamically-stable resonator

Resonator setup

Adopting the dynamically-stable resonator concept, several TEM₀₀ were designed. Only the final highest-power and most simple resonator is presented here, as it served as a building block for all pulsed oscillators presented in the next chapters. Figure 3.13 illustrates the oscillator setup and the corresponding mode profile along the optical axis. A $4 \times 4 \times 30$ mm 0.5 at.% Nd:YVO₄ crystal is pumped by a 400 μm , 0.22 NA Limo fiber-coupled diode imaged to a 1350 μm diameter spot with a 30 mm collimating lens and a 100 mm focusing lens. The transmitted pump light is collimated and retro-reflected, as described for the multimode oscillator. The resonator is formed between a flat HR mirror and a flat output coupler OC, and folded by two dichroic pump mirrors M_1 and M_2 , HR at 1064 nm and HT at 888 nm. The initial experiments were conducted with divergent lenses inserted close to flat pump mirrors to provide easily adjustable thermal lens compensation. Thus for two -500 mm lenses inserted close to flat mirrors M_1 and M_2 , or a thermal lens compensation of 4 m^{-1} , the arm lengths between HR and M_1 and between OC and M_2 were adjusted symmetrically to find the optimum compromise between beam-quality and efficiency. The divergent lenses could then be suppressed and the pump mirrors replaced by $+1000$ mm radius concave mirrors of equal power.

Figure 3.13 (right) illustrates the mode profile once the arm length has been adjusted to 300 mm and at a nominal pump power of 108 W, determined from the measurement of output beam quality and of the waist size directly behind the HR mirror. The waist radius on the HR and OC mirrors is measured at $\omega_M = 365 \mu\text{m}$, while the mode radius in the crystal is calculated to be $\omega_L = 510 \mu\text{m}$ for a thermal lens of $\sim 6.2 \text{ m}^{-1}$. The thermal lens power calculated here directly in a TEM₀₀ resonator being lower than with the direct measurement in Sect. 3.1.3 can be explained by the weaker input-facet bulging with double-pass pump absorption as opposed to single-pass pump absorption, for an equal absorbed pump power. The mode-to-pump diameter ratio is then calculated to be 76%, within the classic range for optimum mode-matching.

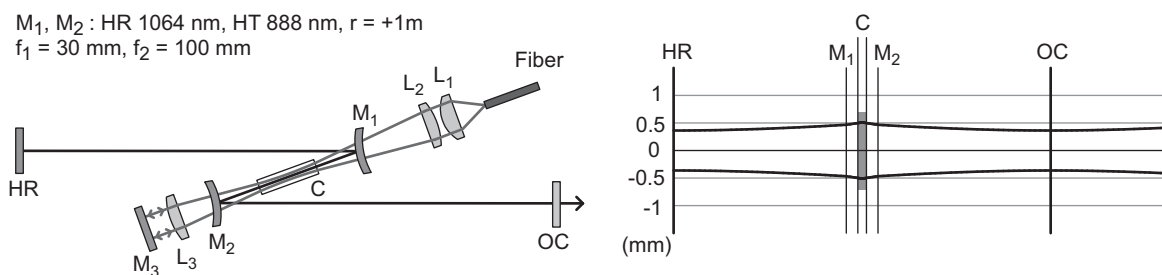


Figure 3.13: Symmetric oscillator setup (left) and corresponding TEM₀₀ mode profile in the resonator (right).

Resonator optimization

Figure 3.14 (left) illustrates the joint evolution of power, optical efficiency, and beam quality when the pump power is increased beyond the optimum operation point of 108 W for an output coupler transmission of 40%. As the resonator is unstable at low pump power due to the static thermal lens compensation of -4 m^{-1} , lasing occurs much higher than the true laser threshold, which explains why an artificial slope efficiency of 200% is observed between 95 and 100 W pump power. As the pump power increases, the beam quality and efficiency improve until the mode size in the crystal is optimally matched to the pump volume, which is achieved at 108 W of pump power, providing 60 W of output power with an overall optical efficiency of 55%. The beam quality is measured with a Coherent ModeMaster scanning knife-edge system at $M^2 < 1.05$, as illustrated in Fig. 3.15. The beam is free of astigmatism and perfectly round with a waist ellipticity > 0.98 . This can be attributed to the 4-side cooling technique and the low 10° angle incidence on the pump mirrors which eliminate any significant source of asymmetry in the resonator. As the pump power is further increased, the mode size in the crystal rises again, resulting in stronger thermally-induced diffraction and aberrations which lead to lower efficiency and deteriorated beam quality.

Optimum output coupling

In order to optimize the output coupling, the fixed OC was replaced by a variable output coupler constituted of a thin-film polarizer, a quarter-wave plate, and an HR mirror, as described in Sect. 4.1.4. Rotating the wave plate allows for a continuous adjustment of the output coupler transmission from 0% when the wave-plate axis is aligned to the laser's vertical polarization, to 100% when it is rotated by 45° . It is observed that the gain should be relatively high as lasing occurs even when almost 100% of the intracavity light is coupled out, as shown in Fig.

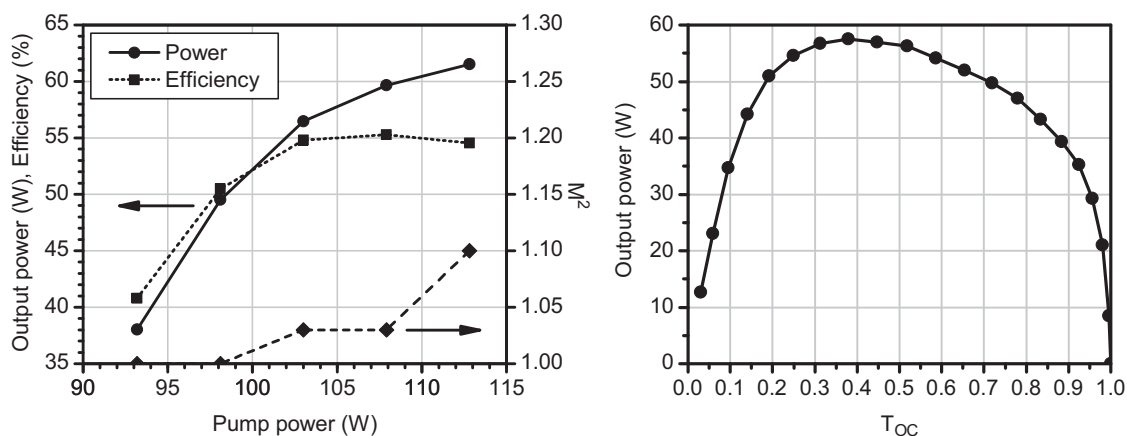


Figure 3.14: Output power, optical efficiency, and beam quality function of pump power around the optimum operation point of 108 W for 40% output coupling (left). Output power function of output coupling for 108 W pump power (right).

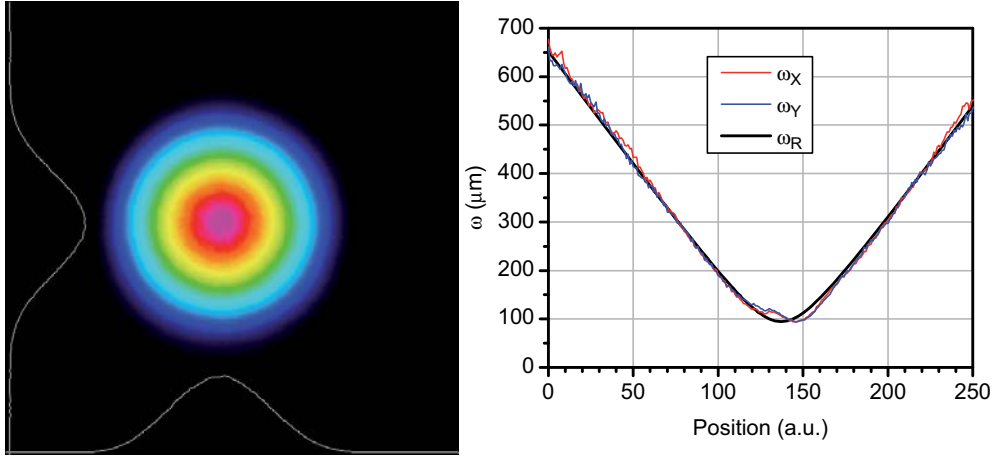


Figure 3.15: TEM₀₀ output beam imaged with a CMOS camera (left), and ModeMaster beam radius measurement in the horizontal and vertical planes, along with the data fit ω_R giving $M^2 = 1.05$ (right).

3.14 (right). The precision of the OC value at such extreme position is limited by the residual reflectivity of the TFP on the p polarization. However, within a normal output coupling range, an almost flat output power curve is observed between 30% and 50% transmission, so that the 40% static output coupler corresponding to the results illustrated in Fig. 3.14 (left) represents the optimum transmission.

In situ small-signal gain measurement

In order to determine the effective small-signal gain seen by the laser mode, many parameters need to be taken into account, such as the space-dependent pump beam profile and non-radiative effects along the crystal. However, as these are difficult to accurately model, a simple calculation for a 700 μm radius collimated pump beam and 108 W of pump power has been presented in Sect. 2.3.3, resulting in a single-pass small-signal gain $g_0l = 3.6$. Nevertheless it has been shown that the beam profile departs from a flat top with higher intensity in the central portion of the beam, especially away from the focus, as illustrated in Fig. 3.5. Thus, the small-signal gain is further investigated by measuring the frequency of the relaxation oscillations [84]. It is shown that the single-pass small signal gain effectively seen by the laser mode is given by:

$$g_0l = \frac{1}{2} \left[(2\pi f_{ro})^2 T \tau + \delta_c \right] \quad (3.6)$$

where f_{ro} is the frequency of the relaxation-oscillation peak, T the cavity roundtrip time, τ the upper-state lifetime, and δ_c the total logarithmic roundtrip losses. The passive losses can be neglected compared to the high output coupling, so that $\delta_c \approx -\ln(1 - T_{oc})$. The roundtrip time is determined by measuring the residual modulation of the RF spectrum at the roundtrip frequency with a photodiode coupled to an electronic spectrum analyzer, leading to $F = 214$ MHz or $T = 4.7$ ns. The relaxation-oscillation frequency is determined from the low frequency RF spectrum measured with a low-noise photodiode, as illustrated in Fig. 3.16, leading to

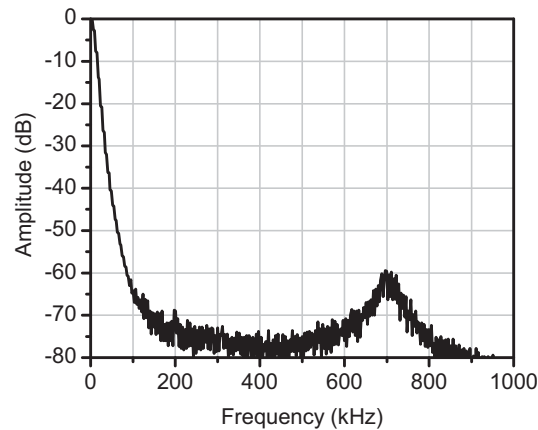


Figure 3.16: Low-frequency RF spectrum illustrating the relaxation-oscillation peak at 700 kHz.

$f_{ro} = 700$ kHz. Thus the single-pass small-signal gain is calculated to be $g_0l = 4.7$. The discrepancy between this measurement and the model ($g_0l = 3.6$) is easily explained by the slightly smaller pump spot and non-flat pump profile in the experiment.

3.2.3 Periodic resonator

When further power scaling is desired, a stronger thermal lensing compensation could be applied to shift the resonator’s stability range to even higher pump powers. However it has been observed that for the same pump–crystal configuration, applying a -6 m^{-1} compensation required to further reduce the cavity length to limit the mode size in the crystal, thus minimizing the effects of the stronger thermally-induced diffraction and aberrations, yet at the cost of a drop in optical efficiency $< 50\%$. Thus static compensation of the thermal lens with spherical optics reaches its limits when aberrations become significant, and further power scaling cannot be achieved by this technique without sacrificing on optical efficiency, beam quality, and stability. Furthermore, small relative pump power variations induce larger thermal lens variations relatively to the resonator’s stability range width, so that they will more likely cause mode-size, output-power, and beam-quality variations.

A possibility for scaling output power is to realize a periodic resonator from the initial optimized oscillator. Figure 3.17 (top) illustrates how the initial resonator is duplicated symmetrically to the original output coupler, which is then moved to the position of the second resonator’s HR mirror. As the original resonator mode possesses waists on its flat end mirrors, the periodic resonator also exhibits waists on its flat end mirrors, and in the middle of the resonator, in the former position of the original output coupler, as illustrated in Fig. 3.17 (bottom). Thus when each crystal is pumped in an identical configuration, and if the extraction is assumed equivalent in both crystals, the thermal lenses are also identical and the resonator mode symmetric.

The cavity now containing two identical gain media, the small-signal gain is measured at $g_0l = 9.5$ for $f_{ro} = 700$ kHz and $F = 106$ MHz, which indicates that the optimal pump–mode

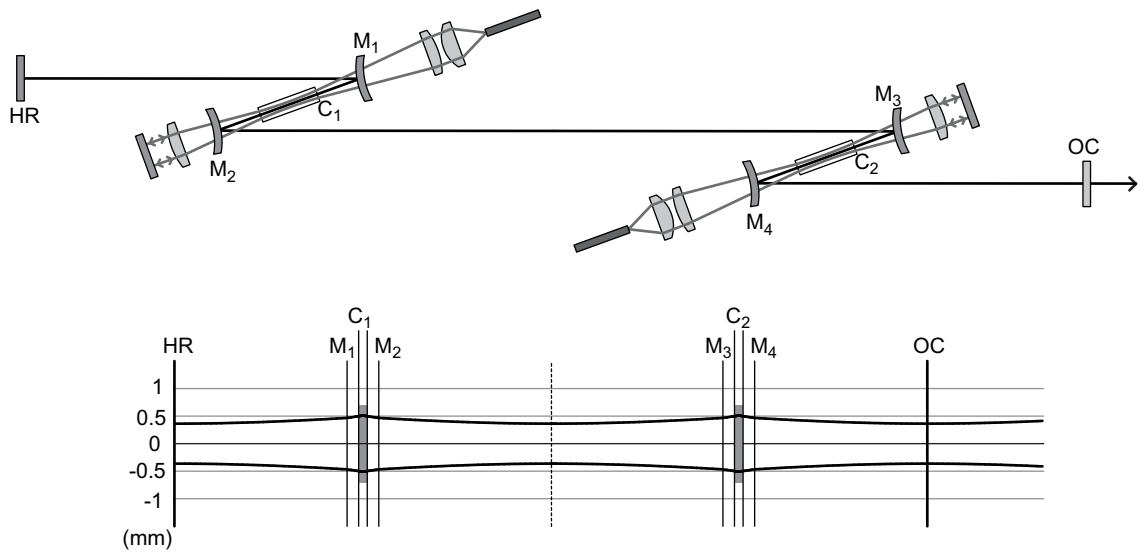


Figure 3.17: TEM₀₀ periodic resonator setup (top) and corresponding mode profile (bottom).

matching is maintained in both crystals. The doubled gain therefore results in a higher optimum output coupling of $\sim 65\%$, as illustrated in Fig. 3.18 (left). The maximum output power of 119 W is sensibly twice that of the single-crystal resonator, confirming the optimum saturated extraction in each crystal. The output beam is diffraction limited with $M^2 < 1.1$ and free of significant astigmatism and asymmetry, as illustrated in Fig. 3.18 (right).

Although this periodic configuration provides an effective means of power scaling while retaining high optical efficiency and beam quality, the resonator's alignment is slightly more critical as is required to ensure that the laser mode is perfectly collinear to each pump volume. If possible, the second pump-crystal assembly will be used in an amplifier configuration, as

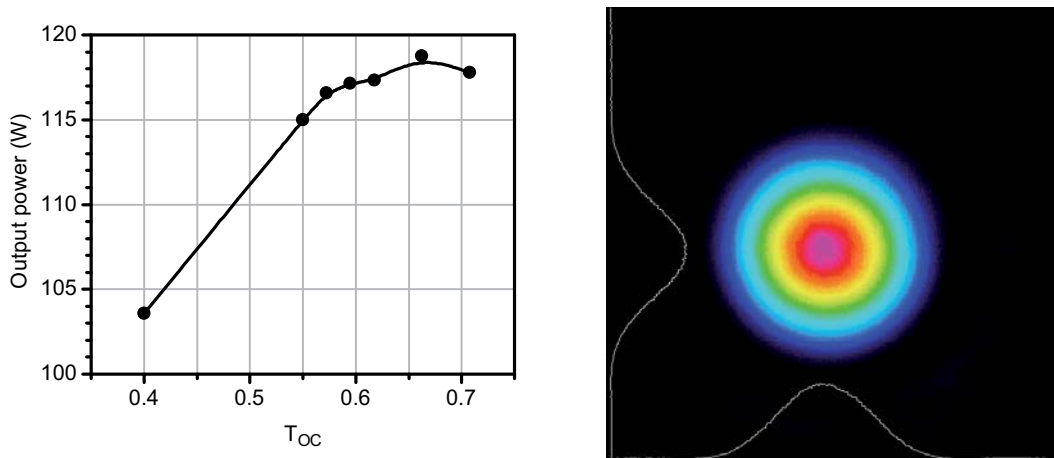


Figure 3.18: Output power function of output coupling (left) and beam image at 119 W output power (right).

presented in the following section, if the oscillator's output power is sufficient to saturate the extraction in the amplifier stage. However, when the oscillator contains non-linear elements such as a frequency-doubling crystal, external amplification is not possible, so that a periodic resonator approach will be adopted, as presented in Sect. 3.4.3.

3.3 Single-pass amplifier

Designing a high-power laser oscillator with the desired efficiency, beam quality, temporal, noise, and spectral characteristics is very challenging. Thus a master-oscillator power-amplifier (MOPA) approach is often preferred, where a low or medium-power oscillator possessing the requested characteristics is amplified in a single or multiple stages to reach the desired power level. Usually, the lower power the oscillator, the easier it is to design with the required characteristics, but the harder it is to amplify efficiently without distorting its beam, spectrum, or pulses.

Double-clad fiber amplifiers offer the highest gain and lowest saturation power, so that only very low input power is needed for an efficient extraction of the energy stored in the amplifier. However, their strong non-linear effects resulting from the small mode size and the long interaction length prohibit their use for producing high power ns or ps pulses without pulse broadening or spectral distortion, and ultimately fiber facet destruction.

As for oscillators, crystal-based amplifiers are limited by thermal effects, so the pump volume needs to be increased. This can be achieved in a slab geometry, but the large asymmetric aperture requires the seed beam to pass multiple times through the medium to cover its entire volume [14], reaching the saturation intensity in the regions of pump–mode overlap, yet at the cost of a deterioration of beam quality resulting from the multiple passes through the strongly asymmetric thermal lens.

End-pumped systems offer the advantage of a small aperture so that the seed beam intensity can be kept relatively high, yet when input power is too low, the seed beam needs to pass multiple times through the gain medium to saturate the extraction. This can be achieved by geometrically separating the multiple passes in one plane or in three dimensions for a larger number of passes [85], but all these techniques lead to beam-quality degradation. The number of geometrical passes can then be doubled by inserting an optical isolator on the path of the input beam, which then extracts the reflected amplified beam, yet at the cost of additional losses, thermal lensing at high power, and additional cost. For a larger gain factor, a multiple-stage approach is necessary, with the first amplifier operating in the small-signal amplification regime with a large gain factor and low extraction efficiency, and the following stages operating in the power extraction regime with a small gain factor but with high extraction efficiency [86].

Thus it is desirable to design a single-pass amplifier that will have minimal effects on the input beam characteristics, coupled to a sufficiently high-power oscillator for efficient extraction. The pump–crystal combination previously used as an oscillator will now be configured for single-pass amplification, and benefit from the high power available from the seed oscillator to operate in the power extraction regime.

3.3.1 Principle

In order to determine the required input power for an efficient extraction in the amplifier, or the gain factor and extraction efficiency for a given input power, a simple model of a single-pass amplifier based on the same pump–crystal configuration as in the oscillator described in Sect. 3.2.2 is presented. The pump and signal mode sizes are left unchanged to achieve the same optimum matching for minimal beam distortion and optimum extraction efficiency. Thus the measured values of the small-signal gain $g_0l = 4.7$ and the mode radius $\omega_l = 510 \mu\text{m}$ are considered for an accurate prediction of the amplifier's behavior. Although the modeling is conducted for a cw input beam, the results are also valid for pulsed lasers such as mode-locked or high repetition-rate Q-switched oscillators, when the time between pulses is significantly shorter than the fluorescence lifetime. Thus the calculations could also be conducted for pulsed systems [87], yet the average output power, gain factor, and extraction efficiency tend to a steady state corresponding to the cw regime.

If we consider a uniform pump rate along the crystal length, the evolution of the laser intensity I in a slice of thickness dz is given by:

$$dI = gI dz \quad (3.7)$$

where

$$g = \frac{g_0}{1 + \frac{I}{I_s}} \quad (3.8)$$

is the saturated gain per unit length. Thus the output intensity I_{out} is calculated as a function of the input intensity I_{in} by integrating Equ. 3.7 on the crystal length l :

$$I_{out} = I_{in} + g_0 I_s \int_0^l \frac{1}{1 + \frac{I(z)}{I_s}} dz \quad (3.9)$$

Figure 3.19 (left) illustrates the term to be integrated as a function of I/I_s , which corresponds to the stimulated emission extraction efficiency η_l studied in Sect. 2.1.3. For $I \gg I_s$, with $I_s = 1560 \text{ W/cm}^2$, the extracted intensity I_{extr} tends to a maximum value of $I_{extr,max} = g_0 l I_s$. Considering the expressions of $g_0 l$ given by Equ. 2.39 and of I_s by Equ. 2.15, the maximum extracted power is:

$$P_{extr,max} = \frac{\lambda_p}{\lambda_l} \left(\frac{\omega_l}{\omega_p} \right)^2 P_{abs} \quad (3.10)$$

when each pump photon within the pump–mode overlap contributes to the amplification.

Figure 3.19 (right) illustrates the evolution of the laser power along the crystal length for different input powers. For 60 W input power, $I_{in} = 7.3 \text{ kW/cm}^2 \approx 4.7 I_s$, so a high extraction efficiency is achieved right from the beginning of the crystal with $\eta_l = 85\%$, and reaches $\eta_l = 90\%$ after almost doubling in power. As the extraction is saturated and almost constant, the power increases linearly along the crystal length, so that making the assumption of a uniform pump

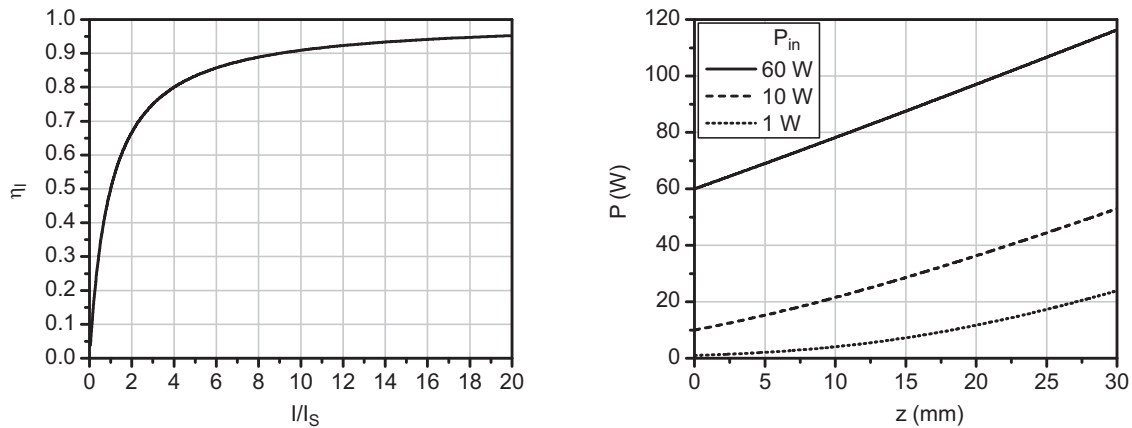


Figure 3.19: Stimulated-emission efficiency η_l function of the local relative intensity I/I_s (left). Evolution of the beam power during its propagation through the uniformly-pumped crystal for different input power levels (right).

volume instead of a stronger pump rate on the input face has no influence on the total extraction. For an input power of 1 W, $I_{in} = 122 \text{ W/cm}^2 \approx 0.08I_s$, so extraction is very low while the gain g is close to its small-signal maximum value g_0 . As the beam is amplified, the extraction increases so that the slope of power steadily rises.

Figure 3.20 (left) illustrates the evolution of output power and extracted power for increasing input powers up to 60 W. At full input power, 56 W are extracted in a single pass through the crystal with an efficiency $\eta_{extr} = 52\%$, coming very close to the 60 W extracted in an oscillator, resulting in an output power of 116 W. Figure 3.20 (right) shows the corresponding extraction efficiency and gain factor $G = P_{out}/P_{in}$ and their inverse evolution. Thus two extreme operating regimes delimited by $I_{in} \approx I_s$ or $P_{in} \approx 13\text{W}$ can be defined. When a high gain factor is desired

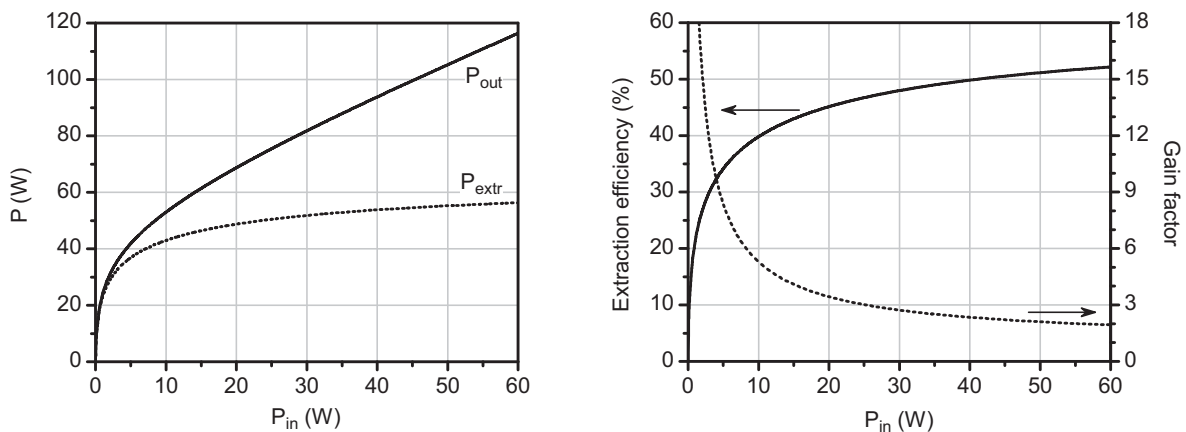


Figure 3.20: Simulated MOPA output power and extracted power in the amplifier stage function of seed power (left). Extraction efficiency and gain factor of the amplifier function of seed power (right).

for amplifying a low-power oscillator, the extraction efficiency will be limited and the amplifier is operating in the small-signal amplification regime, as for $I_{in} < I_s$. When a high-power input is available, the extraction efficiency saturates towards what would be available from an oscillator, but the gain factor is limited. As a 60 W high-power oscillator has been designed, it will be used as a source for the single-pass amplifier presented in the following section. The high input power allows the amplifier to operate in the power extraction or saturation regime, without the need for more complex multiple geometrical or polarization passes which would be detrimental to the output beam quality.

3.3.2 Single-pass CW amplifier

In order to benefit from the optimized pump-crystal configuration used in the oscillator, the single-pass amplifier is built with exactly the same components to achieve an identical pump volume. Figure 3.21 illustrates the MOPA configuration, with the amplifier crystal C_2 along with its pump mirrors and pump diode arranged symmetrically to the oscillator's crystal with respect to the output coupler OC . As a waist is located on the flat output coupler, if the pump-mode matching has been optimized in the oscillator crystal, it will be optimal in the amplifier crystal by design. Thus the mode propagation is identical to that of the periodic resonator presented in Fig. 3.17 (bottom). Such straightforward design brings the advantage of not requiring any redesign and optimization of the amplifier and does not require any telescope to adapt the mode size and divergence in the amplifier crystal. A variable attenuator constituted of a half-wave plate and two thin-film polarizers was inserted on the oscillator's output beam path to allow for a continuous variation of the amplifier's input power without altering the oscillator's output beam characteristics or the amplifier pump-mode matching.

Figure 3.22 illustrates the amplifier's experimental performance as for the simulation presented in Fig. 3.20. For 108 W pump power applied to each of the oscillator and amplifier crystals, the 60 W oscillator output is amplified to 117 W, achieving 57 W of extracted power and 53% optical efficiency in the amplifier stage, for a total MOPA optical efficiency of 54%. As predicted by the simulations, the extraction strongly saturates above 30 W input power, so that the amplifier operates in the saturation regime at 60 W input power. As the extraction efficiency of 53% comes very close to the 55% in the oscillator, the oscillator power is almost doubled with

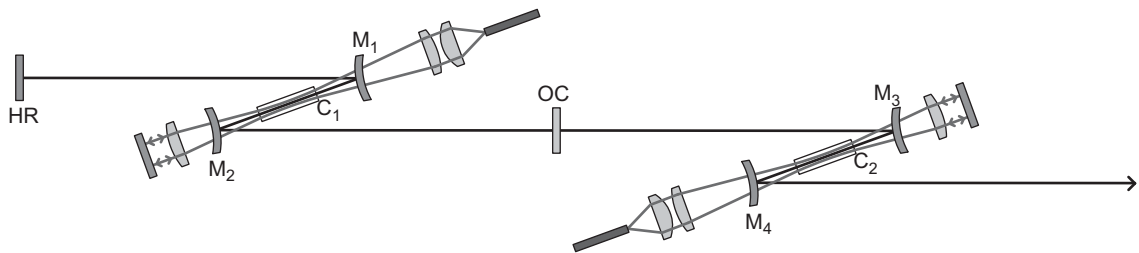


Figure 3.21: Oscillator–amplifier setup with identical pump–crystal configurations for the oscillator and the single-pass amplifier.

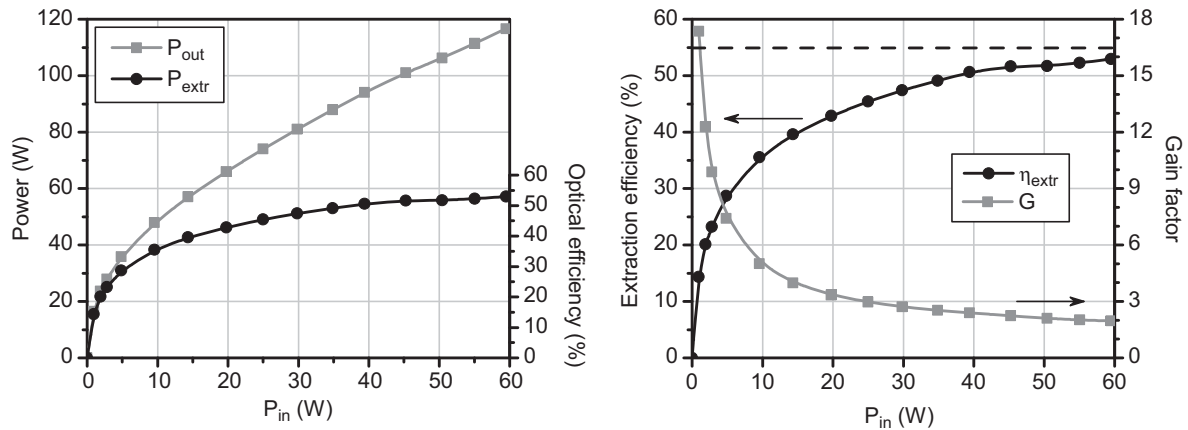


Figure 3.22: MOPA output power and extracted power in the amplifier stage function of seed power (left). Extraction efficiency and gain factor of the amplifier function of seed power (right).

$G \approx 2$. At 10 W input power, the extracted power still amounts to 40 W for $\eta_{extr} = 37\%$ and $G = 5$. Such optical efficiency is still very reasonable for a single-pass amplifier, yet a stronger gain factor is available. The amplifier was also tested in a copropagative situation where the pump and the laser beam propagate in the same direction within the crystal, producing identical results as the contra-propagative situation illustrated in Fig. 3.21. This indicates that the gain distribution along the crystal length has no influence on extraction, as the input beam is of sufficiently high intensity to reach saturation on the whole length of the crystal.

Figure 3.23 (left) illustrates the evolution of extracted power as a function of amplifier pump power for a constant input power of 60 W. The almost linear evolution indicates that the amplifier operates in the saturation regime on the whole length of the crystal even at low pump powers when the laser power does not significantly increase along the length of the crystal. The crossing of the curve with the horizontal axis at $P_p = 4$ W results from the additional passive losses induced by the single pass through the amplifier in the absence of amplification. The beam quality at full pump and input powers is maintained close to the diffraction limit with $M^2 < 1.1$ and the beam profile remains undistorted, as illustrated in Fig. 3.23 (right). At low input powers < 5 W, a slight beam distortion resulting from the stronger and more aberrated thermal lens is visible.

In summary, the pump-crystal configuration optimized for the oscillator has been used in a single-pass amplifier configuration, providing a simple and efficient amplifier operating in the saturation regime thanks to the high power available from the oscillator. This setup will provide the same high extraction efficiency with high repetition-rate Q-switched and mode-locked oscillators, as presented in Sect. 5.2.3.

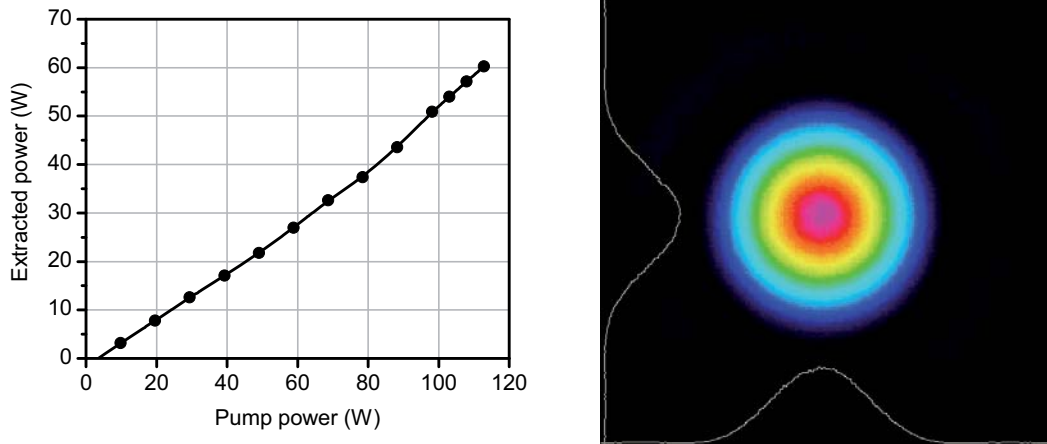


Figure 3.23: Amplifier extracted power function of pump power for a constant seed power of 60 W (left). MOPA output beam at 117 W output power with $M^2 < 1.1$ (right).

3.4 Intracavity-doubled resonator

As the vast majority of efficient solid-state laser materials emit in the near-infrared region around $1 \mu\text{m}$, the generation of high optical power in the visible spectrum is not possible directly from a solid-state material. Thus older and bulkier technologies have long remained unchallenged, often with severe drawbacks such as a low electrical-to-optical efficiency, limited lifetime, and high servicing costs. This applies to argon-ion gas lasers that remained the most powerful sources of cw visible and blue-green light until the mid 1990's. Although the output powers up to 30 W cw in a diffraction-limited beam available from such large-frame argon lasers are sufficient for many applications, their high power consumption of several ten kW and the resulting very low electrical-to-optical efficiency $< 0.1\%$ demand a high water-flow cooling, both leading to significant operational costs. Furthermore the bulkiness of the $\sim 2 \text{ m}$ long tube and of the power supply, and the tube lifetime limited to ~ 5000 hours have been holding back their implementation for certain applications.

The way around the limited availability of solid-state material emission wavelengths is to frequency convert the fundamental laser wavelength in the near IR to its second harmonic in the visible spectrum or its third and higher harmonics in the UV. The resulting doubled wavelength thus often lies in the blue-green region for active ions such as Nd and Yb, in a variety of hosts and through three and four-level laser transitions. As the efficiency of the nonlinear effects involved in harmonic generation increases with fundamental power, high conversion efficiencies are reached with ns or ps pulses exhibiting high peak powers, yet cw beams are much more difficult to convert efficiently in most non-linear materials. For this purpose, intracavity second-harmonic generation (ICSHG) is implemented, where a nonlinear crystal is inserted within a laser resonator oscillating between HR mirrors, providing a nonlinear output coupling for the fundamental mode. Only a small fraction of the high intracavity IR power needs to be converted, although the second-harmonic output will represent a large fraction of the IR output power that

would be available from a conventional oscillator otherwise. This technique was implemented in Nd:YVO₄ systems for the efficient generation of 532 nm cw light, with output powers of up to 5 W in the mid 1990's [88, 89] to ~ 20 W today [90].

This section first introduces the basics of nonlinear optical harmonic generation and the key characteristics for selecting a nonlinear material for the efficient conversion of high-power beams. The specifics of intracavity doubling and the so called "green problem" are then presented to understand the behavior of the high-power intracavity-doubled resonators that were demonstrated with 888 nm pumped Nd:YVO₄.

3.4.1 Second harmonic generation

The process of second harmonic generation relies on the nonlinear properties of materials in which the refractive index is not constant but dependent on the intensity of the electric field. Thus an incident electromagnetic field E generates an electric polarization P that can approximated by a power series:

$$P = P^{(1)} + P^{(2)} + P^{(3)} + \dots = \varepsilon_0 \left(\chi^{(1)} E + \chi^{(2)} E^2 + \chi^{(3)} E^3 + \dots \right) \quad (3.11)$$

where ε_0 is the permittivity of vacuum and $\chi^{(m)}$ is the m-th order susceptibility of the medium. If two monochromatic fields E_1 and E_2 propagating in the z direction are incident on the nonlinear material, with:

$$E = E_1 + E_2 = E_{10} \sin(k_1 z - \omega_1 t) + E_{20} \sin(k_2 z - \omega_2 t) \quad (3.12)$$

the second order susceptibility $\chi^{(2)}$ generates, besides a constant offset leading to optical rectification, oscillating components of the dielectric polarization $P^{(2)}$ at frequencies ω_1 , ω_2 , $2\omega_1$, $2\omega_2$, $\omega_1 + \omega_2$, and $\omega_1 - \omega_2$. Thus these nonlinear effects will be responsible for second harmonic generation (SHG) at 532 nm when an incident wave at 1064 nm interacts with itself, and third harmonic generation (THG) at 355 nm, which is in fact a sum frequency generation (SFG) of a fundamental wave at 1064 nm and a second harmonic at 532 nm. As nonlinear optics and harmonic generation are well described in the literature [31, 33, 73], only the equations essential to the understanding of the behavior of the SHG process and the key parameters of the doubling crystals and of the fundamental beam to be doubled will be discussed.

In the plane-wave approximation, the SHG conversion efficiency defined as the generated second harmonic power $P_{2\omega}$ over the fundamental power P_ω is given by:

$$\frac{P_{2\omega}}{P_\omega} = \tanh^2 \left[\sqrt{\frac{d_{eff}^2}{n^3} \frac{\omega_1^2}{2\varepsilon_0 c_0^3} \frac{P_\omega}{\pi w_0^2} L} \frac{\sin(\Delta k L/2)}{\Delta k L/2} \right] \quad (3.13)$$

where d_{eff} is the nonlinear material's effective nonlinear coefficient for the given direction of propagation, wavelength, and polarization, n the refractive index, ω_1 the angular frequency of the fundamental wave, w_0 the beam's radius, L the crystal's length, and Δk the phase mismatch between the ω and 2ω waves, defined by:

$$\Delta k = \frac{4\pi}{\lambda_1} (n_1 - n_2) \quad (3.14)$$

where n_1 is the refractive index for the fundamental wavelength λ_1 and n_2 for the second harmonic. For low conversion efficiencies when $\frac{P_{2\omega}}{P_\omega} \ll 1$, Eq. 3.13 simplifies to:

$$\frac{P_{2\omega}}{P_\omega} = \frac{d_{eff}^2}{n^3} \frac{\omega_1^2}{2\varepsilon_0 c_0^3} \frac{P_\omega}{\pi w_0^2} L^2 \sin^2(\Delta k L / 2) \quad (3.15)$$

This equation translates the influence of the crystal and beam parameters on the conversion efficiency.

Phase matching

For an efficient harmonic generation, the phase mismatch Δk should first be minimized, as the 2ω wave generated at each location in the crystal should interfere constructively with the ones generated from the input face up to this location. Thus the SHG power will exhibit a periodic evolution along the length of the crystal [33], corresponding to the transfer of energy from the ω to the 2ω wave up to a length l_c , followed by the full back-conversion of the generated 2ω wave to the fundamental after a length of $2l_c$, where l_c is the coherence length defined by:

$$l_c = \frac{\lambda_1}{4(n_1 - n_2)} \quad (3.16)$$

Eq. 3.15 can be expressed as a function of l_c instead of Δk to illustrate this periodic behavior:

$$\frac{P_{2\omega}}{P_\omega} = \frac{d_{eff}^2}{n^3} \frac{\omega_1^2}{2\varepsilon_0 c_0^3} \frac{P_\omega}{\pi w_0^2} \frac{4}{\pi^2} l_c^2 \sin^2\left(\frac{\pi L}{2l_c}\right) \quad (3.17)$$

It becomes apparent that in order to avoid back-conversion and maximize SHG, the phase mismatch should be minimized to increase the coherence length, with the ideal case of perfect phase matching when $n_1 = n_2$ resulting in an infinite coherence length and a maximum conversion efficiency. As the conversion becomes more efficient, Eq. 3.17 cannot be used anymore, and the general expression Eq. 3.13 for the conversion efficiency with depletion of the fundamental wave should be considered instead.

Although it is possible to achieve high conversion efficiencies yet with short coherence lengths by applying quasi-phase-matching, where the sign of the crystal's d_{eff} is artificially reversed every coherence length, such periodically-poled materials as LiNbO₃ generally exhibit poor optical power handling and photorefractive effects. Thus this technique is not applicable to high-power systems, and we will concentrate on the more classical birefringent index phase matching relying on bulk nonlinear crystals. For specific combinations of birefringent nonlinear crystals and wavelengths, it is possible to find a direction of propagation with respect to the crystal's axes for which the fundamental and the second harmonic will remain in phase, which is defined by the phase-matching angles θ and ϕ between the direction of propagation and the z optical axis, and between the projection of the direction of propagation on the xy plane and the x

axis, respectively. Such condition is fulfilled when the index difference between the fundamental and harmonic waves caused by dispersion is compensated by the crystal's birefringence. For example in type I phase matching in a negative crystal such as LBO ($n^e < n^o$), where two ordinarily-polarized ω photons are doubled to one extraordinarily-polarized 2ω photon, the phase matching is achieved when the refractive indices seen by the two waves are equal, resulting in $\Delta k = 0$. Type II phase matching is also feasible, when one o and one e fundamental photons are mixed to produce one e photon at 2ω , which is achieved when the refractive index of the e-polarized harmonic is equal to the average of the indices of the two o and e-polarized fundamental waves. These two interaction types are defined by the following phase-matching conditions at the phase-matching angles θ_m and ϕ_m :

$$n_2^e(\theta_m, \phi_m) = n_1^o \quad \text{Type I} \quad (3.18a)$$

$$n_2^e(\theta_m, \phi_m) = \frac{n_1^o + n_1^e(\theta_m, \phi_m)}{2} \quad \text{Type II} \quad (3.18b)$$

$$(3.18c)$$

For a phase-matching direction other than one of the crystal's axes, known as critical phase matching (CPM), the Poynting vectors of the o and e waves are separated by the walk-off angle ρ , so that the e-polarized beams propagate at a certain angle with the o -polarized beam. Thus, after a certain crystal length, the interaction between the two beams will be limited due to a reduced spatial overlap, leading to a lower conversion efficiency and an elliptical harmonic beam. Therefore non-critical phase matching (NCPM) with a phase-matching direction along an axis of the crystal is sought to overcome this limitation. In that case the Poynting vectors of the o and e-polarized waves coincide, so that no walk-off exists between the beams, thus maximizing the spatial overlap. NCPM is achieved in LBO for $(\theta = 90^\circ, \phi = 0^\circ)$ with the optical axis aligned to the X axis, when the crystal is held at a temperature of 149°C for a fundamental wavelength of 1064 nm.

In the following paragraphs, the influence of the various beam and crystal parameters on conversion efficiency are studied. First a perfect phase-matching is assumed with $\Delta k = 0$ and $\text{sinc}^2(\Delta k L/2) = 1$, and then the variations of parameters that lead to a phase mismatch and conversely a reduction in conversion efficiency are outlined.

Power density

Harmonic generation being a nonlinear effect, when no depletion of the fundamental wave or when little conversion occur, the conversion efficiency given by Eq. 3.15 increases linearly with the fundamental power density, thus the second harmonic increases quadratically with the fundamental power. As soon as the generated wave becomes significant, the depletion of the fundamental wave cannot be neglected anymore so that Eq. 3.13 should be used. The conversion efficiency saturates towards 100% in an ideal case, the 2ω power evolving linearly with the ω power at high intensities. Thus high fundamental power combined to strong focusing are sought for achieving an efficient harmonic generation. The first is given by the laser's output

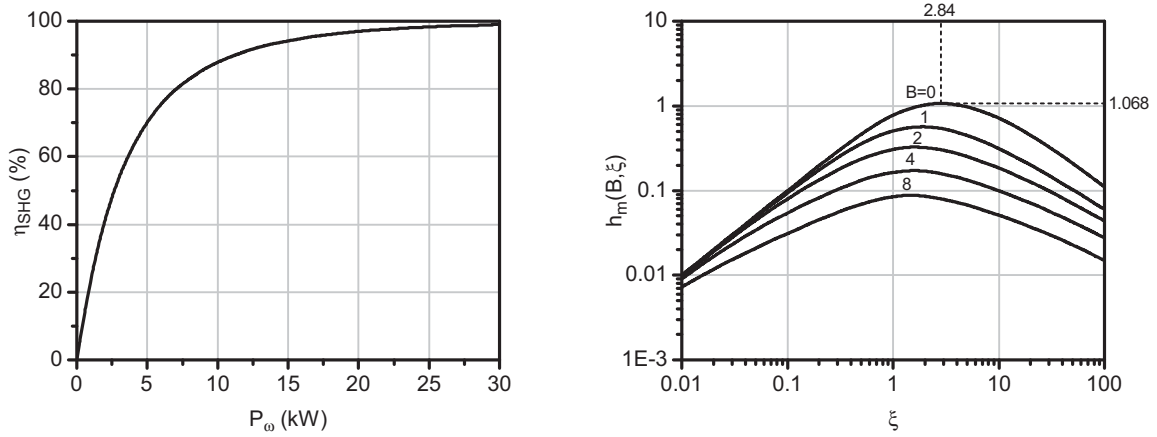


Figure 3.24: SHG efficiency function of 1064 nm power for a 20 mm LBO crystal and optimum focusing of the Gaussian beam down to a waist w_0 of $27 \mu\text{m}$ (left). SHG efficiency following the function $h_m(B, \xi)$ for a range of focusing strength ξ and double-refraction parameters B (right).

characteristics, while the second is limited by the beam quality and the nonlinear interaction acceptance angle described below. Figure 3.24 (left) illustrates the evolution of the conversion efficiency with fundamental power in the practical case of type I non-critical phase matching in a 20 mm long LBO crystal with optimum focusing of a diffraction-limited Gaussian beam down to a waist w_0 of $27 \mu\text{m}$, as defined by Eq. 3.21 for Gaussian beams instead of plane waves. It is directly apparent that efficient doubling is not possible for moderate powers, where the efficiency increases linearly with the fundamental power. Thus pulsed lasers in the ns or ps regime possessing peak powers in the multi-kilowatt range for average powers of a few watts or tens of watts are usually employed for efficient SHG. However, when a cw output is necessary, the nonlinear crystal is placed within the laser resonator or even in an external resonant cavity in which the circulating IR power is much higher than the laser's IR output power. The former technique will be described and experimentally demonstrated in Sect. 3.4.3.

Nonlinearity

The effective nonlinearity d_{eff} expressed in pm/V, of a crystal with a given cut is obtained from the tensor of nonlinear coefficients and the phase-matching angles θ and ϕ . Although a high d_{eff} is obviously desirable for an efficient conversion, many more parameters such as damage threshold, absorption, walk-off angle, temperature, angular, and spectral acceptances need to be taken into consideration for selecting the optimal nonlinear crystal for a given application. However, the nonlinearity of crystals is better compared through their figure of merit defined as:

$$M = \frac{d_{eff}^2}{n^3} \quad (3.19)$$

which has a linear influence on the power necessary for achieving a given conversion efficiency, as expressed in Equ. 3.13.

Crystal length

According to Eq. 3.15, the conversion efficiency increases quadratically with crystal length, assuming that perfect phase-matching is maintained on the whole length of the crystal. Thus for a given power density, this quadratic progression is fulfilled at low conversion efficiencies for plane waves. However for real beams, increasing the crystal length will require augmenting the beam waist optimally located in the center of the crystal to minimize the effect of divergence away from the waist towards the entrance and exit facets. If one keeps a constant ratio $\xi = \frac{L}{b}$ between the crystal length L and the confocal parameter $b = 2z_r$, with $z_r = n \frac{\pi w_0^2}{\lambda}$ the Rayleigh range of a Gaussian beam inside the crystal, one obtains:

$$\frac{L}{\pi w_0^2} = 2\xi \frac{n}{\lambda} \quad (3.20)$$

Thus the conversion efficiency given by Eq. 3.15 is proportional to the fundamental power and crystal length for a real beam, instead of power density and the square of crystal length for plane waves. This behavior is theorized more accurately in the following section.

Although it seems advisable to use a crystal as long as practically feasible for optimum conversion efficiency, absorption and the loss of phase matching along the length of the crystal due to temperature, angular, and spectral acceptances will limit the maximum usable length for optimum performance. As described in the following sections, these acceptances evolve inversely with crystal length, so that if the crystal is too long, the crystal temperature variations due to ambient temperature or absorption will become comparable to the crystal's thermal acceptance. Conversely the beam divergence and the fundamental linewidth will limit the efficient conversion of the whole beam or spectrum, respectively.

Gaussian beam

Equations 3.13 and 3.15 give a good idea of the behavior of SHG efficiency with the various beam and crystal parameters, yet its plane-wave approximation doesn't accurately represent Gaussian beams, which is the beam propagation of interest for all high beam quality lasers. Boyd and Kleinman first devised an expression of conversion efficiency for Gaussian beams encompassing parameters such as waist size, waist position, crystal length and absorption, and walk-off angle [91]. After rather lengthy calculations and a rearrangement of constants for direct comparison with Eq. 3.13 in the plane-wave case with pump depletion, Boyd and Kleinman obtain:

$$\frac{P_{2\omega}}{P_\omega} = \tanh^2 \left[\sqrt{\frac{d_{eff}^2}{n^3} \frac{\omega_1^2}{2\varepsilon_0 c_0^3} \frac{8n}{\lambda} h(\sigma, \beta, \kappa, \xi, \mu) P_\omega L} \right] \quad (3.21)$$

where the function $h(\sigma, \beta, \kappa, \xi, \mu)$ encompasses the following parameters:

$$\sigma = \frac{1}{2} b \Delta k \quad \text{phase mismatch} \quad (3.22a)$$

$$\beta = \frac{\rho}{\theta_0} \quad \text{walk-off} \quad (3.22b)$$

$$\kappa = \frac{1}{2} \alpha b \quad \text{absorption} \quad (3.22c)$$

$$\xi = \frac{L}{b} \quad \text{strength of focusing} \quad (3.22d)$$

$$\mu = (L - 2f)/L \quad \text{focal position} \quad (3.22e)$$

$$(3.22f)$$

where ρ is the walk-off angle, θ_0 is the internal fundamental beam half-angle divergence, α the average absorption coefficient for the fundamental and harmonic, and f the position of the waist from the input facet in the crystal. If absorption is neglected, which is realistic in high-quality crystals such as LBO with $\alpha < 0.1\% \cdot \text{cm}^{-1}$, $\kappa = 0$. It is also demonstrated that optimum conversion occurs when the waist is located in the center of the crystal for $f = L/2$, thus $\mu = 0$. Taking these two conditions into account $h(\sigma, \beta, 0, \xi, 0)$ simplifies to $h(\sigma, B, \xi)$ where $B = \beta\sqrt{\xi} = \rho\sqrt{\frac{\pi n L}{2\lambda}}$. For each focusing strength ξ and walk-off B , one can find an optimum phase mismatch $\sigma_m(B, \xi)$ that maximizes h . Thus $h_m(B, \xi) = h(\sigma_m, B, \xi)$ is the optimum value of h for a given focusing and walk-off. Figure 3.24 (right) illustrates $h_m(B, \xi)$ for a range of focusing strengths ξ and double-refraction parameters B .

For very weak focusing ($\xi \ll 1$ or $L \ll b$), the beams behave as plane waves, but the necessary large beam induces a low power density, thus resulting in low conversion efficiency. At the other extreme, for strong focusing ($\xi \gg 1$ or $L \gg b$), the power density in the focus is very high, but drops dramatically away from the waist, so that the conversion efficiency on the total crystal length is poor. Thus a maximum conversion lies between these two extremes for ξ_m , which is the optimum balance between high power density in the focus and on the end facets. An important case is of NCPM when no walk-off occurs ($B = 0$), which leads to the highest conversion efficiency as the overlap between the fundamental and second harmonic beams is optimal. The function $h_m(0, \xi)$ reaches a maximum value of $h_{mm} = 1.068$ for an optimum focusing of $\xi_m = 2.84$. Thus the optimal waist size w_{0m} is given by:

$$w_{0m} = \sqrt{\frac{\lambda L}{2\pi n \xi_m}} \quad (3.23)$$

In the case of type I NCPM in a 20 mm long LBO crystal, this optimum focusing corresponds to a waist $w_0 = 27 \mu\text{m}$. Figure 3.25 (left) illustrates the dependence of conversion efficiency on waist size for different peak powers, calculated from Equ. 3.21 for this same crystal. One should notice that while the optimum waist size is independent of fundamental power, the range for high conversion efficiency widens at high optical powers as the conversion process saturates. Thus when high fundamental powers are available, the waist is often made larger than the theoretical optimal value to avoid damaging the output facet of the crystal with high green intensities.

In the case of critical phase matching, the maximum conversion $h_{mm}(B) = h_m(B, \xi_m)$ for the optimal focusing ξ_m decreases with increasing walk-off angle or B , as the overall beam overlap is reduced by walk-off. It is also worth noticing that ξ_m decreases with increasing walk-off, which expresses the necessity of weaker focusing with strong walk-off to increase the waist size and the beam overlap.

Thus the linear dependence of conversion efficiency on power and crystal length for low conversion of a Gaussian beam with optimum focusing derived from 3.21 follows that of a plane wave given by 3.15, if the optimum crystal length to Rayleigh range condition is maintained, as shown in Eq. 3.20.

Temperature acceptance

Although the crystal and beam parameters determining the conversion efficiency should be optimized following Eq. 3.21, a perfect phase-matching has been assumed. However nonlinear crystals exhibit finite temperature, angular, and spectral acceptances that should be sufficiently large to encompass the crystal's temperature variations due to its environment or light absorption, the beam's divergence or misalignment, and the laser's linewidth, respectively.

As the crystal's temperature departs from the phase-matching temperature, the dispersion doesn't perfectly compensate for birefringence anymore, which results in $\Delta k \neq 0$. In the case of a low conversion efficiency, as defined by Eq. 3.15, its value will reach one half for $\Delta k L / 2 = 1.39$. Thus, knowing the temperature dependence of the crystal's refractive indices, as given by [92, 93] for LBO, the variations in conversion efficiency with temperature mismatch and the resulting FWHM temperature acceptance $\Delta T \cdot L$ can be calculated. Figure 3.25 (right) illustrates this for an LBO crystal held at 149°C for NCPM. The FWHM temperature acceptance of 4.7 K·cm results in a value of 2.35 K for a 20 mm long crystal, so that an oven regulated to 0.1 K will be sufficient to maintain a constant optimum phase matching. However, when high average power laser beams are converted, residual infrared, green, and green-induced absorption lead to an inhomogeneous temperature profile along the length of the crystal as the green beam is generated. Such effects are very limited in high-quality LBO crystals, and become significant only in high-power intracavity doubled resonators where the average power of several hundred watts inevitably results in crystal heating and stress. Using long crystals further reduces the acceptable temperature variations, which effectively limit the crystal length, so that 24 mm long LBO crystals have not shown higher conversion than 20 mm, yet the sensitivity to oven temperature variations was worse.

Angular acceptance

When optimum phase matching is chosen for one direction of incidence, a beam of too large divergence or that is misaligned will exhibit reduced conversion efficiency. As the index surfaces of the fundamental and harmonic waves intersect in the phase-matching direction, Δk will increase as the two surfaces separate from each other away from this direction. It is shown that for type I CPM, the FWHM external acceptance angle $\Delta \theta \cdot L$ can readily be calculated from [33]:

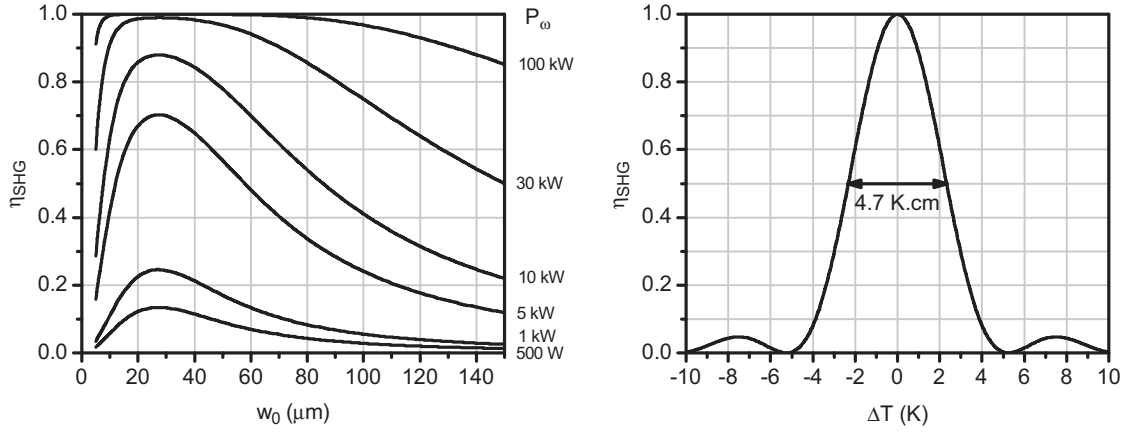


Figure 3.25: SHG efficiency function of waist size for an increasing fundamental power in a 20 mm NCPM LBO crystal (left). SHG efficiency function of the temperature mismatch for a NCPM LBO crystal (right).

$$\Delta\theta \cdot L = n \frac{5.56}{\beta} \quad \text{with} \quad \beta = \frac{4\pi}{\lambda} (n_{2\omega}^o - n_{2\omega}^e) \sin 2\theta_m \quad (3.24)$$

Thus LBO exhibits an external angular acceptance of 12 mrad·cm for type I CPM. In the case of NCPM, the fundamental and harmonic index surfaces are tangential in the direction of phase matching. It is thus shown that the dependence of Δk on misalignment $\delta\theta$ is now a much smaller quadratic term $\Delta k = \beta'_\theta (\delta\theta)^2$, so that the angular acceptance is given by:

$$\Delta\theta \cdot \sqrt{L} = n \sqrt{\frac{2.78}{\beta'}} \quad \text{with} \quad \beta' = \frac{8\pi}{\lambda} (n_{2\omega}^o - n_{2\omega}^e) \quad (3.25)$$

For NCPM in LBO, an external angular acceptance of 90 mrad·cm^{1/2} is readily obtained, which ensures a robust insensitivity to misalignment and allows for the strong focusing of the fundamental beam without loosing on conversion efficiency. Thus for a 20 mm long crystal and an optimum waist of 27 μm , as previously calculated in this section, the corresponding half-angle divergence of 12.5 mrad is well within the FWHM acceptance of 64 mrad.

Spectral acceptance

Spectral acceptance is usually not an issue with solid-state lasers, with the exception of amorphous hosts such as glass, since linewidths are much narrower than the crystal's spectral acceptance. Thus the linewidth of 10 GHz (0.04 nm) or less measured in the various cw or mode-locked systems presented in this work is much narrower than the 0.75 nm·cm spectral acceptance of LBO, allowing the use of a 20 mm long crystal for efficient conversion. Only for ultrashort pulses in the fs regime the correspondingly wide spectrum becomes a limitation for its complete and effective conversion.

Crystal selection

The selection of a nonlinear material for a specific task such as SHG is based on the study of its nonlinear performance parameters such as nonlinearity, walk-off, temperature, angular, and spectral acceptances, but also on more practical characteristics such as size, optical quality, ease of growth, absorption, damage threshold, hygroscopy, and chemical and mechanical stability. The properties of common materials suitable for SHG such as KTP, LiNbO₃, BBO, and LBO are evaluated [33] to select the best candidate for the SHG of high-power diffraction-limited beams at 1064 nm.

LiNbO₃ possesses the largest $d_{eff} = 4.7$ pm/V, higher than that of KTP at 3.18 pm/V, but their respective figures of merit are comparable at 2.0 and 1.9 pm²/V². It offers the advantage of NCPM at 107°C, yet with a narrow thermal acceptance of 0.7 K·cm. Yet its main limitation arises from its low damage threshold and photorefractive effects in the visible and UV, although limited by MgO doping. Its use is thus restricted to low power beams with periodic poling for achieving high conversion efficiencies.

Potassium Titanyl Phosphate KTiOPO₄ (KTP) is widely used for the SHG of Nd lasers thanks to its unique combination of a high nonlinearity, limited walk-off, and wide angular and thermal acceptances. Its use for doubling high-power lasers has been however limited in the recent years, as it suffers from a photochemical degradation (gray tracking) which is a cumulative effect of second harmonic and fundamental radiations.

Beta-Barium Borate (BBO) also possesses a relatively high nonlinearity, with $M = 0.8$ pm²/V², a wide thermal acceptance, and high damage threshold, with the capacity of phase-matching for SHG down to the blue region. These favorable characteristics are however balanced by a large walk-off $\rho = 55$ mrad and an angular acceptance ten times narrower than that of LBO. Thus the two crystals can be compared by evaluating $M \cdot h_m(B, \xi_m)$ which is proportional to the conversion efficiency in the low conversion regime with independently optimizing the focusing for each crystal. For type I CPM in a 10 mm long BBO crystal $B = 8$, and for type I NCPM in LBO $B = 0$, so one obtains the following corrected figure of merit accounting for walk-off:

$$M_{LBO}h_m(0, \xi_m) \approx 3 \cdot M_{BBO}h_m(8, \xi_m) \quad (3.26)$$

BBO requires the use of short crystals and high-quality beams to limit the effects of walk-off and minimize B , and to achieve a low beam divergence within the small angular acceptance.

Lithium triborate LiB₃O₅ (LBO) is the worst candidate in terms of nonlinearity with $d_{eff} = 0.85$ pm/V and $M = 0.2$ pm²/V², but in practice is the material of choice for the SHG of high average power beams. Its most favorable characteristics reside in its capacity to NCPM at 149°C and a very high damage threshold, yet its thermal acceptance is much narrower than that of KTP or BBO. Table 3.2 illustrates its most important characteristics for two type I interactions with critical and non-critical phase-matching, although a type II interaction in the YZ plane is also feasible and of greater interest for the SHG of unpolarized laser beams such as from Nd:YAG. At 1064 nm NCPM is achieved through temperature tuning to 149°C by placing the crystal in a regulated oven, yet type I NCPM for 1342 nm is obtained at a much less practical

Table 3.2: SHG properties of LBO for type I NCPM and CPM. Acceptances are given FWHM. Data from [96, 33].

		NCPM	CPM
Cut		X	XY
θ, ϕ	°	90, 0	90, 11.4
n		1.605	1.605
d_{eff}	pm/V	0.85	0.83
Temperature	°C	149	25
Walk-off angle	mrاد	0	6.9
Temperature acceptance	K·cm	4.7	6.3
Angular acceptance	mrاد·cm ^{1/2} / mrاد·cm	90	12
Spectral acceptance	nm·cm	0.75	0.75
Damage threshold	GW/cm ²		2.5

temperature of 2°C. CPM is achieved at room temperature by orienting the crystal off the X axis in the XY plane. This configuration leads to a moderate walk-off angle of 6.9 mrad, which will be of particular interest for precompensating the walk-off of a second LBO crystal used for THG [94]. As detailed in the previous paragraphs, the temperature, angular, and spectral acceptances are fully compatible with the efficient doubling of a high beam quality laser such as Nd:YVO₄.

Although a damage threshold of 2.5 GW/cm² has been measured for LBO, damage almost always occurs at the crystal's interfaces, and most often on the exit face where the higher-energy green photons exit the crystal through its AR coating. Not only the materials used for the multilayer coating should resist high laser intensities, but surface preparation and cleanliness, including the absence of dust or aerosol contamination, are of crucial importance for avoiding the local destruction of the coating, potentially affecting the bulk of the crystal itself. Two deposition techniques dominate for the realization of AR coatings. Ion-assisted deposition (IAD) consists in a classical evaporation associated to an ion gun pointed to the optical substrate for increasing the energy of the deposited particles, while ion-beam sputtering (IBS) relies on an ion gun directly pointed to a target, effectively depositing higher energy particles on the substrate that are further compacted by a second ion gun. IBS produces lower-reflectivity, denser, harder, and less porous films than IAD, making them very suitable for intracavity harmonic generation where residual losses should be kept at a minimum. They can also sustain faster temperature ramps without peeling, as from room to NCPM temperature [95]. The IAD coatings deposited on the crystals used throughout this work however tend to achieve higher damage thresholds, making them a better choice for extracavity SHG of high-power pulsed lasers where residual losses are of minor importance, yet this is most likely to change with improvements of the more recent IBS technique.

3.4.2 Intracavity doubling

High-power, high-beam-quality green lasers emitting in continuous-wave operation are needed in many applications such as pumping of Ti:Sa or dye lasers, processing of materials exhibiting a low absorption in the infrared, annealing and crystallization of glass, and even large-scale laser shows. Large-frame argon-ion lasers were the first to offer powers in excess of 30 watts in a near diffraction-limited beam, but at the expense of very low efficiency requiring several tens of kilowatts of electrical power and high-flow-rate water-cooling. With the advent of high-power laser diodes and high-quality neodymium-doped vanadate and nonlinear crystals, intracavity frequency-doubled lasers emitting at 532 nm became commercially available ten years ago, offering at first 5 to 10 watts of stable noise-free output power in a diffraction-limited beam [88, 89]. Although the power of such systems has increased up to 23 watts in a laboratory setup and 18 watts commercially [90], they still haven't equaled large-frame ion lasers in terms of power, with the exception of a frequency-doubled Yb:YAG thin-disk ring laser providing up to 50 W at a wavelength of 515 nm [21].

The major issue in the development of high-power intracavity-doubled solid-state lasers is the rise of power instabilities in the μs to ms range, known as the "green problem" [97]. This strong noise arises from a coupling of the resonator's longitudinal modes resulting from the combined effects of sum-frequency generation (SFG) in the doubling crystal and spatial gain saturation in the laser medium between the different longitudinal modes oscillating in the cavity. Several solutions have been proposed that rely on simple resonator designs without added intracavity elements.

Passive stabilization can be achieved by shortening the cavity until the relaxation-oscillation pulses are short enough to undergo significantly stronger conversion to the green than stable cw, the laser operating then in a cw mode so as to minimize its power loss [98]. Another method for achieving a stable cw green output is to reduce the cavity length to maximize mode spacing, thus limiting the number of potentially oscillating longitudinal modes, and place short doubling and laser crystals in the center or in specific locations inside the laser cavity. The resonator tends to oscillate on two neighboring longitudinal modes which effectively use the available gain as their spatial overlap in the gain medium is minimized [99, 100]. Furthermore their limited overlap in the doubling crystal results in the SHG efficiency of each individual mode to be 3 times larger than the SFG efficiency between the two neighboring modes, being thus sufficient to stabilize the laser's output. However these solutions intrinsically need short resonators and/or very specific locations for laser and doubling crystals, which prevents their use in high-power systems generally requiring relatively long resonators in which the position of elements is already determined by geometrical and mode-matching considerations.

These constraints led to the prevalence of two solutions for the realization of high-power systems. One solution is to operate the laser in a single-longitudinal-mode regime by designing a unidirectional ring oscillator with a Faraday rotator and an intracavity Fabry-Pérot etalon for single-mode selection [21, 89, 90]. Another approach for solving the green problem is to build a long linear resonator with a high-gain laser medium to allow many longitudinal modes to oscillate simultaneously, thus averaging out the effect of sum-frequency mixing between modes

[88, 101, 102, 103]. The latter solution was chosen here since it requires fewer intracavity components than a single-mode unidirectional ring-resonator, and can be applied by simply extending an existing linear resonator.

One should notice the recent technology of optically-pumped semiconductor lasers (OPSL) offering a novel solution for the generation of noise-free high optical powers in the visible by intracavity doubling a resonator containing a diode-pumped semiconductor disk chip as the gain medium. The short upper-state lifetime of ~ 10 ns leading to a strong damping of intensity fluctuations, and the gain region of only a few microns thick containing a stack of multiple quantum wells, both contribute to suppressing the green problem [90]. Intracavity-doubled powers of 55 W in TEM₀₀ mode and 66 W in multimode operation have been demonstrated in a periodic resonator containing three OPS chips [23].

3.4.3 Intracavity-doubled TEM₀₀ resonators

Building on the IR performance of the single and two-crystal resonators presented in Sect. 3.2, providing a source of high power and high beam quality with the further advantage of a high gain, two intracavity-doubled resonators were derived by extending both IR cavities to integrate the doubling crystal.

Figure 3.26 (left) depicts the oscillator setup that can be operated with one laser crystal or as a periodic resonator comprising two crystals. The single-crystal resonator contains a 4x4x30 mm *a*-cut, 0.5% at. doped Nd:YVO₄ crystal C₁, end-pumped by a 888 nm, 400 μ m diameter, 0.22 NA fiber-coupled diode laser system. The pump light is focused on a 1350 μ m diameter pump spot in the center of the crystal, providing an almost collimated pump volume along the crystal length. The unabsorbed pump light is retro-reflected by a lens-mirror combination to achieve high and smooth absorption of the pump light, up to a total absorption efficiency of 95%. The folded resonator is formed between flat end-mirror M_5 , convex pump mirrors M_3 and M_4 with $r = +1000$ mm, HR at 1064 nm and HT at 888 nm, concave dichroic mirror M_2 with $r = -75$ mm, HR at 1064 nm and HT at 532 nm, and concave end-mirror M_1 with $r = -100$ mm, HR at 1064 and 532 nm. M_2 focuses the laser mode down to a waist radius of 35 μ m in the 20 mm-long LBO crystal while the laser mode is maintained at 510 μ m in the laser crystal, as illustrated in Fig. 3.26 (right). NCPM LBO was selected for type I second harmonic generation for its high damage threshold, low absorption, absence of walk-off, and large temperature and angular acceptances [93], allowing the strong focusing of the high-power laser mode with minimal thermal effects or mode distortion. The crystal was held at 150°C in a thermally-insulated copper oven regulated to $\pm 0.1^\circ\text{C}$. It was first brought up from room to NCPM temperature in ~ 1 hour to avoid the crystal and its coatings a thermal shock due to LBO's anisotropic thermal expansion. The radii of curvature of M_1 and M_2 and their relative distances to the LBO were optimized to achieve the desired focus size and position, while the distance from M_1 to the LBO was adjusted to compensate for the dispersion of air and minimize the phase mismatch between the green beams generated in the two directions. Thus, the green radiation generated from M_2 to M_1 is back-reflected on M_1 and combined in phase with the green light generated in the opposite direction, both exiting the cavity in one single beam through

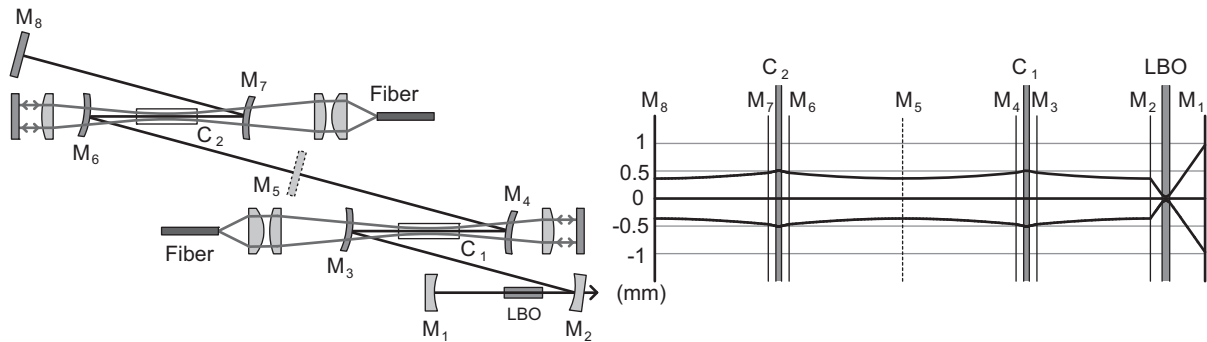


Figure 3.26: Single and two-crystal intracavity-doubled resonator schemes (left). Corresponding TEM_{00} mode profile (right).

dichroic mirror M_2 . However the distance from M_1 to the LBO did not appear to have such a critical influence on the green output power, as would have been expected if just one longitudinal mode was oscillating. Thus, the large measured number of oscillating modes explains this lower sensitivity of output power on the M_1 -LBO separation. The resonator is further extended as a periodic resonator by duplicating the IR cavity between M_2 and M_5 to an identical arrangement between M_5 and M_8 , and removing mirror M_5 to let the cavity oscillate between M_1 and M_8 . Figure 3.26 (right) illustrates the periodicity of the mode profile and the unchanged focusing in the LBO when the cavity is extended.

The single-crystal oscillator was first operated before heating the LBO crystal, thus without generating any green light, and was optimized for TEM_{00} operation at a pump power of 108 W, providing 55.5 W at 1064 nm when the end-mirror M_5 was a 35% transmission optimum output coupler. The LBO crystal was then heated up to achieve non-critical phase-matching, and end-mirror M_5 was replaced by a 1.5% transmission output coupler to limit intracavity power. The oscillator provided an output power of 34 W at 532 nm, corresponding to an IR-to-green conversion efficiency of 61%, with respect to the available fundamental power without frequency doubling and with optimum output coupling, and a diode-to-green optical efficiency of 31%. The one-way circulating intracavity power was calculated from the IR power transmitted through M_5 to be 180 W. The oscillator was then extended to the periodic resonator configuration, producing an IR power of 115 W for a pump power of 211 W with a cold LBO and an output coupling of 65%. Once the LBO was brought to temperature and M_8 replaced by a 5% transmission mirror, the oscillator provided an output power of 62 W at 532 nm, corresponding to an IR-to-green conversion efficiency of 54%, and a diode-to-green optical efficiency of 29%, while the one-way circulating intracavity power was calculated at 250 W.

In both configurations, further reducing the transmission of end-mirror M_5 or M_8 did not permit higher IR intracavity power, nor higher green output power, as the resonator then suffered from high nonlinear losses through off-axis amplification of the laser mode wings in the high-gain edges of the aberrated thermal lens. This effect led to this off-axis stray laser light being amplified and heating the pump mirror mounts, thus disturbing the system's stability. The thermal effects in the LBO crystal increase with the IR mode power, which results from the residual absorption

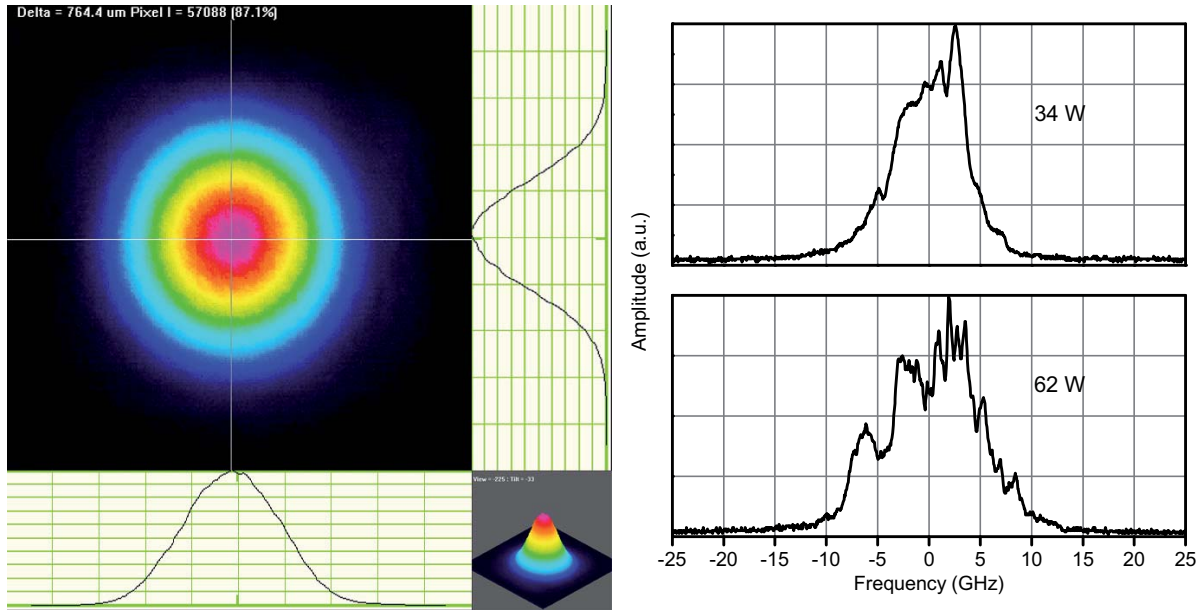


Figure 3.27: Green beam image and profiles at 62 W output power (left). IR mode optical spectra for the one and two-crystal resonators (right).

of the high IR power and of the generated green light. This leads to thermal lensing and mode distortion, which effectively disturbs the resonator's TEM_{00} mode propagation. However, with the transmissions of M_5 and M_8 specified above, a green beam quality of $M^2 = 1.05$ was measured in both resonators, and the beam profile was monitored with a CMOS camera, as illustrated in Fig. 3.27 (left).

Figure 3.28 (left) illustrates the output signal monitored with a 20 ns risetime silicon PIN photodiode and a 1 GHz bandwidth oscilloscope. The residual noise was mainly a result of relaxation oscillations at 25 kHz, also visible as a single peak on a RF spectrum analyzer (right). The RMS noise induced by the 25 kHz residual oscillations measured on the oscilloscope amounted to 0.20% at 34 W (left) and 0.05% at 62 W (right). The output power remained stable over several hours of operation once the air and mechanical components had reached thermal equilibrium, although a sealed temperature-regulated cavity would reduce warm-up time and limit the perturbations induced by air flow and convection.

In order to explain the lower noise for the two-crystal configuration, the optical spectrum of the fundamental laser mode with ICSHG was measured with a 150 GHz free-spectral-range (FSR) scanning Fabry-Pérot interferometer, as illustrated in Fig. 3.27 (right). The single-crystal and periodic resonators exhibited average spectral widths of respectively 7 and 12 GHz, for longitudinal mode spacings of 175 and 100 MHz, corresponding to 40 and 120 oscillating modes respectively. The low-noise operation can therefore be attributed to the large number of simultaneously oscillating modes, therefore providing a constant overall output, although the IR spectrum's profile is constantly changing. However, in order to maintain the random excitation of the different modes, care should be taken to avoid any spectrally selective effect, such as an

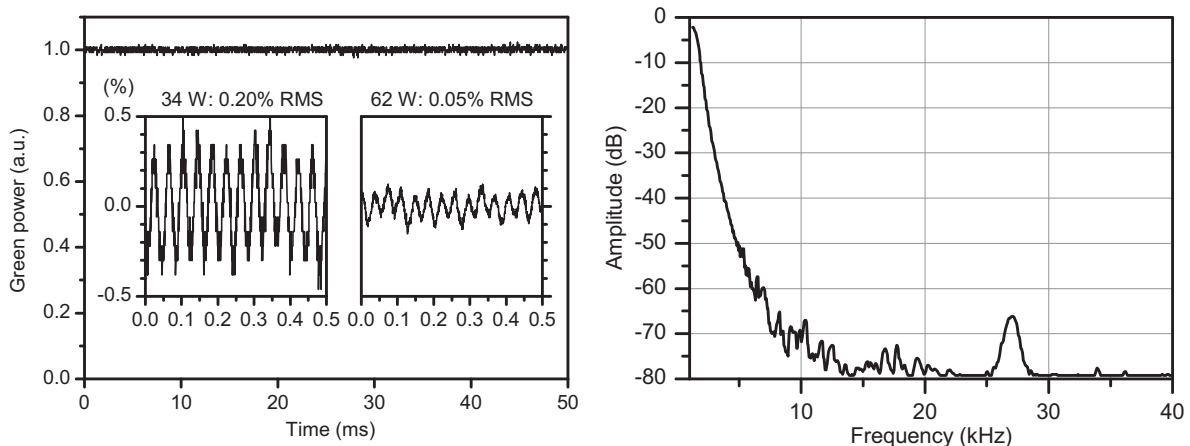


Figure 3.28: Green output signal and close-up views for the single and two-crystal resonators (left). Corresponding electronic spectrum illustrating the single peak around 25 kHz being the main source of amplitude noise (right).

étalon [102]. Therefore the LBO crystal was slightly tilted off its axis to avoid any parasitic reflections along the resonator axis.

Figure 3.29 illustrates the experimental setup of the two-crystal periodic resonator. Although the system covered the whole 1.2 m width of the optical table, it could easily be folded to reduce its longest dimension by a factor of two. The setup needed to be kept covered in an enclosure during operation to prevent the strong air flow of the laminar flow box from distorting the phase fronts of the IR mode and of the second harmonic generated in the first pass, effectively stabilizing the SHG signal.

In summary, a 62 W intracavity-doubled Nd:YVO₄ oscillator was demonstrated, which I believe is the highest output power for a cw laser at 532 nm with diffraction-limited beam quality, more than three times the highest commercially available power [90]. Furthermore, it provides higher output power than large-frame argon-ion lasers, with the definite advantage of low power consumption, compactness, reliability, and ease of use.

3.5 CW performance summary

After a thorough characterization of a high-power 888 nm pumped vanadate gain module, including multimode operation for maximum extraction, and the study of gain, output coupling, thermal lensing, and sensitivity to pump polarization, a simple TEM₀₀ oscillator was developed. From this basis, a periodic resonator, an amplifier, and two intracavity-doubled resonators were built, with their performance summarized in Table 3.3. All have in common a high output power, a high optical-to-optical efficiency, and a diffraction-limited beam quality. They offer a 2–3-fold improvement in output power over 808 and 880 nm pumped commercial systems in their respective 1-crystal, 1-diode, and 2-crystal, 2-diode configurations.

Table 3.3: Performance summary of the demonstrated CW systems, all offering a diffraction-limited output beam with $M^2 \approx 1.05$.

System	P_{out} (W)	P_{pump} (W)	η_{opt} (%)
1-crystal oscillator	60	108	55
2-crystal oscillator	119	216	55
Amplifier stage	57	108	53
MOPA	117	216	54
1-crystal ICSHG oscillator	34	108	31
2-crystal ICSHG oscillator	62	211	29

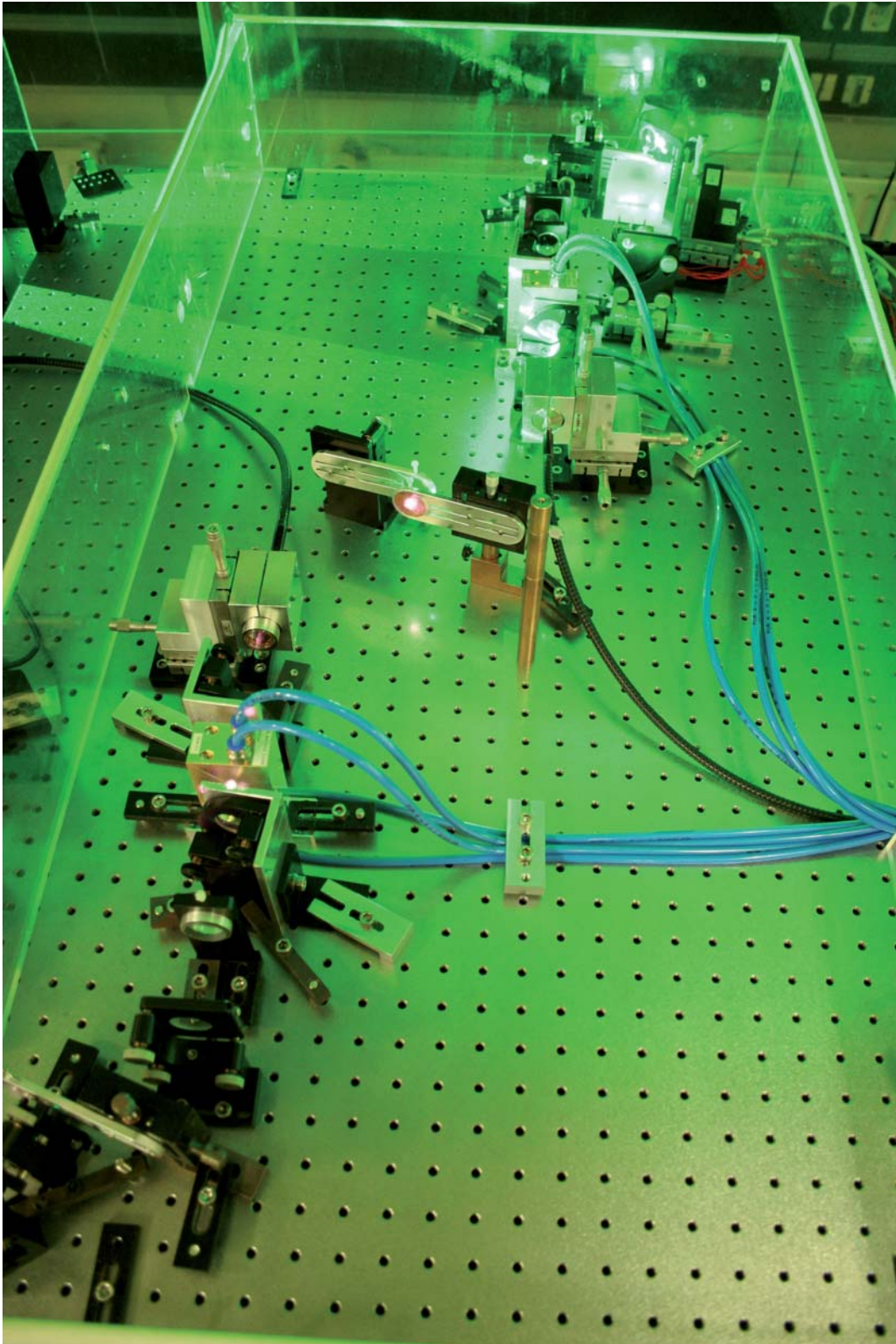


Figure 3.29: 62 W two-crystal intracavity-doubled resonator experimental setup. The two laser crystals are water cooled by the blue tubes, each associated to its fiber-coupled pump delivery. The LBO crystal is located in an oven which is thermally-isolated with a white Delrin sleeve (top right). The output beam is folded and exits horizontally to the left at the back of the table.

Chapter 4

Nanosecond pulse operation

Lasers emitting pulses in the nanosecond regime are the sources of choice for many industrial applications such as micromachining, printed circuit-board via-hole drilling or semiconductor processing. Such tasks require reliable long-term operation with a diffraction-limited beam and increasingly higher output powers and repetition rates to improve machining speed. Many materials are best processed by laser light in the visible or UV spectral region, which is generally achieved by frequency-converting a fundamental IR wavelength in nonlinear crystals, its efficiency increasing with pulse peak power and therefore shorter pulses. For drilling applications there have been numerous accounts of cleaner results obtained when machining with short pulses, the pulse energy being deposited at once in the material, inducing the formation of a plasma and ejecting the hot melted material before it can transfer heat to the surrounding substrate. This is true for fs and ps pulses, and to a lesser extent to short ($\sim 1 - 10$ ns) nanosecond pulses, as opposed to the longer > 100 ns pulse durations obtained with classical Nd:YAG lasers. Therefore the general trend in high-precision machining applications goes towards shorter pulses at high repetition rates and average powers.

A common way of realizing such ns pulse sources is to Q-switch a diode-pumped solid-state oscillator. Neodymium-doped vanadate is the favored gain medium when short pulses and high repetition rates are desired, owing to its high gain and limited upper-state life-time. When coupled to an end-pumping configuration, a diffraction-limited beam along with high optical efficiency can be achieved. Increasing the output power of such oscillators requires a larger pump spot to keep the crystal's thermal load within acceptable limits and maintain the thermal lens and aberrations low enough to allow a diffraction-limited mode to be supported by the resonator. Further power scaling is made possible by pumping the crystal from both ends and/or by splitting the thermal load on two or more crystals [4, 5]. The cavity losses are periodically modulated by an acousto-optic Q-switch, allowing a pulse to build up in the resonator and exit through an output coupler mirror. When shorter Q-switched pulses are sought, the cavity length should be reduced and the gain increased to minimize respectively the round-trip time and the number of round-trips necessary to build-up the pulse and sweep out the energy stored as inversion in the crystal. However, reducing the cavity length generally leads to a smaller fundamental mode in the gain medium, thus limiting the maximum pump

power. When operated at higher repetition rates, the gain available for each pulse to be formed is reduced, leading to increased pulse build-up time and duration. If frequency conversion is applied to such pulses, its efficiency drops as the pulse energy decreases and the pulse duration increases with higher repetition rates.

On the contrary, cavity dumping of a Q-switched cavity allows for the generation of equally short pulses independently of pump power and repetition rate. Thus such sources provide higher peak power pulses and over a much larger range of pulse-repetition frequency (PRF) than regular Q-switched oscillators. In this chapter, both techniques are implemented in the high-power cw oscillator presented in Sect. 3.2.2, and their main characteristics, behaviors and performance compared. Finally frequency doubling is applied to the cavity-dumped oscillator to take full advantage of its constantly short pulses.

4.1 Q-switching

4.1.1 Principle

Q-switching a laser resonator implies changing the cavity's Q factor or losses with time. This variation can be self-constructing in a passively Q-switched oscillator where the intracavity photon flux bleaches a saturable absorber, thus allowing a high-energy pulse to build up with minimal losses. In this technique, the pulsing effect is self-starting and maintained at a PRF which increases with gain and therefore pump power. However many applications demand an instantaneous control of the PRF and the triggering of pulses on an external signal, independently of the pump power and laser dynamics. Thus active Q-switching where the losses are externally controlled allows for a precise adjustment and triggering of the pulse train within a wide range of PRF.

Figure 4.1 (left) illustrates the components essential to an actively Q-switched oscillator. A Q-switch or loss modulator is inserted within a classic resonator oscillating between an end-mirror and an output coupler. As illustrated in Fig. 4.1 (right), when the Q-switch is in high-loss mode, ideally inducing 100% losses, the gain generated in the laser medium is not sufficient to overcome the high losses, thus holding the cavity under threshold and preventing any laser oscillation. During this period, the inversion builds up as only spontaneous emission depletes the upper laser level, resulting in an inversion n_i and gain much higher than that of cw threshold defined by the OC transmission and residual roundtrip losses. When the Q-switch losses are brought down, making it now ideally a purely passive loss-free optical component, the laser threshold comes back to the cavity's lower cw threshold n_{th} . Laser amplification can then start from spontaneous emission, quickly building up intracavity power. When the photons oscillating in the cavity have reached a sufficient number, they rapidly sweep the energy stored as inversion, creating a giant pulse which reaches its peak when the gain is just sufficient to compensate the losses, thus when the inversion has been depleted to its threshold value n_{th} . The intracavity power decreases from there on, but keeps on sweeping the inversion until laser oscillation has ceased, leaving the inversion at a level n_f . During the whole oscillation period, the output pulse emitted through the output coupler is an image of the intracavity photon number q .

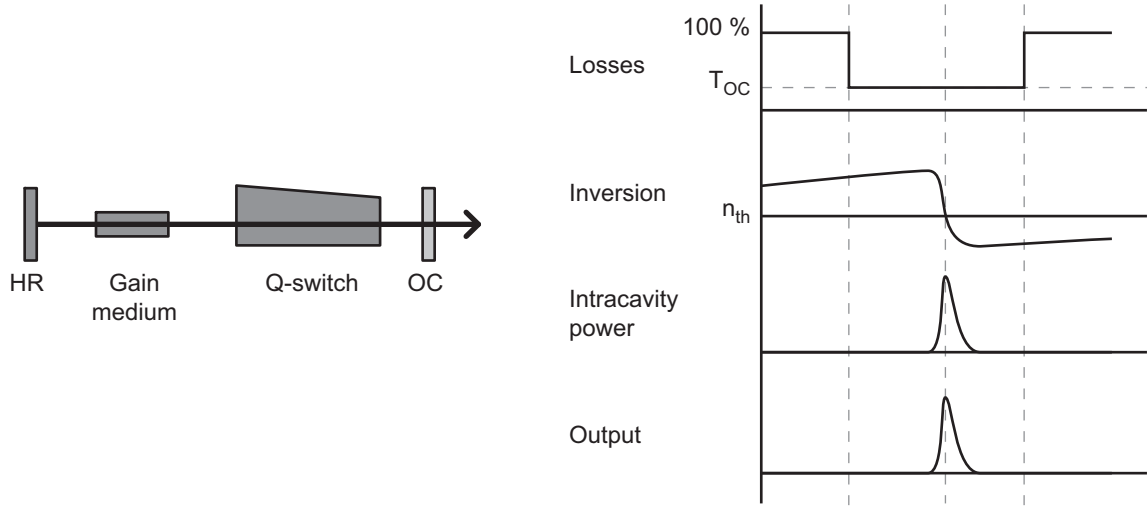


Figure 4.1: Q-switched oscillator principle scheme (left). Evolution of the cavity parameters when the losses are switched from a high value holding the resonator under threshold to a low value limited by the useful losses of output coupling to allow the pulse formation (right).

The temporal evolution of inversion density n and total intracavity photon number q is expressed by the coupled differential rate equations:

$$\frac{dn}{dt} = R_p - \frac{n}{\tau} - \frac{\sigma c}{AL} n q \quad (4.1)$$

$$\frac{dq}{dt} = \sigma c \frac{l}{L} n (q + 1) - \frac{q}{\tau_c} \quad (4.2)$$

where A is the mode area, l the crystal length, L the resonator optical length, and τ_c the cavity lifetime defined by:

$$\tau_c = \frac{2L}{c} \frac{1}{\delta - \ln R} \quad (4.3)$$

where R is the output coupler reflectivity and δ the roundtrip logarithmic losses. The first and second terms of Equ. 4.1 encompassing respectively the pumping process and the spontaneous emission can be neglected during the Q-switch pulse build-up and emission, as the third term representing the inversion depletion due to stimulated emission is orders of magnitude larger during this period. The first term of Equ. 4.2 accounts for the increase in cavity photon number resulting from stimulated emission, while the extra single photon represents the contribution of spontaneous emission starting the amplification process. The second term illustrates the photon number decay resulting from output coupling and passive losses.

When the cavity losses are held at a high level between pulses, no photons are present in the resonator so $q = 0$ and the growth of inversion is solely defined by pumping and spontaneous emission. Thus the temporal evolution of inversion is defined by:

$$n(t) = n_{\infty} - (n_{\infty} - n_f) \exp\left(-\frac{t}{\tau}\right) \quad (4.4)$$

where

$$n_{\infty} = \frac{g_0 l}{\sigma l} \quad (4.5)$$

is the maximum attainable inversion and n_f the inversion remaining after a pulse has been emitted. Thus, for a cw-pumped repetitively Q-switched oscillator at a repetition rate F , the inversion densities n_i and n_f are related to each other by a transcendental equation for the pulse emission period (Equ. 4.7) and for the pumping period (Equ. 4.6):

$$n_i = n_{\infty} - (n_{\infty} - n_f) \exp\left(-\frac{1}{\tau F}\right) \quad (4.6)$$

$$n_i - n_f = n_{th} \ln\left(\frac{n_i}{n_f}\right) \quad (4.7)$$

where the threshold population inversion is defined by:

$$n_{th} = \frac{\delta - \ln R}{2\sigma l} \quad (4.8)$$

The pulse energy E_{out} , pulse duration τ_p , and pulse build-up time τ_{bu} from the closing of the Q-switch to the moment when the output power has reached 10% of its peak value are then expressed as a function of n_i and n_f [31]:

$$E_{out} = A \frac{h\nu}{\sigma} \frac{|\ln R|}{2} \ln\left(\frac{n_i}{n_f}\right) \quad (4.9)$$

$$\tau_p = \tau_c \frac{n_i - n_f}{n_{th} \left[\frac{n_i}{n_{th}} - \ln\left(\frac{n_i}{n_{th}}\right) - 1 \right]} \quad (4.10)$$

$$\tau_{bu} = \frac{\tau_c}{n_{th}} \ln\left(\frac{1}{10} A l n_{th} \left[\frac{n_i}{n_{th}} - \ln\left(\frac{n_i}{n_{th}}\right) - 1 \right]\right) \quad (4.11)$$

The evolution of the output power in time is then calculated from the instantaneous intracavity photon number obtained from the incremental implementation of Equ. 4.1 and 4.2 starting from the initial conditions $q = 0$ and $n = n_i$:

$$P_{out}(t) = |\ln R| \frac{c}{2L} h\nu q(t) \quad (4.12)$$

These expressions will be used in the following section to simulate the evolution of the laser parameters with time and for different repetition rates and output coupling.

4.1.2 Simulations

In order to get a better understanding of the influence of output coupling and repetition rate on inversion, output energy, pulse duration and build-up time, and on the shape of the output pulse itself, a series of simulations is conducted for the basic resonator setup realized in Sect. 4.1.4, based on the cw oscillator presented in Sect. 3.2.2. The measured values for gain $g_0 l = 4.7$ and for mode radius in the crystal $w = 510 \mu\text{m}$ are considered, along with a logarithmic loss $\delta = 0.06$ accounting for the residual losses on optical interfaces, scattering, and diffraction on the aberrated thermal lens, determined by fitting the evolution of output power with output coupling in cw operation shown in Fig. 3.14 (right). The crystal length and resonator optical length are fixed at $l = 30 \text{ mm}$ and $L = 700 \text{ mm}$, respectively. The inversion density and photon number are considered to be uniformly distributed in the crystal and the resonator at a given time for simplifying the calculations, although a high-gain and large output coupling system producing short pulses in the order of the cavity roundtrip time will exhibit strong spatial inversion and photon density variations. It appears however that this simplification doesn't prevent a relatively accurate prediction of the behavior and performance of the Q-switched system investigated experimentally in Sect. 4.1.4.

Figure 4.2 (left) illustrates the temporal evolution of the inversion density in steady-state pulsed operation at different repetition rates for an optimal output coupling transmission of 40%. For each repetition rate F , the coupled equations 4.6 and 4.7 are solved with n_∞ and n_{th} given by Equ. 4.5 and 4.8, respectively. The pulse emission occurring at $t = 0$ and at each multiple of $1/F$ is considered instantaneous compared to the inversion build-up period, during which $n(t)$ is calculated from Equ. 4.4. At low repetition rates of $\sim 1 \text{ kHz}$ and below, when $1/F \gg \tau$, the inversion build-up period is long enough to reach maximum inversion, so that $n_i \rightarrow n_\infty$. As a giant pulse of maximum energy is emitted, it sweeps the inversion almost completely, so $n_f \rightarrow 0$. When the PRF increases, the inversion build-up period is too short for

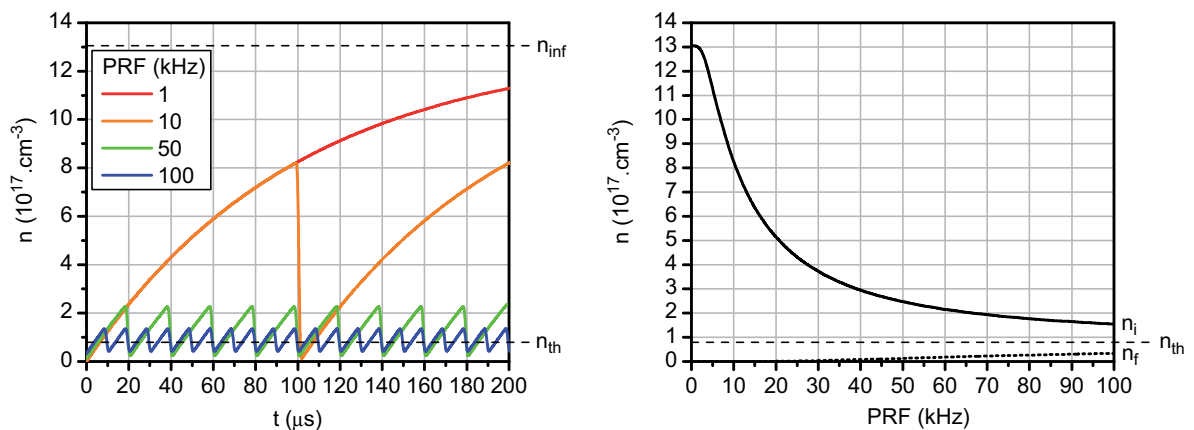


Figure 4.2: Temporal evolution of the population inversion density from n_f to n_i during the pumping period and back to n_f after the pulse emission for different repetition rates (left). n_i and n_f function of repetition rate (right).

n to approach n_∞ , so that n_i and the stored energy are effectively limited. The emitted pulse of lower energy is therefore not powerful enough to sweep the population inversion completely, leaving an inversion n_f that increases with PRF. At very high repetition rates, when $1/F \ll \tau$, the inversion build-up time is so short and the emitted pulse energy so low that both $n_i \rightarrow n_{th}$ and $n_f \rightarrow n_{th}$. This trend is also illustrated in Fig. 4.2 (right) where n_i saturates at low PRF and converges with n_f to n_{th} at high PRF.

Once n_i has been determined, the temporal evolution of n and q can be calculated incrementally from Equ. 4.1 and 4.2, with $n_{t=0} = n_i$ and $q_{t=0} = 0$ the initial conditions at the time of opening of the Q-switch, when the intracavity photon number starts to build up from the first spontaneous-emission photon. The influence of pumping and spontaneous emission can be neglected during the short pulse build-up and emission period, so that the first two terms of Equ. 4.1 are omitted. The instantaneous output power $P_{out}(t)$ is then calculated from $q(t)$ with Equ. 4.12. Figure 4.3 (left) illustrates the formation of a Q-switched pulse at optimum output coupling and 50 kHz PRF and the simultaneous inversion depletion. The pulse is emitted after a build-up time τ_{bu} from the opening of the Q-switch to the time when the instantaneous output power reaches 10% of the pulse peak power. The peak of the pulse corresponds to $n = n_{th}$ while n decreases to n_f as the photons sweep the inversion and exit through the output coupler, forming the pulse tail. Figure 4.3 (right) illustrates the pulses emitted at different PRF for the same configuration. The step increase in peak power and the pulse shortening at low PRF is obvious, but the pulse shape also evolves. At low PRF, the very high gain leads to very short pulse build-up and rise times, while the pulse tail is comparatively longer as the intracavity photons gradually sweep the largest part of the remaining inversion. At higher PRF however, the lower gain results in longer build-up and pulse rise times, so that the pulse tail becomes relatively symmetric to the pulse rise with respect to the pulse peak. This effect is all the more noticeable in under-coupled cavities, where the high OC reflectivity allows a very fast pulse build-up and rise, but leads to a much slower emptying of the cavity photons, effectively leading to a very asymmetric pulse shape.

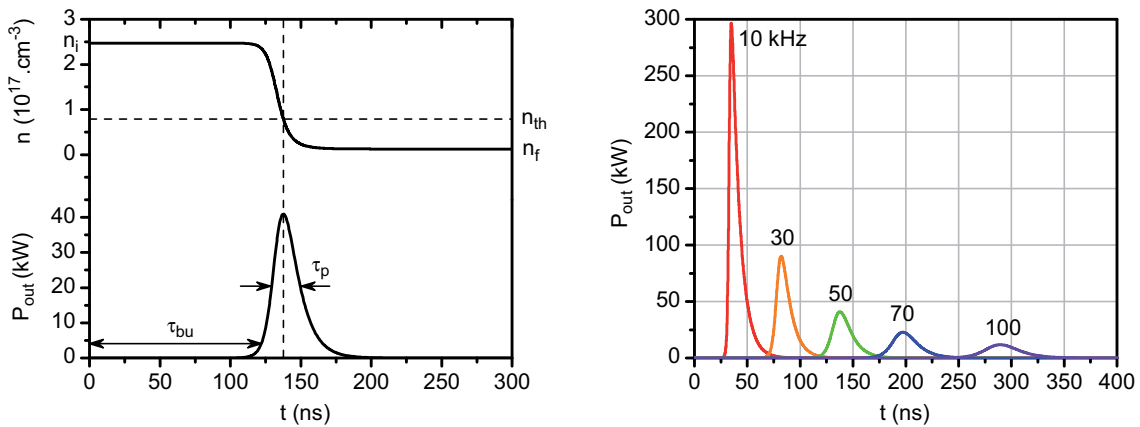


Figure 4.3: Temporal evolution of inversion density n and instantaneous output power P_{out} during pulse build-up and emission for $T_{OC} = 40\%$ and $F = 50$ kHz (left). Output pulses for $T_{OC} = 40\%$ from 10 to 100 kHz PRF (right).

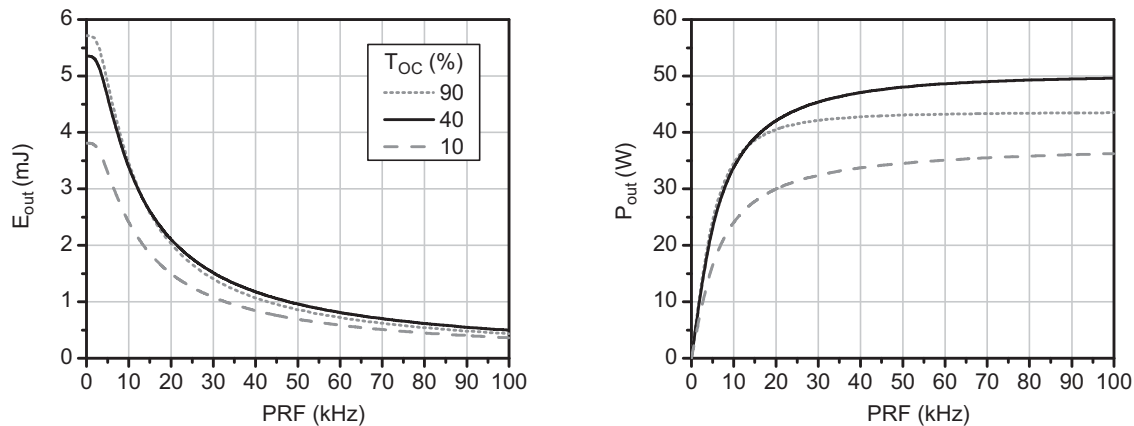


Figure 4.4: Pulse energy function of PRF at optimum output coupling ($T_{OC} = 40\%$) and for strongly over ($T_{OC} = 90\%$) and under-coupled ($T_{OC} = 10\%$) cavities (left), and the corresponding average output power (right).

Figure 4.4 (left) illustrates the evolution of pulse energy with PRF, determined from n_i and n_f with Equ. 4.9, at optimum output coupling and for strongly over and under-coupled cavities, with $T_{OC} = 90\%$ and 10% , respectively. The output energy saturates below a PRF of ~ 1 kHz, when the population inversion approaches its maximum value n_∞ for the given pump rate. The gain is then strong enough for the cavity to oscillate efficiently even with a high output coupling of 90% , producing the largest pulse energy as the roundtrip losses become negligible compared to the output coupling. At higher PRF, the energy decreases as $1/F$, with the cw optimum output coupling of 40% producing the highest energy. The saturation of energy at low PRF demonstrates the importance of choosing another host with longer upper-state lifetimes such as YAG or YLF for neodymium when pulse energy at low PRF is of greater interest than gain and short pulses at higher repetition rates.

The average output power obtained from $P_{out} = E_{out}F$ is also plotted in Fig. 4.4 (right), illustrating the fast increase in average power with PRF at low repetition rates when the pulse energy is saturated. At high PRF, the average power saturates towards the cw output power, when the spontaneous emission from the limited inversion built between pulses becomes negligible compared to the stimulated emission during the pulse emission. The cw optimum output coupling further provides the highest average output power on a wide range of PRF above 10-20 kHz, which will be the case of most practical uses of a vanadate laser.

Figure 4.5 illustrates the evolution of pulse duration (left) and build-up time (right) with PRF, calculated with Equ. 4.10 and 4.11, respectively. At all PRF, the stronger the output-coupler reflectivity, the faster the pulse will build up, as fewer photons exit at each roundtrip, leaving a larger number to oscillate and be amplified through stimulated emission. A low PRF when the gain is very strong, the pulse build-up and rise time are short for any output coupling, yet the large number of photons will take a longer time to exit an under-coupled cavity. Thus pulses are highly asymmetric with a steep rise and a long tail which determines the extent of

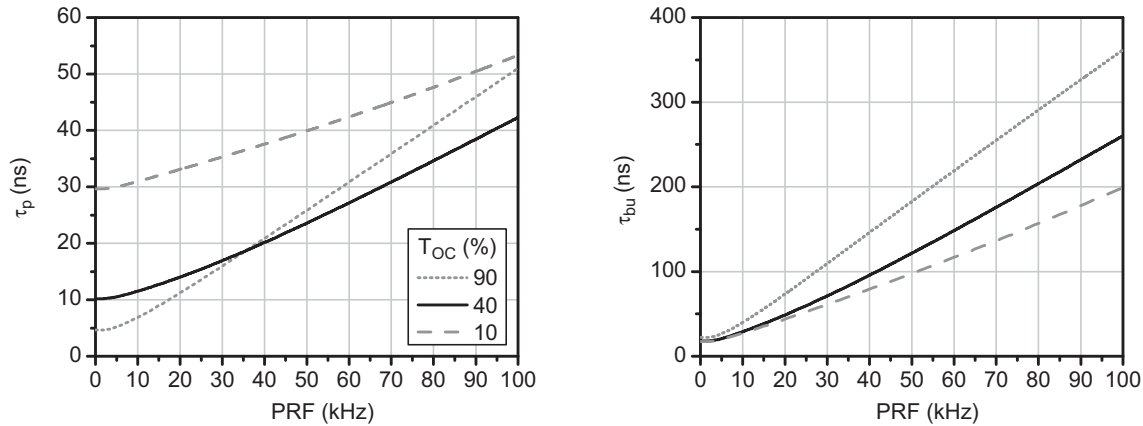


Figure 4.5: Pulse duration (left) and pulse build-up time (right) function of PRF for the cw optimum output coupling and over and under-coupled resonators.

the pulse duration. At higher repetition rates, the pulse duration and build-up time evolve almost linearly with PRF, the cw optimum output coupling providing the shortest pulses at higher PRF. However, when very high frequency operation of $\sim 100 - 300$ kHz is desired, the output coupling should be reduced to lower the laser threshold and allow oscillation with the low inversion available at these repetition rates.

4.1.3 Q-switch technologies

A Q-switch or loss modulator is a device that should provide sufficient losses to prevent any laser oscillation, or hold off the cavity, and then switch to a low-loss state, ideally inducing no loss at all to allow an efficient pulse energy extraction. Thus a Q-switch can be characterized by its maximum and residual losses in its on/off states, switching time, repetition-rate operational range, and more practical considerations such as lifetime, bulkiness, and cost.

Q-switching can be achieved through optomechanical means, with a mirror mounted on a galvanometric resonant scanner or a Porro prism attached to a spinning motor axle, the cavity suffering 100% losses when the mirror is not aligned to the resonator axis, and suddenly oscillating when the mirror or retroreflector passes the mode axis. Such devices are however inherently slow, with repetition rates limited to a few kHz, and suffer from a limited lifetime due to mechanical wear. The continuously moving mirror axis induces a deviation of the beam pointing direction during the pulse emission, resulting in poor beam-pointing stability. The switching time being directly related to the mirror's oscillating frequency, it is usually too slow to be used in conjunction with high gain laser materials such as vanadate. All these reasons contribute to making such technology obsolete in modern lasers. I will thus concentrate on the two major active Q-switching technologies, namely electro-optic (EO) and acousto-optic (AO), which were both implemented in a high-power Q-switched oscillator (see Sect. 4.1.4).

Electro-optic Q-switch

A Q-switch can be designed by exploiting the electro-optic effect in a crystal, where a certain birefringence is generated by applying a voltage along the length or across the section of the crystal, longitudinally or transversally with respect to the optical axis [33]. If a polarized beam enters the crystal orientated at 45° with respect to its axes, it will not be affected if no voltage is applied. However, if the quarter-wave ($V_{\lambda/4}$) or half-wave voltage ($V_{\lambda/2}$) is applied, the two polarizations will respectively undergo a quarter-wave and half-wave retardation. Thus the cell behaves as a quarter or half-wave plate, transforming the incident linear polarization in a circular or a linear polarization rotated by 90° , respectively. Placing such a cell operated from 0 V to $V_{\lambda/2}$ between two crossed polarizers allows for switching the system's transmission from 0% at $V = 0$ to 100% at $V = V_{\lambda/2}$. The cell can also be placed between a polarizer and the cavity's HR end-mirror, and operated between 0 V and $V_{\lambda/4}$. When no voltage is applied, the system behaves as a 100% reflectivity mirror, while when $V = V_{\lambda/4}$ the cell rotates the polarization by 90° in double pass, effectively suppressing the laser light on the second incidence on the polarizer. In order to limit the duration for which a voltage is applied to the cell, thus reducing heating and parasitic thermally-induced birefringence, a quarter-wave plate also orientated at 45° to the polarizer's axis is inserted between the polarizer and the end-mirror. This leads to an inverted behavior of the system, with 100% losses when no voltage is applied and no losses when $V = V_{\lambda/4}$. Such configuration will be implemented in Sect. 4.1.4 to allow for the high repetition-rate operation of the Q-switched oscillator, and in Sect. 4.2.2 for a cavity-dumped Q-switched resonator.

The choice of electro-optic material and cell design is much dependent on parameters such as optical aperture, repetition rate, tolerable residual losses, and optical power. Materials such as KDP or KD*P can be grown in large dimensions and benefit from relatively large electro-optic coefficients, so that when a voltage is applied longitudinally, very large aperture cells can be produced. However their main drawback arises from their hygroscopicity which requires the crystal to be placed in an air-tight cell with AR-coated windows. Thus such cells suffer from insertion losses of $\sim 4\%$, which prevents their use when low losses are critical, such as in a cavity-dumped oscillator. These crystals also suffer from piezo-electric ringing at repetition rates above a few kHz, when an acousto-optic wave is created by the piezo-electric effect, resulting in an uncontrolled birefringence after the voltage has been suppressed.

KTP and RTP benefit from a high electro-optic coefficient, making them very suitable for high repetition-rate operation [104], as the high-voltage switch can achieve faster rise and fall times together with higher repetition rates for lower voltages. However, its damage threshold of 1.8 GW/cm^2 lies well below that of BBO of 20 GW/cm^2 , which can limit its use in high-power small-aperture systems. Furthermore its susceptibility to thermally-induced birefringence often leads to the design of cells containing two crystals rotated by 90° to compensate for the parasitic birefringence of one crystal by the other's.

BBO offers the high optical power handling capabilities necessary to high-power small-aperture intracavity applications, yet its relatively high quarter-wave voltage of $\sim 3 \text{ kV}$ for a 4 mm aperture cell prevents the high-voltage switching electronics to be driven at repetition

rates much higher than 100 kHz. When higher repetition rates are sought, a dual switch can be designed to ease the load on the high-voltage switch. Considering the high intracavity intensities of the systems developed in this work, such a BBO cell was chosen to achieve Q-switching and cavity-dumped Q-switching, where the intracavity intensity reaches much higher levels.

The strength of electro-optic cells resides in their capability of very short rise and fall times of ~ 5 ns and high contrast ratios with high-quality polarizers, minimum and maximum transmissions coming close to 0% and 100% respectively. These unique characteristics make them essential to the realization of pulse-pickers, when a single ps pulse should be extracted from a ~ 100 MHz mode-locked pulse train, to ultrashort Q-switched resonators exhibiting fast build-up times and pulse durations below 1 ns [105], or to high-gain Q-switched oscillators that cannot be held off with the diffraction efficiency available with an acousto-optic Q-switch. However, for many Q-switching applications the longer opening time and lower contrast ratio of an AO Q-switch are sufficient and do not disturb the pulse formation, yet at a cost of ~ 2500 Euros for a complete crystal-RF driver system, as opposed to ~ 6 times more for an EO cell accompanied by its high-voltage power supply and switch. It is for these reasons of costs, bulkiness, and ease of use that AO Q-switches are implemented in the vast majority of Q-switched lasers. An electro-optic switch provided by Bergmann Messgerete Entwicklung KG, Germany [106], will be employed in the following sections for the realization of a Q-switched and a cavity-dumped Q-switched oscillator.

Acousto-optic Q-switch

An acousto-optic Q-switch relies on the diffraction of light on an index grating created by an acoustic wave traveling in an interaction medium, as first predicted by Brillouin in 1922. A piezo-electric transducer deposited on one side of the crystal emits a traveling acoustic wave perpendicularly to the laser beam entering and exiting the crystal by its AR-coated end-facets. The acoustic wave generates a grating of high and low pressures which translates into a grating of high and low indices. Thus a light beam at a wavelength λ_0 and with a diameter ϕ travels through a volume grating of length l and height h defined respectively by the length and the height of the transducer. The transducer is driven by a radio frequency (RF) driver generating a sine wave at a fixed frequency F which results in an acoustic wavelength or grating period $\Lambda = v/F$, where v is the medium's acoustic velocity. Two interaction regimes are possible, depending on the quality factor Q defined as:

$$Q = \frac{2\pi\lambda l}{n\Lambda^2} \quad (4.13)$$

For $Q \ll 1$, the acousto-optic interaction operates in the Raman-Nath regime, where the incident laser beam is incident roughly normal to the acoustic beam and scattered on several symmetric diffraction orders with intensities given by Bessel functions. This is achieved for thin crystals and thus for short acousto-optic interaction lengths when $\lambda l \ll n\Lambda^2$.

When $Q \gg 1$, the AO crystal operates in the Bragg regime. If the laser beam is incident at the Bragg angle θ_B the vast majority of the incident beam is diffracted in a single first order, the others being annihilated by destructive interference. The diffraction angle θ with respect

to the incident beam is then twice the Bragg angle, increasing with shorter grating periods for higher acoustic frequencies and slower materials:

$$\theta = 2\theta_B = \frac{\lambda F}{v} \quad (4.14)$$

Most acousto-optic devices such as modulators and deflectors operate in the Bragg regime, providing a maximum efficiency on the first order which is the beam of interest. However Q-switches and mode-lockers usually operate between the Bragg and Raman-Nath regimes, when a maximum loss on the zero-order is sought and the higher orders are simply waste-beams.

In the Bragg regime the diffraction efficiency is given by:

$$\frac{I_1}{I_0} = \sin^2 \left[\frac{\pi}{2} \sqrt{\frac{2}{\lambda^2} \frac{l}{h} M_2 P_{ac}} \right] \quad (4.15)$$

where M_2 is the acousto-optic figure of merit of the crystal and P_{ac} the RF power applied to the transducer. M_2 depends on the material and interaction mode, either longitudinal (isotropic) or shear-wave (anisotropic), where the acoustic wave fronts are not normal to the direction of propagation of the acoustic wave. Longitudinal mode generally results in a higher acoustic velocity but lower figure of merit than shear wave, so that the former is used for high-speed modulators, while the second for slower high-efficiency systems with large diffraction angles. Fused silica or crystalline-quartz is the fastest material in longitudinal mode with $v = 5960$ m/s but with a rather small $M_2 = 1.5 \times 10^{-15}$ S³/kg, while TeO₂ in shear-wave mode is the most efficient material with $M_2 = 1200 \times 10^{-15}$ S³/kg but also much slower with $v = 620$ m/s, and suffering from a low blooming and damage threshold limiting the CW power density to 5 W/mm² [107].

The modulator's risetime or the Q-switch's opening time τ_R is determined by the time necessary for the incoming acoustic wave to travel through the laser beam:

$$\tau_R = \beta \frac{\phi}{v} \quad \text{with } \beta = 0.66 \text{ for a TEM}_{00} \text{ beam} \quad (4.16)$$

so that fast materials such as SiO₂ and tight focusing down to 50 μ m diameter are employed to achieve a fast modulation. For fused silica and a gaussian beam, $\tau_R = 110$ ns/mm, so that a risetime of 5 ns is reached for the above-mentioned focusing conditions. However such strong focusing results in a limited diffraction efficiency of $\sim 60\%$ and beam ellipticity.

For most Q-switching applications of polarized 1 μ m lasers, a fused-silica cell driven at 27, 44, or even 66 MHz provides up to 90 % diffraction efficiency with opening times in the 30–100 ns range, which is fast enough to fully open during the pulse build-up time. Very high gain cavities may demand two Q-switches to hold off emission between pulses, and very short cavities can suffer from the long opening time of an acousto-optic system, making an electro-optic cell a more adequate solution.

A water-cooled 66 MHz, 2 mm aperture fused-silica Q-switch driven by up to 70 W of RF power, and providing 95% diffraction efficiency was implemented for the realization of a high-power nanosecond system, as described in the following section.

4.1.4 Q-switched oscillator

Building on the performance of the symmetric cw resonator presented in Sect. 3.2.2, two Q-switched oscillators were designed with an electro-optic and an acousto-optic modulator. Both presented similar behaviors and produced very comparable performance, so that only the electro-optic Q-switch design is presented here, since it will be used for cavity-dumped Q-switched operation, as described in Sect. 4.2. Of course the acousto-optic solution would be much preferred in the design of a product for its much lower cost and bulkiness, and its ability to operate at high PRFs > 100 kHz.

Resonator design

The Q-switched resonators were based on the cw resonator described in Fig. 3.13 (left). The pump source, pump optics, crystal, and resonator mirrors are kept identical, with the exception of the Q-switch inserted in the arm of the cavity opposite the output coupler. Both optical arm lengths are left unchanged at 300 mm, the acousto-optic Q-switch being simply inserted in the cavity close to the HR end-mirror. Figure 4.6 (left) illustrates the electro-optically Q-switched resonator setup, in which the arm containing the Q-switch between M_3 and HR is folded with a thin-film polarizer (TFP). As the crystal's c axis is orientated vertically, the laser mode coming from the crystal is s -polarized and totally reflected on the TFP designed for $R_s > 99.9\%$ and $T_p > 97\%$ at an incidence angle of 56° . Between pulses, no high voltage is applied to the BBO cell, so that any s -polarized light reflected on the TFP is rotated by 90° in double pass through the quarter-wave plate orientated with its axes at 45° to the incident polarization. Thus this reflected p -polarized light is almost fully transmitted through the TFP, providing high losses which effectively prevent laser oscillation.

When a pulse is to be emitted, the cavity is closed by applying the quarter-wave voltage of ~ 4 kV to the cell, thanks to a 5 ns risetime HV switch. The s -polarized light reflected on the TFP undergoes two quarter-wave retardations in double pass, resulting in no net rotation of polarization, and consequently full reflection on the TFP back to the laser crystal. The high voltage is maintained for a duration of $0.5\text{--}1$ μs which is sufficient for a pulse to build up and totally exit the cavity for repetition rates up to 100 kHz. The output pulse exits the cavity through output coupler M_1 , while only very small leakage is observed through the TFP, which results from the imperfect net full wavelength retardation when double-passing the quarter-wave plate and the BBO cell. This effect can be attributed to residual thermally-induced birefringence in the BBO cell, which increases with repetition rate and duty cycle.

Performance

The performance of the Q-switched oscillator was evaluated by inserting a holographic beam sampler (HBS) in the output beam, allowing the simultaneous measurement of output power with a power meter, beam profile with a CMOS camera, beam quality with a Coherent ModeMaster, and pulse duration, pulse build-up time, and noise with a 200 ps risetime photodiode coupled to a 1 GHz bandwidth oscilloscope.

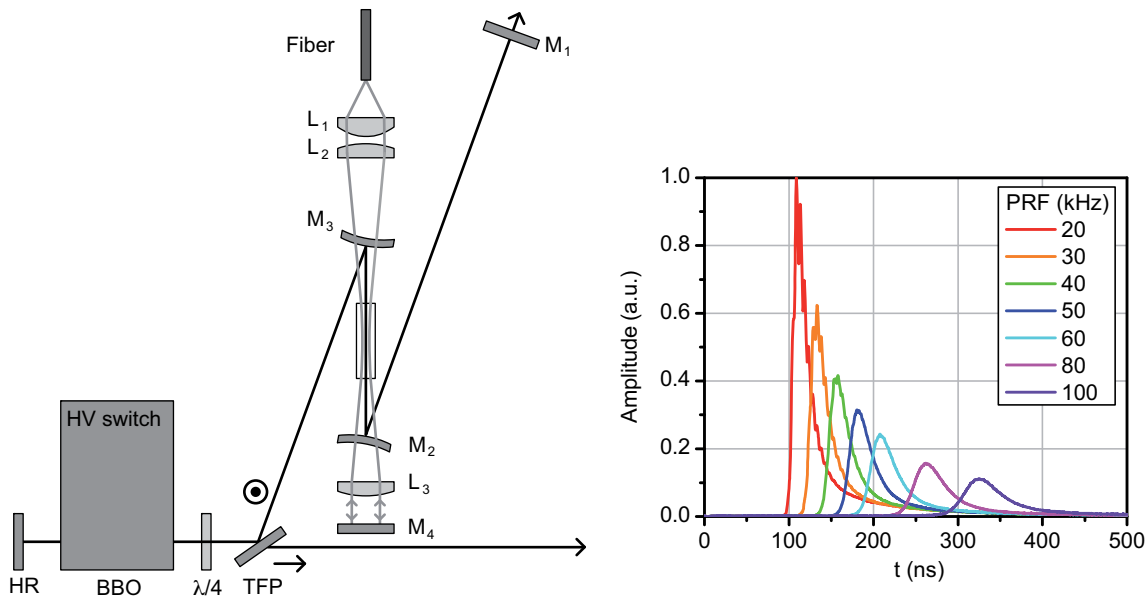


Figure 4.6: Electro-optically Q-switched resonator scheme with output coupler M_1 , the Q-switch being formed by the BBO cell driven by a high-voltage switch, a quarter-wave plate, and a thin-film polarizer (left). Q-switch output pulses monitored with a 1 GHz bandwidth oscilloscope and a photodiode, starting from a Q-switch trigger signal at $t = 0$ (right).

Figure 4.6 (right) illustrates the output pulses when the cavity was operated with a 40% transmission output coupler, previously chosen for maximum output power in cw operation. The time origin is taken from the trigger signal sent to the high-voltage switch, so that the absolute optical opening time of the electro-optic Q-switch is shifted by the signal transmission and processing time. Thus the measured pulse build-up time contains a slight offset from the true time taken for the pulse to build up from the opening of the Q-switch. As predicted from the simulations in Fig. 4.3 (right), the pulse build-up time and duration increases with repetition rate, while the peak power drops quicker than the pulse energy because of the pulse lengthening. The pulse evolves from a strongly asymmetric shape with a fast rise and a long tail at low PRF, to a more symmetric shape with almost equal rise and fall times at high repetition rates. This behavior can be explained by the high gain at low PRF which allows a fast rise of the intracavity photons to a large number, which consequently take a comparatively longer time to be emptied out of the cavity through the output coupler and the roundtrip losses. Inversely, at high PRF the lower gain leads to a longer build up of the intracavity photons, reaching a relatively lower level, thus requiring comparatively less time to be emptied from the resonator.

The amplitude modulations on the Q-switch envelope with a frequency corresponding to the resonator mode spacing are much more visible at low PRF, with a modulation depth increasing with output coupler reflectivity. This effect can be attributed to longitudinal mode competition and most likely to some mode coupling. It has been shown that the emission spectrum and number of oscillating longitudinal modes increase at low PRF in solid-state Q-switched lasers

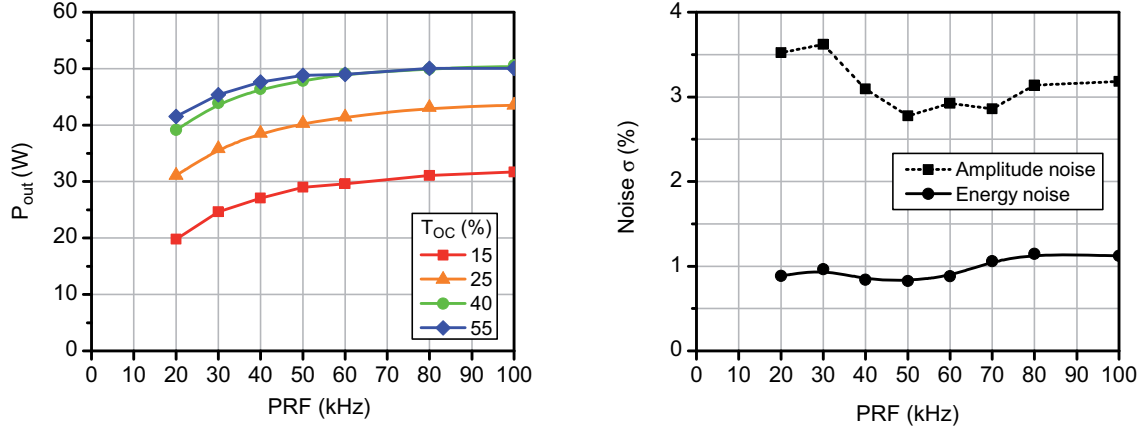


Figure 4.7: Average output power function of repetition-rate for various output couplers (left). Amplitude and energy noise function of PRF for $T_{OC} = 40\%$ (right).

[108], so that the effect of simple mode beating should be more pronounced at high repetition rates when less modes oscillate, the larger number of modes at low PRF producing a smoother envelope on the contrary. Thus it seems that non-linear effects such as self-phase modulation (SPM) introduce some mode coupling which results in a modulation of the Q-switch envelope. This effect is then more pronounced at low PRF or with a high output-coupler reflectivity, which both induce higher intracavity peak powers.

Figure 4.7 (left) illustrates the evolution of average output power with repetition rate for various output couplers. The optimum output coupler chosen in cw operation also provides the highest average power in pulsed mode, reaching 50 W at high PRF. Although the average output power should theoretically approach the cw power at high PRF, the additional losses of the electro-optic Q-switch and the residual thermally-induced birefringence result in some loss of average output power compared to the cw oscillator. It is apparent that the average power is maintained above 90% of its maximum value if the PRF is kept above 30 kHz, corresponding to the optimal operating range of most vanadate lasers. The beam remained diffraction-limited throughout the operating repetition-rate range with $M^2 = 1.1$.

Figure 4.7 (right) depicts the evolution of pulse amplitude and energy noise with repetition rate. The former is measured on the pulse peak, while the latter is determined from the pulse area calculated by the oscilloscope, corresponding to the pulse energy. Both exhibit a slight increase at high PRF when oscillation begins closer to threshold, yet the pulse amplitude noise suffers from a strong rise at low PRF, resulting from the amplitude modulations induced by longitudinal mode coupling. The amplitude noise being very sensitive to any modulation of the envelope, it amounts to an RMS value of $\sigma \sim 3\%$, while the pulse energy noise is limited to $\sigma \sim 1\%$.

Figure 4.8 illustrates the evolution of pulse duration (left) and pulse build-up time (right) with repetition-rate for various output coupler transmissions. Both are in good agreement with the simulations illustrated in Fig. 4.5, if a Q-switch opening time lag of ~ 60 ns is assumed. The optimum output coupling of 40–50% offers the highest average output power while producing

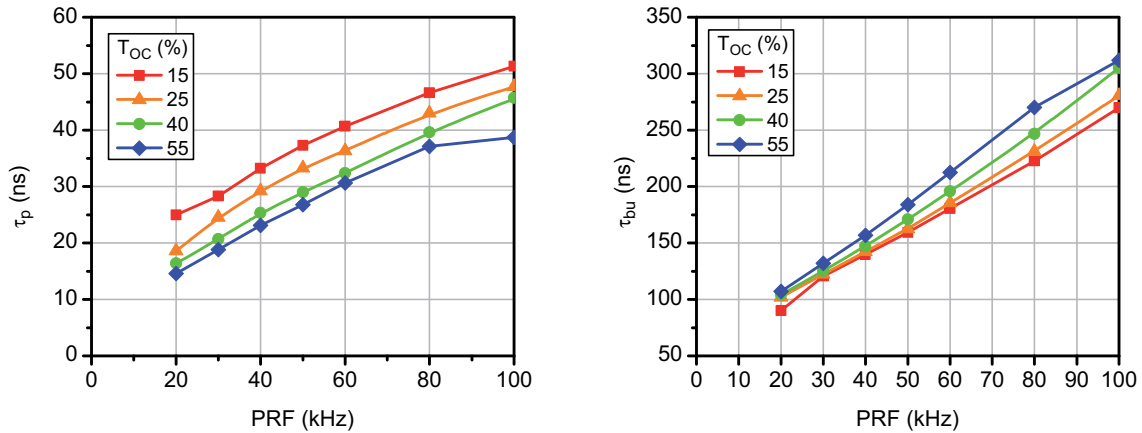


Figure 4.8: Pulse duration function of PRF (left) and pulse build-up time (right).

short pulses, both contributing to reaching high peak powers. The measured pulse build-up time remaining above 100 ns at PRFs higher than 20 kHz, an acousto-optic Q-switch with an opening time of ~ 90 ns for a mode diameter of $800 \mu\text{m}$ provides a sufficiently fast opening for the loss-free emission of the laser pulse and the avoidance of double pulses. Therefore very similar performance was achieved with acousto-optic Q-switching, in a much simpler and cost-effective system.

The electro-optic Q-switched oscillator will however be operated in a cavity-dumped mode to limit the fast decrease of peak power at high repetition-rates by keeping a constantly low pulse duration at all PRF, as described in the following section.

4.2 Cavity-dumped Q-switching

Since the limitations of Q-switched resonators in terms of pulse lengthening and peak-power drop at high repetition rates have been exposed in the previous section, the technique of cavity-dumped Q-switching is presented and implemented in the following section. The principle of operation and its expected behavior are first described, followed by the realization of a high-power oscillator derived from that described in Sect. 4.1.4. Finally its stability is investigated before applying frequency doubling to achieve high peak-power green light.

4.2.1 Principle

Cavity-dumped Q-switching was proposed as early as 1963 by A. Vuylsteke under the denomination of pulsed transmission mode (PTM) [109]. Systems relying on an electro-optic switch were first demonstrated [110, 111, 112], followed by resonators containing an acousto-optic modulator as the switching element [113, 114, 115]. Further theoretical calculations were proposed by R. B. Chesler and D. Maydan [116].

Figure 4.9 (left) illustrates a basic cavity-dumped Q-switched (CDQS) two-mirror resonator scheme. Instead of building the resonator between an HR mirror and an output coupler mirror

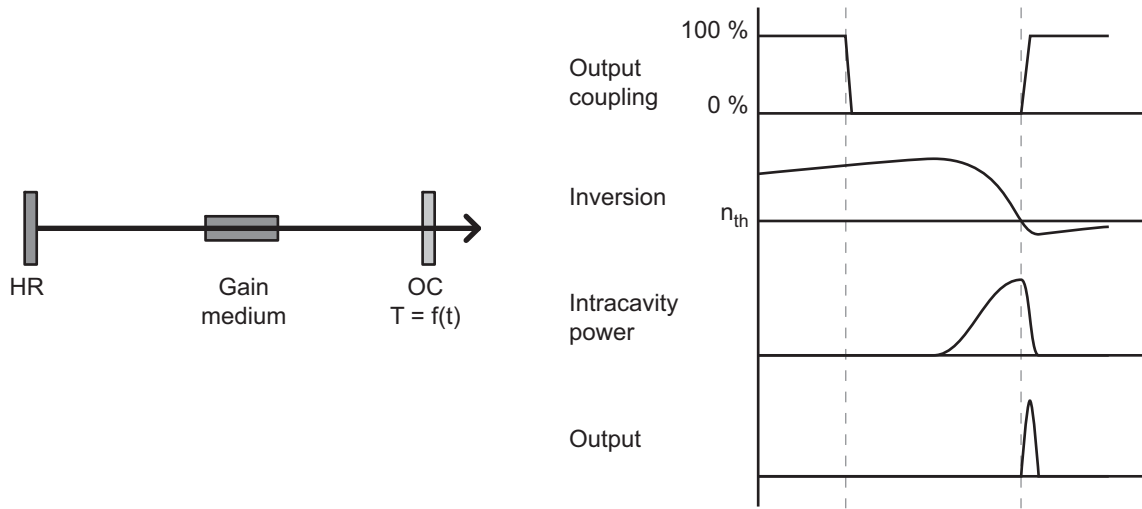


Figure 4.9: Cavity-dumped Q-switched oscillator principle scheme (left). Evolution of the cavity parameters when the output coupling is switched from 100 to 0% to allow a pulse formation in a closed cavity, followed by a full opening of the cavity to release the intracavity photons and form the output pulse (right).

of fixed reflectivity, a device providing time-varying transmission is employed to generate the output coupling. Figure 4.9 (right) describes the evolution of the cavity and output parameters as a function of time during inversion build-up, intracavity photon flux amplification, and output pulse release. Between pulses, the cavity is held under threshold just like any other Q-switched resonator by switching the output coupling to 100%, providing sufficient losses to prevent laser oscillation. After one pulse repetition period, the output coupler switches to full reflectivity, effectively closing the cavity between equivalent HR mirrors. The resonator is then equivalent to a high-Q cavity with losses determined only by the intracavity elements, resulting in a low threshold inversion n_{th} . The photon flux builds up quicker and reaches a higher level than in a classic Q-switched resonator containing a fixed-reflectivity output coupler. Once the photon flux has reached its peak, corresponding to a depleted gain just sufficient to compensate the low intracavity losses, the output coupler transmission is switched back to 100%. During that previous period no light was exiting the resonator since the output coupler exhibited full reflectivity, yet now the cavity is fully open. All intracavity photons can then exit within one roundtrip, producing a short giant pulse. Ideally the output coupler should switch instantaneously to produce the shortest output pulse duration. In practice the transmission switching period can be approximated by a linear ramp with rounded start and end points [104]. For a ramp duration comparable to the cavity roundtrip time, the output pulse is essentially triangular, after which no intracavity photons remain to produce a pulse tail like in Q-switched lasers.

Thus if an OC of sufficiently fast switching time is employed, the output pulse duration is solely defined by the cavity roundtrip time, making it insensitive to gain and consequently to PRF and pump level. For a given pump power, when the PRF is increased, the inversion available before each pulse emission is reduced, but only the intracavity pulse build-up time

rises and not the output pulse duration. The pulse peak power drops with increasing PRF only due to the reduced pulse energy, and not with the combined effects of lower pulse energy and longer pulse duration as in Q-switched lasers. Conversely, for a given pump power the pump spot area can be increased to minimize thermo-optical effects, effectively reducing the gain but not affecting the pulse duration.

Electro-optic modulators provide switching times down to ~ 5 ns with high contrast ratios, assuring low losses during the oscillation period and fast and effective dumping of the intracavity photons. Acousto-optic modulators can also provide fast switching times, yet at the cost of diffraction efficiency and beam ellipticity, resulting in a limited contrast ratio which will not allow the full extraction of the intracavity photons within one roundtrip. Thus the electro-optic switch contained in the Q-switch resonator presented in Sect. 4.1.4 will be implemented for the realization of a high-power CDQS oscillator.

4.2.2 CDQS oscillator

Resonator design

Cavity-dumped operation of the Q-switched oscillator presented in Fig. 4.6 (left) is achieved by replacing the 40% transmission output coupler M_1 by a HR mirror. Output coupling is then achieved with the TFP, half-wave plate, BBO cell, and HR combination previously described. During the inversion build-up period, no voltage is applied and any s -polarized laser light is rotated by 90° in a double-pass through the quarter-wave plate, effectively providing close to 100% losses. When the cavity is closed for laser oscillation by applying the quarter-wave voltage to the BBO cell, the cavity switches to low losses and a large intracavity photon number can quickly build up. During this period, the main sources of intracavity losses are thermally-induced aberrations in the laser crystal just as in a cw oscillator, and residual thermally-induced birefringence in the quarter-wave plate and the BBO crystal. These losses only amount to a few percent and would not affect significantly the output power of a cw or a Q-switched laser since they are much smaller than the output-coupler transmission. However, the much higher intracavity power attained in a high-Q resonator such as a CDQS laser during the photon build-up oscillation period leads to small intracavity losses strongly affecting the output power. Thus reducing such losses is critical to the efficient operation of a CDQS laser. For this purpose, an air-spaced zero-order quarter-wave plate is preferred over multiple-order plates for its low sensitivity to temperature variations, and a BBO cell equipped with high-performance AR-coated windows is selected .

The optical length of the resonator is similar to that of the cw resonator with $L = 70$ cm, resulting in a roundtrip period of ~ 5 ns. Consequently the output pulse duration will not be limited by the electro-optic modulator switching time of 5 ns.

Performance

Figure 4.10 (left) illustrates intracavity and output pulse traces during the photon build-up period followed by the dumping event. Once the resonator starts oscillating, the photon flux

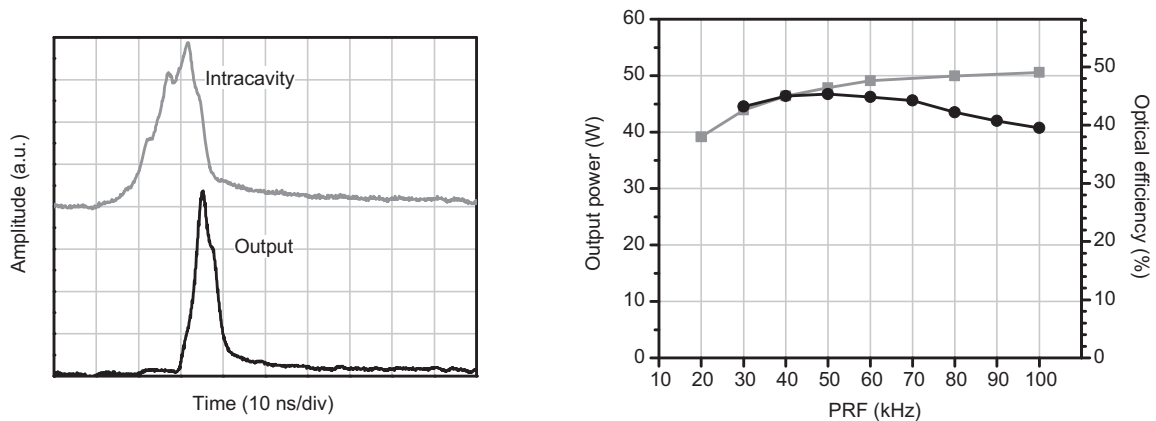


Figure 4.10: Intracavity and output pulses (left). Average output power and optical efficiency (black) compared to that of the Q-switched oscillator (grey) (right).

quickly rises to its peak, the moment when the output coupler begins its 5 ns ramp from 0 to 100% transmission, equivalent to a roundtrip time. Thus within one roundtrip duration, the output coupler is fully transmissive and the output power reaches its peak. From there on the fully open cavity empties within one more roundtrip, producing an essentially symmetric triangular shape pulse with rise and fall times equal to one roundtrip duration and consequently an equal FWHM pulse length. The tail visible on the intracavity and output pulses results from thermally-induced birefringence in the BBO cell caused by the heating of the crystal operated with a high-voltage electric field at high repetition-rate, and to a lesser extent to residual absorption of the high-power laser mode.

Figure 4.10 (right) presents the evolution of output power with repetition rate, compared to the performance of the same oscillator operated in Q-switched mode with a 40% transmission output coupler. The output power rises up to 47 W at a PRF of 50 KHz, closely following that of the Q-switched laser, thanks to a decreasing inversion and smaller losses through spontaneous emission between pulses. From this point on, the output power steadily decreases down to 40 W at 100 kHz. This power loss results from the decreasing gain at high repetition rates, inducing longer intracavity pulse build-up times and therefore a larger number of roundtrips before the dumping event is triggered. Consequently the high intracavity power strongly suffers from intracavity losses, so that maximum care should be taken in selecting low-loss high damage-threshold mirrors and optical components. Some performance variations were observed when using various components, yet the best performance was achieved with a 4 mm aperture sealed BBO cell from Cleveland Crystals inducing transmission losses lower than 2%, an air-spaced zero-order quarter-wave plate from Bernhard-Halle, and a TFP from Layertec. The beam quality measured with a Coherent ModeMaster remained better than $M^2 = 1.15$ throughout the PRF range.

Figure 4.11 illustrates the evolution of output pulse duration (left) and oscillating time (right) with repetition rate. For each repetition rate, the time for which a high voltage is applied to the BBO crystal corresponding to the time the cavity remains closed is adjusted to

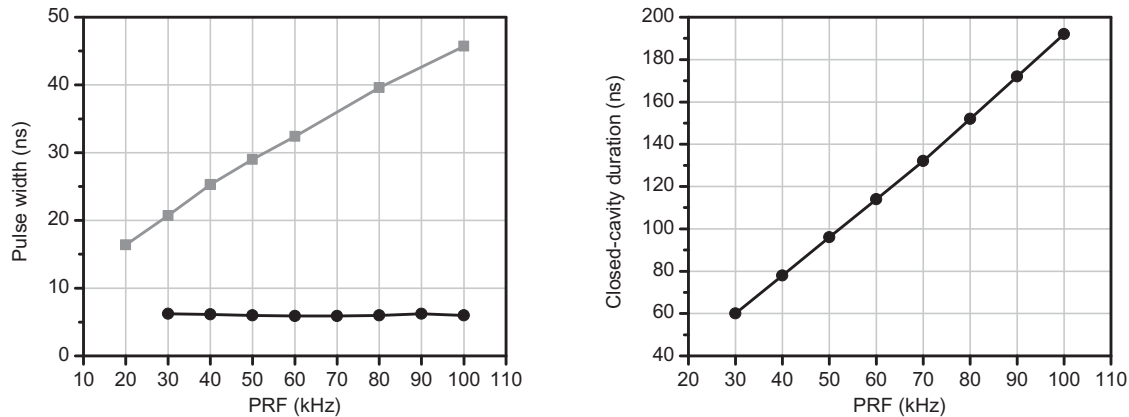


Figure 4.11: Pulse duration function of PRF (left) for the CDQS oscillator (black) and the Q-switched laser (grey). Cavity-closed time (right).

dump the intracavity photons when they have reached their peak. Thus a maximum power is extracted in a stable pulse train. Just as the pulse build-up time of a Q-switched laser almost linearly increases with PRF, the cavity-closed time of the CDQS oscillator increases from 60 ns at 30 kHz to 195 ns at 100 kHz, further explaining the higher losses suffered by the laser mode at high PRF. Although the intracavity pulse takes a longer time to build up at high PRF, owing to the lower gain, the dumped output pulse duration remains unchanged at 6.0 ± 0.2 ns on the whole frequency range.

Figure 4.12 (left) provides a comparison of the pulse amplitude and energy noises, both measured with a fast photodiode coupled to a 1 GHz bandwidth oscilloscope. Similarly to the Q-switched laser, the amplitude noise is significantly higher than that of the pulse energy, as the longitudinal mode competition causes a modulation of the Q-switch envelope which introduces noise on the intracavity pulse peak amplitude and consequently on the dumped pulse amplitude and to a lesser extent its energy. Both noise figures are however ~ 2 times larger than for the Q-switch operation illustrated in Fig. 4.7 (right). This larger noise can be explained by the forced character of the pulse emission in CDQS operation, compared to a self-regulating interplay of gain, build-up time, and pulse energy in Q-switched mode. This specific source of noise and ultimately of instability is developed in the following section.

Figure 4.12 (right) illustrates the decline of pulse peak power P_{peak} with increasing PRF. For a given average power P , a Q-switch laser suffers from a linear increase of pulse duration with PRF added to the natural inverse evolution of pulse energy E . In a CDQS oscillator with constant pulse duration, the peak power remains proportional to pulse energy:

$$P_{peak} = \frac{E}{\tau_p} = \frac{P}{\tau_p F} \quad (4.17)$$

so that much higher peak powers are available at high PRF in CDQS operation. Thus 250 kW and 68 kW are achieved in CDQS respectively at 30 kHz and 100 kHz, to be compared to 70 kW and 11 kW for the Q-switched oscillator.

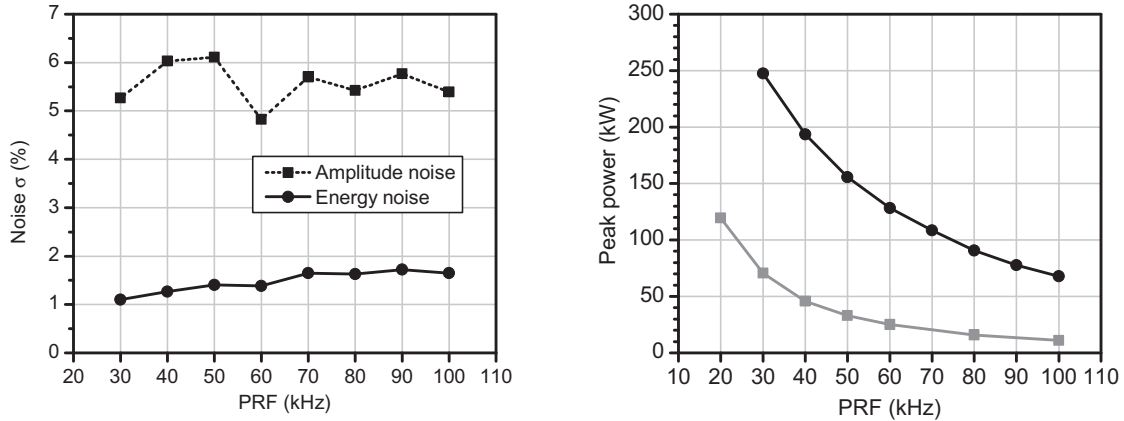


Figure 4.12: Amplitude and energy noise (left) and peak power function of PRF (black) compared to that of the Q-switch oscillator (grey) (right).

4.2.3 Stability

The closed-cavity time illustrated in Fig. 4.11 (right) is manually adjusted to achieve the highest output power at each repetition rate, also providing a stable train of even output pulses. This optimum duration corresponds to triggering the dumping event exactly when the intracavity pulse has reached its peak, as seen in Fig. 4.10 (left). Since the intracavity pulse risetime of $\sim 10\text{--}20$ ns is too short for a monitoring photodiode to detect the pulse peak or a certain threshold level and trigger the dumping event, the switching of the HV applied to the BBO cell must happen after a fixed delay following the closing of the cavity, regardless of the possible jitter or drift of the intracavity pulse build-up time. Once the optimum closed-cavity time has been experimentally determined for a set of repetition rates, it can be interpolated for any repetition rate in-between.

However if some pump-power instability or degradation arises, the gain is reduced, leading to a longer intracavity pulse build-up time. If the closed-cavity time is not readjusted, the opening of the cavity will be triggered before the intracavity pulse has reached its peak. This is equivalent to opening the cavity before the optimum duration determined for each PRF in the normal pump and loss conditions. Figure 4.13 illustrates the behavior of the intracavity pulses (left) and of the CDQS output pulses (right) when a resonator operated at 50 kHz and 76 W pump power is opened after 184 ns instead of the optimum 190 ns determined at this specific PRF and pump power. The intracavity and output pulses switch to a bistable regime, with a low and a high-amplitude intracavity pulse, producing respectively a low and large-amplitude output pulse. On the contrary, when the closed-cavity time is increased above the optimum value, the intracavity and output pulses exhibit a stable behavior, with a decreasing output energy with longer delays.

These three operating regimes were simulated on a sequence of several pulses to illustrate the transitory period quickly leading to a stable or bistable operation. The rate equations introduced in Sect. 4.1 are used for incrementally calculating the simultaneous build-up of the intracavity

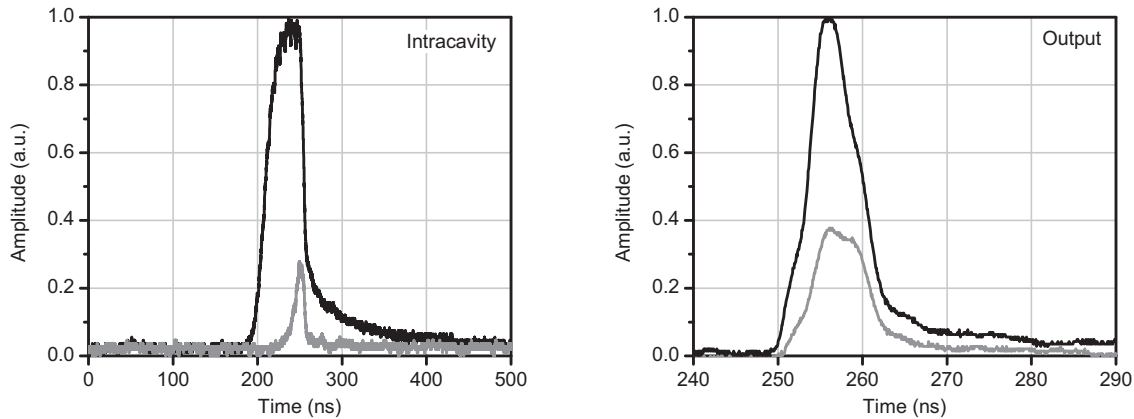


Figure 4.13: Bistable behavior of the intracavity Q-switched pulses (left) and of the cavity-dumped output pulses (right) when the cavity is dumped before the intracavity power has reached its peak.

photons and the inversion depletion. The dumping event is considered to be instantaneous so that all intracavity photons are emptied simultaneously without taking into account the Pockels cell opening time nor the gain depletion in the final roundtrip. This assumption is over-simplistic for accurately simulating the output power and pulse duration of the CDQS system, since the roundtrip and Pockels cell opening times are only a few times shorter than the intracavity pulse rise time. Yet the final roundtrip shouldn't have a significant effect in terms of intracavity photons amplification and inversion depletion since the low-loss cavity induces a low gain at threshold, so that the inversion is already much depleted when the intracavity pulse peak is attained. Nevertheless this simple model is sufficient to simulate the formation and the behavior of the bistable regime.

Figure 4.14 illustrates the evolution of inversion, intracavity photons, and output pulses simulated by taking the same parameters as for the Q-switched oscillator in Sect. 4.1.2, only the output coupling being reduced to 0% during the closed-cavity time T_{ON} . The optimum oscillation time $T_{ON} = 107$ ns at 50 kHz is in good agreement to the 96 ns determined experimentally on Fig. 4.11 (right).

When the cavity is dumped at the intracavity pulse peak (middle column), the inversion, intracavity energy, and consequently output pulses follow a stable pattern. The inversion remaining at the instant of dumping corresponds to a very low threshold inversion n_{th} , a consequence of the low losses during the closed-cavity period. Thus the pumping process starts from this low level close to 0 up to a constant inversion available for pulse build-up which is solely defined by the length of the pumping period. Since the gain available before each pulse creation is constant, the intracavity pulse build-up time is also constant, and the dumping event is then regularly triggered at the intracavity pulse peak.

If the cavity is dumped later than the optimum ($T_{ON} = 120$ ns in the right column), the intracavity photons are left longer to oscillate after the pulse peak, effectively sweeping the remaining inversion. Thus the pumping process starts from an empty population after each

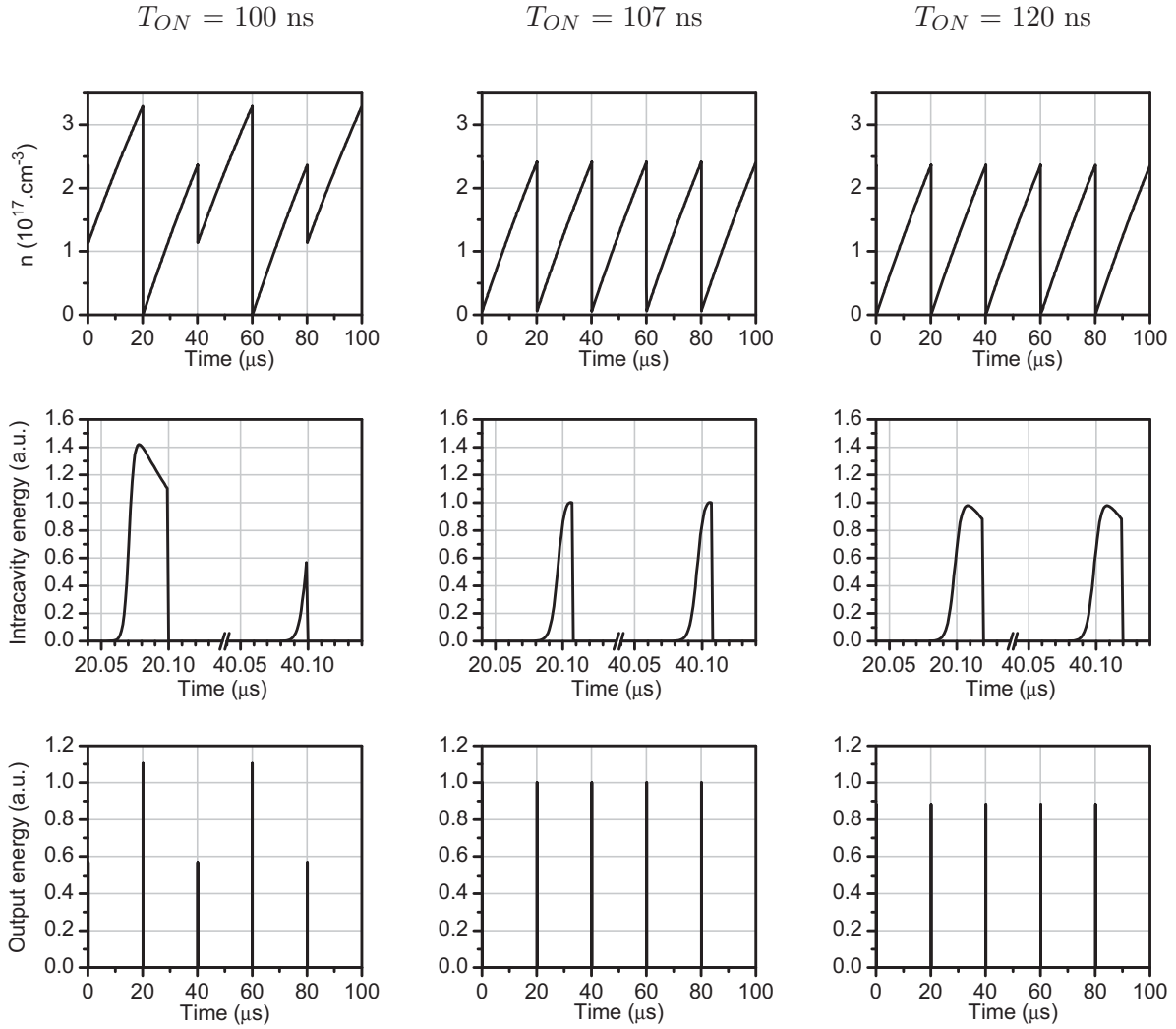


Figure 4.14: Inversion, intracavity and output energy, both normalized to their level for an optimum closed-cavity time T_{ON} of 107 ns. Early dumping (left) with a bistable behavior, optimum dumping (center) with a stable pulse train and optimum performance, and late dumping (right) with stable operation and reduced output energy illustrate the different possible operating regimes of a CDQS oscillator.

dumping event, leading to a constant build-up time and therefore to the dumping of the cavity at a reproducible level of intracavity photons. The output pulses are even, although with a lower energy than at optimum T_{ON} .

The bistable behavior resulting from an early dumping is illustrated for $T_{ON} = 100$ ns (left column). It can be understood as the following sequence of pulses. Considering a stable train of even intracavity and output pulses when the cavity is dumped at the peak of the intracavity pulse, the oscillating-cavity duration is suddenly shortened. Thus the following pulse is dumped before reaching its peak, producing a lower-amplitude output pulse and leaving a higher residual inversion than after each pulse in stable operation, since the intracavity power has been dumped before being able to sweep the remaining gain. Therefore the following pulse builds up faster

thanks to the larger available gain, and is consequently dumped close to or after it has reached its peak, producing a large-amplitude output pulse and effectively sweeping the gain in the last roundtrip. Thus the following pulse builds up from an empty population and is dumped before it has reached its peak again. A bistable regime of high and low-amplitude pulses is quickly established, with a difference in amplitudes increasing with the time shift from the optimum dumping moment.

Considering the relatively high susceptibility of the CDQS system to bistability, such system will be favorably operated at a T_{ON} slightly longer than the optimum value, at the cost of a moderate output pulse energy reduction, yet with a stable long-term operation tolerating moderate shifts in gain and losses.

4.2.4 Second harmonic generation

Harmonic generation is among the applications that benefit the most from high peak-power pulses, so SHG is applied to the CDQS oscillator's output beam to take advantage of its constantly short pulses. The same 20 mm long NCPM LBO crystal as described in Sect. 3.4.3 for an intracavity-doubled cw resonator is used for single-pass extra-cavity doubling. The oscillator's output is continuously attenuated by a half-wave plate followed by two TFPs to allow for the measurement of conversion efficiency function of average power at a given PRF. It is then focused in the center of the crystal for maximum conversion efficiency. Although the optimum focusing determined for this crystal in Sect. 3.4.1 is $w = 27 \mu\text{m}$, the damage threshold of AR coatings is easily exceeded with the high peak powers available. The exit facet of the crystal is always the one subject to damage, owing to the lower damage threshold for the green than for the fundamental radiation. Even with a waist $w = 150 \mu\text{m}$ and a peak power of 250 kW at 30 kHz, the IR peak power density in the center of the gaussian beam amounts to $700 \text{ MW}/\text{cm}^2$, twice the average peak power density calculated over the diameter at $1/e^2$. This power exceeds the $500 \text{ MW}/\text{cm}^2$ on 10 ns damage threshold often given for such AR coatings, yet it can only be used as a guideline since many parameters such as conversion efficiency to the green, converted beam waist and divergence strongly influence the effective power density on the exit surface. Thus for a waist $w = 125 \mu\text{m}$, damage occurred already at 50 kHz, while for a waist $w = 150 \mu\text{m}$, damage occurred just below 30 kHz, so that operating the system at such PRF will not be considered safe for reliable long-term operation. Knowing the desired PRF range of operation, the optimum focusing can be determined so that the damage threshold is not reached at the lowest PRF, yet it shouldn't be taken lower than necessary for the final application. This would result in a larger beam inevitably limiting the conversion efficiency at high repetition rates. Another solution is to reduce the pump power at lower repetition rates to effectively limit the pulse energy and peak power, permitting low frequency operation while maintaining an efficient conversion at high PRF.

Figure 4.15 (left) illustrates the progression of green power and SHG efficiency with average fundamental power for a PRF of 50 kHz and $w = 150 \mu\text{m}$. For a maximum IR power of 45 W, 30 W of green are generated, corresponding to 67 % SHG efficiency. The green power quickly evolves to an almost linear progression as the conversion efficiency tends to saturate. At low

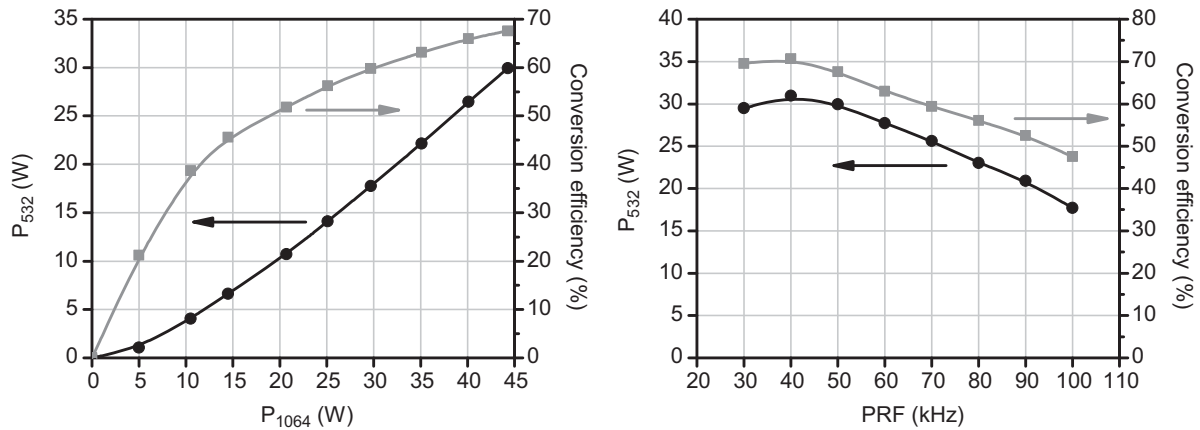


Figure 4.15: Second harmonic power and doubling efficiency function of fundamental power at 50 kHz PRF (left) and function of PRF at full power (right).

conversion efficiencies where the green power follows a quadratic evolution, the green beam waist is $\sqrt{2}$ smaller than the IR beam, while the pulses are also shortened by the same factor. However, the saturation of SHG results in the waist sizes and pulse durations not to differ by such a large factor. Thus, at 45 W IR and 50 kHz, the pulse duration is shortened only from 6.2 ns down to 5.5 ns.

Figure 4.15 (right) shows the evolution of green power and SHG efficiency at full power for repetition rates between 30 and 100 kHz. The drop in conversion at high PRF is a combined effect of the reduction of pulse energy caused by the larger number of pulses and by the reduced average power. The conversion efficiency is almost constant from 30 to 50 kHz as a result of the saturation of the conversion process, with a maximum conversion of 71% and output power of 31 W obtained at 40 kHz. Considering the ~ 6 times larger waist than that determined in Sect. 3.4.1 for a gaussian beam, the same high conversion efficiency could easily be achieved at high PRF with a tighter focusing, provided that operation at lower frequencies is forbidden to avoid facet damage.

4.3 Comparison

Comparing the two nanosecond pulse sources presented in this chapter, namely a Q-switched resonator and a cavity-dumped Q-switched oscillator requires not only to look at their sheer performance numbers, but also at other practical parameters which will determine whether or not a technology is mature enough to be taken out of the lab and developed into a product.

Average power

Figure 4.10 (right) illustrates the evolution of average power and optical efficiency with PRF for the two lasers. Optical-to-optical efficiency is $> 40\%$ for both systems in the 30–100 kHz range, with a drop in optical efficiency from 50 to 100 kHz for the CDQS oscillator caused by

the increasing number of roundtrips necessary for pulse build-up. However this slight drop in output power shouldn't be a determining factor for choosing one system or the other.

Pulse duration

Figure 4.11 (left) gives a direct comparison of pulse duration. The QS system produces pulses increasing almost linearly in duration from 16 ns at 20 kHz to 45 ns at 100 kHz, while the CDQS oscillator's pulses remain constantly at 6 ns, almost 3 to 8 times shorter than the QS pulses across the PRF range.

Peak power

The difference in peak power between the two systems is a direct consequence of the similar average powers and the large factor in pulse duration. Figure 4.12 (right) shows that the CDQS resonator produces from 250 kW down to 70 kW at 100 kHz, the same peak power as the QS system at 30 kHz. Thus the CDQS laser will permit the same efficient harmonic generation at high PRF as the QS oscillator at low frequencies.

Noise

Figures 4.7 (right) and 4.12 (left) producing the noise figures for the QS and the CDQS systems respectively, give an advantage to the QS system with an pulse-to-pulse energy noise $\sigma \approx 1\%$ compared to $\sigma \approx 1.5\%$ for the CDQS oscillator. Both resonators see their noise increase with PRF as less gain is available for pulse build up, yet the noise figures should be sufficiently low for most industrial applications for not making it a factor of decision between the two systems. Pulse envelope modulation resulting from longitudinal mode beating induces a stronger noise on the pulse amplitude for both systems, although the energy noise should be a more relevant figure in most cases.

Stability and reliability

A Q-switched oscillator produces self-stabilizing pulses provided that there is enough gain to produce a pulse at every period. The time jitter between the triggering of the Q-switch and the emission of the pulse has no effect on the pulse energy itself outside of the pulse-to-pulse energy noise. The CDQS oscillator on the contrary requires a precise definition of the cavity-closed time for each repetition rate and pump power. An early dumping will push the resonator in a bistable behavior, so that a certain margin should be kept by triggering the dumping always a little later than optimal, at the cost of a slight power loss, yet with the added benefit of a safer stable operation.

Cost and manufacturability

The two systems are built with almost the same components, yet the QS system can accommodate the slower and lower-contrast acousto-optic Q-switch, while the CDQS oscillator demands

a high-speed high-contrast electro-optic modulator, along with high-power low-loss intracavity optics and a high-quality polarizer. The major cost difference between these two solutions will be a strongly limiting factor for the implementation of cavity-dumped Q-switching in industrial products. However applications requiring the combination of high average powers and short pulse durations may justify the price premium.

The more complex high-voltage power supply, high-speed switch and EO cell will also make integration and product development more difficult than a simpler off-the-shelf AO Q-switch and RF driver combination.

Chapter 5

Picosecond pulse operation

As shown in Chap. 4, the Q-switching of a high-power oscillator allows for the production of high-energy pulses with durations from a few to several tens of nanoseconds. If shorter pulses are needed, the cavity should be made as short as possible, resulting in short pulse build-up times and durations. Since the build-up time eventually becomes shorter than the opening time of an acousto-optic Q-switch, electro-optic Q-switches are employed for the realization of actively Q-switched oscillators with pulse durations down to 500 ps [105]. Extremely short cavities with lengths in the millimeter range are accomplished by bonding a saturable absorber such as Cr^{4+} :YAG to a laser crystal such as Nd:YAG and depositing the end-mirror and output coupler directly on the crystals' facets. Such passively Q-switched microlasers can produce pulses of ~ 300 ps [117], yet their output power is inevitably limited to a few hundred milliwatts [118].

When even shorter pulses are sought, mode locking of a cw oscillator allows for the generation of pulses as short as a few femtoseconds to several tens of picoseconds or more, depending on the laser medium, the resonator configuration, and the mode-locking device. The general principle of mode locking is first presented, followed by the specific technique of passive mode locking with a saturable absorber. The essential parameters and the basic structure of semiconductor saturable absorber mirrors (SESAM) are discussed. Then, passive mode locking with a SESAM is applied to the high-power cw oscillator previously developed in this work. Its design, performance, and behavior are presented, followed by power scaling with a MOPA architecture. This source is then efficiently frequency doubled and tripled, thanks to the high available peak-power.

5.1 Theory of passive mode locking

5.1.1 Principle of mode locking

When a laser is operated in cw, all the longitudinal modes of the resonator that lie within the gain spectrum of FWHM $\Delta\nu$ and which are above laser threshold can potentially oscillate, as illustrated in Fig. 5.1 (left). However in practice the ones close to the gain maximum dominate and reduce the gain available for the others to rise, so that the cw emission spectrum is much narrower than the gain bandwidth. Thus a fluctuating 4 GHz FWHM emission spectrum was

measured for the cw oscillator presented in Sect. 3.2.2, to be compared to the 210 GHz gain bandwidth of vanadate. For a resonator of optical length L , the longitudinal mode spacing is given by $\delta\nu = c/2L$, so that the electric field $E(t)$ is the sum of all the modes simultaneously oscillating:

$$E(t) = \sum_{k=-n}^n A_k \exp\{i[2\pi(\nu_0 + k\delta\nu)t + \Phi_k]\} \quad (5.1)$$

where ν_0 is the center frequency of the emission spectrum, $2n + 1$ the total number of oscillating modes, A_k and Φ_k the amplitude and phase of each mode, respectively. If the relative phase $\Phi_k - \Phi_{k-1}$ between two neighboring modes is random from mode to mode, the output intensity is constant, with a noise level resulting from mode beating depending on the number of simultaneously oscillating modes, which can ultimately appear as large-amplitude spiking. However if the longitudinal modes are locked in phase, with a constant relative phase $\Phi_k - \Phi_{k-1} = \Delta\Phi$, the output presents a periodic structure in time. If each oscillating mode has the same amplitude A_0 , as for a flat spectral gain profile, the sum of electric fields of each mode simplifies to $E(t) = A(t)e^{i\omega_0 t}$ where the amplitude $A(t)$ of the total electric field is given by:

$$A(t) = A_0 \frac{\sin\left[(2n+1)\frac{\delta\omega t + \Delta\Phi}{2}\right]}{\sin\left[\frac{\delta\omega t + \Delta\Phi}{2}\right]} \quad (5.2)$$

where $\omega_0 = 2\pi\nu_0$ and $\delta\omega = 2\pi\delta\nu$. The beam intensity is consequently obtained by $I(t) = A^2(t)$. Figure 5.1 (right) illustrates the temporal evolution of the normalized output intensity in the case of 7 and 100 oscillating modes of equal amplitude. The time interval between pulses is the cavity roundtrip time $\Delta\tau_p = 2L/c = 1/\delta\nu$, while the pulse duration is given by:

$$\tau_p = \frac{\Delta\tau_p}{2n+1} = \frac{1}{\delta\nu} \frac{1}{2n+1} \quad (5.3)$$

Thus if all oscillating modes have the same amplitude, the pulse duration is the inverse of the emission spectrum:

$$\tau_p = \frac{1}{\Delta\nu} \quad (5.4)$$

From Equ. 5.3 and as illustrated in Fig. 5.1 (right), a shorter pulse duration is obtained when many modes are oscillating simultaneously. Thus a laser medium with a wide gain spectrum will allow for the generation of short pulses, provided that no other element narrows the emission spectrum. The central modes benefiting from the largest gain, they tend to suppress their neighbors, which strongly reduces the emission spectrum. Such an effect as enhanced spatial hole burning can contribute to reducing the gain of the strongest mode to allow for the simultaneous oscillation of a larger number of neighboring modes, effectively widening the output spectrum and consequently shortening the pulse duration [119, 120, 121]. It should be noted that the intensity is normalized in Fig. 5.1 (right), yet the pulse peak power naturally increases with a larger number of modes and a shorter pulse duration.

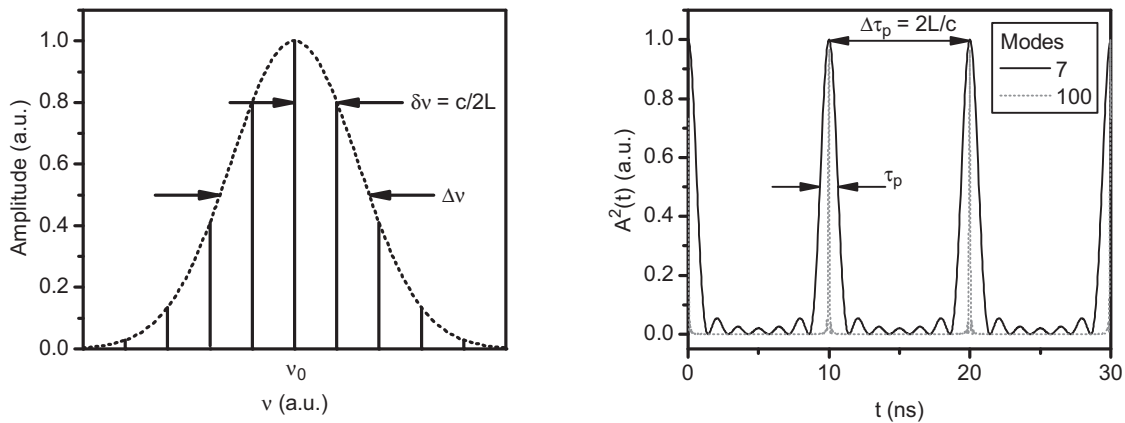


Figure 5.1: Longitudinal modes of a cavity of optical length L with a longitudinal mode spacing $\delta\nu$, under a gain spectrum centered on the frequency ν_0 and of FWHM $\Delta\nu$ (left). Time evolution of the output intensity of a mode-locked laser with 7 and 100 oscillating modes of equal amplitude (right). The roundtrip time of 10 ns results in a pulse repetition rate of 100 MHz.

5.1.2 Active mode locking

Mode locking can be achieved with two techniques: active mode locking where the gain or the losses are actively modulated in time, or passive mode locking where an intracavity element produces an intensity-dependent loss. In active mode locking, the gain or losses modulated at a frequency $\Delta\Omega$ give rise to side-bands at a frequency $\nu_k \pm \Delta\Omega$ from a mode oscillating at a frequency ν_k . If the modulation frequency is adjusted to match the longitudinal mode spacing ($\Delta\Omega = \delta\nu$), an energy coupling is created between neighboring modes since the side-band of a mode matches the neighboring mode. This coupling from mode to mode eventually results in the locking of all oscillating modes on a common phase. In the time domain, the amplitude modulation of the gain or losses at the cavity roundtrip frequency increases the net gain of a pulse synchronized to that modulation, so that it gradually builds up and supersedes the cw background. In the case of a sinusoidal modulation the net gain is maximum at the peak of the sine wave, which results in the shortening of the pulse roundtrip-after-roundtrip.

Active mode locking may be achieved through gain modulation with a pulsed pump beam in a solid-state laser, or by directly modulating the current of a diode-laser [122]. However high-speed gain modulation is not feasible in a DPSSL such as Nd:YVO₄ due to the long upper-state lifetime, so a loss modulator must be inserted in the cavity. Acousto-optic mode lockers allow for a large-contrast-ratio sine-wave modulation at frequencies in the 100 MHz range. They differ from AO Q-switches in that the acoustic-wave is back-reflected on the crystal facet opposite the transducer to produce a standing wave. This results in a fixed index grating with an amplitude varying at the RF frequency, which must be tuned to match the cavity roundtrip frequency. Such oscillator must therefore integrate a feedback to keep the RF frequency optimized even if thermal or mechanical variations come to modify the cavity length.

The relatively slow modulation of the losses in an actively mode-locked oscillator limits the pulse-shortening effect, so that pulses much longer than what is theoretically achievable given the laser material's gain spectrum are produced. For that matter passive mode-locking is the only technique providing ultra-short pulses of a few ps for Nd:YVO₄ down to < 5 fs for Ti:Sa.

5.1.3 Passive mode locking

As opposed to active mode locking where an external signal is applied to modulate the intracavity losses, passive mode locking relies on a passive intracavity component which generates the time-varying losses with the influx of the laser mode itself. The mode-locking device must exhibit a nonlinear loss function of light intensity, with a high loss at low power densities and a lower saturated loss at high intensities. Thus a short high-intensity pulse will suffer less losses than cw oscillation, and a pulsed regime will gradually build up from noise, suppressing the lower intensity cw background. The mode-locking process in the picosecond regime can be explained with two models: the slow saturable absorber with gain saturation, and the fast saturable absorber. Soliton mode locking which is essential to many shorter-pulse mode-locked systems is not developed here, as it is not necessary to the comprehension of the mode-locking process developed in this chapter.

Mode locking with a slow saturable absorber

Figure 5.2 (left) illustrates the evolution of losses, gain, and output intensity function of time when a pulse is emitted. The high losses drop as soon as the incoming pulse bleaches the absorber, so that the rising edge of the pulse is effectively steepened. When the pulse peak has passed, the slow saturable absorber remains bleached and does not recover its high losses before the end of the pulse trailing edge. Thus no shortening effect would apply to the trailing edge, and a narrow-spectrum cw background benefiting from a larger gain at the center frequency of the gain spectrum would build up. These two counteracting effects wouldn't allow for the formation of a stable and short mode-locked pulse. However, if the traveling of the pulse through the gain medium induces a significant gain saturation, the effective gain is reduced for the trailing edge of the pulse. Thus a net gain is available only for the central part of the pulse close to its peak. A short high-intensity pulse is therefore stabilized by the sole loss saturation on its rising edge, and by the gain saturation and slow - yet faster - recovery of the losses on its trailing edge [123, 124].

Slow saturable absorber mode locking is possible only with a certain combination of gain medium and absorber. The relaxation time of both the absorber and the amplifier must be comparable to the cavity round-trip time. Additionally their saturation fluences should be sufficiently low to allow both media to be saturated by the intracavity laser fluence [31]. This type of mode locking can occur in short-lifetime, large emission cross-section gain media such as dyes or semiconductors, while saturable absorbers such as dyes with lifetimes of a few nanoseconds are often used. In the case of Nd:YVO₄, the upper-state lifetime of 100 μ s is much larger than the cavity roundtrip time, and the gain isn't effectively saturated by the intracavity pulse, as

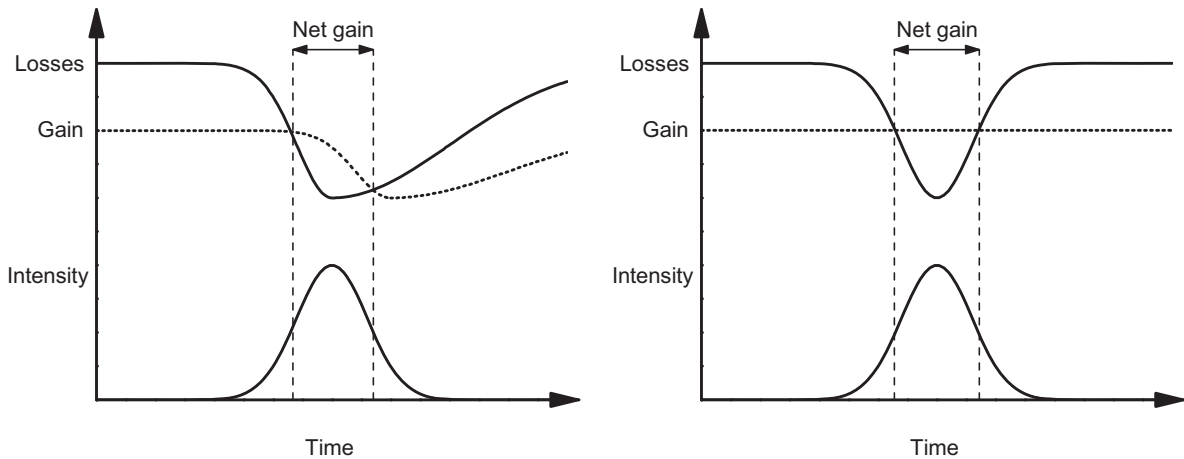


Figure 5.2: Time-evolution of the losses and gain with an incoming pulse for slow saturable-absorber mode locking (left) and fast saturable-absorber mode locking (right).

calculated in Sect. 5.2.2. Thus slow saturable-absorber mode locking is not achievable in a vanadate laser.

Mode locking with a fast saturable absorber

In a long-lifetime (hundreds of microseconds) gain medium such as vanadate, very little gain reduction occurs during the passage of the pulse. This case is illustrated in Fig. 5.2 (right) where the constant gain plays no role in the mode-locking process. If the absorber is recovering instantaneously or in a few picoseconds, the trailing edge of the pulse is also steepened by the recovery of the saturable absorber [125]. Thus the pulse is shortened from both sides at each roundtrip, effectively widening its spectrum. The predominant amplification of the modes close to the central wavelength of the gain spectrum counteracts the shortening of the pulse by narrowing the spectrum. Thus a stable pulse duration is reached with a balance of pulse shortening in the absorber and spectrum narrowing in the gain medium.

Instantaneous-recovery saturable absorbers rely on the intensity-dependent variation of the refractive index, or Kerr effect. Kerr-lens mode locking occurs thanks to the stronger focusing of high-intensity pulses in a given medium, allowing for the spatial filtering of a cw beam which will be less focused [126, 127]. In order to function, these resonators need to be operated close to a stability limit, so that a small change in the power of the Kerr lens induces a large variation of the mode size in the cavity. Furthermore Kerr-lens mode locking is not self-starting and requires the addition of an intracavity element such as an acousto-optic modulator or a vibrating mirror to generate an instability and start the mode-locking process.

Additive-pulse mode locking (APM) is achieved by adding a second coupled resonator integrating a nonlinear element such as a single-mode fiber which generates a significant amount of self-phase modulation (SPM) for high-intensity pulses [128, 129]. The coupled-cavity length is

adjusted to match that of the main resonator, so that a pulse traveling in the coupled resonator interferes with the main pulse on the coupling mirror common to both cavities, with an intensity-dependent phase. Given the right choice of parameters, a constructive interference is achieved at the pulse peak, while the lower-intensity pulse edges interfere destructively with the main pulse. This system behaves as an intensity-dependent reflectivity mirror, shortening the pulse at each roundtrip by enhancing the reflectivity of the pulse peak. Such system requiring the injection of the laser mode in a single-mode fiber and the stabilization of the coupled-cavity length to an interferometric level, the thermal and mechanical stability of the cavity must meet the most stringent requirements. Thus APM is not well suited to the realization of commercial or industrial-grade laser sources.

Semiconductor saturable absorbers presented in the next section don't provide the instantaneous recovery time of the Kerr effect, yet careful design allows for the realization of such absorbers with relaxation times of ~ 1 ps, sufficient for the mode locking of lasers in the picosecond range, such as vanadate-based oscillators.

5.1.4 The semiconductor saturable-absorber mirror

Principle

Semiconductor saturable absorbers rely on the transfer of electrons from the valence to the conduction band, forming an electron/hole pair in a semiconductor material with a direct band-gap slightly lower than the photon energy. As there is only a limited number of sites for the electrons in the conduction band, the absorption saturates as soon as these sites are filled and the material becomes transparent. Thus low-intensity light will be absorbed more strongly than high intensities, resulting in a nonlinear absorber [130]. The electrons in the conduction band then relax in two phases. First they can relax with lattice defects or dopants present in the semiconductor with time constants in the 10–100 fs range, and through intraband thermalization to the lower levels. The much slower second phase consists in the electron/hole recombination on the nanosecond time scale.

As the electron/hole recombination times are too slow for the generation of ps or fs pulses, the first phase is artificially enhanced to shorten dramatically the recovery time. Growing the semiconductor structure between 200°C and 400°C with the low-temperature molecular beam epitaxy (LT-MBE) technique allows for a controlled creation of lattice defects [131]. After epitaxy the wafer can be ion-implanted (As ions for InGaAs semiconductors) through ion bombardment, further shortening the relaxation time [132], and subsequently annealed to reduce the non-saturable losses. Thus saturable absorbers with recovery times of ~ 10 ps down to 500 fs are readily available commercially [133].

Parameters

The relaxation time τ_a of the saturable absorber defines how fast its absorption will recover after being bleached. The reflectivity of a SESAM or its bleaching behavior can be characterized by defining several macroscopic parameters. Figure 5.3 illustrates the evolution of the reflectivity R

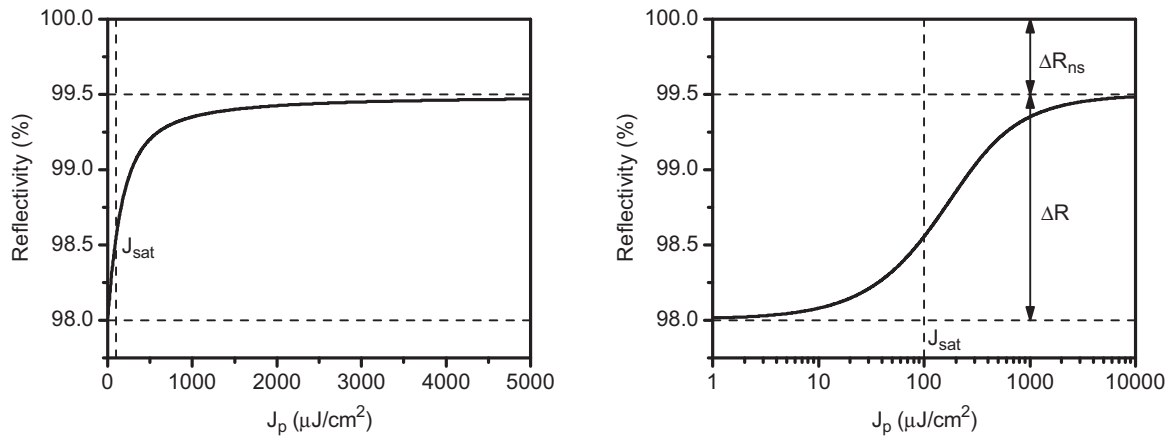


Figure 5.3: Reflectivity of a saturable absorber mirror function of the pulse fluence in linear scale (left) and logarithmic scale (right). The absorber parameters are $\Delta R_{ns} = 0.5\%$, $\Delta R = 1.5\%$, and $J_{sat} = 100 \mu\text{J}/\text{cm}^2$.

with increasing pulse fluence J_p for a typical absorber. At low fluences the reflectivity is limited to 98%, while it saturates at 99.5% for high fluences well above the saturation fluence J_{sat} . Thus the saturable losses or modulation depth are $\Delta R = 1.5\%$ and the remaining non-saturable losses are $\Delta R_{ns} = 0.5\%$. The latter arise essentially from the limited reflectivity of the mirror under the absorber layer, scattering on the absorber surface and defects, and the inherent initial absorption bringing electrons from the valence to the conduction band. These three parameters are adequate to fit experimental reflectivity data with the following equation [134]:

$$R(J_p) = (1 - \Delta R_{ns}) \left(1 - \Delta R \frac{J_{sat}}{J_p} \left[1 - \exp\left(-\frac{J_p}{J_{sat}}\right) \right] \right) \quad (5.5)$$

Stable cw mode locking

For the vast majority of applications, a stable cw mode-locked pulse train is desired. Q-switch mode locking produces a train of ultrashort pulses emitted at the roundtrip frequency under a modulated envelope on the ns to μs scale, as illustrated in Fig. 5.7. It should be avoided for its strongly modulated envelope is deleterious to most applications, but also for the risk of damage its high-intensity peaks pose to the saturable absorber and possibly to following nonlinear crystals used for harmonic generation. For a given oscillator and pump configuration, one can expect to produce a train of pulses with an intracavity energy E_p at a PRF given by the roundtrip frequency. Thus the pulse fluence on the absorber can be varied by adjusting the focusing of the laser mode on the absorber, with $J_p = E_p/A_A$, where A_A is the mode area on the absorber.

J_p should well exceed J_{sat} to bleach the absorber and use a good portion of its modulation depth. However if $J_p \gg J_{sat}$, the absorber's damage threshold will ultimately be exceeded, but before that the oscillator will switch to multiple-pulse operation. This behavior can be explained as following. As J_p is increased, the effective modulation depth between the non-

saturated reflectivity and the reflectivity for an incoming pulse rises, leading to a reduction of the pulse duration and a simultaneous widening of its spectral width. As such wider-spectrum pulses suffer from a lower effective gain than lower-intensity narrower-spectrum longer pulses, the oscillator eventually switches to a double-pulse operation. In this regime, a series of two lower-energy and therefore longer and narrower-spectrum pulses is emitted. It has been shown experimentally that the pulse fluence should be $\sim 3 - 5$ times larger than the saturation fluence on the absorber to avoid multiple pulses [135].

In order to obtain short mode-locked pulses, the modulation depth ΔR should be chosen as high as possible. The pulse duration τ_p is given by:

$$\tau_p \propto \frac{1}{\Delta R^\beta}, \quad \beta > 0 \quad (5.6)$$

where β is an exponential factor varying in the different passive mode-locking theories. Thus generally the pulse duration will be reduced for larger saturable losses [136]. However the modulation depth cannot be increased without ultimately reaching the Q-switched mode-locked regime. It is shown that for a laser operated far above threshold and for small modulation depths ($\Delta R < 5\%$), the simplified condition for stable cw mode locking can be expressed as follows [137]:

$$E_p^2 > J_{sat,L} J_{sat,A} A_L A_A \Delta R \quad (5.7)$$

where $J_{sat,L}$ and $J_{sat,A}$ are the saturation fluences of the laser medium and the absorber, respectively, and A_L and A_A the mode areas on the two components. The Q-switched mode-locking threshold is lowered by using laser materials with relatively low saturation fluences or large stimulated-emission cross sections, as $J_{sat,L} = h\nu/\sigma_L$. Furthermore the mode size should be reduced on the absorber and laser crystal, yet the fluence on the absorber cannot be arbitrarily increased since multiple pulsing and absorber damage will ultimately occur. It is then easier to exceed the Q-switched mode locking threshold with a higher intracavity pulse energy, achieved by designing long resonators with reduced roundtrip frequencies, and by increasing the output coupler reflectivity above the optimum cw output coupling, yet at the cost of a loss of average output power. Disk lasers suffering from a relatively low gain because of the large mode area on the gain medium must therefore be operated with long cavities with PRFs limited to a few ten kilohertz [19].

Thus, when increasing the pump power of a passively mode-locked oscillator, it will first go through Q-switched mode locking before reaching a stable cw mode-locked regime, then multiple pulsing will arise and ultimately the SAM will be destroyed by the excessive pulse energy.

SESAM structure

A saturable absorber mirror (SAM) essentially consists of a substrate, a high-reflectivity Bragg mirror, and an absorber layer. Some elaborate structures including resonant and anti-resonant Fabry-Pérot saturable absorbers (A-FPSA) allow for strongly decreasing or increasing the saturation fluence by placing the single or multiple absorber layers within a resonant or anti-resonant

Fabry-Pérot cavity, close to the nodes or the anti-nodes of the electric field. However, the simpler structure of the SAM provided by the Ferdinand-Braun-Institut für Höchstfrequenztechnik (FBH), Berlin, implemented in Sect. 5.2 will be described here [138].

The substrate is a GaAs semiconductor wafer providing the mechanical support and the bulk of the volume of the device. A Bragg mirror is then grown on the substrate by depositing a series of high/low-index quarter-wave layers. AlAs/GaAs is a typical film combination used to build the stack, with > 15 pairs to achieve reflectances $> 99\%$ [133]. The absorber layer is a single quantum well of InGaAs embedded in a half-wave GaAs layer. After epitaxy the wafer was As implanted and annealed to reduce the carrier lifetime. Finally, as the high index of GaAs results in a Fresnel reflection of $\sim 30\%$ at its interface with air, a SiN anti-reflection layer is deposited on top of the stack. The ~ 1 mm-thick absorber chip is glued on a copper heatsink to drain the heat generated in operation.

5.2 Mode-locked oscillator with a saturable absorber mirror

The implementation of passive mode locking in high-power oscillators led to the demonstration of picosecond-pulse systems with increasing output powers. A 27 W output power Nd:YAG system operating at 55 MHz and providing 19 ps long pulses has been presented [139], but required three pump heads and exhibited a limited optical efficiency of 20%. Another system based on an Yb:YAG thin-disk pump head provided 80 W of average power in 705 fs pulses at a repetition rate of 57 MHz [3], yet at the cost of a complicated resonator and pump setup and an optical efficiency under 30%. The choice of Nd:YVO₄ as a gain medium allows much higher repetition rates thanks to its large stimulated-emission cross section, thus reducing the stable cw mode-locking threshold [137], yet output powers have been limited to 23.5 W in 21.5 ps pulses at 147 MHz [140], mainly because of the difficulties associated to the design of a high average power TEM₀₀ resonator [141]. Thus Nd:YVO₄ is the material of choice for realizing compact, high optical efficiency and high repetition-rate picosecond-pulse sources needed in quasi-cw applications, yet output power has been limited by thermo-optical effects in the laser crystal. In this section, passive mode locking of a high-power 888 nm pumped vanadate oscillator is demonstrated, keeping the benefits of Nd:YVO₄ for mode locking, while pushing the output power to higher levels. More recently, 175 W of output power with 80 ps pulses at 120 MHz has been demonstrated by amplifying a pulsed laser diode, yet with the complexity of four fiber-amplifier stages with multiple optical isolators [25], which will limit its integration into a product.

5.2.1 Mode-locked oscillator design

The high-power cw oscillator presented in Sect. 3.2.2 is used as the starting point for the realization of a mode-locked oscillator. Figure 5.4 (left) illustrates the oscillator followed by the single-pass amplifier presented in Sect. 5.2.3. The initial symmetric cw oscillator illustrated in Fig. 3.13 is modified to extend one arm of the resonator and allow for the adjustment of the mode size on the saturable absorber, while the other arm is left unchanged to provide output

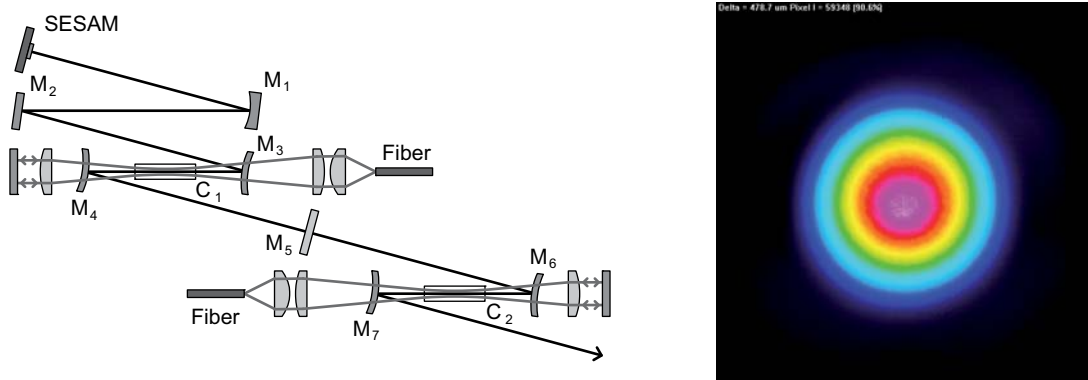


Figure 5.4: Mode-locked oscillator with flat output coupler M_5 followed by a symmetrical single-pass amplifier (left). MOPA output beam profile measured with a beam quality factor $M^2 = 1.05$ (right).

coupling through mirror M_5 . The mode propagation is left unaffected in the resonator section from M_2 to M_5 , while the choice of the curved HR mirror M_1 and its relative distance to M_2 and to the SAM allows for the re-imaging of the waist of M_2 on to the SAM.

Since the pulse fluence on the absorber should be high enough to exceed the Q-switch mode-locking threshold as defined by Equ. 5.7, yet not too high to avoid multiple pulsing or the absorber's destruction, the mode size on the absorber should ultimately be optimized to achieve stable cw mode locking with the optimum output coupling for maximum average output power. Since modifying the geometric configuration of the cavity to alter the roundtrip frequency or the mode size on the absorber is more time-consuming than changing the output-coupler reflectivity, the latter is first achieved either by physically changing OC mirrors or by building a variable output coupler with a thin-film polarizer, a quarter-wave plate, and a HR mirror, as for the optimization of output coupling in Sect. 3.2.2. Once a stable operation point was found for a given output coupling and mode size on the absorber, the focusing of the mode on the absorber was modified to keep the same fluence on this component, yet with an optimum output coupling. The mode could be characterized by replacing the SAM by an HR mirror and accessing the mode leakage for measurement.

The resonator was set up with a $r = -750$ mm concave HR mirror M_1 to provide a 1:1 imaging of the waist on M_2 onto the SESAM, with $d_{M_1-M_2} = 300$ mm and $d_{M_1-SAM} = 360$ mm, extending the optical cavity length from 700 mm to 1360 mm. The lengthening of the cavity results in a reduction of the cavity roundtrip frequency from 214 MHz to 110 MHz, making it easier to exceed the Q-switched mode-locking threshold. The beam waists on the SESAM, folding mirror M_2 , and output coupler M_5 are therefore identical with a radius of $370 \mu\text{m}$. Care was taken in the selection and the mounting of the 5×5 mm SAM chips to avoid strain that would result in applying a curvature to the reflector. Thus soldered samples would exhibit convex radii of curvature down to 2 m, while simple epoxy gluing on the sample's periphery limited the curvature to ~ 10 m, which has no significant effect on the mode propagation.

5.2.2 Mode-locked oscillator performance

As the pump power was ramped-up, the oscillator first ran in cw just after reaching lasing threshold, then went in an unstable Q-switched mode-locked regime, before reaching stable Q-switched mode-locking just under the threshold for stable cw mode-locking. The oscillator equipped with a 35% transmission OC provided 56 W of average power at a repetition-rate of 110 MHz, for a pump power of 108 W, corresponding to 52% optical-to-optical efficiency. The beam remained diffraction limited with $M^2 = 1.05$.

The pulse duration was calculated from the FWHM of the intensity autocorrelation $\Delta\tau_{autocor}$ measured with an APE PulseCheck autocorrelator offering a ± 75 ps delay between the two split beams focused in a doubling crystal for non-colinear phase-matching. Making the assumption of a sech^2 temporal pulse shape typical of SESAM mode-locked solid-state lasers, the FWHM pulse duration τ_p is given by:

$$\tau_{p, \text{sech}^2} = \frac{\Delta\tau_{autocor}}{1.543} \quad (5.8)$$

Thus a pulse duration of 33 ps was calculated from the autocorrelation trace's sech^2 pulse fit FWHM of 51 ps, as illustrated on Fig. 5.5 (left).

The optical spectrum was measured with a 75 GHz free-spectral-range (FSR) plano-mirror scanning Fabry-Pérot interferometer (FPI). When measuring the spectrum of ultrashort pulses, the FSR should be chosen as a function of the pulse duration [142]. Thus if the FSR is too narrow, the Fabry-Pérot roundtrip time will become longer than the pulse duration itself, so that no interference of the pulse with itself will occur. On the contrary if the FSR is too large, the measurement's resolution will suffer. Here a 75 GHz FSR corresponds to a 13 ps roundtrip time, which allows sufficient overlap of the 33 ps pulse with itself for an accurate measurement. Figure 5.5 (right) illustrates the signal provided by the FPI, with a FWHM $\Delta\nu = 12.4$ GHz. The time-bandwidth product $\tau_p\Delta\nu = 0.409$ calculated from these two measurements is close to the Fourier limit for a sech^2 pulse of 0.315 [143].

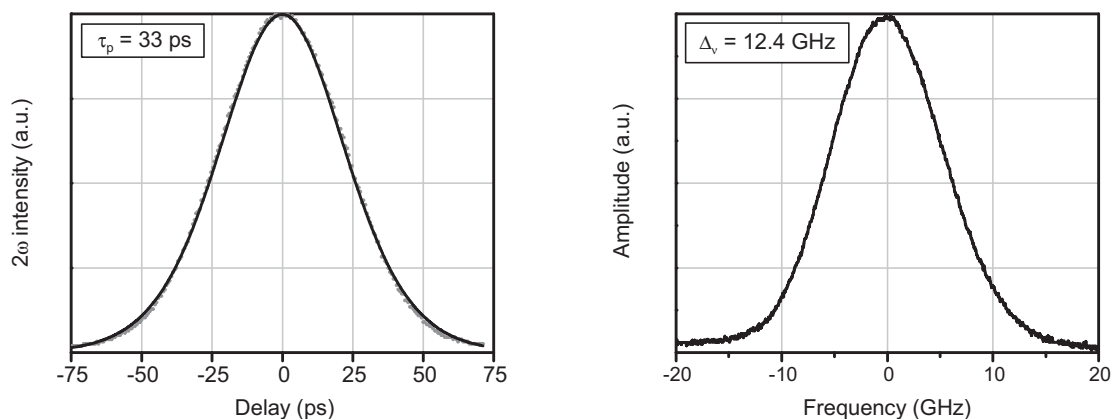


Figure 5.5: Autocorrelation trace (grey dots) and fit with the autocorrelation of a sech^2 pulse shape (black line) (left), and optical spectrum (right) of the mode-locked oscillator.

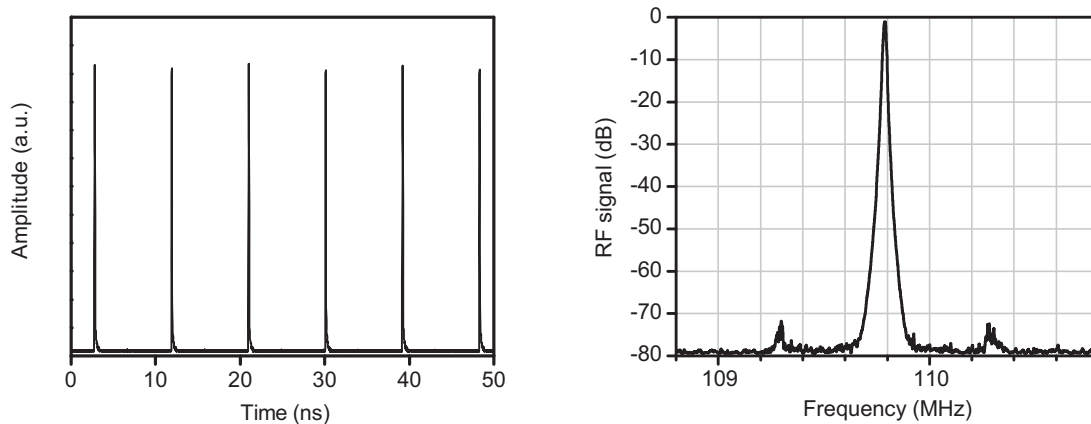


Figure 5.6: Pulse train measured with a high-speed photodiode and sampling oscilloscope (left). RF spectrum measured with an electronic spectrum analyzer (right).

In order to verify the stable cw mode-locked operation of the system without multiple pulsing, a time trace of the pulse should be acquired on a wider range to detect any secondary pulse. Since this would require a longer delay line than that of the available autocorrelators, a high-speed photodiode is employed for directly visualizing the pulse train. Figure 5.6 (left) shows a full pulse train measured with a 18.5 ps risetime New Focus Model 1454 photodiode coupled to a Tektronix CSA 803 A sampling oscilloscope offering a 7 ps risetime. No after-pulse could be detected on a large scale, as illustrated, nor on a much smaller scale resolving the pulse with a FWHM of ~ 50 ps. Therefore the combination of the autocorrelation measurement coupled to the high-speed oscilloscope trace provides a complete characterization of the pulses in the time domain.

The radio-frequency (RF) spectrum was monitored with a 200 ps risetime photodiode coupled to an electronic spectrum analyzer, as illustrated in Fig. 5.6 (right) for RF and video bandwidths of 10 kHz. The main peak at the roundtrip frequency of ~ 110 MHz is only surrounded by relaxation-oscillation peaks suppressed to better than -70 dB, confirming the stable cw mode-locked operation regime in a diffraction-limited fundamental transversal mode.

Figure 5.7 illustrates the major differences between cw and Q-switched mode locking through the observation of the pulse train and the RF spectrum for both operating regimes. The two sets of measurements were gathered just below and above the QSML threshold, so that the output power and gain are almost identical. The time traces (top row) were acquired with the same vertical scale to demonstrate the ~ 3 times larger pulse peak amplitude of the QSML bursts than of the stable cw pulse train. The ~ 500 ns FWHM Q-switch pulse envelopes are repeated with a ~ 300 kHz frequency defined by the gain, absorber, and resonator parameters. The larger peak power reached in the QSML regime is often responsible for the local destruction of the SAM, so QSML should be avoided in high-power operation. Yet the absorber did not suffer any damage in the resonator's final configuration, even with QSML during the ramping

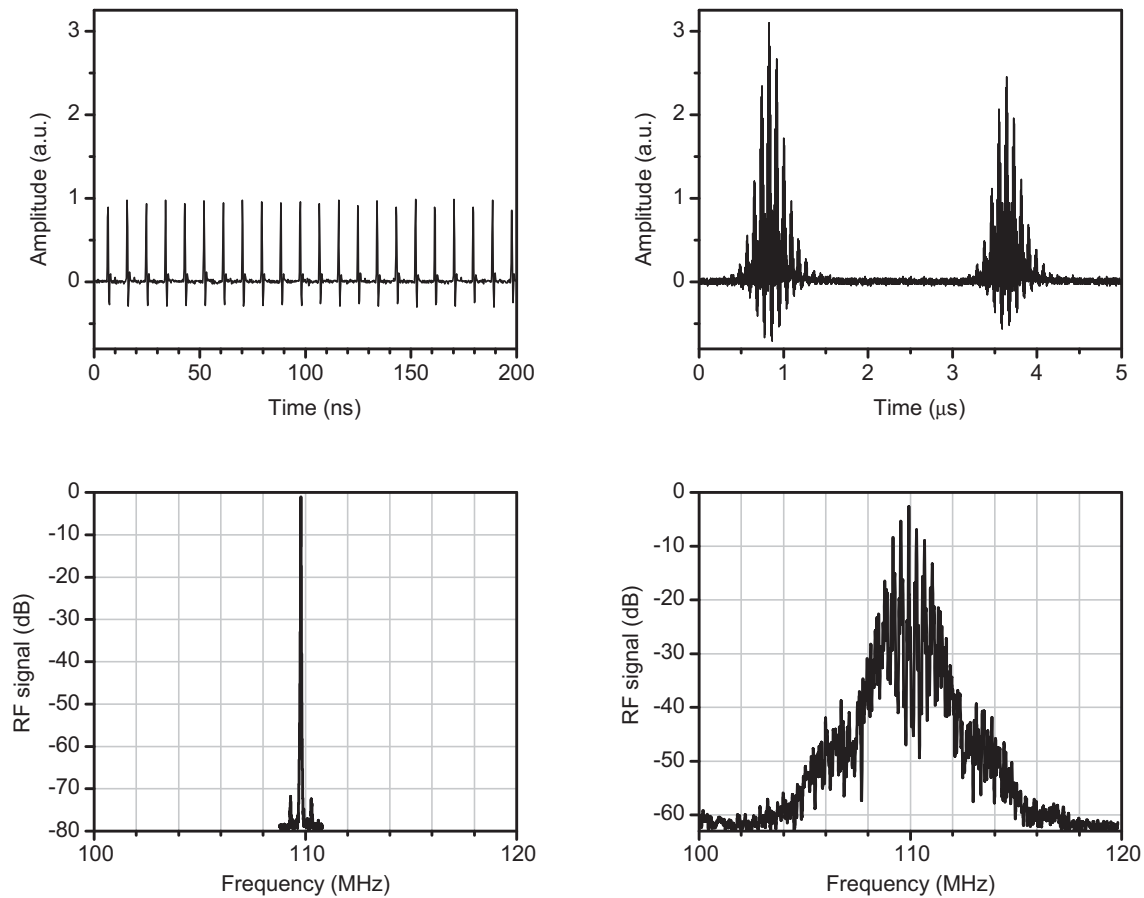


Figure 5.7: Pulse train (top row) and RF spectrum (lower row) in cw mode-locked regime (left column) and Q-switched mode-locked operation (right column).

up of the pump power. Thus the mode size on the absorber should be made just small enough to reach a stable cw mode-locking regime, without increasing the pulse fluence unnecessarily and risking absorber damage.

The RF spectrum traces (lower row) are plotted with the same horizontal scale to illustrate the much narrower spectrum in CWML, presenting a single peak at the PRF with side-bands suppressed to better than -70 dB, compared to QSML where the spectrum spreads on more than 10 MHz.

Since an output pulse energy of $0.5 \mu\text{J}$ is achieved in CWML operation, the intracavity pulse energy is $\sim 1.2 \mu\text{J}$ on the absorber, corresponding to a fluence $J_p = 280 \mu\text{J}/\text{cm}^2$ on the absorber surface. As no data was available for this absorber, it is difficult to draw any conclusion on how many times above the saturation fluence the SAM is operated. However if it is assumed that the absorber would be operated at 3 times its saturation fluence, the latter would be $\sim 90 \mu\text{J}/\text{cm}^2$, a typical value for commercially-available SAM [133].

Considering the very short ~ 10 ns roundtrip time compared to the $100 \mu\text{s}$ upper-state lifetime of vanadate, the variations of inversion during the pumping phase and when a pulse travels through the gain medium should be minimal, so that the inversion is essentially constant

at its cw threshold value $n_{th} = 8 \times 10^{16} \text{ cm}^{-3}$ calculated with Equ. 4.8. Thus the $0.5 \mu\text{J}$ pulse energy extracted at each roundtrip corresponds to a reduction in the inversion density $\Delta n = E_p/(h\nu V_l)$, where V_l is the laser mode volume in the crystal. $\Delta n \approx 10^{14} \text{ cm}^{-3}$ represents only a gain reduction of $\sim 0.1\%$ after a pulse has been extracted, much smaller than the supposed $> 0.5\%$ modulation depth of the absorber. As no dynamic gain saturation occurs, the fast saturable-absorber mode-locking model is adequate to explain the behavior of this system.

5.2.3 Mode-locked MOPA

Since scaling up the output power of the mode-locked oscillator would require building a two-crystal periodic resonator based on the cw setup presented in Sect. 3.2.3, the cavity length, gain, repetition rate, and therefore the whole mode-locking dynamics and output characteristics would be altered. However it has been shown in Sect. 3.3.2 that a simple and equally efficient MOPA configuration could be assembled by placing the same pump-crystal configuration as in the oscillator, symmetrically to the flat output coupler where the output beam waist is located. Since the mode propagation in the output arm of the mode-locked oscillator is identical to that of the cw oscillator, the exact same amplifier configuration can be applied. Figure 5.4 (left) illustrates the complete mode-locked MOPA system's scheme.

The amplifier was seeded with the full output power of the mode-locked oscillator of 55 W after a variable attenuator and provided 111 W of output, corresponding to an extracted power of 56 W and an optical efficiency of 52% in the amplifier stage. The beam quality remained unaffected by the amplifier at the full pump power of 108 W with $M^2 = 1.05$, as illustrated in Fig. 5.4 (right). The pulse duration of 33 ps and the optical spectrum of 12.4 GHz FWHM both remained unaltered in shape and width after amplification. The absence of temporal or spectral alteration of the pulses during amplification is explained by the relatively long pulses, large beam cross-section and moderate peak power, limiting the effects of dispersion, gain narrowing, and self-phase modulation in the 30 mm long crystal. The $\sim 9 \text{ ns}$ pulse repetition period being much shorter than the upper-state lifetime of $100 \mu\text{s}$, the extraction efficiency achieved with a mode-locked seed is identical to that of a cw source of comparable average power.

The mode-locked MOPA provides a 110 MHz high-repetition-rate quasi-cw source, with a pulse energy of $1 \mu\text{J}$ and a peak-power of 30 kW, which should be sufficient for efficient harmonic generation.

5.3 Harmonic generation

Some applications requiring cw sources in the visible or UV, such as laser direct imaging (LDI) for the printed circuit board industry, would benefit from higher average powers. Yet high-power intracavity doubled or tripled cw sources are difficult to realize, so that the extra-cavity harmonic generation of a quasi-cw high repetition-rate mode-locked IR source is a convenient alternative, provided that the application can tolerate the high PRF instead of pure cw. Thus the 111 W average output power and the 30 kW peak power available from the mode-locked MOPA are put to contribution for producing large amounts of quasi-cw green and UV light.

5.3.1 Frequency doubling

Similarly to the frequency doubling of the CDQS oscillator (see Sect. 4.2.4), the ML MOPA output beam is focused in a 20 mm long LBO crystal cut for type I NCPM at 150°C, with a plano-convex lens following a variable attenuator. The fundamental and second harmonic are separated by two dichroic mirrors (HR 532 nm, HT 1064 nm) to remove any residual fundamental for measuring the green power. The constant 33 kW IR peak power and 1 μ J energy being much lower than the 250 kW and 1.5 mJ of the CDQS system at 30 kHz, the ML IR beam should be focused much tighter in the LBO crystal to achieve high conversion efficiencies, yet without risking the destruction of the crystal's output AR coating. Furthermore, the shorter ps pulses provide a much lower pulse fluence than the ns pulses when both are focused to achieve the same peak power density, and consequently similar conversion efficiency. Thus the theoretical optimum focusing of $w = 27 \mu\text{m}$ determined in Sect. 3.4.1 can be approached.

Figure 5.8 (left) illustrates the green power and doubling efficiency function of the IR average power continuously adjusted with the variable attenuator, when the fundamental beam was focused down to $w = 30 \mu\text{m}$. Thus the peak power density at the waist location in the center of the crystal reaches $\sim 1 \text{ GW}/\text{cm}^2$, yet it remains $< 200 \text{ MW}/\text{cm}^2$ thanks to the larger beam size on the input and output facets. For a maximum average power of 109 W after the variable attenuator, 87 W of 532 nm light is generated, corresponding to 80% conversion efficiency. Such high conversion efficiency comes at the cost of a slight degradation of the gaussian beam profile, the wings exhibiting a high conversion while the center suffers saturation or even back-conversion, yet an M^2 of 1.2 was achieved. This slight flattening of the beam profile is visible in Fig. 5.8 (right). With a weaker focusing of $w = 55 \mu\text{m}$, 70 W of green were generated, yet without any beam degradation with $M^2 = 1.05$ remaining equal to that of the IR.

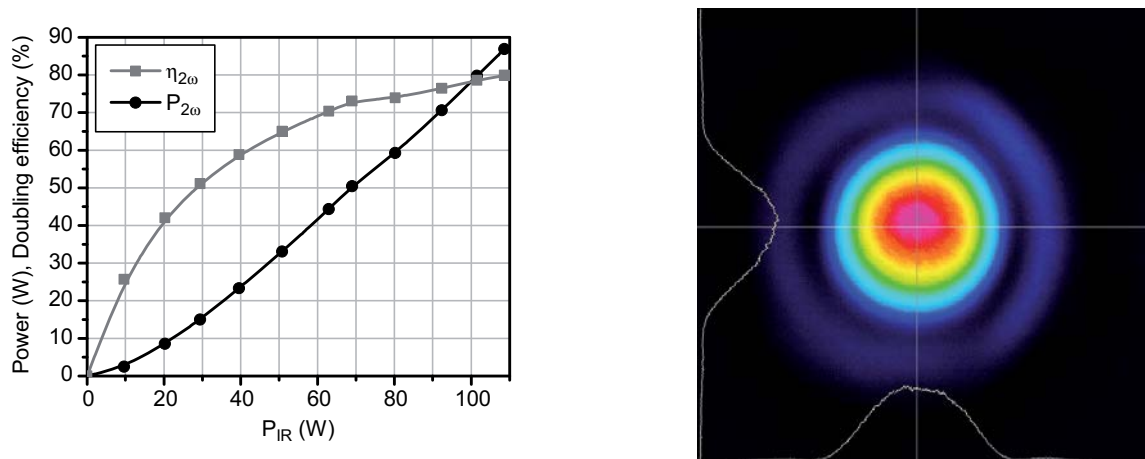


Figure 5.8: Second harmonic power and doubling efficiency of the mode-locked MOPA (left), and 87 W green beam profile (right).

5.3.2 Frequency tripling

Principle

Direct frequency tripling in a single nonlinear crystal being very inefficient due to the very small third-order nonlinear coefficients $\chi^{(3)}$ in Equ. 3.11, the third harmonic is generally obtained by sum-frequency mixing (SFM) of the second harmonic and the fundamental. Thus third-harmonic generation (THG) comprises a doubler crystal followed by a SFM stage, possibly with imaging optics and walk-off compensation in-between.

In theory, the most efficient THG is achieved when each green photon is matched to one IR photon, corresponding to 1/3 IR power and 2/3 green power due to the two-times higher energy of the green photons. However, achieving a 66% doubling efficiency in the SHG stage leads to an inevitable depletion of the center part of the fundamental beam and therefore a loss in beam quality and spatial overlap with the green beam in the SFM crystal, effectively reducing the global tripling efficiency. Furthermore, the second-harmonic waist is smaller than the IR, from a factor $\sqrt{2}$ at low conversion efficiencies, to equal diameters when the conversion efficiency saturates. It has been demonstrated that high tripling efficiencies up to 50% from IR to UV are achieved when the doubler is operated at $\sim 50\%$ efficiency [144].

LBO being very efficient for the SFM of two IR photons, it can also be phase-matched for the SFM of 1064 nm and 532 nm radiation [145], with a transparency range extending down to 160 nm. Type I (oo-e) and type II (oe-o) phase matching is feasible, yet type II will always be preferred for its smaller walk-off and for its easy setup after a doubler crystal that produces orthogonally-polarized IR and green beams. Thus type II critical phase matching is achieved at 50°C for the THG of 1064 nm for $\theta = 43.9^\circ$ and $\phi = 90^\circ$, cut in the yz plane. The nonlinearity $d_{eff} = -0.8$ pm/V is similar to that of SHG, the walk-off angle is limited to $\rho = 9.5$ mrad, the angular acceptance is $\Delta\theta \cdot L = 3.47$ mrad·cm, while the thermal acceptance is $\Delta T \cdot L = 3.4$ °C·cm.

Setup

Figure 5.9 provides a schematic of the THG setup implemented on the output of the ML MOPA. The IR beam is focused down to a $w = 50$ μm waist in the $3 \times 3 \times 20$ mm NCPM LBO doubler crystal, generating a green beam collinearly to the IR beam without any walk-off. The two beams are then refocused with a 60 mm focal length achromat in a $2f - 2f$ configuration, re-imaging the waist from the doubler into the tripler crystal with a 1 : 1 ratio. Since the incoming IR and green beams are collinear, directly focusing the two beams in the tripler would result in limiting the interaction length between the two because of walk-off (see Fig. 5.11a). The o -polarized IR and UV beams propagate in the same direction as their wave vectors, while the e -polarized green beam propagates in the direction of the Poynting vector S_2 making a walk-off angle with the wave vector k_2 . Such effect can be partly compensated by using a CPM LBO doubler with its walk-off direction opposite that of the tripler [94], but since a NCPM doubler is used, an external compensation should be applied. Thus a $3 \times 3 \times 8$ mm BBO crystal cut off phase-matching angle ($\theta = 86.3^\circ$, $\phi = 0^\circ$) is inserted between the achromat and the THG LBO

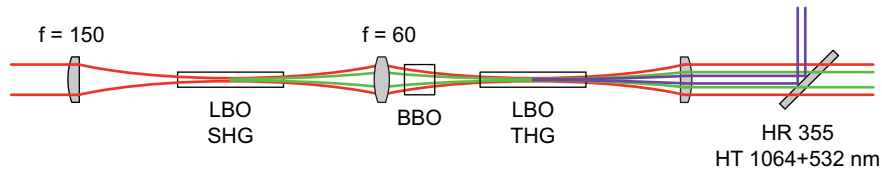


Figure 5.9: Frequency-tripling setup.

[146]. It simply provides a lateral offset between the IR and green beams, similarly to what is obtained after a CPM SHG LBO crystal, so that the two cross in the center of the crystal, as illustrated in Fig. 5.11b, instead of walking off right after the entrance facet, thus effectively increasing the interaction length between the two. The $3 \times 3 \times 15$ mm THG LBO crystal is anti-reflection-coated on both facets (AR 1064 + 532 nm on the input, and AR 355 nm on the output). The generated 355 nm beam is then collimated and separated from the IR and green with two dichroic mirrors (HR 355 nm, HT 1064 + 532 nm).

Performance

The phase-matching angle is easily found by applying moderate power and turning the LBO crystal around the incident polarization axis until fluorescence of the 355 nm radiation is detected on a white paper card. However, at full IR power the angle needs to be readjusted because of UV absorption resulting in crystal heating. For this reason temperature-regulated crystal holders are generally used to keep the crystal at a constant temperature above room temperature, regardless of the UV-induced crystal heating. Then the doubling efficiency was adjusted by moving the IR waist position along the beam axis to optimize the green/IR power balance. For a fundamental input power of 107 W, up to 35 W of 355 nm UV radiation was produced, corresponding to a conversion efficiency of 33 %, when 69 W of green were generated in the doubler. The beam shown in Fig. 5.10 was measured with a beam quality of $M^2 = 1.4$ and a waist asymmetry of

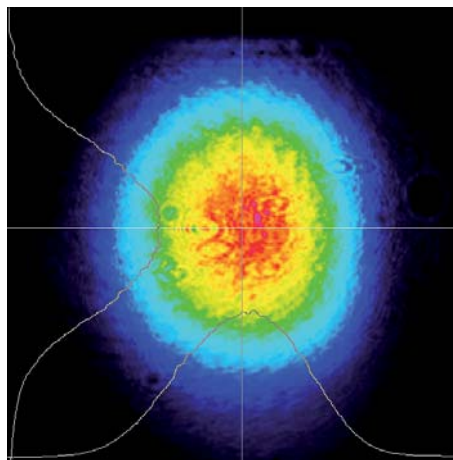


Figure 5.10: 355 nm third harmonic beam profile.

90%. The conversion efficiency was limited by green-induced damage of the crystal's input facet anti-reflection coating for 1064 and 532 nm, which didn't have the same high damage threshold as the doubling crystal, preventing stronger focusing.

Optimized tripler configurations

Applying a more sophisticated tripling configuration with non-collinear phase-matching (see Fig. 5.11c) and higher-quality coatings should provide conversion efficiencies of 40% to 50%, as previously demonstrated for similar peak-power picosecond systems [144]. In this technique, a certain tilt is applied between the incoming IR and green beams, so that the angle between their wave vectors inside the crystal is exactly the opposite of the walk-off angle. Thus the IR and green beams will propagate along the same direction with a perfect spatial overlap, while the UV beam walks off with a smaller angle given by $\vec{k}_3 = \vec{k}_1 + \vec{k}_2$.

Some specific crystal-cut angles and wedged facets allow for non-collinear phase matching with collinear input IR and green beams, which probably constitutes the most effective and robust technique for achieving a long interaction length and thus a high conversion efficiency

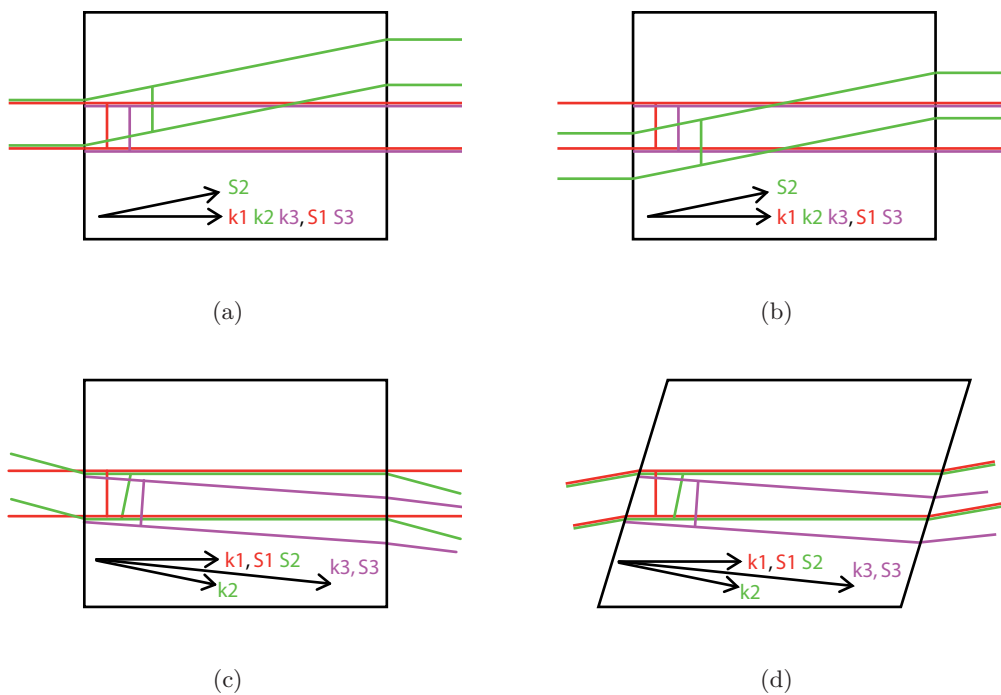


Figure 5.11: Walk-off compensation techniques. The directions of propagation of the IR, green, and UV beams are determined by the Poynting vector S , while the crossing lines indicate their respective wavefronts following the wave-vector k . No walk-off compensation (a), input beam offset (b) [94, 146], non-collinear phase-matching with angled input beams (c) [144], and non-collinear phase-matching with an angle-cut crystal and collinear input beams (d) [147, 148].

and limited UV beam ellipticity [147, 148]. In this technique, the IR and green beams enter the crystal with a specific angle of incidence calculated so that the difference in refraction angles resulting from dispersion is exactly the opposite of the walk-off angle. Thus the IR and green beams will perfectly overlap in the tripler crystal, while the UV beam walks off as it is generated, as shown in Fig. 5.11d.

Additionally, applying elliptical focusing with weaker focusing in the walk-off plane would allow maintaining the power density necessary to the nonlinear process, while minimizing the effect of walk-off on conversion efficiency and third harmonic beam ellipticity [149].

5.4 Picosecond performance summary

Applying saturable-absorber mode locking to an 888 nm pumped oscillator provided a high-power and high repetition-rate quasi-cw source of picosecond pulses. The oscillator achieved 56 W average output power with 33 ps pulses at 110 MHz repetition rate, in a diffraction-limited beam. Further single-pass amplification increased the output power to 111 W without altering the beam quality and the temporal and spectral characteristics. Thus the 1 μJ pulse energy and 33 kW peak power was advantageously used for frequency doubling and tripling, achieving 87 W at 532 nm and 35 W at 355 nm, respectively. Therefore such source exhibits a strong potential for the realization of high average power quasi-cw visible sources, such as RGB systems integrating SFM stages and OPOs, and high-power UV quasi-cw sources for the electronics industry.

In subsequent work, Christoph Schäfer demonstrated the benefits of enhanced spatial hole burning in a gain-at-the-end configuration, achieving 16 ps pulse duration instead of 36 ps in a gain-in-the-middle resonator [121]. Thus shorter pulse durations are achievable with an adequate resonator design, providing even higher peak powers for easier high conversion efficiency nonlinear interactions.

Chapter 6

Summary

Although the initial motivation for my thesis was the realization of a high-power RGB laser system, and most specifically the design of a > 100 W mode-locked IR source for driving an existing RGB generation unit, the white-light source was not built, yet a 111 W picosecond IR source was assembled and its potential for efficient harmonic generation demonstrated by frequency-doubling with 80% efficiency. The choice was made not to investigate the RGB source and instead demonstrate the potential of 888 nm pumping on a wider range of systems.

The benefits of end-pumping Nd:YVO₄ at 888 nm over 808 nm and even 880 nm were demonstrated both theoretically through thermal and ETU simulations, and experimentally with the 60 W single-crystal and the 120 W two-crystal cw oscillators, offering a 2–3-fold improvement in output power over 808 and 880 nm state-of-the-art systems with an identical number of pump sources and crystals. The scalability is proven by the near equally-efficient periodic resonator and single-stage MOPA, which provides a great flexibility in the design of high-power systems in cw, ns, or ps regime, yet always with identical pump–crystal modules.

Table 6.1 summarizes the main characteristics of the cw and pulsed systems, along with their second and third-harmonic extensions. The 55% optical efficiency and beam-quality $M^2 = 1.05$ of the 60 W output power single-crystal cw oscillator are perfectly maintained in the 119 W two-crystal resonator. The same pump–crystal module applied as a single-pass amplifier provides almost equal optical efficiency thanks to its high gain and to the high power available from the oscillator for saturating the amplifier’s extraction.

Intracavity-doubling of the single and two-crystal configurations provided up to 62 W of low-noise cw green light, thanks to the long resonator and the limited thermal effects in the LBO crystal. Such performance represents a ~ 3 times higher power than what had been previously demonstrated with an intracavity-doubled Nd:YVO₄ laser [90].

There is a strong need for high-power high-repetition-rate short-pulse sources, for which vanadate is very well suited, but for its limitation in average output power. Thus a choice must often be made between the short pulses and high repetition-rate, yet limited output power of a vanadate system, and the high average output power yet longer pulses and lower repetition rate of Nd:YAG lasers or Yb:YAG thin-disk systems. Since the quality of many material-processing interactions improves with shorter pulses, a higher average-power and higher repetition-rate

Table 6.1: Performance summary of the demonstrated cw, ns, and ps systems.

System	P_{out} (W)	P_{pump} (W)	η_{opt} (%)	M^2	τ_p	PRF	E_p	P_{peak}
cw								
1-crystal oscillator	60	108	55	1.05				
2-crystal oscillator	119	216	55	1.10				
Amplifier stage	57	108	53	1.05				
MOPA	117	216	54	1.05				
1-crystal ICSHG oscillator	34	108	31	1.05				
2-crystal ICSHG oscillator	62	211	29	1.05				
Nanosecond					ns	kHz	mJ	kW
Q-switched oscillator	50	108	46	1.10	16–45	20–100	0.5–2	11–120
Cavity-dumped QS oscillator	47	108	44	1.15	6	30–100	0.4–1.5	70–250
CDQS +SHG	31		71	1.2	5.5	30–100	0.18–1	33–180
Picosecond					ps	MHz	μ J	kW
Mode-locked oscillator	56	108	52	1.05	33	110	0.5	15
Mode-locked MOPA	111	216	52	1.05	33	110	1	30
Mode-locked MOPA + SHG	87		80	1.2			0.79	
Mode-locked MOPA + THG	35		33	1.4			0.32	

source such as the Q-switched oscillator and to a greater extent the cavity-dumped Q-switched laser demonstrated in this work will allow for increasing the speed of existent processes operated with lower repetition-rate short-pulse lasers.

High cw powers in the visible or UV spectral region are difficult to achieve, since the design of intracavity-doubled and to a much greater extent intracavity-tripled oscillators can be very problematic. Furthermore when wavelengths other than the harmonics of the IR fundamental wavelength are sought, OPOs or a combination of an OPO and SFM stages, such as for RGB generation, are necessary. Thus the high peak power of a pulsed source is needed to reach high conversion efficiencies, yet the low repetition rate and high pulse energy is not acceptable for applications that essentially need a cw radiation. Mode-locked lasers producing high repetition-rate but low-energy picosecond pulse trains are often used as quasi-cw sources, yet allowing efficient extracavity nonlinear interactions. The 56 W 110 MHz mode-locked oscillator demonstrated in this work, efficiently amplified to 111 W, proved to be very efficiently converted to the green and UV, although more advanced tripling concepts should allow for the generation of > 45 W at 355 nm.

The wide range of high-power systems demonstrated in this work illustrates the benefits of the optimized pumping of Nd:YVO₄ at 888 nm, maintaining its highly-desirable characteristics such as a high gain and polarized output, while extending its power capabilities far beyond regular 808 nm pumped systems. This improvement should allow Nd:YVO₄ systems to compete

in the ~ 100 W average output power range with high-power technologies such as disks and fibers, which often struggle in the generation of short pulses because of their low gain and strong non-linear effects, respectively.

Bibliography

- [1] D. Lee and P. F. Moulton, “High-efficiency, high-power, OPO-based RGB source,” in *Conference on Lasers and Electro-Optics*, Summaries of papers presented at the Conference (Optical Society of America, 2001), 424.
- [2] R. Wallenstein, B. Henrich, T. Herrmann, J. Kleinbauer, R. Knappe, and A. Nebel, “Concepts and technologies of advanced RGB sources,” in *Advanced Solid-State Lasers*, M. Fermann and L. Marshall, eds., Vol. 68 of Trends in Optics and Photonics Series (Optical Society of America, 2002), TuA1.
- [3] F. Brunner, E. Innerhofer, S. V. Marchese, T. Südmeyer, R. Paschotta, T. Usami, H. Ito, S. Kurimura, K. Kitamura, G. Arisholm, and U. Keller, “Powerful red-green-blue laser source pumped with a mode-locked thin disk laser,” *Opt. Lett.* **29**, 1921–1923 (2004).
- [4] Y. F. Chen, Y. P. Lan, and S. C. Wang, “Efficient high-power diode-end-pumped TEM₀₀ Nd:YVO₄ laser with a planar cavity,” *Opt. Lett.* **25**, 1016–1018 (2000).
- [5] N. Hodgson, D. Dudley, L. Gruber, W. Jordan, and H. Hoffman, “Diode end-pumped, TEM₀₀ Nd:YVO₄ laser with output power greater than 12 W at 355 nm,” in *Conference on Lasers and Electro-Optics*, Technical Digest (Optical Society of America, Washington, D.C., 2001), 389–390, paper CThC4.
- [6] C. X. Wang, G. Y. Wang, A. V. Hicks, D. R. Dudley, H. Y. Pang, and N. Hodgson, “High-power q-switched TEM₀₀ mode diode-pumped solid state lasers with > 30 W output power at 355 nm,” in *Proc. SPIE*, Int. Soc. Opt. Eng. **6100**, 610019 (2006).
- [7] M. Frede, R. Wilhelm, and D. Kracht, “250 W end-pumped Nd:YAG laser with direct pumping into the upper laser level,” *Opt. Lett.* **31**, 3618–3619 (2006).
- [8] D. Dudley, N. Hodgson, H. Hoffman, and F. Kopper, “Direct 880 nm diode-pumping of vanadate lasers,” in *Conference on Lasers and Electro-Optics*, Technical Digest (Optical Society of America, Washington, D.C., 2002), 176–177.
- [9] R. Wilhelm, M. Frede, and D. Kracht, “Power Scaling of End-Pumped Nd:YAG Rod Lasers into the Kilowatt Region,” in *Advanced Solid-State Photonics*, OSA Technical Digest Series (CD) (Optical Society of America, 2007), paper MB19.

- [10] D. Freiburg, R. Wilhelm, M. Frede, D. Kracht, K. Dupré, and L. Ackermann, “End-Pumped Nd:YAG Laser Applying a Novel Laser Crystal with Longitudinal Hyperbolic Dopant Distribution,” in *Advanced Solid-State Photonics*, Technical Digest (Optical Society of America, 2006), paper WE6.
- [11] Onyx Optics, www.onyxoptycs.com.
- [12] D. J. Ripin, J. R. Ochoa, R. L. Aggarwal, and T. Y. Fan, “165 W cryogenically cooled Yb:YAG laser,” *Opt. Lett.* **29**, 2154–2156 (2004).
- [13] Y. Hirano, Y. Koyata, S. Yamamoto, K. Kasahara, and T. Tajime, “208-W TEM₀₀ operation of a diode-pumped Nd:YAG rod laser,” *Opt. Lett.* **24**, 679–681 (1999).
- [14] A. Dergachev and P. F. Moulton, “Short-pulse, high-repetition rate, high-power Nd:YLF MOPA system,” in *Advanced Solid-State Photonics*, Technical Digest (Optical Society of America, 2002), paper WD2.
- [15] K. Dua, D. Li, H. Zhang, P. Shi, X. Wei, and R. Diart, “Electro-optically Q-switched Nd:YVO₄ slab laser with a high repetition rate and a short pulse width,” *Opt. Lett.* **28**, 87–89 (2003).
- [16] N. Hodgson, H. J. Hoffman, V. Ter-Mikirtychev, and W. Jordan, “Diode-pumped, 220 W ultra-thin slab Nd:YAG laser with near-diffraction limited beam quality,” in *Lasers and Electro-Optics*, Technical Digest (Optical Society of America, 2002), 264–265.
- [17] A. Minassian, B. Thompson, and M. Damzen, “Ultrahigh-efficiency TEM₀₀ diode-side-pumped Nd:YVO₄ laser,” *Appl. Phys. B* **76**, 341–343 (2003).
- [18] A. Giesen, H. Hügel, A. Voss, K. Wittig, U. Brauch, and H. Opower, “Scalable concept for diode-pumped high-power solid-state lasers,” *Appl. Phys. B* **58**, 365–372 (1994).
- [19] E. Innerhofer, T. Südmeyer, F. Brunner, R. Häring, A. Aschwanden, R. Paschotta, C. Hönniger, M. Kumbar, and U. Keller, “60 W average power in 810 fs pulses from a thin-disk Yb:YAG laser,” *Opt. Lett.* **28**, 367–369 (2003).
- [20] Trumpf Laser GmbH, www.trumpf-laser.com.
- [21] ELS Monodisk-MP data sheet, www.sahajanand.eu.
- [22] Time-bandwidth products, www.tbwp.com.
- [23] L. E. Hunziker, Q.-Z. Shu, D. Bauer, C. Ihli, G. J. Mahnke, M. Rebut, J. R. Chilla, A. L. Caprara, H. Zhou, E. S. Weiss, and M. K. Reed, “Power-scaling of optically-pumped semiconductor lasers,” in *Proc. SPIE*, Int. Soc. Opt. Eng. **6451**, 64510A (2007).
- [24] A. Liu, M. A. Norsen, and R. D. Mead, “60-W green output by frequency doubling of a polarized Yb-doped fiber laser,” *Opt. Lett.* **30**, 67–69 (2005).

- [25] P. Dupriez, J. K. Sahu, Y. Jeong, A. Malinowski, D. J. Richardson, and J. Nilsson, “High-power high-brightness green laser based on a frequency doubled picosecond fiber laser,” in *Proc. SPIE*, Int. Soc. Opt. Eng. **6453**, 64531H (2007).
- [26] J. Limpert, O. Schmidt, J. Rothhardt, F. Röser, T. Schreiber, A. Tünnermann, S. Ermeneux, P. Yvernault, and F. Salin, “Extended single-mode photonic crystal fiber lasers,” *Opt. Express* **14**, 2715–2720 (2006).
- [27] J. R. O’Connor, “Unusual crystal-field energy levels and efficient laser properties of YVO₄:Nd,” *Appl. Phys. Lett.* **9**, 407–409 (1966).
- [28] A. A. Kaminskii, *Laser Crystals*, Springer-Verlag, second ed., 1990.
- [29] P. P. Yaney and L. G. DeShazer, “Spectroscopic studies and analysis of the laser states of Nd³⁺ in YVO₄,” *J. Opt. Soc. Am.* **66**, 1405–1414 (1976).
- [30] Z. Ichalalène, *Étude par spectroscopies Fourier et Raman du matériau laser YVO₄ dopé au néodyme*. PhD thesis, Université de Sherbrooke, 1999.
- [31] O. Svelto, *Principle of Lasers*, Plenum Press, fourth ed., 1998.
- [32] Casix Nd:YVO₄ data sheet, www.casix.com.
- [33] W. Koechner, *Solid-State Laser Engineering*, Springer, 1999.
- [34] Nd:YVO₄ absorption spectrum, formerly available on the NASA website.
- [35] R. D. Peterson, H. Jenssen, and A. Cassanho, “Investigation of the spectroscopic properties of Nd:YVO₄,” in *Advanced Solid-State Lasers*, M. Fermann and L. Marshall, eds., *Trends in Optics and Photonics Series* **68**(paper TuB17), 294–298 (2002).
- [36] R. Lavi, S. Jackel, Y. Tzuk, M. Winik, E. Lebiush, M. Katz, and I. Paiss, “Efficient pumping scheme for neodymium-doped materials by direct excitation of the upper lasing level,” *Appl. Opt.* **38**, 7382–7385 (1999).
- [37] A. W. Tucker, M. Birnbaum, C. L. Fincher, and J. W. Erler, “Stimulated-emission cross section at 1064 and 1342 nm in Nd:YVO₄,” *J. Appl. Phys.* **48**, 4907–4911 (1977).
- [38] C. Czeranowsky, M. Schmidt, E. Heumann, G. Huber, S. Kutovoi, and Y. Zavartsev, “Continuous wave diode pumped intracavity doubled Nd:GdVO₄ laser with 840 mw output power at 456 nm,” *Opt. Commun.* **205**, 361–365 (2002).
- [39] Z. Huang, Y. Huang, Y. Chen, and Z. Luo, “Theoretical study on the laser performances of Nd³⁺:YAG and Nd³⁺:YVO₄ under indirect and direct pumping,” *J. Opt. Soc. Am. B* **22**, 2564–2569 (2005).
- [40] L. J. Rosenkrantz, “GaAs diode-pumped Nd:YAG laser,” *J. Appl. Phys.* **43**, 4603 (1972).

- [41] F. S. Ermeneux, C. Goutaudier, R. Moncorgé, Y. Sun, R. L. Cone, E. Zannoni, E. Cavalli, and M. Bettinelli, “Multiphonon relaxation in YVO₄ single crystals,” *Phys. Rev. B* **61**, 3915–3921 (2000).
- [42] Nd:YVO₄ absorption spectrum measurements provided by Dr. Johannes L’huillier, Technische Universität Kaiserslautern.
- [43] C. Theobald, *Diode-pumped ultrafast lasers for the generation of picosecond pulse-bursts with high average power and energy using Q-switch mode locking*. PhD thesis, Technische Universität Kaiserslautern, 2007.
- [44] V. Lupei, N. Pavel, and T. Taira, “Highly efficient laser emission in concentrated Nd:YVO₄ components under direct pumping into the emitting level,” *Opt. Commun.* **201**, 431–435 (2002).
- [45] M. Okida, M. Itoh, T. Yatagai, H. Ogilvy, J. Piper, and T. Omatsu, “Heat generation in Nd doped vanadate crystals with 1.34 μm laser action,” *Opt. Express* **13**, 4909–4915 (2005).
- [46] C. Bibeau, S. A. Payne, and H. T. Powell, “Direct measurements of the terminal laser level lifetime in neodymium-doped crystals and glasses,” *J. Opt. Soc. Am. B* **12**, 1981 (1995).
- [47] L. Krainer, R. Paschotta, M. Moser, and U. Keller, “77 Ghz soliton modelocked Nd:YVO₄ laser,” *Electron. Lett.* **36**, 1846–1848 (2000).
- [48] Y. Chen, C. Liao, Y. Lan, and S. Wang, “Determination of the Auger upconversion rate in fiber-coupled diode end-pumped Nd:YAG and Nd:YVO₄ crystals,” *Applied Physics B* **70**, 487–490 (2000).
- [49] T. Chuang and H. R. Verdún, “Energy transfer up-conversion and excited state absorption of laser radiation in Nd:YLF laser crystals,” *IEEE J. Quantum Electron.* **32**, 79–91 (1996).
- [50] L. Fornasiero, S. Kück, T. Jensen, G. Huber, and B. H. T. Chai, “Excited state absorption and stimulated emission of Nd³⁺ in crystals. Part 2: YVO₄, GdVO₄, and Sr₅(PO₄)₃F,” *Appl. Phys. B* **67**, 549–553 (1998).
- [51] Y. Guyot and R. Moncorgé, “Excited-state absorption in the infrared emission domain of Nd³⁺-doped Y₃Al₅O₁₂, YLiF₄, and LaMgAl₁₁O₁₉,” *J. Appl. Phys.* **73**, 8526–8530 (1993).
- [52] S. Guy, C. Bonner, D. Shepherd, D. Hanna, A. Tropper, and B. Ferrand, “High-inversion densities in Nd:YAG: upconversion and bleaching,” *IEEE J. Quantum Electron.* **34**, 900–909 (1998).
- [53] I. O. Musgrave, W. A. Clarkson, and D. C. Hanna, “Detailed study of thermal lensing in Nd:YVO₄ under intense diode end-pumping,” in *Conference on Lasers and Electro-Optics*, Technical Digest (Optical Society of America, 2001), CTuM26, 171–172 .

- [54] S. Reuter, “Numerische und experimentelle Untersuchung der mechanischen und optischen Eigenschaften von Neodym-dotierten Lasermaterialien unter thermischer Belastung,” Master’s thesis, Universität Kaiserslautern, 2000.
- [55] M. Pollnau, P. J. Hardman, W. A. Clarkson, and D. C. Hanna, “Upconversion, lifetime quenching, and ground-state bleaching in $\text{Nd}^{3+}:\text{LiYF}_4$,” *Opt. Commun.* **147**, 203–211 (1998).
- [56] V. Ostroumov, T. Jensen, J.-P. Meyn, G. Huber, and M. A. Noginov, “Study of luminescence concentration quenching and energy transfer upconversion in Nd-doped $\text{LaSc}_3(\text{BO}_3)_4$ and GdVO_4 laser crystals,” *J. Opt. Soc. Am. B* **15**, 1052–1060 (1998).
- [57] Y. F. Chen, L. J. Lee, T. M. Huang, and C. L. Wang, “Study of high-power diode-end-pumped Nd:YVO₄ laser at 1.34 μm : influence of Auger upconversion,” *Opt. Commun.* **163**, 198–202 (1999).
- [58] Y. F. Chen, “Design criteria for concentration optimization in scaling diode end-pumped lasers to high powers: influence of thermal fracture,” *IEEE J. Quantum Electron.* **35**, 234–239 (1999).
- [59] Y. Chen, T. Liao, C. Kao, T. Huang, K. Lin, and S. Wang, “Optimization of fiber-coupled laser-diode end-pumped lasers: influence of pump-beam quality,” *IEEE J. Quantum Electron.* **32**, 2010–2016 (1996).
- [60] N. Hodgson and H. Weber, “Influence of spherical aberration of the active medium on the performance of Nd:YAG lasers,” *IEEE J. Quantum Electron.* **29**, 2497 (1993).
- [61] X. Peng, A. Asundi, Y. Chen, and Z. Xiong, “Study of the mechanical properties of Nd:YVO₄ crystal by use of laser interferometry and finite-element analysis,” *Appl. Opt.* **40**, 1396–1403 (2001).
- [62] Y. F. Chen, “Influence of thermal fracture on scaling diode end-pumped lasers to high powers,” in *Conference on Lasers and Electro-Optics*, Technical Digest (Optical Society of America, Washington, D.C., 1999), CTuK28, 128.
- [63] E. Cheng, D. Dudley, W. Nighan, J. Kafka, D. Spence, and D. Bell, *Lasers with low-doped gain medium*, U.S. Patent 6,185,235 (February 6, 2001).
- [64] R. N. Hall, G. E. Fenner, J. D. Kingsley, T. J. Soltys, and R. O. Carlson, “Coherent Light Emission From GaAs Junctions,” *Phys. Rev. Lett.* **9**, 366–368 (1962).
- [65] LIMO Lissotschenko Mikrooptik GmbH, www.limo.de.
- [66] Laserline GmbH, www.laserline.de.
- [67] DILAS Diodenlaser GmbH, www.dilas.de.
- [68] JENOPTIK Laserdiode GmbH, www.jold.de.

- [69] Y. F. Chen, T. M. Huang, C. F. Kao, C. L. Wang, and S. Wang, "Optimization in scaling fiber-coupled laser-diode end-pumped lasers to higher power: influence of thermal effect," *IEEE J. Quantum Electron.* **33**, 1424–1429 (1997).
- [70] LAS-CAD GmbH, www.las-cad.com.
- [71] A. Petersen, "Diode pumped, fiber coupled laser with depolarized pump beam." U.S. Patent 5,999,544 (December 7, 1999).
- [72] R. Knappe and A. Nebel, "Device and method for optically exciting laser-active crystals with polarization-dependent absorption," European Patent EP1466392 (Oct. 13, 2004).
- [73] N. Hodgson and H. Weber, *Laser resonators and beam propagation*, Springer, second ed., 2005.
- [74] M. S. Keirstead, J. W. L. Nighan, and T. M. Baer, "Thermal lens of controlled ellipticity," U.S. Patent 5,561,547 (Oct 1, 1996).
- [75] Bookham, www.bookham.com.
- [76] W. A. Clarkson and D. C. Hanna, "Two-mirror beam-shaping technique for high-power diode bars," *Opt. Lett.* **21**, 375 (1996).
- [77] A. Mikhailov, "Arrangement and apparatus for optical beam transformation," U.S. Patent 7,027,228 (April 11, 2006).
- [78] K. Du and P. Loosen, "Device with at least one beam source and an arrangement for geometric reshaping of the radiation field emitted by the beam source," U.S. Patent 6,324,190 (Nov 27, 2001).
- [79] V. Krause and C. Ullmann, "Laser optics and diode laser," U.S. Patent 5,986,794 (November 16, 1999).
- [80] W. A. Clarkson, "Thermal effects and their mitigation in end-pumped solid-state lasers," *J. Phys. D: Appl. Phys.* **34**, 2381–2395 (2001).
- [81] V. Magni, "Multielement stable resonators containing a variable lens," *J. Opt. Soc. Am. A* **4**, 1962–1969 (1987).
- [82] C. X. Wang, A. V. Hicks, and J. E. C. Rea, "Laser rod thermalization," U.S. Patent 6,414,980 (Jul 2, 2002).
- [83] I. Moshe, S. Jackel, and R. Lallouz, "Working beyond the static limits of laser stability by use of adaptive polarization-conjugation optics," *Appl. Opt.* **37**, 6415–6420 (1998).
- [84] K. J. Weingarten, B. Braun, and U. Keller, "In situ small-signal gain of solid-state lasers determined from relaxation oscillation frequency measurements," *Opt. Lett.* **19**, 1140–1142 (1994).

- [85] S. Forget, F. Balembois, P. Georges, and P. J. Devilder, “A new 3D multipass amplifier based on Nd:YAG or Nd:YVO₄ crystals,” *Appl. Phys. B* **75**, 481–485 (2002).
- [86] J. Kim, M. Yarrow, and W. Clarkson, “High power single-frequency continuous-wave Nd:YVO₄ master-oscillator power amplifier,” *Appl. Phys. B* **85**, 539–543 (2006).
- [87] S. Forget, *Une source ultraviolette*. PhD thesis, Université Paris-Sud, 2003.
- [88] W. L. Nighan, Jr., and J. Cole, “>6W of stable, 532nm, TEM₀₀ output at 30% efficiency from an intracavity-doubled, diode-pumped multi-axial mode Nd:YVO₄ laser,” in *Advanced Solid State Lasers*, OSA Trends in Optics and Photonics Series **1** (Optical Society of America, 1996), PD4.
- [89] M. D. Selker, T. J. Johnston, G. Frangineas, J. L. Nightingale, and D. K. Negus, “>8.5 Watts of single frequency 532-nm light from a diode pumped intra-cavity ring laser,” in *Conference on Lasers and Electro-Optics*, Technical Digest (Optical Society of America, Washington, D.C., 1996), CPD21.
- [90] N. Hodgson, “Continuous-wave blue and green TEM₀₀ mode solid state lasers: state-of-the-art and applications,” in *Solid State Lasers XIV*, Proc. SPIE **5707**, 1–15 (2005).
- [91] G. D. Boyd and D. A. Kleinman, “Parametric interaction of focused gaussian light beams,” *J. Appl. Phys.* **39**, 3597–3639 (1968).
- [92] Castech products catalogue, www.castech.com.
- [93] J. T. Lin, J. L. Montgomery, and K. Kato, “Temperature-tuned noncritically phase-matched frequency conversion in LiB₃O₅ crystal,” *Opt. Commun.* **80**, 159 (1990).
- [94] J.-W. Pieterse, A. B. Petersen, C. Pohalsky, E. Cheng, R. Lane, and W. L. Nighan, Jr., “Q-switched laser system providing uv light,” U.S. Patent 5,835,513 (Nov. 10, 1998).
- [95] Private communications with M. A. Herrmann from Cristal Laser, France.
- [96] SNLO nonlinear optics simulation software, www.snlo.com.
- [97] T. Baer, “Large-amplitude fluctuations due to longitudinal mode coupling in diode-pumped intracavity-doubled Nd:YAG lasers,” *J. Opt. Soc. Am. B* **3**, 1175 (1986).
- [98] L. R. Marshall, “Solving the green problem,” in *Advanced Solid State Laser*, OSA Trends in Optics and Photonics Series **10** (1997), VL4.
- [99] T. Baer, “Low amplitude noise, intracavity doubled laser,” U.S. Patent 5,627,849 (May 6, 1997).
- [100] C. Czeranowsky, V. Baev, and G. Huber, “Stabilization of intracavity frequency-doubled lasers with type I phase matching,” *Opt. Lett.* **28**, 2100 (2003).

- [101] W. Nighan, J. Cole, and T. Baer, “Diode pumped, multi axial mode, intracavity doubled laser,” U.S. Patent 5,446,749 (August 29, 1995).
- [102] V. Magni, G. Cerullo, S. D. Silvestri, O. Svelto, L. J. Qian, and M. Danailov, “Intracavity frequency doubling of a cw high-power TEM₀₀ Nd:YLF laser,” *Opt. Lett.* **18**, 2111 (1993).
- [103] X. Peng, L. Xu, and A. Asundi, “High-power efficient continuous-wave TEM₀₀ intracavity frequency-doubled diode-pumped Nd:YLF laser,” *Appl. Opt.* **44**, 800 (2005).
- [104] J. Kleinbauer, *Diode-pumped ultrafast lasers for the generation of picosecond pulses with a high energy and repetition rate based on Nd:YVO₄ and Nd:GdVO₄*. PhD thesis, Technische Universität Kaiserslautern, 2006.
- [105] Advanced Optical Technology Ltd, www.aotlasers.com.
- [106] Bergmann Messgeräte Entwicklung KG, www.bme-bergmann.de.
- [107] A.-A. Opto-Electronic, “Do you know acoustooptics?”, www.a-a.fr.
- [108] C. Veltkamp, A. B. Petersen, and J. D. Kafka, “Detailed single shot spectral diagnostics of Q-switched solid state lasers,” in *Solid State Lasers XVI: Technology and Devices*, Proc. SPIE **6451**, 64511E, 2007.
- [109] A. Vuylsteke, “Theory of laser regeneration switching,” *J. Appl. Phys.* **34**, 1615–1622 (1963).
- [110] W. R. Hook, R. H. Dishington, and R. P. Hilberg, “Laser cavity dumping using time variable reflection,” *Appl. Phys. Lett.* **9**, 125–127 (1966).
- [111] W. J. Rundle, “A ruby laser modified for pulse-transmission-mode cavity dumping,” *J. Appl. Phys.* **39**, 5338–5339 (1968).
- [112] W. J. Rundle, “Design and characteristics of a narrow-pulse PTM ruby oscillator-amplifier laser,” *IEEE J. Quantum Electron.* **5**, 342–343 (1969).
- [113] D. Maydan, “Fast modulator for extraction of internal laser power,” *J. Appl. Phys.* **41**, 1552–1559 (1970).
- [114] D. Maydan and R. B. Chesler, “Q-switching and cavity dumping of Nd:YAlG lasers,” *J. Appl. Phys.* **42**, 1031–1034 (1971).
- [115] H. A. Kruegle and L. Klein, “High peak power output, high PRF by cavity dumping a Nd:YAG laser,” *Appl. Opt.* **15**, 466–471 (1976).
- [116] R. B. Chesler and D. Maydan, “Calculation of Nd:YAlG cavity dumping,” *J. Appl. Phys.* **42**, 1028–1030 (1971).
- [117] F. Druon, F. Balembois, P. Georges, and A. Brun, “High-repetition-rate 300-ps pulsed ultraviolet source with a passively Q-switched microchip laser and a multipass amplifier,” *Opt. Lett.* **24**, 499–501 (1999).

- [118] CryLaS GmbH, www.crylas.de.
- [119] B. Braun, K. J. Weingarten, F. X. Kärtner, and U. Keller, “Continuous-wave mode-locked solid-state lasers with enhanced spatial hole burning - part I: Experiments,” *Appl. Phys. B* **61**, 429–437 (1995).
- [120] F. X. Kärtner, B. Braun, and U. Keller, “Continuous-wave mode-locked solid-state lasers with enhanced spatial hole burning - part II: Theory,” *Appl. Phys. B* **61**, 569–579 (1995).
- [121] C. Schäfer, “Aufbau und Charakterisierung passiv modengekoppelter, 888 nm gepumpter Nd:YVO₄-Hochleistungslaser,” Diplomarbeit, Technische Universität Kaiserslautern, 2007.
- [122] D. Woll, J. Schumacher, A. Robertson, M. A. Tremont, R. Wallenstein, M. Katz, D. Eger, and A. Engländer, “250 mW of coherent blue 460-nm light generated by single-pass frequency doubling of the output of a mode-locked high-power diode laser in periodically poled KTP,” *Opt. Lett.* **27**, 1055–1057 (2002).
- [123] H. A. Haus, “Theory of mode locking with a slow saturable absorber,” *IEEE J. Quantum Electron.* **11**, 736–746 (1975).
- [124] R. Paschotta and U. Keller, “Passive mode locking with slow saturable absorbers,” *Appl. Phys. B* **73**, 653–662 (2001).
- [125] H. A. Haus, “Theory of mode locking with a fast saturable absorber,” *J. Appl. Phys.* **46**, 3049–3058 (1975).
- [126] D. E. Spence, P. N. Kean, and W. Sibbett, “60-fsec pulse generation from a self-mode-locked Ti:sapphire laser,” *Opt. Lett.* **16**, 42–44 (1991).
- [127] M. Piche and F. Salin, “Self-mode locking of solid-state lasers without apertures,” *Opt. Lett.* **18**, 1041–1043 (1993).
- [128] J. Mark, L. Y. Liu, K. L. Hall, H. A. Haus, and E. P. Ippen, “Femtosecond pulse generation in a laser with a nonlinear external resonator,” *Opt. Lett.* **14**, 48–50, 1989.
- [129] E. P. Ippen, H. A. Haus, and L. Y. Liu, “Additive pulse mode locking,” *J. Opt. Soc. Am. B* **6**, 1736–1745 (1989).
- [130] U. Keller, “Ultrafast all-solid-state laser technology,” *Appl. Phys. B* **58**, 347–363 (1994).
- [131] M. Kaminska, Z. Liliental-Weber, E. R. Weber, T. George, J. B. Kortright, F. W. Smith, B.-Y. Tsaur, and A. R. Calawa, “Structural properties of As-rich GaAs grown by molecular beam epitaxy at low temperatures,” *Appl. Phys. Lett.* **54**, 1881–1883 (1989).
- [132] H. H. Tan, C. Jagadish, M. J. Lederer, B. Luther-Davies, J. Zou, D. J. H. Cockayne, M. Haiml, U. Siegner, and U. Keller, “Role of implantation-induced defects on the response time of semiconductor saturable absorbers,” *Appl. Phys. Lett.* **75**, 1437–1439 (1999).

- [133] BATOP GmbH, www.batop.de.
- [134] Hönninger, *Ultrafast Ytterbium-Doped Bulk Lasers and Laser Amplifiers*, no. ISBN: 3-89649-391-2, Hartung-Gorre Verlag, Konstanz, 1999.
- [135] U. Keller, K. J. Weingarten, F. X. Kärtner, D. Kopf, B. Braun, I. D. Jung, R. Fluck, C. Hönninger, N. Matuschek, and J. A. der Au, “Semiconductor saturable absorber mirrors (SESAM’s) for femtosecond to nanosecond pulse generation in solid-state lasers,” *IEEE J. Select. Topics Quantum Electron.* **2**, 435–453 (1996).
- [136] U. Keller, *Semiconductors and Semimetals*, vol. 59, ch. Semiconductor Nonlinearities for Solid-State Laser Modelocking and Q-Switching, pp. 211–286. Academic Press, San Diego, 1999.
- [137] C. Hönninger, R. Paschotta, F. Morier-Genoud, M. Moser, and U. Keller, “Q-switching stability limits of continuous-wave passive mode locking,” *J. Opt. Soc. Am. B* **16**, 46–56 (1999).
- [138] Private communications with M. Zorn at the Ferdinand-Braun-Institut für Höchstfrequenztechnik (FBH), Berlin, 2006.
- [139] G. Spühler, T. Südmeyer, R. Paschotta, M. Moser, K. Weingarten, and U. Keller, “Passively mode-locked high-power Nd:YAG lasers with multiple laser heads,” *Appl. Phys. B* **71**, 19–25 (2000).
- [140] Y. F. Chen, S. W. Tsai, Y. P. Lan, S. C. Wang, and K. F. Huang, “Diode-end-pumped passively mode-locked high-power Nd:YVO₄ laser with a relaxed saturable Bragg reflector,” *Opt. Lett.* **26**, 199–201 (2001).
- [141] D. Burns, M. Hetterich, A. I. Ferguson, E. Bente, M. D. Dawson, J. I. Davies, and S. W. Bland, “High-average-power (20-W) Nd:YVO₄ lasers mode locked by strain-compensated saturable Bragg reflectors,” *J. Opt. Soc. Am. B* **17**, 919–926 (2000).
- [142] S. Marzenell, R. Beigang, and R. Wallenstein, “Limitations and guidelines for measuring the spectral width of ultrashort light pulses with a scanning Fabry-Pérot interferometer,” *Appl. Phys. B* **71**, 185–191 (2000).
- [143] K. Sala, G. Kenney-Wallace, and G. Hall, “CW autocorrelation measurements of picosecond laser pulses,” *IEEE J. Quantum Electron.* **16**, 990–996 (1980).
- [144] B. Ruffing, A. Nebel, and R. Wallenstein, “High-power picosecond LiB₃O₅ optical parametric oscillators tunable in the blue spectral range,” *Appl. Phys. B* **72**, 137–149 (2001).
- [145] B. Wu, N. Chen, C. Chen, D. Deng, and Z. Xu, “Highly efficient ultraviolet generation at 355 nm in LiB₃O₅,” *Opt. Lett.* **14**, 1080–1081 (1989).
- [146] A. Nebel, B. Henrich, and T. Herrmann, “Device and method for converting an optical frequency,” Patent WO 03029892, DE 10147362 (Dec. 2, 2004).

-
- [147] J. L. Nightingale, "Poynting vector walk-off compensation in type II phasematching," U.S. Patent 5,136,597 (August 4, 1992).
 - [148] H. Hoffman, D. Spence, A. B. Petersen, and J. D. Kafka, "Methods and systems to enhance multiple wave mixing process," U.S. Patent Application 2006/0250677 (Nov. 9, 2006).
 - [149] Y. Taira, "Apparatus for wavelength conversion of laser light," U.S. Patent 5,309,454 (May 3, 1994).

Acknowledgments

I wish to address my most profound gratitude to Prof. Dr. Richard Wallenstein who gave me the opportunity to pursue a fascinating project in his research group. I couldn't have hoped stronger support for the technical choices that were made, although many involved costly long-term investments. I got the perfect blend of guidance and freedom for making my research work a fascinating and extremely motivating experience. Finally I will not forget the many informal discussions we had about lasers and physics, all very stimulative and informative.

I warmly thank Prof. Dr. René Beigang for accepting to act as second examiner of my work.

My collaboration with Lumera Laser GmbH and the input from Dr. Achim Nebel and Dr. Ralk Knappe allowed me to benefit from their immense knowledge in the field of laser design and nonlinear optics, which was strengthened by their successful industrialization of picosecond sources. I would also like to thank Dr. Bernhard Henrich and Dr. Thomas Herrmann who kindly shared their know-how on DPSS and mode-locked lasers. I can only wish the ever-growing Lumera team to make the best use of 888 nm pumping to develop and establish a large range of high-power industrial-grade lasers.

I was most lucky to work with Dipl.-Phys. Christoph Schäfer who brilliantly took over the development of 888 nm pumped sources and demonstrated much shorter ps pulses and ultra-low repetition-rate mode-locked oscillators. I was impressed by his sense of perfection, his ability to instantly grasp new ideas, and his creativity in devising new systems with striking performance.

The advice, availability, and friendliness of Peter Bohnert, Peter Fronhöffer, Karl Köhl, and Hermann Krenz were essential to getting crucial mechanical and electronic designs available for assembling new systems in the shortest time.

I am grateful to the members of the DPSS laser team in building 58, including Dr. Markus Serr, Dr. Jochen Kleinbauer, Dr. Sascha Reuter, Dr. Christian Theobald, Dr. Marco Weitz, Dr. Dirk Krennrich, and Dipl.-Phys. Markus Lührmann for the stimulative work atmosphere and for sharing their knowledge and know-how during our many conversations. I shall not forget Dr. Johannes L'huillier, Dipl.-Phys. Peter Haag, and Dr. Thorsten Andres who widened my knowledge by making me benefit from their expertise in laser and nonlinear crystals.

I wish to thank my colleagues from the diode-laser team, Dr. Marc Tremont, Dr. Harry Fuchs, Dr. Oliver Casel, Dr. Dirk Woll, Dipl.-Phys. Jahn Harlfinger, and Dipl.-Phys. Thorsten Ulm for their friendliness and the great atmosphere in the office.

I also wish to acknowledge the people who brought me to the world of lasers from the beginning of my studies, and gave me the opportunity to acquire know-how on lasers. What I learned during those practicals proved to be essential for the reflection, design, and experimental phases of my research project. My greatest thanks go to Dr. Patrick Georges and Dr. François Balembois at the Institut Supérieur d'Optique (Orsay, France) and Dr. Norman Hodgson, Dr. Hanna Hoffman, Dave Dudley, Dr. Oliver Mehl, and Will Jordan of Spectra-Physics, California.

None of this would have been possible without the constant support of my parents throughout my studies, ever trusting my choices and pushing me into achieving my goals.

Lebenslauf

Persönliche Daten

Name		Louis McDonagh
geboren am	28.08.1977	in Paris
Nationalität		französisch
Familienstand		ledig

Ausbildung

Promotion	07/2002 - 06/2007	Promotionsstudium an der TU Kaiserslautern
Studium	06/2001	Abschluß: DEA, Université Paris-Sud, Orsay
	09/1998 - 06/2001	Diplôme de l'Ecole Supérieure d'Optique
	09/1995 - 05/1998	Ecole Supérieure d'Optique, Orsay, Frankreich
Schulbildung	05/1995	Classes préparatoires PCSI, PSI, PSI* , Lycée Chaptal, Paris
	1994-1995	Abschluß: Baccalauréat S
	1992-1994	Terminale S, Lycée Charlemagne, Paris
	1988-1992	Lycée Louis Le Grand, Paris
	1983-1988	Collège La Rochefoucauld, Paris
		Ecole primaire La Rochefoucauld, Paris

Beruf

02/2009 -	Nanosekunden-Laser Produktmanager bei der Firma Lumera Laser, Kaiserslautern
06/2007 - 01/2009	F&E Laser Ingenieur bei der Firma Eolite Systems, Bordeaux, Frankreich
07/2002 - 06/2007	Wissenschaftlicher Mitarbeiter am Fachbereich Physik der TU Kaiserslautern
05/2001 - 06/2002	F&E Praktikum bei der Firma Spectra-Physics, Mountain View, California
06/2000 - 07/2000	Praktikum bei der Institut d'Optique Théorique et Appliquée, Orsay

